Title
High Resolution Photoelectron Spectroscopy of Metal Clusters and High Temperature Species

Author
Wang, L.-S.

Publication Date
1990-02-01

LBL-28606

Lawrence Berkeley Laboratory
UNIVERSITY OF CALIFORNIA

Materials & Chemical
Sciences Division

High Resolution Photoelectron Spectroscopy of Metal Clusters and High Temperature Species

L.-S. Wang
(Ph.D. Thesis)

February 1990

Prepared for the U.S. Department of Energy under Contract Number DE-AC03-76SF00098.

DISCLAIMER

LBL-28606

High Resolution Photoelectron Spectroscopy of Metal Clusters and High Temperature Species

Lai-Sheng Wang
Ph.D. Thesis

Department of Chemistry
University of California at Berkeley

and

Materials and Chemical Sciences Division
Lawrence Berkeley Laboratory
University of California
Berkeley, CA 94720

February 1990

This work was supported by the Director, Office of Energy Research, Office of Basic Energy Sciences, Chemical Sciences Division of the U.S. Department of Energy under Contract No. DE-AC03-76SF00098.

High Resolution Photoelectron Spectroscopy of Metal Clusters and High Temperature Species

by

Lai-Sheng Wang

Abstract

The thrust of this dissertation is to investigate the high resolution photoelectron spectroscopy of metal clusters and high temperature species. To that end, a high temperature molecular beam source has been built, which is capable of generating continuous and internally-cooled beams of cluster species and high temperature species. A number of high temperature species (SnSe, SnTe, PbSe, and PbTe; Se_2 and Te_2; $ZnCl_2$, $MnCl_2$, and $NiCl_2$) and group V element clusters (As_2, Sb_2, and Bi_2; P_4, As_4, and Sb_4) have been measured with 12 -15 meV resolution. Vibrational structure is resolved for the first time for most of these species, and fundamental spectroscopic constants are obtained. Information about the electronic structure and chemical bonding is derived from the high resolution spectra and from comparisons with theoretical calculations.

Chapter 3 presents the vibrationally-resolved photoelectron spectra of the heavy group IV-VI diatomics, where experimentally-obtained ionization potentials and spectroscopic constants are compared with theoretical calculations by Balasubramanian. The agreement is very good, and relativistic effects are shown to play an important role in these heavy diatomics, resulting in avoided curve crossings in the $^2\Sigma^+_{1/2}$ and $^2\Pi_{1/2}$ states for all the four molecular ions ($SnSe^+$, $SnTe^+$, $PbSe^+$, and $PbTe^+$). The importance of the relativistic effects and chemical bonding in the heavy diatomics are discussed. The Se_2 and

Te_2 molecules are the subjects of Chapter 4, where vibrationally-resolved photoelectron spectra of the ground states of Se_2^+ and Te_2^+ are reported.

Chapter 5 describes the experiments on the group V element clusters. Vibrational structure is resolved explicitly for As_2^+ and for the $^2A_1$ state of P_4^+ and As_4^+. Strong Jahn-Teller distortion takes place in the ^2E state of the tetrameric ions in the $\nu_2(e)$ vibrational mode, reducing the tetrahedral geometry of the neutral molecule to D_{2d} symmetry in the ground state of the cations. The experimental spectra are compared with the theoretical calculations of the E⊗e Jahn-Teller problem by Ghelichkhani and Grant, and Jahn-Teller stabilization energies of 0.65 eV, 0.84 eV, and 1.4 eV are derived for P_4^+, As_4^+, and Sb_4^+, respectively. Both Jahn-Teller and spin-orbit effects are found to be operative in the $^2T_2$ states of the tetrameric ions, with the spin-orbit effect being dominant in Sb_4^+ and the Jahn-Teller effect dominant in P_4^+.

Chapter 6 deals with the high resolution photoelectron spectra of $ZnCl_2$, $MnCl_2$, and $NiCl_2$. Vibrational structure is resolved for $ZnCl_2$ and the $C^2\Sigma_g^+$ state of $ZnCl_2^+$ is found to have a double-well potential along the Q_3 coordinate, with an asymmetric $ZnCl_2^+$ geometry of $[Cl\cdots Zn{-}Cl]^+$ in its ground vibrational state. Involving the open-shell transition elements, $MnCl_2$ and $NiCl_2$ are much more complicated in terms of both their electronic structure and their spectroscopy. Even though many final states are anticipated for ionization of the open-shell d orbitals, only a few states are observed, which is explained in $MnCl_2$ by the one-electron spin selection rule. Besides the spin selection rule, a propensity toward high spin states is proposed to explain the spectrum of $NiCl_2$. From the metal d orbital and ligand orbital splittings, the degree of covalent bonding is inferred to be in the order of : $MnCl_2 > NiCl_2 > ZnCl_2$.

High Resolution Photoelectron Spectroscopy of Metal Clusters and High Temperature Species

Contents

Abstract 1

Chapter 1 Introduction 1

1.1 Photoelectron Spectroscopy 1

1.2 High Temperature Photoelectron Spectroscopy and Studies of Metal Clusters 4

References 6

Chapter 2 Experimental Aspects 8

2.1 Introduction 8

2.2 The Photoelectron Spectrometer 9

2.2.1 The Photoelectron Analyzer and Vacuum System 9

2.2.2 The Photon Source 10

2.3 The Quadruple Mass Spectrometer 12

2.4 The High Temperature Molecular Beam Source 13

2.4.1 Design Considerations 13

2.4.2 Construction 14

2.4.3 Operation 17

2.4.4 Performance 18

References 21

Figure Captions 22

Figures 25

Chapter 3 Photoelectron Spectroscopy and Electronic Structure of Heavy Group IV-VI Diatomics 42

Abstract 42

3.1 Introduction 44

3.2 Experimental 45

3.3 Method of Theoretical Calculations 46

3.4 Results and Data Analysis 49

3.5 Discussion 51

3.5.1 Comparison between experimental and Theoretical Spectroscopic Constants 51

3.5.2 Nature of the Electronic States and the Potential Energy Curves 53

3.5.3 Nature of the Chemical Bonds of the Heavy Group IV-VI Diatomics 55

3.6 Conclusions 57

References 59

Tables 62

Figure Captions 68

Figures 69

Chapter 4 Vibrational Spectra of Se_2^+ and Te_2^+ in Their Ground States 79

Abstract 79

4.1 Introduction 80

4.2 Experimental 80

4.3 Results and Discussion 81

References 84

Tables 85

Figure Captions 87

Figures 88

Chapter 5 Photoelectron Spectroscopy of Clusters of Group V Elements 92

Abstract 92

5.1 Introduction 94

5.2 Experimental 96

5.3 The Dimers: As_2, Sb_2, and Bi_2 97

5.4 The Tetramers: P_4, As_4, and Sb_4 100

5.4.1 The Jahn-Teller Theorem and the Ham Effect 100

5.4.1.1 The Jahn-Teller Theorem 100

5.4.1.2 The Ham Effect: Jahn-Teller Effect vs. Spin-Orbit Effect 102

5.4.2 Results. 102

5.4.3 The $(1e)^{-1}$ Bands: Theoretical Treatment of the E⊗e Jahn-Teller Effect 104

5.4.3.1 Theoretical Background of the E⊗e Jahn-Teller Problem 104

5.4.3.2 Exact Nonadiabatic Calculations 107

5.4.3.3 Distortion and Hindered Fluxionality in the Ground State of P_4^+ 108

5.4.3.4 Strong Vibronic Couplings in As_4^+ and Sb_4^+: The Case for Cone Resonances in Realistic Systems 112

5.4.4 The $(2t_2)^{-1}$ Bands: Jahn-Teller Effect vs. Ham Effect 113

5.4.5 The $(1a_1)^{-1}$ Bands: Franck-Condon Analysis 117

5.5 Discussion 118

5.6 Summary 121

References 123

Tables 128

Figure Captions 135

Figures 138

Chapter 6 Electronic Structure and Chemical Bonding of the First Row Transition Metal Dichlorides, $MnCl_2$, $NiCl_2$, and $ZnCl_2$: A High Resolution Photoelectron Spectroscopic Study 160

Abstract 160

6.1 Introduction 162

6.2 Experimental 164

6.3 Results and Discussion 165

6.3.1 General Remarks 165

6.3.2 $ZnCl_2$ 167

6.3.3 $MnCl_2$ 170

6.3.4 $NiCl_2$ 173

6.3.5 Discussion 174

6.4 Summary 176

References 178

Tables 181

Figure Captions 188

Figures 189

Appendix

Publications From Graduate Work 198

Acknowledgment 201

Chapter 1

Introduction

1.1 Photoelectron Spectroscopy

Photoelectron spectroscopy (PES) is the application of the photoelectric effect[1] to studies of the electronic structure of matter. In PES, monochromatic radiation interacts with matter and emit photoelectrons, and the kinetic energy spectrum of the photoemitted electrons is measured, from which information about the electronic structure of the underling subjects (atoms, molecules, surfaces, solids, etc.) is derived. Historically, PES was divided into ESCA (electron spectroscopy for chemical analysis) or XPS (x-ray photoelectron spectroscopy),[2] where x-ray photons were used to eject core-electrons, and UPS (ultraviolet photoelectron spectroscopy) or simply PES,[3] where ultraviolet photons were used to eject valence electrons. With increasing availability of laser sources and synchrotron radiation light sources, there is now available a continuous spectrum of photons from a few eV to thousands of eV, which are being used in photoelectron spectroscopy. This thesis concerns only molecular PES with the HeI (584Å) line, and the main theme is to investigate the most chemically-relevant electrons, the valence electrons of high temperature species and metal clusters, at the highest resolution possible. The HeI line is still a preferred photon source in this study, because it has higher flux and narrower

line width than the current synchrotron radiation light sources, and has higher energy than the available laser sources, allowing ionization of a range of valence electrons. However, higher flux and resolution synchrotron radiation beam lines and new laser methods of UV photon generation are beginning to be available, which will surely advance PES to a new level of sophistication.

In molecular PES, a molecule absorbs a photon of energy hν and emits an electron. The resulting molecular ion can be left in one of its many electronic states and ro-vibrational states. The photoionization process can be expressed as:

$$AB\ (X;\ v''=0,\ j''=0) + h\nu \rightarrow AB^{+}\ (X, A, B, C,...;\ v';\ j') + e^{-}\ . \qquad (1)$$

In a molecular beam experiment, the molecule, AB, can be assumed to be in its ground vibrational and rotational state. However, in a conventional gas cell experiment, the molecule can have considerable rotational excitation, and some vibrational excitation as well. Energy conservation dictates that the photon energy equals the ionization energy (E_I) plus the electron kinetic energy (E_k):

$$h\nu = E_I + E_k\ . \qquad (2)$$

The kinetic energy of the molecule is negligible because of the mass disparity between the molecule and the electron. The outstanding feature of PES is that one obtains an ionization energy spectrum by measuring the electron kinetic energy spectrum, through Eq. (2). Interpretation of PES is usually made through the one-electron molecular orbital (MO) theory by what is called Koopmans' Theorem,[4] which states that each ionization energy, $(E_I)_j$ is approximately equal in magnitude to an orbital energy, ε_j:

$$(E_I)_j \cong -\varepsilon_j\ . \qquad (3)$$

This means that each electron is removed from a MO during photoionization, and the PE spectrum is a direct representation of the MO energy level of the molecule. In spite of its various limitations, Koopmans' Theorem is a useful and powerful approximation for interpreting PE spectra. Indeed, PES provided unique evidence for the validity of the MO

model, and profoundly advanced our understanding of electronic structure and chemical bonding in molecules.

The ionization energy, E_I, in Eq. (2) contains internal energies of the molecular ion AB^+:

$$E_I = E_A + E_V^+ + E_R^+ \qquad (4)$$

where E_A is the adiabatic ionization energy, E_V^+ the vibrational energy, and E_R^+ the rotational energy. Vibrational energy levels are usually well resolved in PES for light small molecules, while rotational resolution has been possible only for the lightest diatomics, the hydrogen molecule and its deuterides.[5] It is through the individual terms in Eq. (4) that important information is derived about the underlying molecule. E_A gives the ionization energy spectrum, while E_V^+ yields valuable spectroscopic information about the molecular ion. In fact, spectroscopic constants for most molecular ions have been derived by PES.[6] An individual photoelectron band shape, determined by E_V^+, provides information about the MO from which an electron is removed: e.g., whether it is bonding, nonbonding, or antibonding. Since the rotational energy levels cannot be resolved except in the lightest diatomics, E_R^+ often appears only as line broadening in molecular PES.

It is, therefore, of paramount importance in PES to have high resolution. A major advance was achieved in 1981 by Pollard, Trevor, Lee, and Shirley,[7] who combined the supersonic molecular beam technique with PES, which eliminated the rotational broadening and Doppler broadening. Photoelectron spectra with about 11 meV resolution have been obtained routinely with this molecular beam PE spectrometer for gas phase molecules.[8] Some aspects of this spectrometer will be presented briefly in Chapter 2.

1.2 High Temperature Photoelectron Spectroscopy and Studies of Metal Clusters

High temperature PES added another dimension to the photoelectron spectroscopic technique. It offers opportunities to study transient species, vapor species, and clusters of solid substances. It flourished in the 1970's, when a large number of spectra were measured.[9] It has been an active field of research and continues to provide important experimental results concerning the electronic properties of radical species and vapor molecules in the gas phase.[10] However, there are a number of difficulties which hinder high temperature PES and make it impossible to resolve vibrational structures for most systems studied: (1) most high temperature species are heavy molecules and intrinsically have smaller vibrational frequencies; (2) thermal effects, including thermal populations of the molecules and drift of energy scale under high temperature conditions; (3) interference of high temperature production with the photoelectron measurement. Although ways have been developed to cope with the last, high temperature PES is still done at fairly low resolution. Thus much opportunity exists for further progress.

An emerging field of research is the study of metal clusters, which has attracted great attention in recent years. PES, with its unique capability to probe the electronic structure of matter, should be a powerful technique for studying metal clusters. However, because of difficulties of producing cluster species, especially in abundance and in a size-selective manner, laser evaporation,[11] sputtering source,[12] and conventional thermal evaporation[13], in conjunction with negative ion photodetachment, have all been used in a number of investigations. Photoelectron-photoion coincidence with a conventional thermal source has recently been employed to study neutral clusters size-selectively.[14-16]

This work has two motivations: (1) to study high resolution PES of high temperature species; (2) to study high resolution PES of small metal clusters. To facilitate these studies, a unique high temperature supersonic molecular beam source has been built,

which has the capability to entrain carrier gases. The molecular beam technique was used to reduce the thermal effects, and electron bombardment heating was applied to eliminate the stray field associated with conventional resistive heating. The goal was to generate an intense, continuous, and seeded molecular beam of high temperature species and small clusters. Coupling this source with the PE spectrometer of Pollard *et al.*, high resolution PES of high temperature species has been successfully achieved.

The rest of the thesis is organized as follows. In Chapter 2, the design and construction of the high temperature molecular beam source is described in detail, and the photoelectron spectrometer and other experimental aspects are presented. Chapters 3 and 4 deal with diatomic systems: the heavy group IV-VI diatomics (SnSe, SnTe, PbSe, and PbTe) and the heavy group VI diatomics (Se_2 and Te_2), respectively. The relativistic effects and the chemical bonding are studied for the heavy group IV-VI diatomics in detail in collaboration with relativistic quantum chemical calculations. In Chapter 5, clusters of the group V elements are investigated, the dimers (As_2, Sb_2, and Bi_2) and the tetramers (P_4, As_4, and Sb_4). The Jahn-Teller effect is examined in detail for the tetramer species. Chapter 6 reports the investigation of the first row transition metal dichlorides ($MnCl_2$, $NiCl_2$, and $ZnCl_2$). The complexity of photoionizing the open d-shell (in $MnCl_2$ and $NiCl_2$) and the chemical bonding properties of the 3d electrons are studied.

References

1. A. Einstein, *Ann. Phys.* **17**, 132 (1905).
2. (a) K. Siegbahn, C. Nordling, A. Fahlman, R. Nordberg, K. Hamrin, J. Hedman, G. Johansson, T. Bergmark, S.E. Karlson, I. Lindgren, and B. Lindberg, *ESCA, Atomic, Molecular, and Solid State Structure Studied by Means of Electron Spectroscopy,* Nova Acta Regiae Soc. Sci. Upsaliensis, Ser. IV, V20, Uppsala, 1967; (b) K. Siegbahn, C. Nordling, G. Johansson, J. Hedman, P.F. Heden, K. Hamrin, H. Gelius, T. Bergmark, L.O. Werme, R. Manne, and Y. Baer, *ESCA Applied to Free Molecules* (North Holland, Amsterdam, 1969).
3. (a) D.W. Turner, C. Baker, A.D. Baker, and C.R. Bundle, *Molecular Photoelectron Spectroscopy* (Wiley, New York, 1970); (b) J.W. Rabalais, *Principles of Ultraviolet Photoelectron Spectroscopy* (Wiley, New York, 1977).
4. T. Koopmans, *Physica* **1**, 104 (1934).
5. J.E. Pollard, D.J. Trevor, J.E. Reutt, Y.T. Lee, and D.A. Shirley, *J. Chem. Phys.* **77**, 34 (1982).
6. K.P. Huber and G. Herzberg, *Molecular Spectra and Molecular Structure IV. Constants of Diatomic Molecules* (Van Nostrand Reinhold, New York, 1979).
7. J.E. Pollard, D.J. Trevor, Y.T. Lee, and D.A. Shirley, *Rev. Sci. Instrum.* **52**, 1837 (1981).
8. (a) J.E. Pollard, D.J. Trevor, J.E. Reutt, Y.T. Lee, and D.A. Shirley, *J. Chem. Phys.* **81**, 5302 (1984). (b) J.E. Reutt, L.S. Wang, Y.T. Lee, and D.A. Shirley, *J. Chem. Phys.* **85**, 6928 (1986); (c) L.S. Wang, Y.T. Lee, and D.A. Shirley, *J. Chem. Phys.* **87**, 2489 (1987).
9. (a) J. Berkowitz, *J. Chem. Phys.* **56**, 2766 (1972); (b) J. Berkowitz, J.L. Dehmer, and T.E.H. Walker, J. *Chem. Phys.* **59**, 3645 (1973); (c) A.W. Potts, T.A. Williams, and W.C. Price, *Proc. Roy. Soc. London* **A341**, 147 (1974); (d) E.P.F.

Lee and A.W. Potts, *Proc. Roy. Soc. London* **A365**, 395 (1979); (e) J.E. Bice, G.M. Bancroft, and L.L. Coatsworth, *Inorg. Chem.* **25**, 2181 (1981); (f) S.-T. Lee, S. Suzer, and D.A. Shirley, *Chem. Phys. Lett.* **41**, 25 (1976); (g) D. Bulgin, J. Dyke, F. Goodfellow, N. Jonathan, E. Lee, and A. Morris, *J. Electron Spectrosc. Relat. Phenom.* **12**, 67 (1977).

10. (a) J.M. Dyke, N. Jonathan, and A. Morris, *Int. Rev. Phys. Chem.* **2**, 3 (1982); (b) A. Morris, J.M. Dyke, G.D. Josland, M.P. Hastings, and P.D. Francis, *High Temp. Sci.* **22**, 95 (1986); (c) E.J. Baerends, P. Vernooijs, J.M. Dyke, A.M. Ellis, M. Feher, and A. Morris, *J. Chem. Phys.* **89**, 5363 (1988); (d) B. Ruscic, G.L. Goodman, and J. Berkowitz, *J. Electron Spectrosc. Relat. Phenom.* **41**, 357 (1986).
11. O. Cheshnovsky, S.H. Yang, C.C. Pettiette, M.J. Craycraft, R.E. Smalley, *Rev. Sci. Instrum.* **58**, 2131 (1987).
12. K.M. Ervin, J. Ho, and W.C. Lineberger, *J. Chem. Phys.* **89**, 4514 (1988).
13. K.M. McHugh, J.G. Eaton, G.H. Lee, H.W. Sarkas, L.H. Kidder, J.T. Snodgrass, M.R. Manaa, and K.H. Bowen, *J. Chem. Phys.* **91**, 3792 (1989).
14. K. Rademann, B. Kaiser, U. Even, and F. Hensel, *Phys. Rev. Lett.* **59**, 2319 (1987).
15. K. Rademann, B. Kaiser, T. Rech, and F. Hensel, *Atoms, Molecules, and Clusters* **12**, 431 (1989).
16. K. Rademann, *Ber. Bunsenges. Phys. Chem.* **93**, 653 (1989).

Chapter 2

Experimental Aspects

2.1 Introduction

In this chapter, we describe the experimental apparatus which has been used for the experiments contained in this dissertation. Three principal parts will be described in the next three sections: (1) the photoelectron spectrometer (Section 2.2); (2) the quadrupole mass spectrometer (Section 2.3); (3) the high temperature molecular beam source (Section 2.4). The high resolution molecular beam photoelectron spectrometer was built by Pollard, Trevor, Lee, and Shirley, has been described previously[1] and was well documented in Pollard's thesis.[2] Thus, it will be presented briefly for completeness. The quadrupole mass spectrometer was originally installed by Trevor, and a new set of quadrupole rods was employed for the work in this dissertation. Some aspects can be found in Trevor's[3] and Reutt's[4] theses. Much of the design and construction of the high temperature source was accomplished by Reutt, and summarized in her thesis.[4] However, there have been a few vital modifications and extensive diagnosis, which led to its workability and current performance. It will, therefore, be described in detail, including its performances and an assessment of its limitations.

2.2 The Photoelectron Spectrometer

2.2.1 The Photoelectron Analyzer and Vacuum System

A schematic top view of the molecular beam photoelectron spectrometer is shown in Figure 1. It consists of a supersonic molecular beam source, the photoelectron energy analyzer, the quadrupole mass spectrometer, and a photon source, which is not shown. The photon beam, coming into the plane of the paper from the photon source, crosses with the molecular beam perpendicularly. For the work described in this dissertation, the molecular beam source (1 in Figure 1) is replaced with the high temperature molecular beam source, which will be described in Section 2.4; the beam catcher (2 in Figure 1) is replaced with a copper-sheet beam collector at room temperature, on which the high temperature vapors are condensed and collected. The main chamber, to which the molecular beam source, the mass spectrometer, the photon source, and the photoelectron analyzer are connected, has a double layer of mu-metal shielding, and is evacuated by two liquid-nitrogen-baffled diffusion pumps (Varian VHS-6) with a combined speed of 1800 l/s. During experiments, the main chamber vacuum is usually kept at 2×10^{-6} Torr or better.

The analyzer is connected to the main chamber through a 0.15 cm diameter aperture for sampling the photoelectrons, and is pumped in two stages by a pair of liquid-nitrogen-baffled diffusion pumps (Varian VHS-4) having a speed of 460 l/s each. The vacuum in the analyzer is maintained at 3×10^{-8} Torr or better. The photoelectrons pass through the 0.15 cm diameter aperture, which defines a 1.8° acceptance angle, and are transported by two asymmetric three-element cylindrical lenses and focused to the entrance of the 90° spherical sector preanalyzer, which is designed to reduce the background and eliminate the scattered electrons. Following the preanalyzer, another three-element asymmetric lens decelerates the electrons to 1 eV (for 1 eV analyzer pass energy) and focuses the electrons to the virtual entrance slit of the hemispherical analyzer, which has a mean radius of 10.16

cm. The electrons are then dispersed according to their kinetic energies through the analyzer, accelerated to 5 eV to a pair of 40 mm microchannel plates, and detected by a resistive anode and the associated position-encoding electronics. A 256 channel buffer memory is used for the temporary storage of the photoelectron signals. The data acquisition is controlled by a dedicated microcomputer (DEC LSI-11/2), which transfers the data from the buffer to the computer memory and scans the kinetic energy. The data are subsequently plotted and stored on floppy disks.

The best energy resolution achieved is 10 meV at 1 eV pass energy, as measured from the PE spectrum of Ar. The following analyzer pass energies can be chosen: 0.5 eV, 1 eV, 2 eV, and 4 eV. The smaller the pass energy, the better the theoretical resolution. The 0.5 eV pass energy gives the best resolution; but the transmission is dramatically rduced and non-uniform across a range of kenetic energy. Thus it cannot be used for any practical measurements. The 2 eV and 4 eV pass energies give too poor resolutions and are not used. Therefore, the 1 eV analyzer pass energy was the optimized one, and was employed exclusively.

The photoelectron kinetic energy is usually calibrated with the rare gases, Ar, Kr, or Xe, for which the ionization energies are very accurately known. The energy scale drift is normally very small for room temperature experiments (<1meV/hr). For the high temperature experiments, however, the energy scale drift is more severe, and each photoelectron scan is kept within an hour. The resolution achieved ranges from 12 to 15 meV.

2.2.2 The Photon Source

The photon source sits on the top of the main chamber, and is a windowless, differentially-pumped cold-cathode rare gas DC discharge lamp. The experiments described in this dissertation have been carried out exclusively with the HeIα (584.354 Å,

21.2175 eV) resonance line. The photons produced in a water-cooled 2 mm diameter x 5 cm long quartz capillary are directed by a 2 mm diameter x 35 cm long quartz collimating capillary toward the ionization region. The collimating capillary extents to about 2 cm from the ionization region, where the photon beam crosses with the molecular beam and creates the photoelectron/photoion pairs. This capillary is coated with aquadag to prevent charging. The windowless design and the differentially-pumped cold cathode plus the low VUV absorption of the quartz capillary allow the maximum intensity. The photon flux on the HeI resonance line is estimated to be ~10^{13} photons/s based on the measurement from a home-made copper photodiode. The contributions from the other resonance lines of helium are ~2.4% HeIβ (537.046Å), 0.4% HeIγ (522.229Å), and less than 0.1% for all higher lines, as measured from the photoelectron spectrum of Ar. For low signal experiments, the photoelectron signals from these impurity lines are negligible. The typical operating conditions of the lamp is 1.0 Torr He and 180 mA discharge current, which produces a photon linewidth of <2meV FWHM. The higher the He pressure and discharge current, the higher is the photon flux. For the high temperature experiments, the maximum signal is sought. Therefore, an operating condition of 1.2-1.5 Torr He and 200 mA discharge current is normally used. The photon flux increase justifies the pressure broadening of the photon linewidth, which is <2meV.

The resonance lines of the other rare gases, Ne, Ar, Kr, Xe, can also be produced. The lower energies of these lines give another parameter to change in PES. For example, they can be used for some metal cluster experiments, for which the HeI line would produce too high energy electrons. Unfortunately, radiations from higher resonance lines of these elements are severe, which seriously limits their applications if not monochromatized. Monochromatization will decrease substantially the photon flux. Thus, they were not used in any of the current experiments.

2.3 The Quadrupole Mass Spectrometer

The quadrupole mass spectrometer (Extranuclear Laboratory) has played a vital part in the high temperature experiments. It is used to monitor the evaporation processes, and to diagnose the beam compositions extensively. The mass spectrometer is connected to the main chamber with a 26.7 cm (10.5 in.) flange, as shown in Figure 1. It has a 0.64 cm diameter aperture to the main chamber for passage of the ions and is pumped by a 500 l/s turbomolecular pump (Pfeiffer TPU-500) to a vacuum better than $1x10^{-8}$ Torr when no beam is on. Two modifications have been made for the cluster and high temperature experiments: (1) a smaller quadrupole mass filter (0.95 cm diameter rod, Extranuclear #7-162-8) has been installed, which extents the mass range now up to 1400 AMU; (2) the mass spectrometer has been interfaced to the computer so that mass spectra can be digitally stored. Other parts of the mass spectrometer include the ion optics for extracting and transporting the ions to the mass filter, a detection system consisting of a Spiraltron multiplier and a current amplifier.

For the photoelectron measurement, it is preferable to keep the ionization region as open as possible. Thus, the mass spectrometer is usually not present during photoelectron measurements. However, it is necessary in the high temperature experiments to have it for *in situ* diagnostics. As a compromise, a single-element asymmetric ion extraction was adopted. A grounding plate with a 2 cm diameter hole for the transmittance of the molecular beam had to be introduced to provide a uniform electric field around the ionization region in order to be able to extract the ions. The single-element asymmetric ion extraction is still less efficient than the normal double-element symmetric ion extraction. Nonetheless, the photoions in most experiments are abundant enough to facilitate analog detection.

The ions emerging from the quadrupole mass filter typically strike on the Spiraltron multiplier with the cathode at -1.8 KV. The anode is at -50 V and the collector at ground.

The low anode voltage was found to be preferable, since this implied that the electrons would strike on the collector with a smaller kinetic energy and reduce the secondary emission. This was found to suppress the current noise substantially. In a pulse counting mode, however, the anode is typically operated at a higher negative potential, about -1.0 KV. The current signal from the collector is fed into a current amplifier (Keithley 427). The voltage signal from the current amplifier is then read by a digital voltmeter, which is interfaced with the microcomputer. The computer stores the ion signals and controls the mass scan. The dwell time for each voltage reading is variable, allowing fast scans to be taken; or the dwell time can be set longer to have better signal/noise ratios.

The Spiraltron multiplier alone as an ion detector tends to discriminate heavy particles, e.g., larger cluster ions. A multiplier with a conversion dynode (Extrel # 051-9) has been purchased, whose installation should improve the heavier ion detection efficiency in the future.

2.4 The High Temperature Molecular Beam Source

2.4.1 Design Considerations

Our design criteria were dictated by the photoelectron spectrometer. A high number density (~10^{12}-10^{13} molecules/cm^3) is necessary for the photoelectron measurement. This number density, further, must be produced without a significant magnetic field, which would perturb the photoelectron measurement. In order to obtain well-resolved PE spectra, internal cooling of the high temperature species is essential. This poses a conflicting requirement with the high temperature environment necessary. Fortunately, this can be resolved through the seeded supersonic molecular beam technique. In brief, what we need is a source that can cleanly generate an intense, continuous and internally-cooled molecular beam.

A number of designs were considered for this source. The very successful laser evaporation technique was attractive, in that it is simple to construct and can evaporate virtually any materials.[5] The low average number density output of this technique, however, precludes its use in our photoemission studies. A direct resistive heating source has the advantage of simplicity and ease to operate.[6] But the enormous current necessary in this method would not be desirable. A pulsed RF heating source[7] has been successfully applied to UV photoemission studies. The disadvantage is that the photoelectron measurement must be gated with respect to the heating periods, reducing the collecting efficiency of the electron spectrometer.

An electron bombardment heating source provides an attractive alternative.[8] It requires relatively low heating current (<40 A for a 0.51 mm tungsten filament). Further, the filament can be wound noninductively and thus introduce little magnetic field. The heating power will be controlled by the thermionic emission current and the accelerating high voltage. So continuous high power can be achieved easily. Therefore, the electron bombardment heating technique became the choice in our design.

2.4.2 Construction

The first thing to consider in building an e-beam heating source is the ability to apply high enough accelerating voltage to achieve the desirable heating power without having electrical breakdown at the same time. In our case, we would like to have up to 1 A emission current and up to 2.5 KV accelerating voltage. Since the vacuum in our molecular beam source chamber with a molecular beam running is usually maintained at ~10^{-4} Torr, all the floated components must be placed in a differentially-pumped vacuum region and operated at a vacuum better than ~10^{-5} Torr.

A schematic cross-sectional view of the e-beam heating oven is shown in Figure 2. It consists primarily of a 0.51 mm coiled W filament (15, Figure 2) for thermionic

emission, a Mo cylinder electrostatic deflector (9, Figure 2), inner and outer W vacuum jackets (12 and 13, Figure 2), a graphite crucible (11, Figure 2) and a carrier gas inlet system (1, Figure 2). The W filament is noninductively wound, supported by a ceramic filament support (14, Figure 2) and screw-mounted onto two Mo filament mount posts (8, Figure 2). The bus (see 17, Figure 4), supplying power for the filament and running through a triple-tubing section (19, Figure 2), is not shown in Figure 2. The filament and the electrostatic deflector are floated at negative high voltage with respect to the surroundings, and are insulated from the surroundings through the ceramic high voltage standoff (16, Figure 2). Hence, the electrons emitted from the filament are accelerated toward the inner vacuum jacket, which in turn heats up the crucible radiatively.

The inner and outer vacuum jackets define a separate vacuum region which is differentially pumped by a 200 l/s Turbomolecular pump (see Figure 4). This is necessary to operate under high voltage condition. A pair of bevelled Mo spacers (5, Figure 2) are placed at the end of the inner W jacket. Being springy, these spacers serve as a differential pumping barrier between the filament region and the main beam source chamber during a whole heating cycle.

The crucible is spring-pressed against the inner jacket to allow thermal expansion during heating (3 and 4, Figure 4). The top of the crucible makes direct contact with the inner jacket, and therefore is the hottest part of the crucible. This is essential to assure the nozzle is not clogged. A 4.76 mm (3/16 in.) o.d. Mo tube (1, Figure 2) is tightly fitted into the end of the graphite crucible cap (also see Figure 3). Graphite cement is applied at this joint for sealing. Since the thermal expansion coefficient of graphite is the smallest among the common high temperature materials, it is essential to cool the Mo/graphite joint (2, Figure 2).

The design and fabrication of the W filament, the vacuum jackets and the graphite crucible deserve special mention. The W filament is customer-designed and can be purchased from Emissive Products (part # 060183). The W vacuum jackets were

fabricated by a chemical vapor deposition process. Tantalum was found to be applicable as a vacuum jacket material. The Ta vacuum jackets can be easily cold-formed out of 1 mm Ta sheets.

A central question in making the crucible was the ability to load samples and to seal off the crucible. High density graphite was chosen as the crucible material, because of its chemical inertness and its ease to be machined. Three kinds of crucible configurations were used, as shown in Figure 3. They are composed of three parts, the crucible body with a nozzle, the crucible cap with the gas inlet, and the front disk to prevent sample from getting to the nozzle. It is essential to polish the crucible body and the crucible cap contact surfaces and have a tight fit in order to prevent leaks from this joint, which is further applied with graphite cement from outside. In configuration (a), the gas inlet opening is placed at front to prevent it from getting clogged. The clogging was not a serious problem and the configuration (a) can be simplified to (b), with which a sample cell can be used if desired. It should be kept in mind that there is a temperature gradient along the crucible body with the nozzle being at the hottest part, which posed a conflicting condition for the desire to generate internally-cooled beams. Configuration (c) was designed as a compromise, for the nozzle temperature gets reduced to some degree compared with (a) and (b) as a result of more radiation loss. The graphite cement applied on the crucible can be chipped off after an experiment and the crucible can be reused. The nozzle sizes used range from 0.1 mm to 0.2 mm i.d.

The overall view of the beam source is shown in Figure 4. A conical skimmer of 5.1 mm diameter is used and is not heated. The skimmer diameter is much bigger than normal to prevent clogging of the skimmer during the course of an experiment. The nozzle / skimmer alignment is achieved through the XYZ translation stage (15 and 16, Figure 4) and the fine alignment rods (1, Figure 4). The outer vacuum jacket is shielded with a stainless steel water cooling cylinder (6, Figure 4). Not shown is the front shielding which consists of five layers of Ta sheet. A ceramic spacer (2, Figure 4)

electrically insulates the oven system from ground. A copper wire is connected to this part to collect the emission current, which is used as feedback for the filament heating control system (see below). All the cooling water lines and gas inlet line (11, Figure 4) are also electrically isolated from the oven system.

The 200 l/s Turbomolecular pump evacuates the filament region through a long 10 cm i.d. stainless steel tubing (14, Figure 4). The filament bus bars (17, Figure 4), running through this tubing, are connected with the Mo filament mount posts (8, Figure 2). The crucible gas inlet tubing is clamped to a clamp base plate (4, Figure 4) and spring-loaded (3, Figure 4). The crucible receives the spring force. The main beam source chamber is pumped by a 4000 l/s diffusion pump with a water trap.

2.4.3 Operation

The oven system is accessed from the front. The crucible is first sealed off with the desired sample. Sample changing is done simply by taking off the vacuum jackets and changing the crucible.

A schematic diagram of the e-beam heating system is shown in Figure 5. The temperature of the oven is controlled by the emission current and the applied accelerating voltage. The desired emission current is manually set on a proportional bandwidth controller (Eurotherm 984), which provides a voltage pulse to trigger a Silicon Controlled Rectifier assembly (Eurotherm 931, SCR assembly). The SCR assembly then outputs phase-controlled power (up to 240 V, 25 A peak power) to the primary of the transformer in the isolated filament power supply. The output direct current from the filament supply (up to 40 A, 30 V) is floated at a negative high voltage manually set on the high voltage supply (up to -5 KV, 1 A) and is sent through the W filament. The emission current is collected and fed back to the temperature controller. The controller reaches a stable condition once the amount of the emission current equals the set value.

The oven temperature is functionally dependent on the emission current and the high voltage, which can be changed independently to arrive at a different temperature. The temperature is measured at the back of the crucible (18, Figure 2) with Type C (W/Re) or Type K (Cr/Al) thermocouples. Due to the thermal gradient along the crucible and the thermal loss at the back of the crucible, the measured temperature is normally much lower than the real oven temperature.

During an experiment, the temperature is slowly increased to let the oven system outgas with carrier gas running. The temperature is continuously increased until there is an appreciable evaporation. This is monitored by the quadrupole mass spectrometer. The temperature, which is only relative, is then stabilized at a value where a satisfactory photoelectron count is read. The whole spectrum will be taken at this temperature. About 0.1-0.2 mole of material can be charged into the crucible. This would usually last for more than 20 hours, which is enough for one experiment.

2.4.4 Performance

A photographic illustration of some of the main components is given in Figures 6-11. To demonstrate the high resolution achieved at high temperatures, Figures 12 and 13 show the atomic PE spectra of Zn and Pb, respectively, with 12 meV resolution. Besides the main lines are some correlation satellites, as labelled in the spectra. Complete discussions of the nature of these spectra can be found in Refs. 9 and 10 for Zn and Pb, respectively. The Zn spectrum was taken with the crucible configuration (a) (Figure 3) at a temperature of about 900 K. The nozzle size was 0.1 mm diameter with a Ne carrier gas of 370 Torr. The power supply was run at 1 KV high voltage and 150 mA emission current. The Pb spectrum demonstrates the importance of materials compatibility under high temperature conditions. The Pb spectrum shown in Figure 13 was the result of attempting to take a PE spectrum of PbO, which is a strong oxiding agent at high temperature and very

reactive with graphite. The Pb spectrum was actually the result of using a Ta tube as a sample cell, which was still oxidized to give free lead at a temperature of about 1350 K.

Figures 14-17 show some typical mass spectra. Figure 14 is a quick mass scan during the As_2 experiment, which will be discussed in detail in Chapter 5. The As_2 dimer was obtained by evaporating Cu_3As alloy at about 1400 K. Pure arsenic evaporates mainly as the tetramer species. It is seen that a small amount of tetramer was still present, as well as minute amount of oxide species. Figure 15 shows a mass spectrum of $PbSe^+$, which was taken during the PbSe experiment described in Chapter 3. Besides the parent ion and the daughter ions, a minute amount of Se_2^+ was also observed. The unlabeled peaks represent the chamber background and outgases, mainly H_2O and N_2. Since the ion extraction and detection were favored for the lighter ions, they showed up in the mass spectrum more prominently. They tend to diminish with time. Figure 16 illustrates a mass spectrum during the evaporation of $MnCl_2$, whose PE spectrum will be discussed in Chapter 6. This spectrum was taken at the beginning of the evaporation, when outgases were serious. The two peaks around mass 150 and some of the unlabeled peaks at lower masses are from the diffusion pump oil desorbed from the wall of the source chamber. These outgases also diminish with time. Figure 17 shows the mass spectrum of Ga, which represents the highest temperature evaporation. It was taken at a temperature of 1850 K and 1 KW heating power (500 mA at 2 KV). The unlabeled peaks were from the outgases.

The power supply system can provide up to 5 KW heating power (1A x 5KV). The actual power output is limited by the breakdown voltage, which depends upon the temperature and the vacuum around the filament region. We were able to operate the oven source at ~1900 K with 1 KW heating power. Heating power of 1.5 KW can be achieved. However, the thermal inhomogeneity along the crucible often makes it difficult to evaporate refractory materials. More efficient pumping of the filament region to suppress high voltage breakdown and more extensive thermal shielding at the back of the crucible can make the source work at even higher temperature.

The scope of applications of the current oven source should be addressed. The current set-up works well to generate continuous and internally-cooled molecular beams of high temperature species. Thus the original goal has been met. However, two points should be made about generating metal clusters with supersonic cooling for PES work. First, to generate metal clusters relying on the supersonic cooling with the current set-up is difficult, because (1) the high temperature conditions are inherently in contradiction with the cold environment required for metal atoms to nucleate; (2) in the current set-up, the nozzle temperature cannot be controlled separately, and the nozzle temperature is often too high relative to the oven temperature; this ensures that the nozzle will not be clogged; however, it makes it more difficult for nucleation to occur; (3) liquid metallic systems have high surface tensions, and higher supersaturation conditions are required for nucleation to take place. All the above imply to have harder supersonic expansions in order to produce metal clusters. However, in a continuous beam, the pumping speed eventually limits the stagnation pressure that can be applied. Second, if clusters can be generated, there are still additional complications for PES work. Clusters generated in a supersonic expansion have a continuous distribution of sizes. PES is a non-resonance method itself and does not have size-selectivity. Therefore, clusters would preferrably be produced in a size-selective manner for PES work. Hence, the targets have to be well chosen in order to study clusters with the current set-up. Chapter 5 represents such examples.

References

1. J.E. Pollard, D.J. Trevor, Y.T. Lee, and D.A. Shirley, *Rev. Sci. Instrum.* **52**, 1837 (1981).
2. J.E. Pollard, *Ph. D. Thesis*, Department of Chemistry, University of California, Berkeley (1982); LBL-14285.
3. D.J. Trevor, *Ph. D. Thesis*, Department of Chemistry, University of California, Berkeley (1980); LBL-11434.
4. J.E. Reutt, *Ph. D. Thesis*, Department of Chemistry, University of California, Berkeley (1986); LBL-21322.
5. J.B. Hopkins, P.R.R. Langridge-Smith, M.D. Morse, and R.E. Smalley, *J. Chem. Phys.* **78**, 1627 (1983).
6. D.R. Preuss, S.A. Pace, and J.L. Gole, *J. Chem. Phys.* **71**, 3553 (1979).
7. D. Bulgin, J. Dyke, F. Goodfellow, N. Jonathan, E. Lee, and A. Morris, *J. Electron Spectrosc. Relat. Phenom.* **12**, 67 (1977).
8. J.L. Margrave and R.H. Hauge, in: B. W. Rossiter (Ed.), *Techniques of Chemistry, Vol. IX: Chemical Experimentation under Extreme Condition* (John Wiley & Sons, New York, 1980) pp. 300-301.
9. S. Suzer, S.-T. Lee, and D.A. Shirley, *J. Chem. Phys.* **65**, 412 (1976).
10. S. Suzer, M.S. Banna, and D.A. Shirley, *J. Chem. Phys.* **63**, 3473 (1976).

Figure Captions

Figure 1 A schematic top view of the molecular beam photoelectron spectrometer: (1) beam source, (2) beam catcher, (3) pass energy selector lens, (4) field lens, (5) kinetic energy scan lens, (6) deflectors, (7) 90° spherical sector preanalyzer, (8) conductance barrier, (9) 8:1 decelerator lens, (10) hemispherical analyzer, (11) multichannel detector, (12) ion extraction lenses, (13) quadrupole mass filter, (14) differential pumping. Not shown are two layers of mumetal magnetic shielding that line the main chamber and the electron path, a perforated grounding plate directly opposite the molecular beam on the far side of the ion optics. The photon source is located above the plan of the drawing.

Figure 2 A cross sectional view of the oven assembly. (1) Ta carrier gas inlet tube, (2) water cooling block, (3) graphite crucible cap, (4) graphite radiation shield, (5) Mo springy conduction barrier, (6) Mo retainer, (7) ceramic insulator, (8) Mo filament mount post, (9) Mo electrostatic deflector and radiation shield, (10) sample, (11) graphite crucible body, (12) outer W (or Ta) vacuum jacket, (13) inner W (or Ta) vacuum jacket, (14) ceramic filament support rod, (15) W filament, (16) ceramic high voltage standoff, (17) Mo (or ceramic) support plate for filament posts, (18) thermocouple, (19) stainless steel triple-tubed flange section (shown in two-fold symmetry for easier viewing). Not shown are the bus lines, some radiation shields, and W wires for supporting the filament.

Figure 3 The three graphite crucible configurations.

Figure 4 A schematic view of the high temperature molecular beam source: (1) rods for fine alignment of the nozzle and skimmer (shown one of three), (2) ceramic spacer, (3) guiding rod, spring, and lock nuts for spring loading (shown one of three), (4) clamp base plate (receiving spring force), (5) water cooling block, (6) water cooled thermal shield, (7) oven assembly (shown in Figure 2), (8)

reducer cap, (9) water cooling coil, (10) triple-tubed flange, (11) carrier gas inlet line, (12) ceramic insulating tube, (13) emission return conductor, (14) stainless steel arm, (15) bellow, (16) XYZ translation stage, (17) filament busbar, (18) vacuum feedthru. Not shown are the various water lines and thermocouples. All water lines have electrical breaks and are made of flexible tubing or plastic tubing to free the motion of the stainless steel arm.

Figure 5 Schematic diagram of the electron bombardment heating system.

Figure 6 The high temperature molecular beam source without the reducer and skimmer, showing the filament emission return with the operator holding, the water-cooled radiation shield, and the thermal couples. At far back is the Turbomolecular pump, which is used to differentially pump the filament region.

Figure 7 View of the oven without the water-cooled radiation shield, showing the outer tungsten vacuum jacket. Note that the cooling water lines are not connected. The line which is connected is the carrier gas inlet line.

Figure 8 View of the filament region without the inner and outer tungsten vacuum jackets and the graphite crucible, showing the 0.5 mm diameter tungsten filament, its mounting and supports, ant the electrostatic deflector and thermal shields.

Figure 9 The stainless steel triple-tubed flange section, showing the spring-loaded crucible support and mounting, and the insulation of the electrostatic deflector. Note the power input connectors through two of the triple tubes.

Figure 10 The assembled graphite crucible and the tantalum inner vacuum jacket with the thermal couple.

Figure 11 The disassembled graphite crucible. Note that this corresponds to configuration (a) in Figure 3.

Figure 12 The HeI photoelectron spectrum of Zn^+ at a resolution of 12 meV. The oven temperature and carrier gas pressure are 900 K and 370 Torr Ne.

Figure 13 The HeI photoelectron spectrum of Pb^+ at a resolution of 12 meV. The oven temperature and carrier gas pressure are 1350 K and 120 Torr He.

Figure 14 The mass spectrum of evaporating Cu_3As at 1400 K with 350 Torr Ne carrier gas.

Figure 15 The mass spectrum of evaporating PbSe at 1010 K with 500 Torr Ne carrier gas.

Figure 16 The mass spectrum of evaporating $MnCl_2$ at 1000 K with 120 Torr He carrier gas. The unlabeled features are from chamber outgases.

Figure 17 The mass spectrum of evaporating Ga at 1850 K with 100 Torr Ne carrier gas. The unlabeled features are from chamber outgases

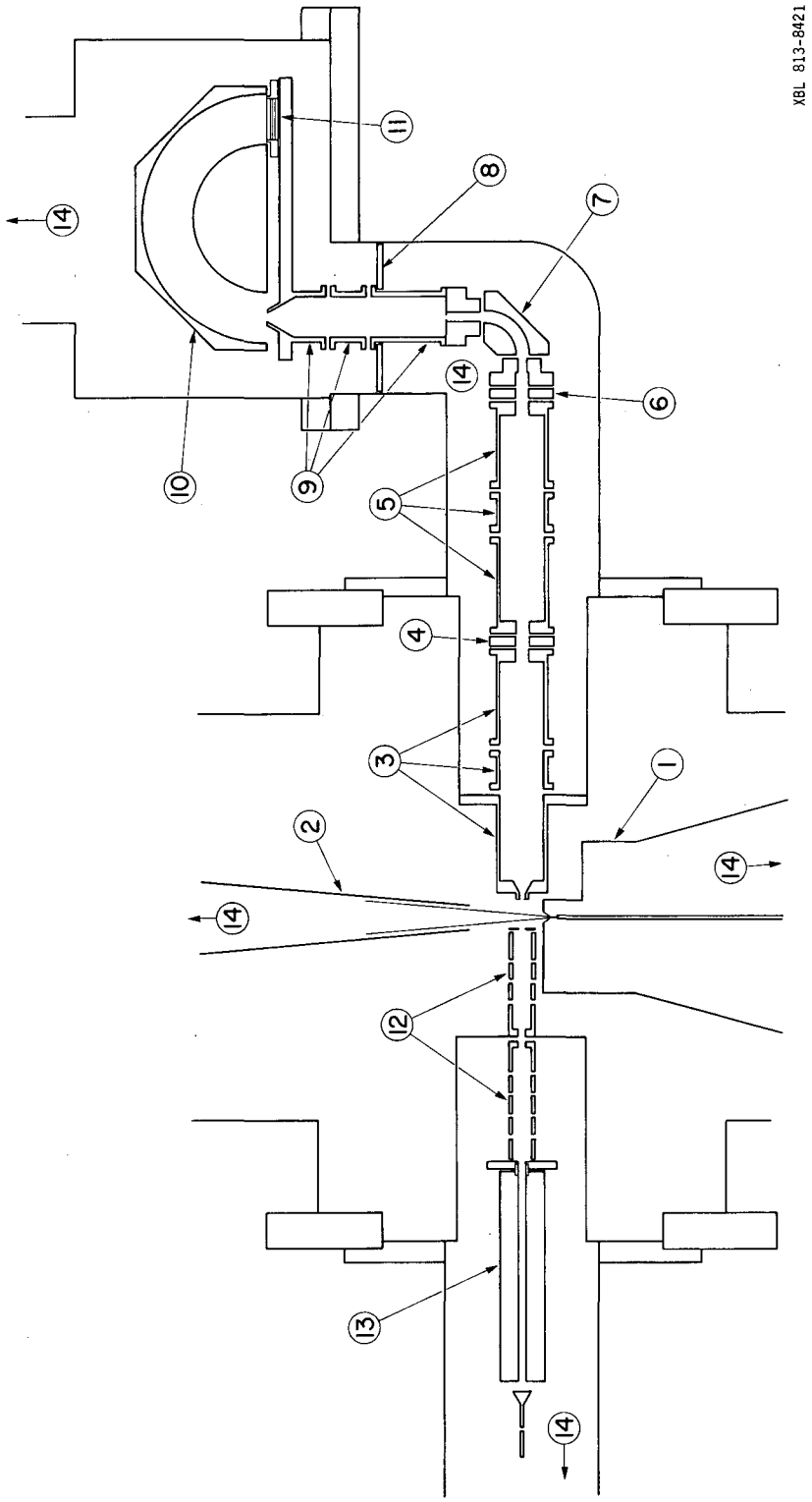

Figure 1

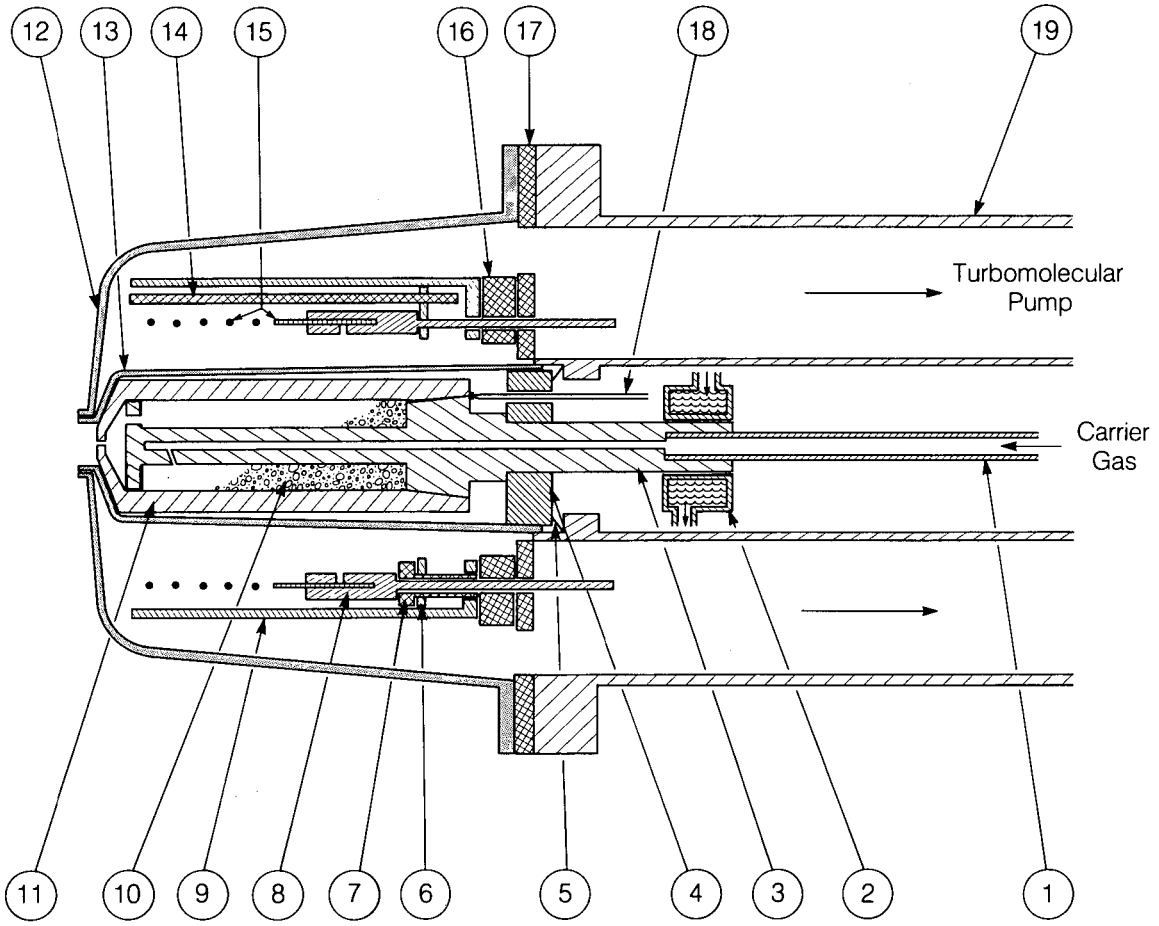
12
13
14
15
16
17
18
19
Turbomolecular
Pump
Carrier
Gas
11
10
9
8
7
6
5
4
3
2
1
XBL 8712-10503

Figure 2

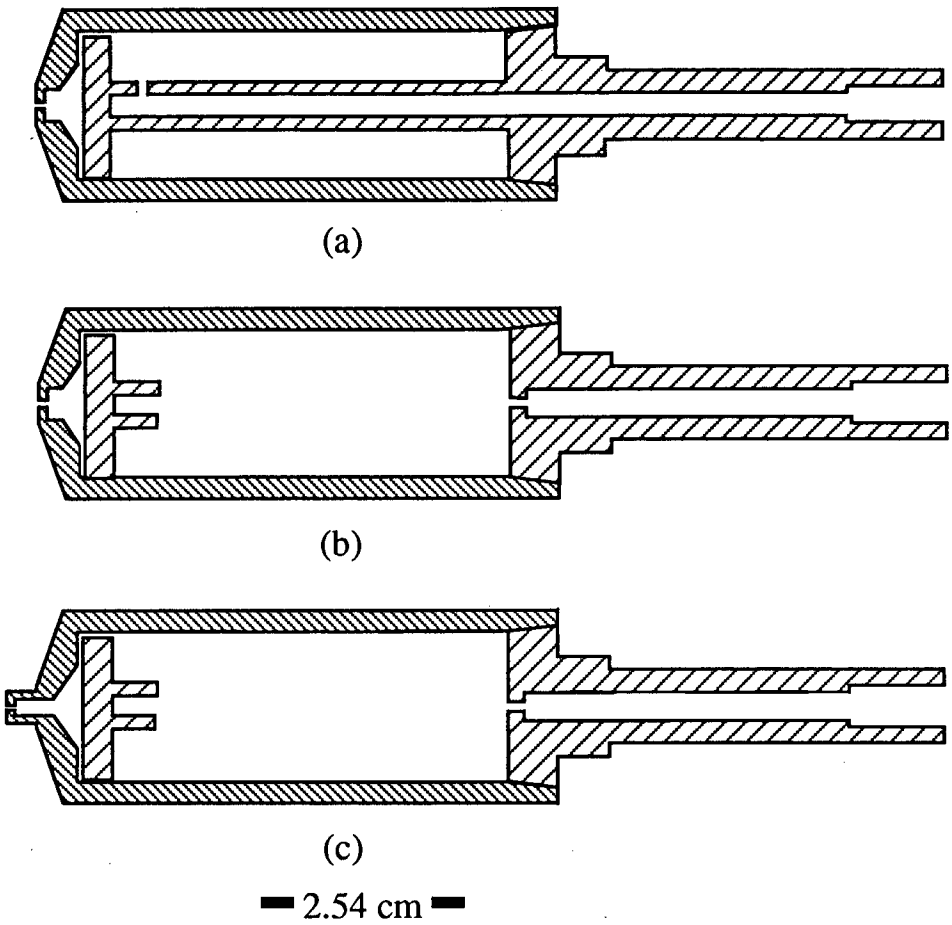

Figure 3

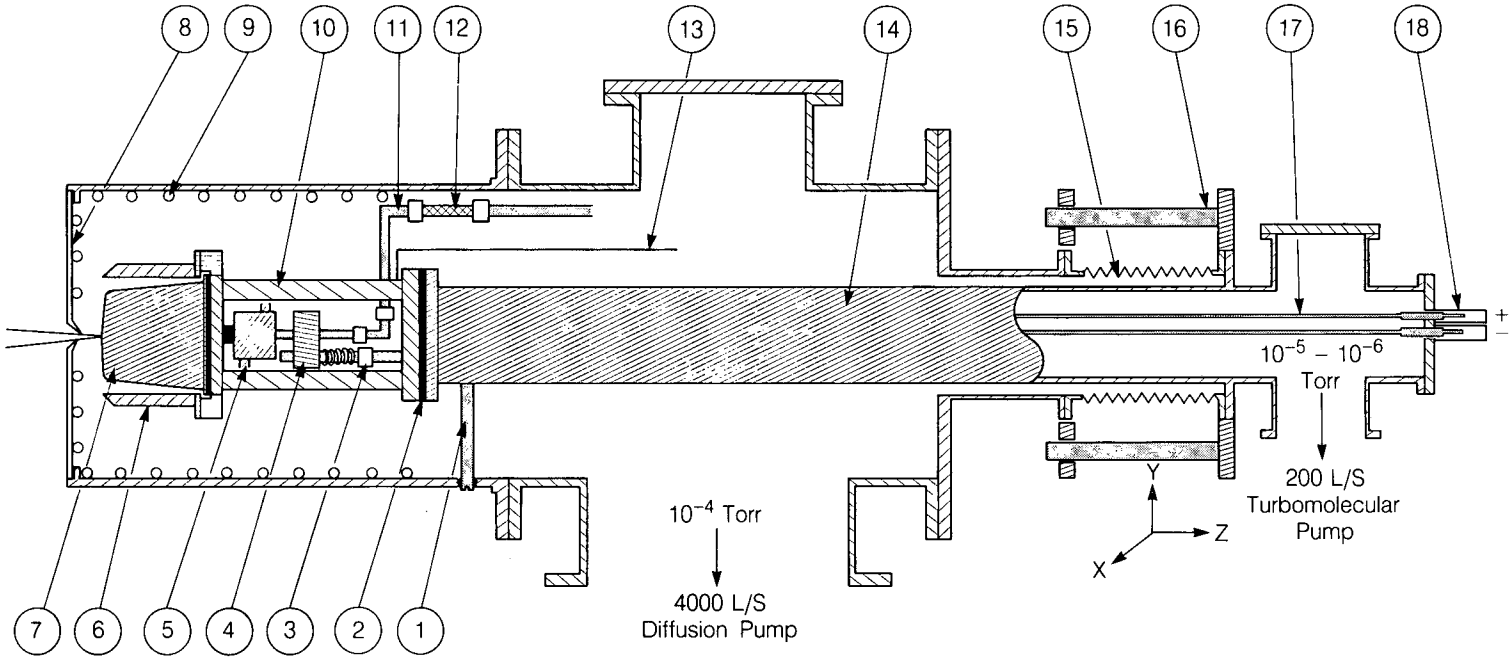
8
9
10
11
12
13
14
15
16
17
18
7
6
5
4
3
2
1
10^{-4} Torr
4000 L/S
Diffusion Pump
10^{-5} – 10^{-6}
Torr
200 L/S
Turbomolecular
Pump
Y
Z
X
+
–
XBL 8712-10502

Figure 4

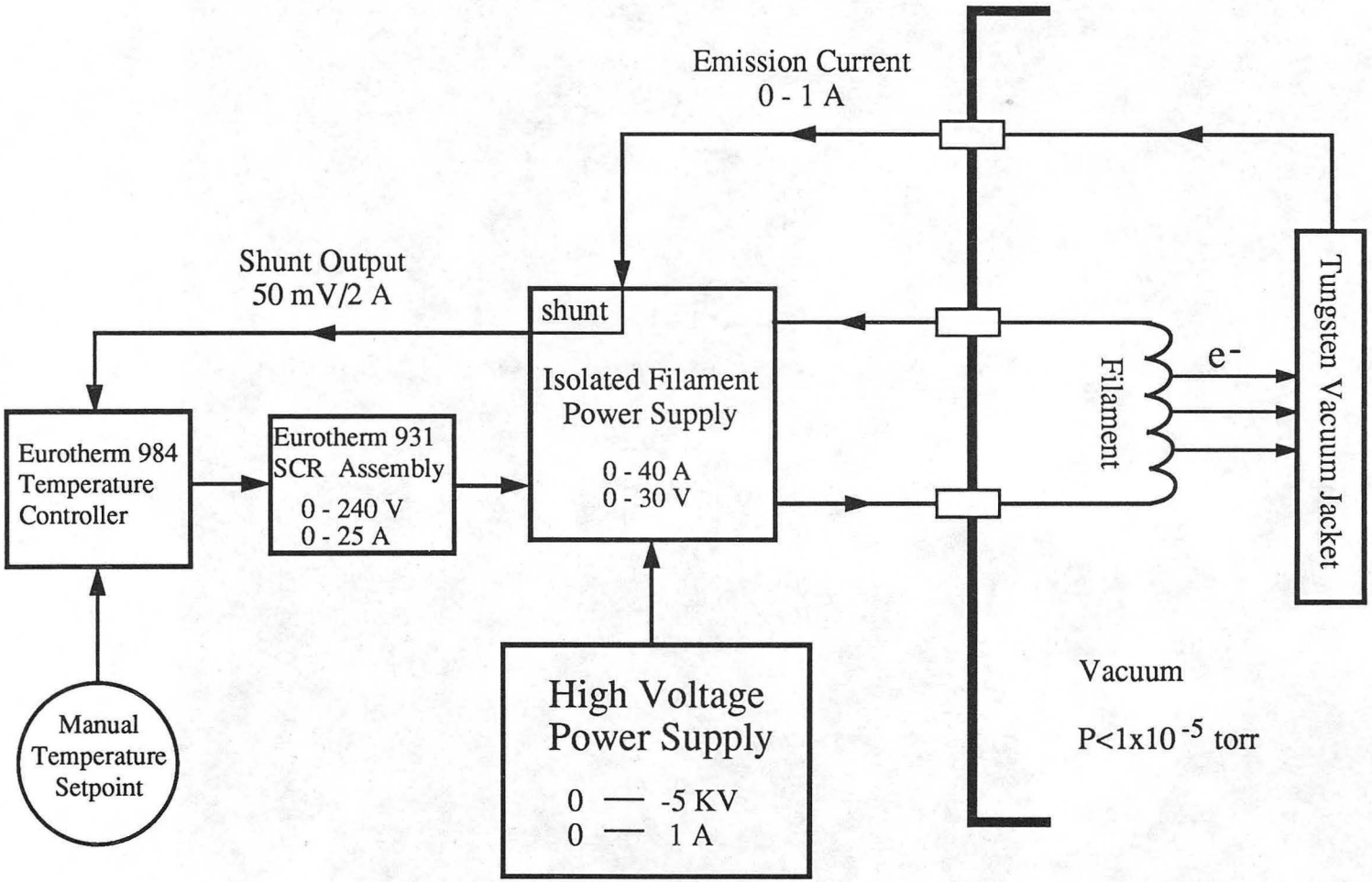
Emission Current
0 - 1 A
Shunt Output
50 mV/2 A
shunt
Isolated Filament
Power Supply
0 - 40 A
0 - 30 V
Eurotherm 984
Temperature
Controller
Eurotherm 931
SCR Assembly
0 - 240 V
0 - 25 A
Filament
e-
Tungsten Vacuum Jacket
Manual
Temperature
Setpoint
High Voltage
Power Supply
0 — -5 KV
0 — 1 A
Vacuum
P<1x10 -5 torr

Figure 5

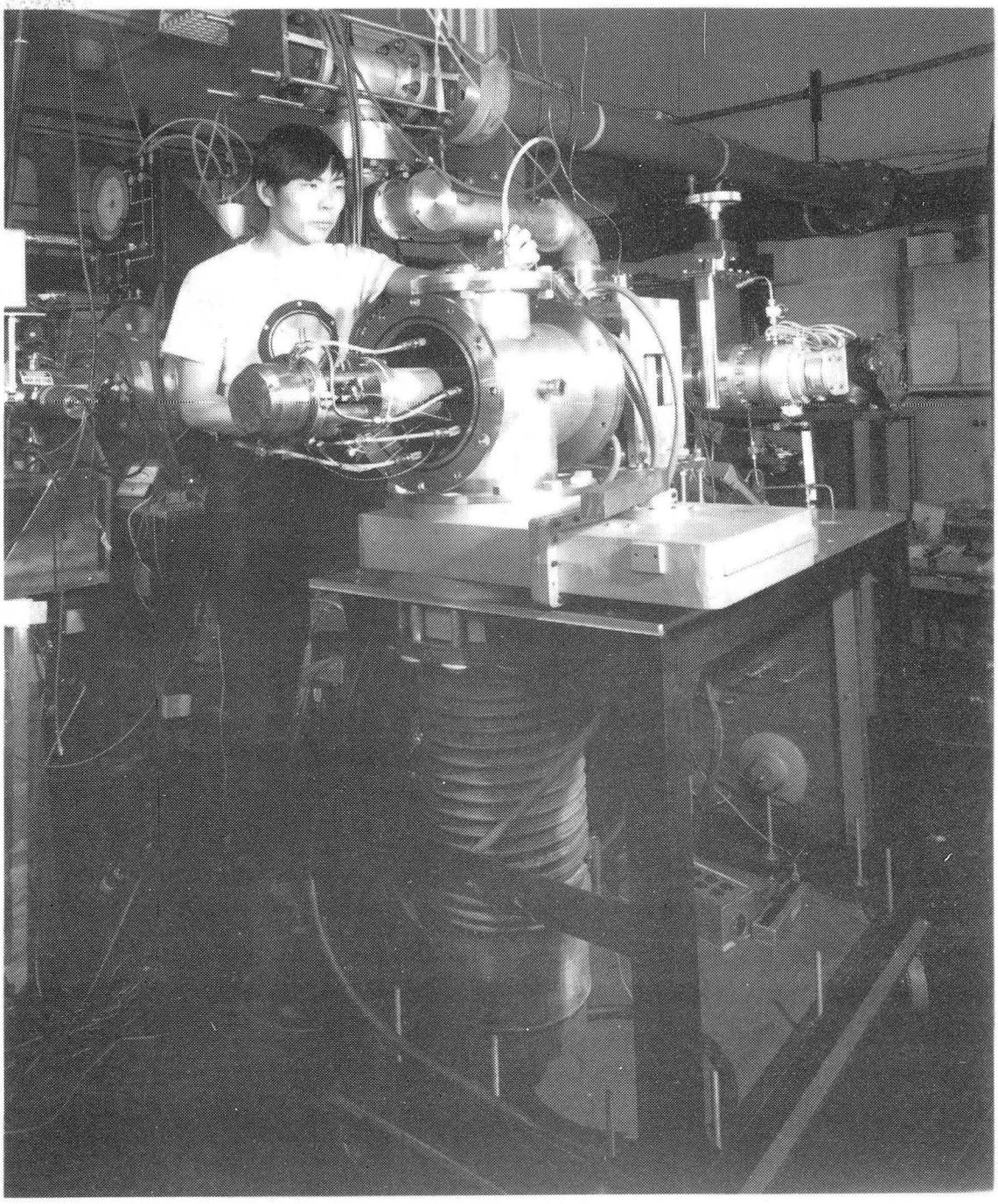

CBB 8712-10774

Figure 6

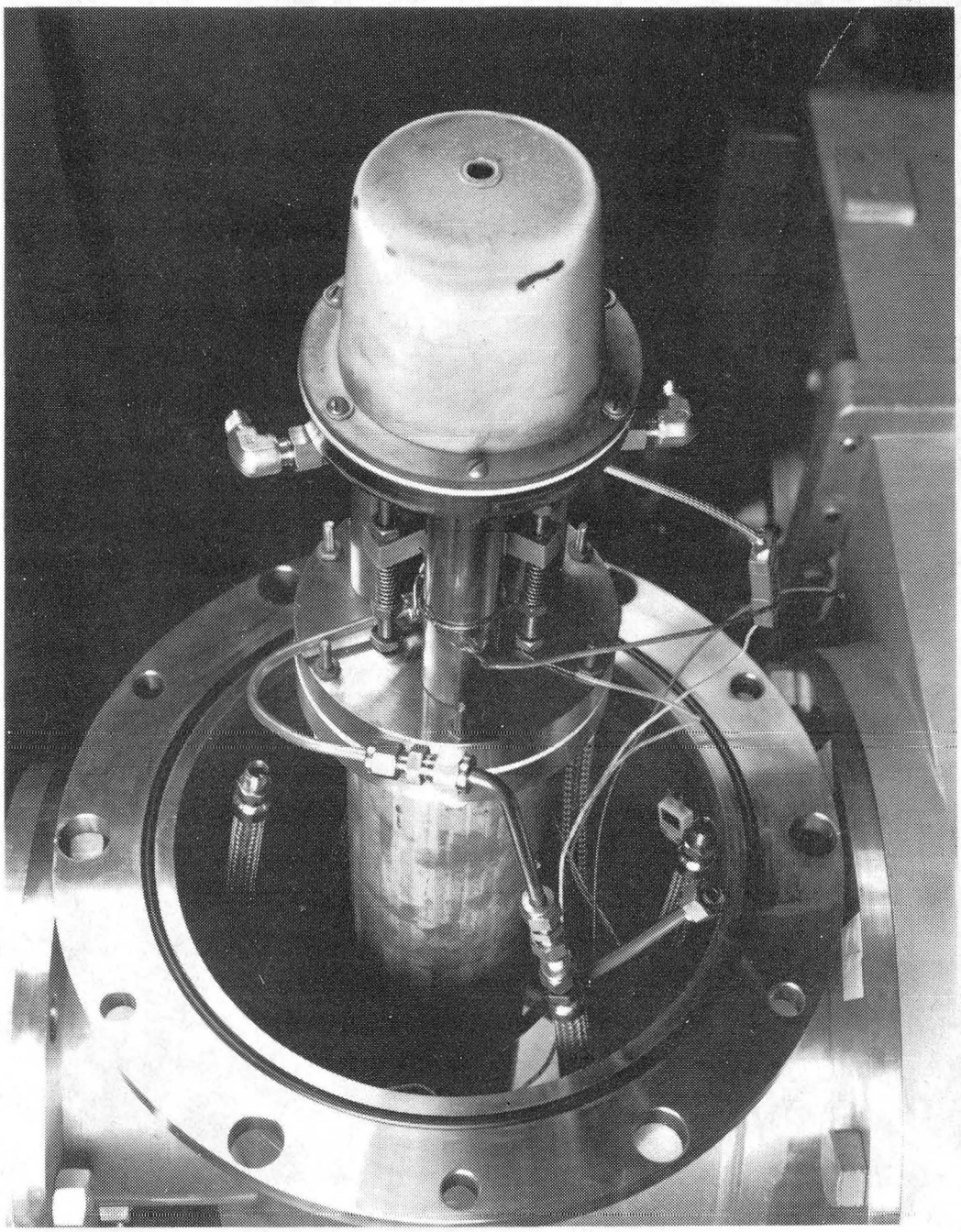

CBB 8712-10778

Figure 7

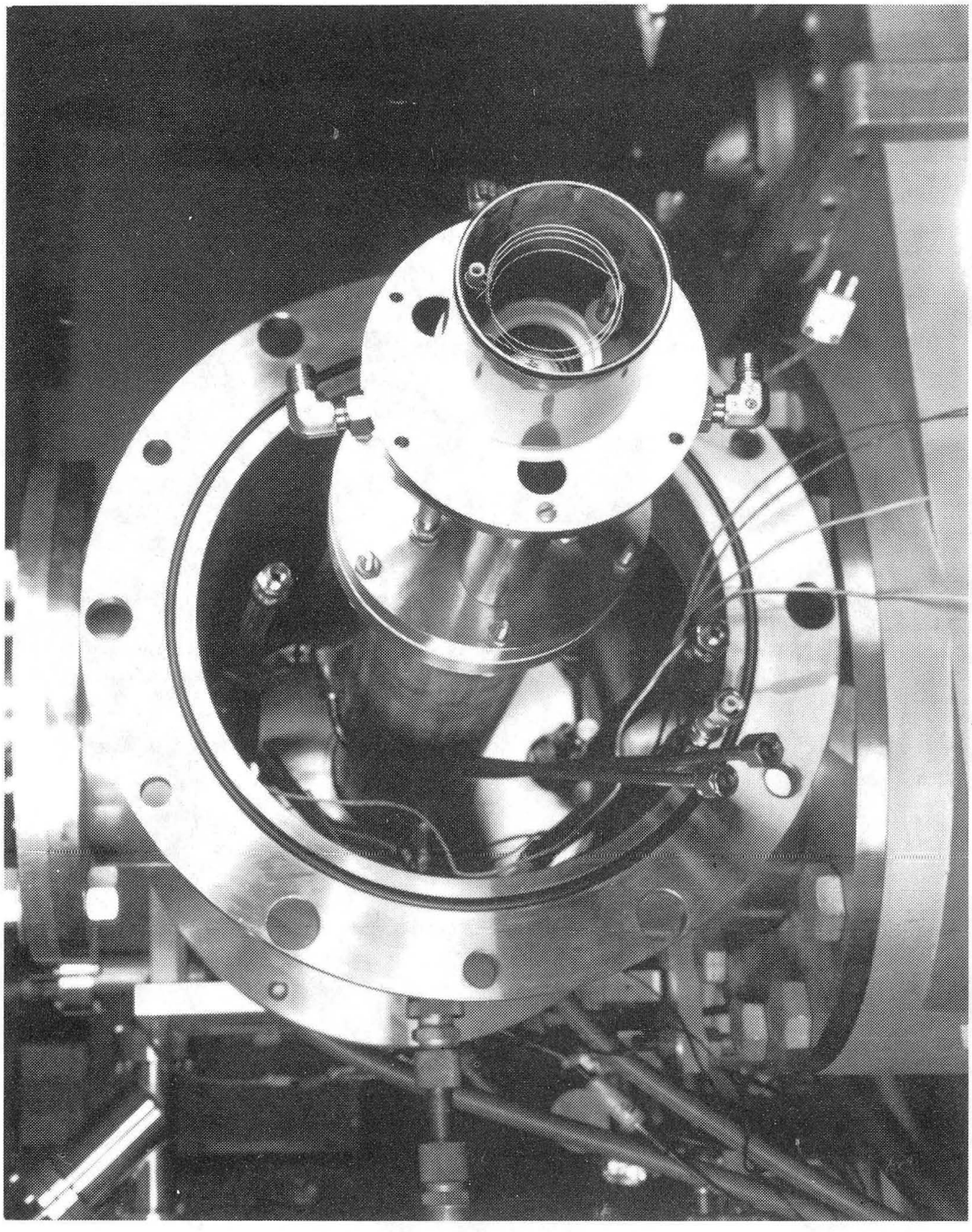

CBB 8712-10782

Figure 8

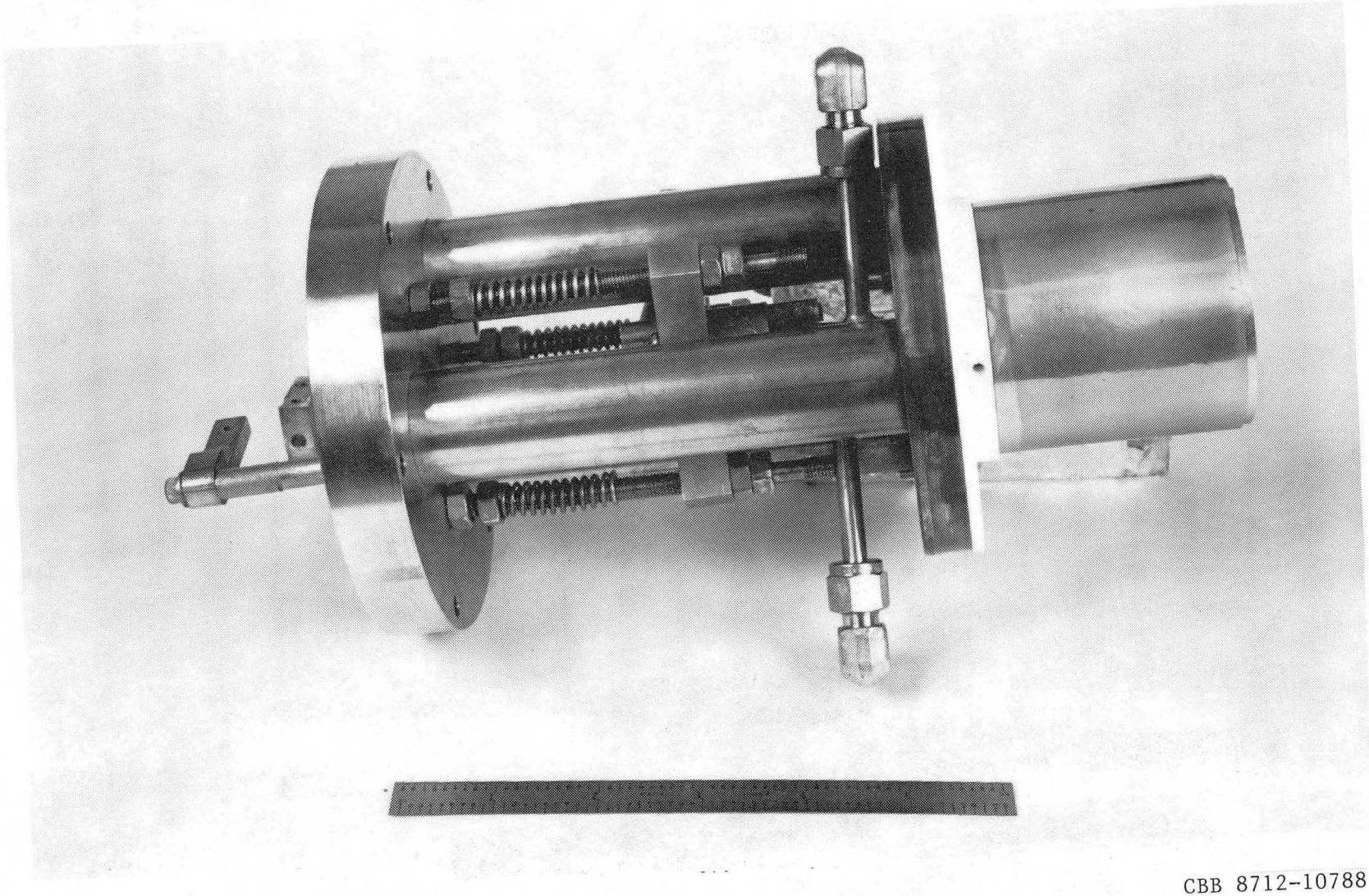

CBB 8712-10788

Figure 9

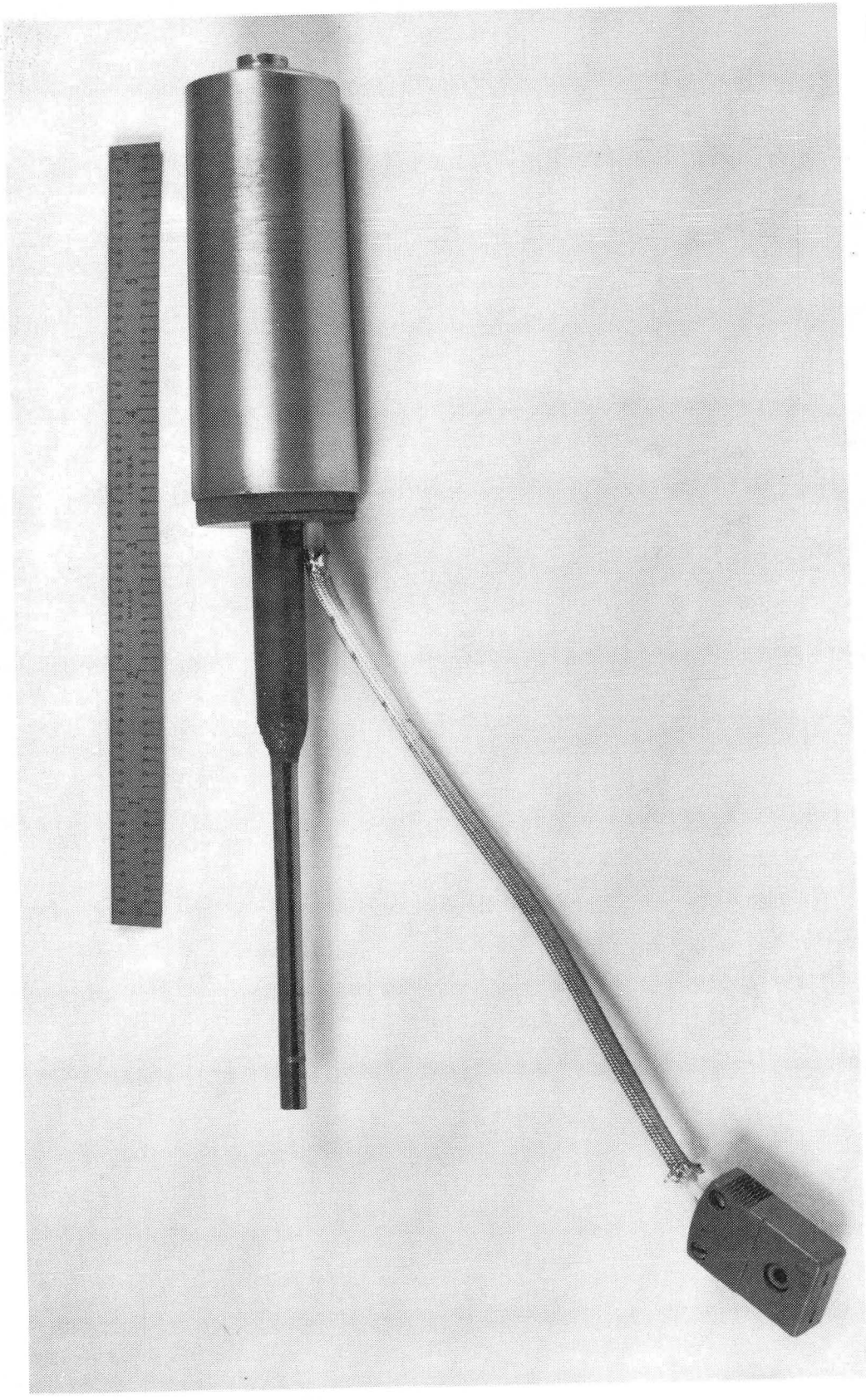

CBB 8712-10792

Figure 10

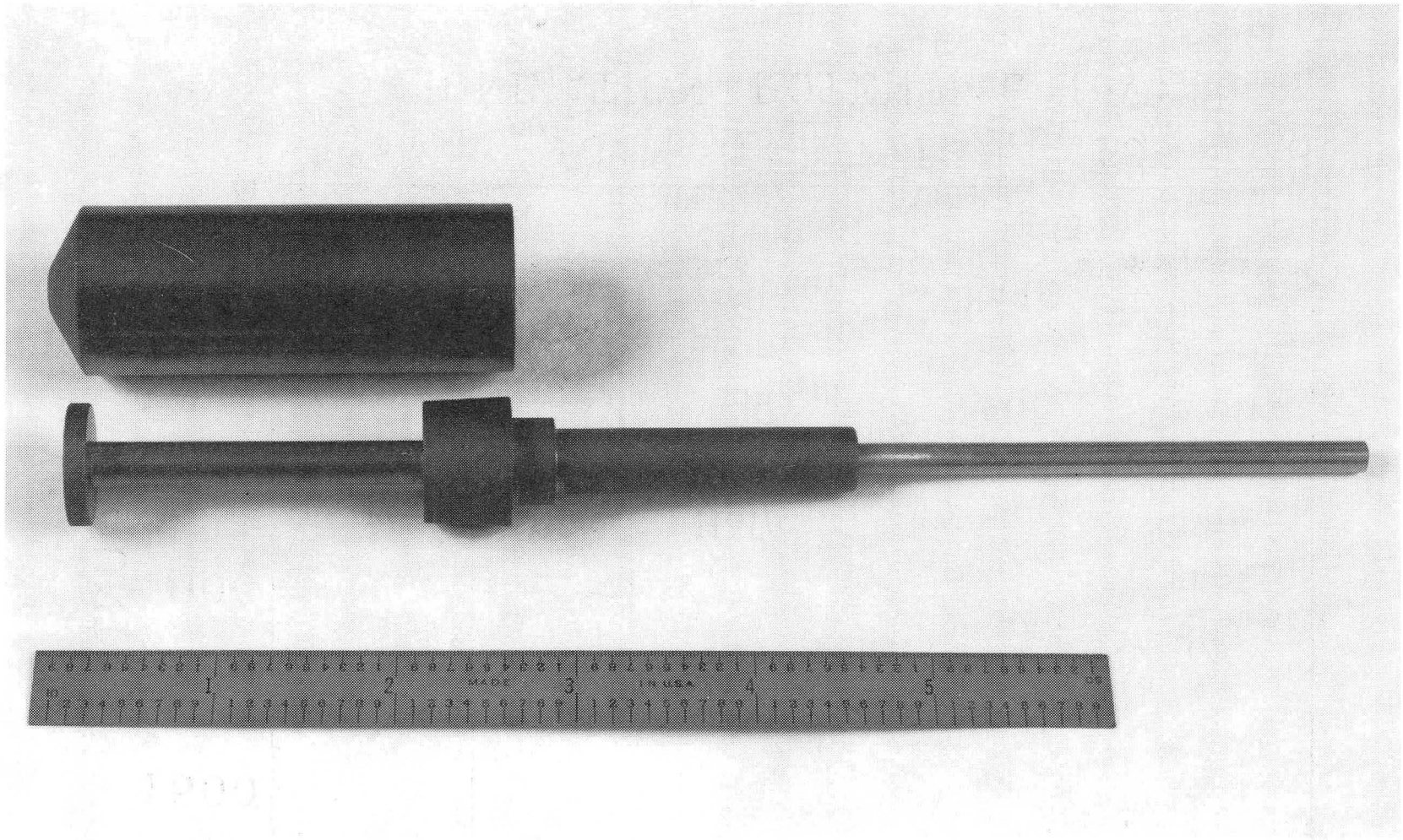

CBB 8712-10796

Figure 11

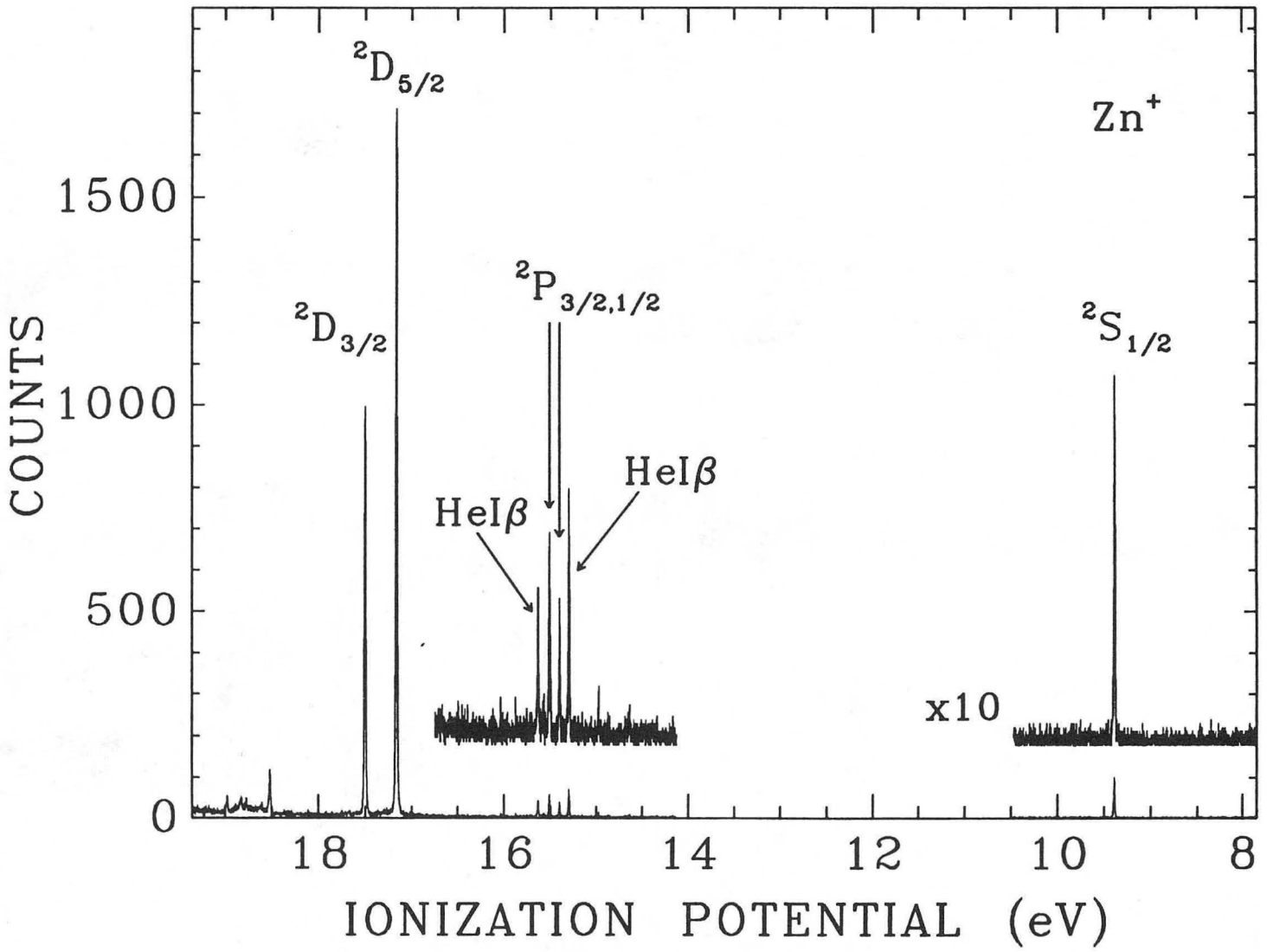

XBL 902-395

Figure 12

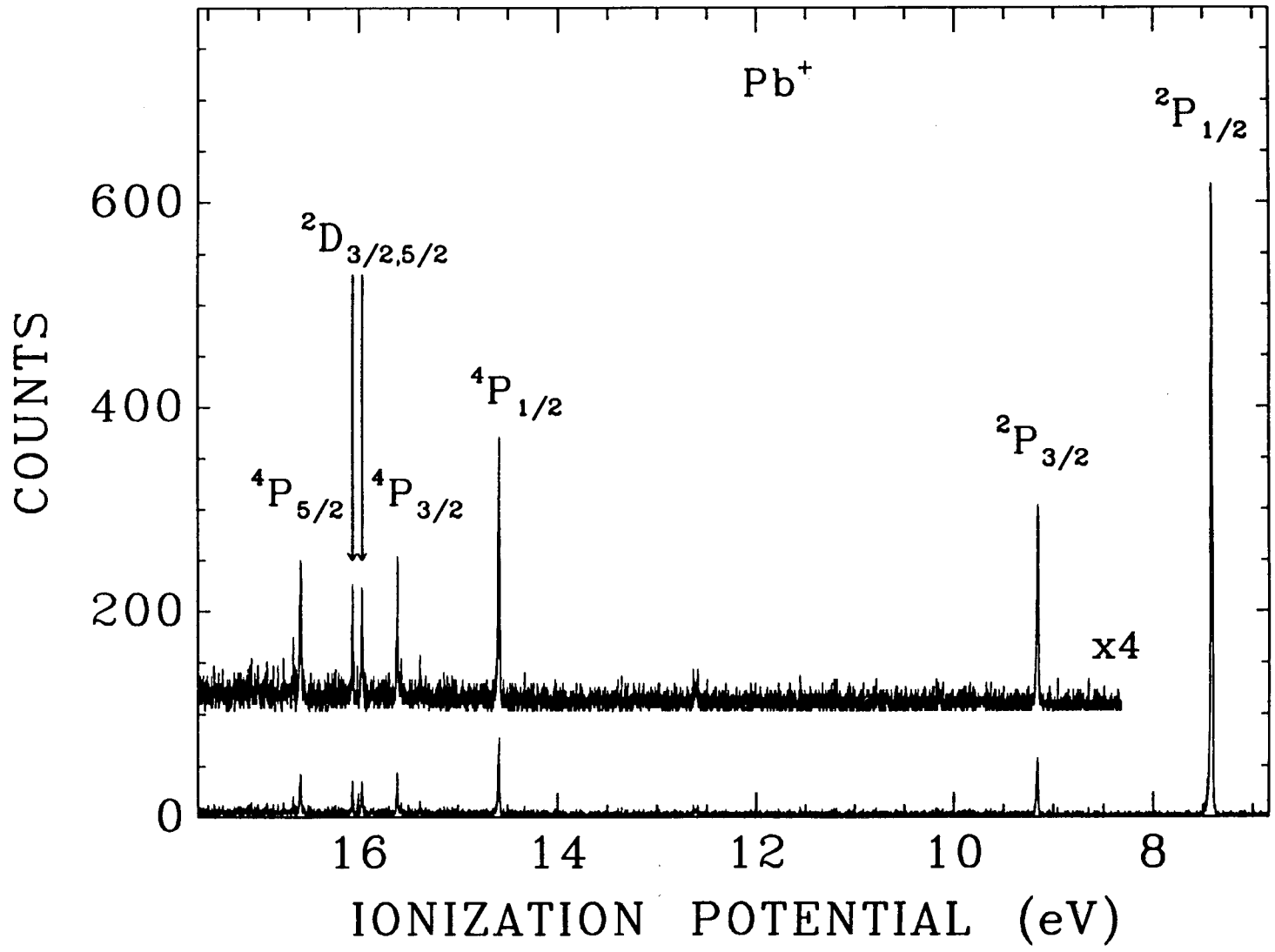

Figure 13

XBL 902-396

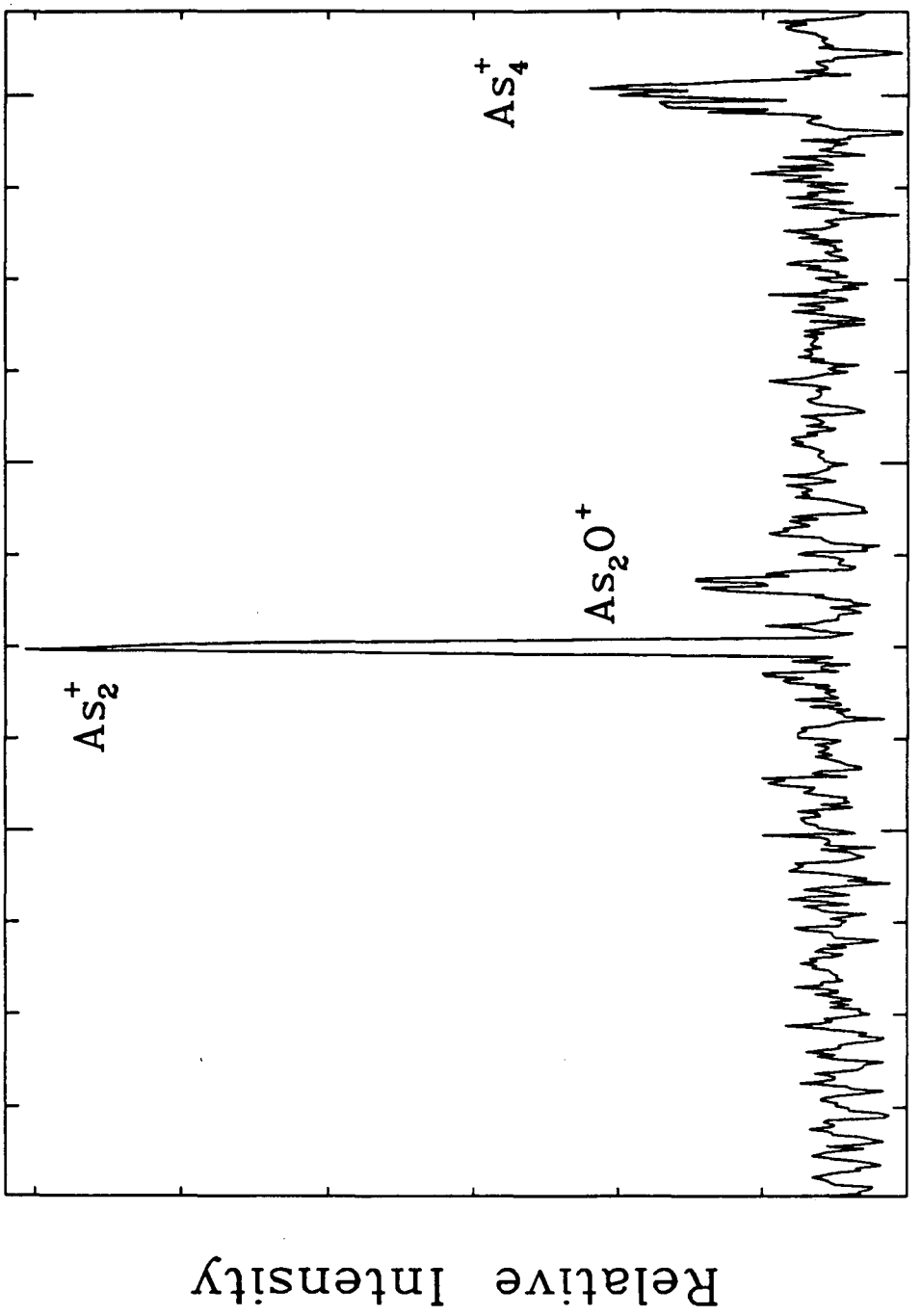

XBL 902-397

Figure 14

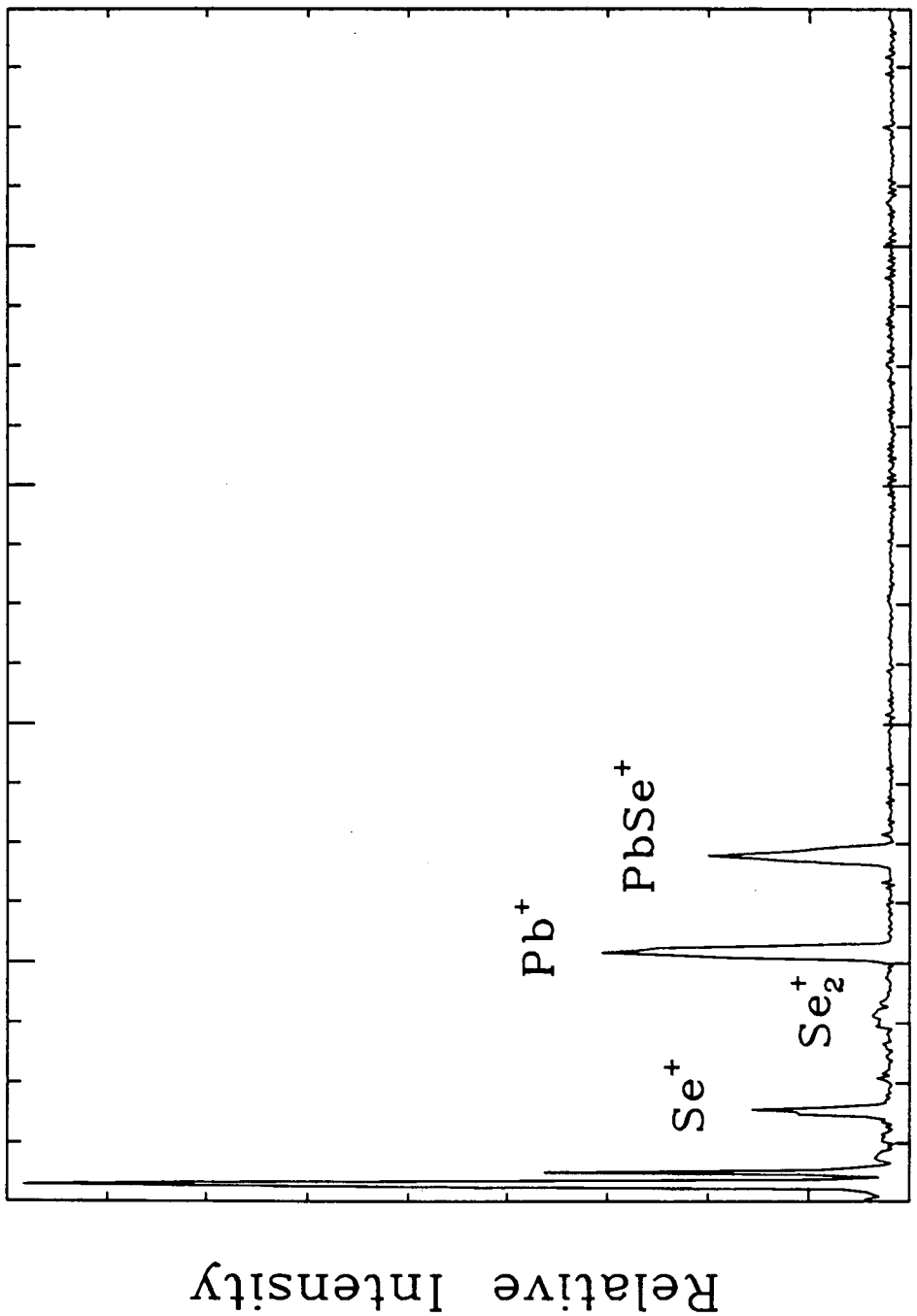

XBL 902-398

Figure 15

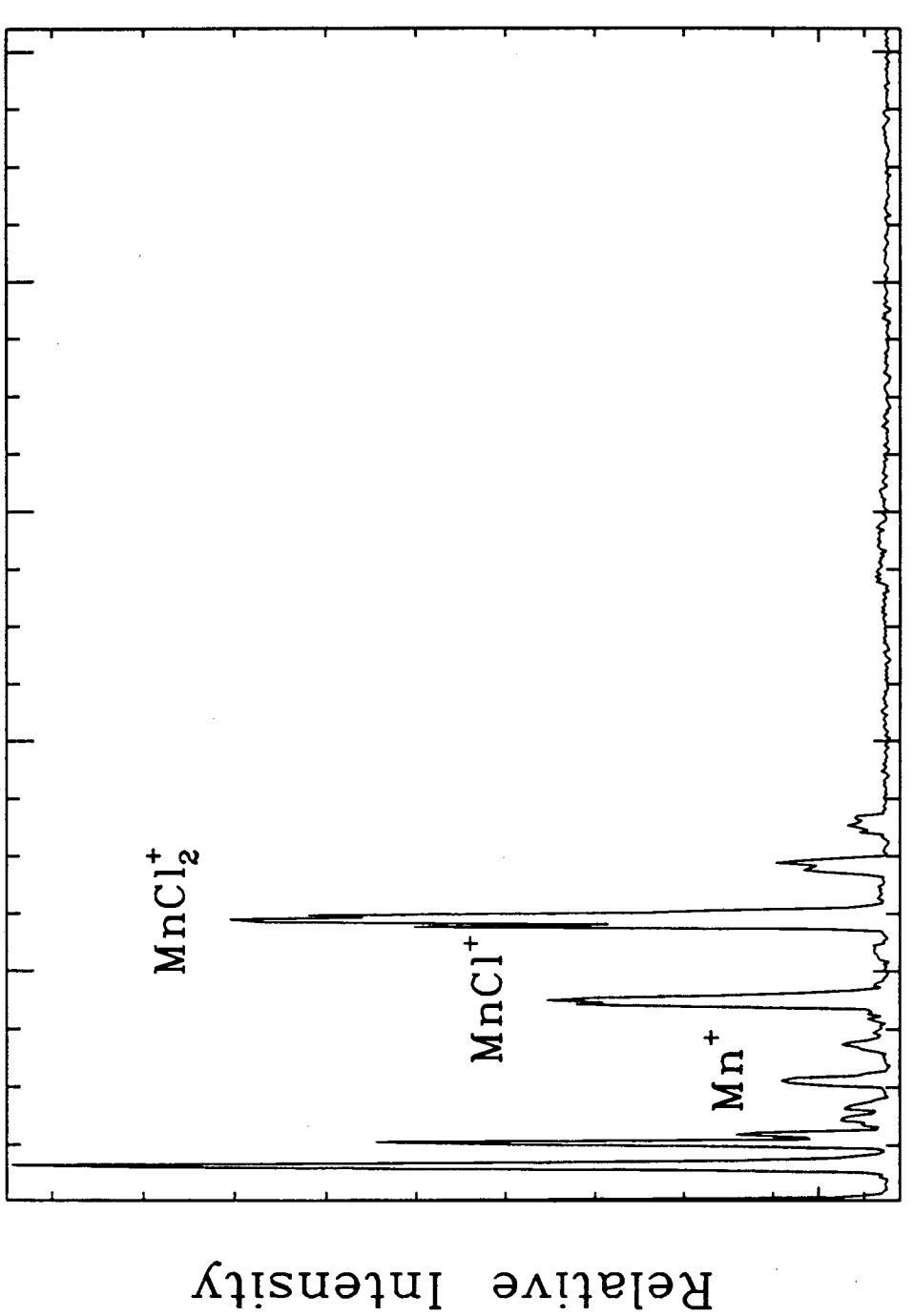

XBL 902-399

Figure 16

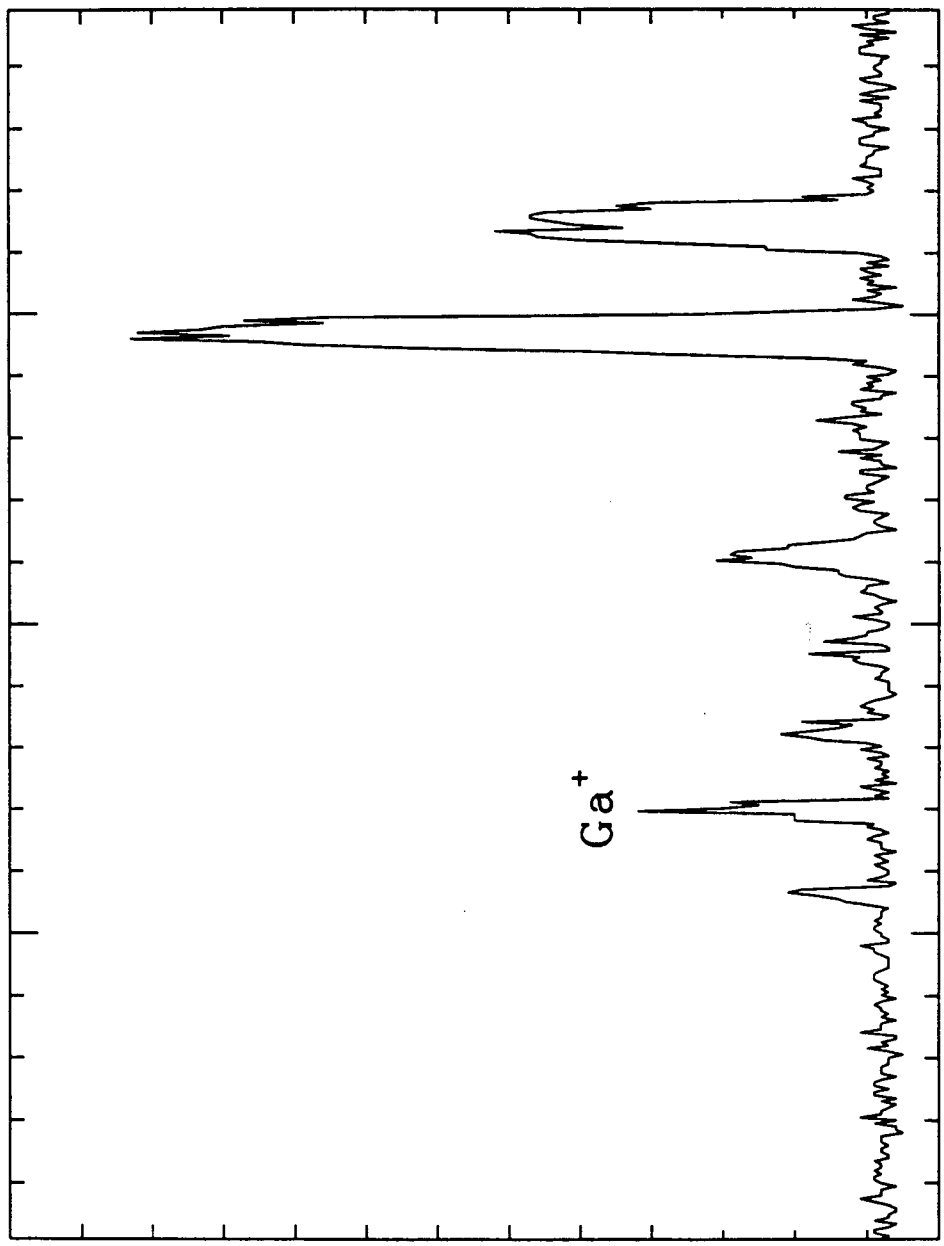

XBL 902-400

Figure 17

Chapter 3

Photoelectron Spectroscopy and Electronic Structure of Heavy Group IV-VI Diatomics*

Abstract

Vibrationally-resolved HeI (584Å) photoelectron spectra of the heavy group IV-VI diatomics SnSe, SnTe, PbSe, and PbTe were obtained with a new high temperature molecular beam source. Ionization potentials and spectroscopic constants are reported for all the ionic states observed. Relativistic complete active space Multi-Configuration Self-Consistent Field (MCSCF) followed by multi-reference singles + doubles relativistic Configuration Interaction (CI) calculations which included up to 200,000 configurations were made on both the neutral diatomics and their positive ions, in collaboration with Balasubramanian. Ionization potentials and spectroscopic constants were calculated and were in good agreement with the experimentally-measured values. Relativistic CI potential energy curves were calculated for all the neutral ground states and the ionic states involved. Relativistic effects were shown to play an important role in these heavy diatomics. The $^2\Sigma^+_{1/2}$ and $^2\Pi_{1/2}$ states for all four molecular ions showed avoided curve crossings, which resulted in pronounced shoulders in the Ω=1/2 potential energy curves of $PbTe^+$.

Experimentally, autoionization transitions were also observed for the $PbTe^+$ spectrum. The importance of the relativistic effect and chemical bonding in the heavy diatomics are discussed.

3.1 Introduction

The heavy group IV-VI diatomics SnSe, SnTe, PbSe, and PbTe are interesting at least in two respects. The bulk materials corresponding to these molecules are low band gap semiconductors[1] and have been the subjects of numerous investigations due to their technological importance as infrared and visible radiation detectors. Clusters of these molecules, which conceptually link the individual molecules to the bulk, may soon also become important subjects of study.[2,3] A detailed understanding of the monomers would be the first step toward the understanding of the series through cluster species up to bulk properties. On the other hand, these diatomics molecules are interesting in their own right, because relativistic effects are expected to play an important role in the chemistry of heavy elements,[4] and these molecules provide some good examples of these effects in small chemical systems.

Photoelectron spectroscopy is the method of choice because it gives unique information about the electronic properties of matter.[5] Study of the photoelectron spectra of heavy group IV-VI molecules has been hindered mainly by the difficulty of producing the molecules in the gas phase. Consequently, there have been very few reports on these molecules. In particular, there have been no studies on the lead chalcogenides except a tentative one by Wu and Fehlner.[6] They also obtained the spectra of GeS, GeSe, SnS, and SnTe, at a low signal level and resolution. White et. al.[7] studied all the germanium and tin chalcogenides with about 85 meV resolution. A few oxides also have been studied: GeO,[8] SiO[9] and SnO.[10]

Theoretically, there have been no studies on the molecules reported here, except for PbSe.[11-13] Theoretical investigations are available for other lighter group IV-VI diatomics: SnO,[13,14] SnS,[15] PbO,[13,16] and PbS.[11-13,17] The information accumulated to date on the spectroscopic constants and potential energy curves of heavy p-block elements hydrides, halides and chalcogenides have been reviewed recently.[18]

In the present study, we combined experiment and theory, trying to understand the bonding and the relativistic effects in these heavy diatomics systematically. We have obtained high resolution HeI (584Å) photoelectron spectra of SnSe, SnTe, PbSe and PbTe, with a new high temperature molecular beam source. Vibrational structure was resolved for all the spectra except for the Π bands of $PbTe^+$, which has very low vibrational frequencies, on the order of our resolution (15-20 meV). With a Franck-Condon factor analysis, we were able to obtain all the spectroscopic constants for all the relevant ionic states. We carried out relativistic quantum chemical calculations to compare with and assist the interpretation of the experimental results.

In what follows, we will give a brief account of the experimental procedures in Section 3.2, and the theoretical method in Section 3.3. The results and data analysis are presented in Section 3.4. We discuss the results in Section 3.5. The conclusions are given in Section 3.6.

3.2 Experimental

The experimental apparatus has two principal parts: the photoelectron spectrometer and the high temperature molecular beam source. Both of these have been described in detail elsewhere[19,20] and in Chapter 2. Thus, only aspects special to the current experiments will be given here.

For the experiments reported here, less than 500 W heating power was needed in all cases. The nozzle-skimmer alignment and the size of the nozzle are also important factors. A large nozzle and good alignment would facilitate lower temperature evaporations, so the heating power and temperature measurement only have relative meanings. In general, we need about 1 to 10 Torr vapor pressure in order to obtain an acceptable spectrum. We normally heat up the oven slowly at the beginning for the source to outgas, using the

quadrupole mass spectrometer to monitor the beam compositions. Then we continuously raise the temperature until a reasonable photoelectron signal strength is achieved.

The SnSe, SnTe, PbSe, and PbTe diatomics are known to be stable vapor species.[21-23] We only observed minor amount of Se_2 and Te_2 as outgases for the SnSe and SnTe runs at low temperature.[24] All samples were purchased commercially from CERAC with better than 98% purity. The experimental conditions are listed in Table 1. The temperatures were measured at the rear of the crucible, and are usually 100 to 200 degrees lower than the effective evaporation temperatures. The carrier gas types and pressures were not optimized for each individual experiment. For the PbTe run alone, we used both He and Ne carrier gases, which gave effectively identical spectra. We were able to estimate vibrational temperatures (Tvib's) of the molecules in the beams from hot band transitions with Franck-Condon analyses (see Section 3.4). These are also listed in Table 1. It can be seen that the vibrational coolings were only moderate. The rotational coolings were expected to be much greater, but we could not make a good estimate of their magnitudes.

The calibration of the photoelectron kinetic energy was done with the $Ar^+ {}^2P_{3/2}$ photoelectron peak, which had a resolution of 13 meV when the analyzer was operated at 1 eV pass energy. Under the high temperature conditions, the kinetic energy scale drifted faster, so we took shorter scans within less than an hour, and then added the spectra later to achieve better statistics. The resolution was degraded to the range 15 - 20 meV in the final spectrum.

3.3 Method of Theoretical Calculations

The ground states of all the group IV-VI diatomics are $^1\Sigma^+$ states arising from the valence configuration $1\sigma^2 2\sigma^2 3\sigma^2 1\pi^4$. The 3σ orbital is expected to be a strongly bonding orbital formed from the p_z orbitals of the two atoms along the internuclear axis. The 1π

orbital should be a bonding orbital formed from the p_x and p_y orbitals of the two atoms, with the group VI atom contributing more than the group IV atom for the heavier species. For oxides and sulfides, this is a nonbonding or weakly bonding chalcogen orbital.

The ionization of an electron from the 1π orbital should lead to a $^2\Pi$ state described by a $1\sigma^2 2\sigma^2 3\sigma^2 1\pi^3$ configuration. The removal of a 3σ electron would result in a $^2\Sigma^+$ state with a $1\sigma^2 2\sigma^2 3\sigma 1\pi^4$ configuration. Spin-orbit interaction would split the $^2\Pi$ state into two spin-orbit components, $^2\Pi_{1/2}$ and $^2\Pi_{3/2}$. As the relativistic effect becomes stronger for the heavy molecules, it is more appropriate to represent these two states with the Ω quantum numbers, 1/2 and 3/2. The same is true for the $^2\Sigma^+$ state, for which the Ω designation 1/2 would be more appropriate in the relativistic limit. For convenience, however, we will still use the labellings $^2\Pi_{1/2}$, $^2\Pi_{3/2}$ and $^2\Sigma^+$ or $^2\Sigma^+{}_{1/2}$, or where needed for clarity, we shall use both labellings interchangeably.

It is known from earlier relativistic calculations[13] that the $^2\Pi$ and $^2\Sigma^+$ states cross for SnO, PbO and PbS. In the relativistic limit, the $^2\Pi_{1/2}$ and $^2\Sigma^+{}_{1/2}$ states have the same symmetry and can interact with each other. Consequently, the influence of the spin-orbit coupling and the exact region of avoided crossings for the heavier molecules could be very interesting.

We carried out complete active space MCSCF (CASSCF), followed by multi-reference singles + doubles CI (MRSDCI) calculations on the low-lying electronic states of $SnSe^+$, $SnTe^+$, $PbSe^+$ and $PbTe^+$, and the ground state of the corresponding neutral species. These calculations were supplemented by relativistic configuration interaction (RCI) calculations of the entire potential energy curves. We used relativistic effective core potentials for all the four atoms described in earlier investigations.[13,15,17,25,26] For the CASSCF and MRSDCI calculations, flexible valence gaussian basis sets were employed. For Pb and Sn, the outer $d^{10}s^2p^2$ shells were explicitly retained in the MO calculations. The Pb and Sn valence basis sets were of (4s4p4d) quality described in an earlier investigation on PbH_2 and SnH_2.[27] For Se and Te, the outer s^2p^4 shells were explicitly

retained in all the calculations. We used comparable (4s4p) valence + 2 sets of diffuse d-type polarization functions basis resulting in (4s4p2d) basis sets.

In the CASSCF calculations, the orbitals which correlated into the valence s and p orbitals of the individual atoms at infinite separation were included in the active space. These calculations were actually made in the C_{2v} group with the C_2 axis chosen as the intermolecular axis. In this orientation, the active space is composed of four a_1 orbitals, two b_2 orbitals and two b_1 orbitals. The ten outermost electrons were distributed in all possible ways (full CI) among these orbitals in the CASSCF of the neutral species; the corresponding nine electrons were distributed in all possible ways among these orbitals for the positive ions. Separate CASSCF/CI calculations were carried out for each state of the positive ions and the ground state of the neutral species.

The CASSCF calculations were followed by MRSDCI calculations which included excitations of electrons both into internal and external orbitals. The MRSDCI calculations included all configurations in the CASSCF with coefficients ≥ 0.07 as reference configurations. Subsequently, single and double excitations from all these configurations into all the orbitals were allowed in MRSDCI. The MRSDCI calculations included up to 200,000 configurations.

The spin-orbit effect on the electronic states of these species was addressed through the RCI method. The spin-orbit integrals obtained from relativistic effective core potentials (RECP) were introduced into the CI Hamiltonian matrix. Then all important configurations which mix in the presence of spin-orbit coupling were included in the RCI as reference configurations. For example, the Ω=3/2 states of the ions included, $^2\Pi_{3/2}$ ($1\sigma^2 2\sigma^2 3\sigma^2 1\pi^3$), $^2\Pi_{3/2}$ and $^4\Pi_{3/2}$ ($1\sigma^2 2\sigma^2 3\sigma 4\sigma 1\pi^3$) and Ω=3/2 states arising from $1\sigma^2 2\sigma^2 3\sigma^2 1\pi^2 2\pi$ configuration. The final RCI calculations of the 3/2 states included 20 reference configurations. The RCI calculations for the 1/2 states included $^2\Pi_{1/2}$ ($1\sigma^2 2\sigma^2 3\sigma^2 1\pi^3$), $^2\Sigma^+_{1/2}$ ($1\sigma^2 2\sigma^2 3\sigma 1\pi^4$, $1\sigma^2 2\sigma^2 3\sigma 4\sigma 1\pi^3$) and 1/2 states arising from

$1\sigma^2 2\sigma^2 3\sigma^2 1\pi^2 2\pi$ configuration. The RCI calculations were done for the entire potential energy curves of the neutral and ionic species.

All the CASSCF/MRSDCI calculations were done using a modified version[28] of the ALCHEMY II codes[29] to include RECPs. The RCI calculations were done using the method described in Ref. 27.

3.4 Results and Data Analysis

The photoelectron spectra of $SnSe^+$, $SnTe^+$, $PbSe^+$, and $PbTe^+$ are shown in Figures 1-4, respectively. The four spectra look very similar except that the spin-orbit splitting in the Π bands increases from $SnSe^+$ to $PbTe^+$. The $^2\Sigma^+$ bands, arising from removal of electrons from the 3σ orbitals, are very sharp, with relatively little vibrational excitation. This implies that the 3σ orbital is a nonbonding or weakly bonding orbital, just opposite to what we would have expected. The $^2\Pi$ bands are split into two spin-orbit bands $^2\Pi_{1/2}$ and $^2\Pi_{3/2}$ with very rich vibrational excitation, indicating that the π orbital is a rather strongly bonding orbital. The two bands overlap heavily in $SnSe^+$, and become well-separated in $PbTe^+$ as the spin-orbit effect gets stronger. It is interesting to note that the spin-orbit splitting is larger in $SnTe^+$ than that in $PbSe^+$, indicating that the group VI atom contributes more to the π orbital than the group IV atom does.

No other photoelectron bands were observed at higher binding energy than that of $^2\Sigma^+$ in all cases. The 1σ orbitals presumably have too high energies to be accessed by the HeI (584Å) radiation. At the HeI energy, the 2σ orbitals have too low ionization cross sections to be observed under our experimental conditions.[7] However, we observed two extra bands marked as "AI" in the $PbTe^+$ spectra at low energy. These two bands or shoulders, resembling the two Π bands, do not arise from impurities, and were not affected by changing from Ne to He carrier gas. Based on the resemblance of these two bands to the two main Π bands, we assign them as autoionization transitions, as it is well known

that autoionization can markedly alter the Franck-Condon factors from those of the direct ionization processes.[30] This would imply that there must be a resonant absorption at about 584Å for PbTe, which has not been observed to our knowledge.

Vibrational structure was well resolved for all the spectra except $PbTe^+$, which has very low vibrational frequencies. There are pronounced hot band transitions in $SnTe^+$ and $PbSe^+$, labelled as "HB" in the figures. The ionization potentials (IPs) and vibrational frequencies were easily obtained for the $^2\Sigma^+$ states from the sharp spectra. For the Π bands, the vertical IPs were obtained by fitting a Gaussian to each band, and the mean values of the Gaussians were taken as the vertical IPs. Two factors complicate extraction of the adiabatic IPs: the hot band transitions and the overlapping nature of the two Π bands. The observation of autoionizations in $PbTe^+$ indicates that the ground vibrational levels in the Π bands may not be reached by vertical transitions. Therefore, the experimentally-derived adiabatic IPs may be taken only as upper bounds.

In order to obtain the equilibrium bond lengths for the individual ionic states, we have performed Franck-Condon factor calculations. In addition to the equilibrium bond length, a Franck-Condon factor analysis also can yield the vibrational temperature and a refined value of the vibrational frequency. It can also help estimate the adiabatic ionization potential.

The Franck-Condon factor calculation adopted here is similar to that used in Ref. 31. It employs a Morse oscillator, described by expansion as a power series in $(r-r_e)$, where r_e is the equilibrium bond length. The $(r-r_e)^3$ and $(r-r_e)^4$ terms were taken as perturbation corrections to the harmonic oscillator Hamiltonian. During the analysis, r_e and Tvib (the vibrational temperature) were varied systematically until the calculated spectrum was best fitted to the experimental spectrum. For a well-resolved spectrum, r_e was sensitive to within $\pm$ 0.005 Å, Tvib $\pm$ 50 K. In the current analyses, we first calculated the $^2\Sigma^+$ bands because they have sharp structure and easily recognizable hot bands. A fit for the $^2\Sigma^+$ band of $PbSe^+$ is shown in Figure 5, from which we obtained r_e = 2.547 Å, and

Tvib = 500 K. We then used the Tvib to fit the Π bands, for which we adjusted the r_e and the adiabatic IP to get the best fit. Figure 6 shows such a fit for the $^2\Pi_{3/2}$ band of $PbSe^+$. It can be seen from Figure 5 and Figure 6 that the hot bands can make the spectrum very complicated. The experimental spectrum is really a superposition of the transitions from the ground vibrational state and all the hot band transitions. This could be more serious without the supersonic cooling.

It should be pointed out that the Franck-Condon factor calculation is only approximate. It tends to underestimate the Franck-Condon factors for high vibrational levels in the final states. For the Π bands of $PbTe^+$, too many vibrational levels were needed, and the calculation was no longer feasible. It may also be that the final-state potential energy curves are too shallow for a Morse oscillator representation to be adequate.

All the derived IPs and spectroscopic constants are tabulated in Tables 2-5 for $SnSe^+$, $SnTe^+$, $PbSe^+$ and $PbTe^+$, respectively, along with the theoretical values. The experimental vibrational frequencies for the Π bands of $PbTe^+$ are only estimates. The Tvib's have been given in Table 1.

3.5 Discussion

3.5.1 Comparisons between Experimental and Theoretical Spectroscopic Constants

The theoretical potential energy curves near the minima were fitted to a cubic polynomial to obtain the theoretical r_e and ω_e values of the various states. Figures 7-10 show the RCI potential energy curves of the (SnSe, $SnSe^+$), (SnTe, $SnTe^+$), (PbSe, $PbSe^+$) and (PbTe, $PbTe^+$) pairs, respectively. Tables 2-5 show the experimental and theoretical spectroscopic constants of the ground neutral and ionic states of the four

molecules. The experimental spectroscopic constants of the neutral ground states $^1\Sigma^+$ (0^+) are from Ref. 32.

Tables 2-5 show the theoretical r_e values of the neutral species to be 0.04-0.08 Å longer than the experimental values, the worst case being PbTe. This is anticipated for the level of theory employed here which used relativistic ECPs in conjunction with valence-plus-polarization Gaussian basis sets. The ω_e values are within 2.4-6.5% of the experimental values for the ground states of the four species. The dissociation energies of the ground states of the neutral species are within 0.7-10% of the experimental values. The best agreement in the D_es is obtained in SnSe for which the spin-orbit effect is negligible (0.03 eV).

The r_e values of the ionic species are also in very good agreement (3-6%) with the experimental values. Note that the bond length of the $^2\Sigma^+_{1/2}$ states for all four ions are shorter in comparison to those of the $^2\Pi_{1/2}$ and $^2\Pi_{3/2}$ states and similar to those of the ground $^1\Sigma^+$ states, in agreement with the experimental observation that there is very little vibrational excitation in the $^2\Sigma^+_{1/2}$ bands.

The theoretical IPs are within 0.6-6% of the experimental values. Considering that our basis sets and electron correlation inclusions were just adequate to calculate the IPs of such species, this agreement is very gratifying. For the $^2\Sigma^+_{1/2}$ states, the adiabatic IPs (IP_{ad}s) coincide with the vertical IPs (IP_{vt}s), because the equilibrium bond lengths in the $^2\Sigma^+_{1/2}$ states do not differ much from the neutral ground states ($^1\Sigma^+$), as seen above.

Although the absolute theoretical and experimental energy separations of the $^1\Sigma^+$ state of the neutral species and $^2\Pi_{3/2}$ state of the ions are not in exact agreement, the theoretical and experimental energy separations of the $^2\Pi_{1/2}$ and $^2\Sigma^+_{1/2}$ of the ions relative to $^2\Pi_{3/2}$ agree very well. The ground state theoretical spin-orbit splitting ($^2\Pi_{3/2}$ - $^2\Pi_{1/2}$ separation) of $PbTe^+$ is 4518 cm^{-1} compared to an approximate value of 4680 cm^{-1} obtained from the photoelectron spectrum of PbTe. Similarly, the $^2\Pi_{3/2}$ - $^2\Sigma^+_{1/2}$ experimental and theoretical vertical separations are 1.23 eV and 0.93 eV, respectively.

As seen from Table 4, the agreement between theoretical and experimental IPs for PbSe are in the best agreement among the four species, indicating that both electron correlation effects and spin-orbit effects were included in a consistent way for PbSe. The theoretical spin-orbit splitting for the ground state ($^2\Pi_{3/2}$-$^2\Pi_{1/2}$) is 2585 cm^{-1} compared to the present experimental value of 2660 cm^{-1}.

The experimental D_es of the ionic states were calculated using the formula:

$$D_e(MCh^+) = IP(M) - IP(MCh) + D_e(MCh)$$

where IP(M) is the ionization potential of the group IV atom taken from Ref. 33, IP(MCh) is the ionization potential of the group IV-VI diatomics and D_e(MCh) is the experimental dissociation energy of the neutral $^1\Sigma^+$ ground state of the chalcogenide. The theoretical D_es of MCh^+ were obtained from the RCI calculations at r_e and long distance. Consequently, the theoretical values include the spin-orbit coupling effect more accurately than the electron correlation effects.

3.5.2 Nature of the Electronic States and the Potential Energy Curves

The ground states of all four species are described predominantly by the $1\sigma^2 2\sigma^2 3\sigma^2 1\pi^4$ valence electronic configuration near the equilibrium geometries. As mentioned before, the ionization of a π electron leads to the spin-orbit split $^2\Pi_{1/2,3/2}$ states arising from the $1\sigma^2 2\sigma^2 3\sigma^2 1\pi^3$ configuration. The removal of a 3σ electron leads to $^2\Sigma^+_{1/2}$ state.

The relative ordering of the $^2\Sigma^+$ and $^2\Pi$ states depends on the internuclear distance. At short distances, the $^2\Sigma^+$ state is lower in energy while at longer distances the $^2\Pi$ state is lower. In CO^+, which has a very short bond length, the $^2\Sigma^+$ state is indeed lower than the $^2\Pi$ state.[34] This is in contrast to the current situation, where the $^2\Pi$ states are lower than the $^2\Sigma^+$ state, because here the bond lengths are much longer. The $^2\Sigma^+$ and $^2\Pi$ potential

energy curves would cross in the absence of the spin-orbit coupling for all four ions. This crossing induces an avoided crossing in the Ω=1/2 states in the presence of spin-orbit coupling, as shown in Figures 7-10. The avoided crossing has been found also in PbO^+, PbS^+ and SnO^+,[13] indicating the importance of the relativistic effect in these heavy molecules.

The avoided crossings in the Ω=1/2 states can be best understood through analyses of the RCI wave functions versus internuclear distances. For example, the lowest 1/2 state denoted by 1/2(I) of $PbTe^+$ is 82% $^2\Sigma^+_{1/2}$ and 0.4% $^2\Pi_{1/2}$ at 4.75 bohr. However, at 5.00 bohr, it becomes 83% $^2\Pi_{1/2}$ and 0.4% $^2\Sigma^+_{1/2}$. The second root of the Ω=1/2 RCI calculations denoted by 1/2(II) exhibits approximately the opposite behavior. That is, at short distances, the 1/2(II) state is predominantly $^2\Pi_{1/2}$, but it switches to $^2\Sigma^+_{1/2}$ at 5.0 bohr.

The avoided crossing discussed above results in shoulders in the 1/2 states of $PbTe^+$ and $PbSe^+$. The crossing of the $^2\Pi_{3/2}$ curve with the $^2\Pi_{1/2}$ curve is also due to the above-mentioned avoided crossing.

Photoelectron spectroscopy is sensitive to the final-state potential energy surfaces. It especially probes the global ionic potential energy curves for diatomic molecules. From Figures 7-10, we can see that the $^2\Sigma^+_{1/2}$ states have equilibrium bond lengths very close to that of the $^1\Sigma^+$ ground states, indicating that a Franck-Condon transition from the ground $^1\Sigma^+$ state will fall close to the minimum of the $^2\Sigma^+_{1/2}$ potential energy curve, with a very narrow Franck-Condon region. This is consistent with the observed photoelectron spectra shown in Figures 1-4.

However, the equilibrium bond lengths of the $^2\Pi_{3/2}$ and $^2\Pi_{1/2}$ states are significantly longer than that of the $^1\Sigma^+$ ground state, and the Franck-Condon transitions should reach the repulsive sides of the $^2\Pi_{3/2}$ and $^2\Pi_{1/2}$ potential energy curves, resulting in broad photoelectron bands as seen in Figures 1-4. The band shapes should reflect the curvatures of the upper potential energy surfaces. A shallow curve will result in a narrower

Franck-Condon region, hence, a narrower band, and a steep curve would give rise to a broader band.

If we closely examine the $^2\Pi_{3/2}$ and $^2\Pi_{1/2}$ bands in Figures 1-4, we find that the $^2\Pi_{1/2}$ bands are somewhat narrower than the $^2\Pi_{3/2}$ bands. This is particularly obvious in the cases of $SnTe^+$ and $PbTe^+$ where there is less overlap. This difference in band shapes reflects the avoided curve crossing between the $^2\Sigma^+_{1/2}$ and the $^2\Pi_{1/2}$ states, because it is the avoided curve crossing which makes the $^2\Pi_{1/2}$ curves look shallower than the $^2\Pi_{3/2}$ curves. These two curves would otherwise look similar at least on the repulsive sides, and give rise to similar photoelectron bands as observed in light molecules such as CO.[34]

The vibrational frequencies, in principle, should also be different. But the difference is too small to be easily observed. There is, nevertheless, a noticeable difference in the case of $SnTe^+$, as seen in Table 3.

3.5.3 Nature of the Chemical Bonds of the Heavy Group IV-VI Diatomics

Table 6 shows the Mulliken population analyses of the MRSDCI natural orbitals of both the neutral and ionic chalcogenides. Although Mulliken populations cannot be used in an absolute sense due to their basis set dependence, they provide important insight into the nature of bonding in a relative sense. As seen from Table 6, all the neutral chalcogenides in the $^1\Sigma^+$ ground states are quite ionic with the polarity of M^+Ch^-. For example, 0.43 negative charge moves from Pb to Te in the $^1\Sigma^+$ state of PbTe. This charge transfer is even larger for PbSe (0.53 electron), as expected.

As seen from Table 6, $PbTe^+$ in the $^2\Pi$ ground state loses the Pb^+Te^- ionic polarity of the bond, in that the gross population of Te is close to six (6.07). The bonding in $PbTe^+$ is thus considerably less ionic in comparison to PbTe. For $SnTe^+$, also only 0.06 excess charge was found on Te.

For selenides, about 0.16-0.18 excess electron populations are found on Se in the ions. Again, the selenides are similar to the tellurides in that neutral species exhibit greater polarity of bonds.

Comparing the Sn and Pb chalcogenides, we notice that Sn has more charge transfer than Pb, which is opposite to the periodic trend. This is an illustration of the relativistic effect in Pb. The spin-orbit effect and the relativistic inert pair effect in Pb is so strong that the Pb atomic ground state configuration can be approximately described as $(core)6s^2(6p_{1/2})^2(6p_{3/2})^0$. Actually, Pb in its ground state is composed of 88% $^3P_0$ and 12% $^1S_0$.[35] Both the inert-pair effect and the spin-orbit effect result in less charge transfer in the case of Pb compared to Sn.

Another way of viewing the differences in the gross populations of the two atoms in neutral and ionic species is that removal of an electron in the neutral chalcogenides does not take place from the metal atom alone. For example, in the case of PbTe, 63% of the removed electron is from Pb, while the remaining 37% is from Te. Similarly, for PbSe, 65% of the removed electron is from Pb, while 35% is from Se. Note that this trend in the population is consistent with the lower ionization potential of Te compared to Se.

For SnTe, 57% of the removed electron comes from Sn, while 43% comes from Te. For SnSe, 56% of the removed electron comes from Sn, while 44% is from Se. Thus, for SnTe and SnSe, the ionization of a π electron is divided almost equally between the two atoms, while, for PbSe and PbTe, the lead atom sheds a greater percentage of the electron charge.

The individual gross s and p populations of the two atoms are also of interest. The valence populations of the Pb atom are $s^{1.84}p^{1.63}d^{0.10}$ in the ground state of PbTe. For the ion, the corresponding distribution is $s^{1.84}p^{1.02}d^{0.06}$. This implies that most of the 63% of the removed electron is from the Pb 6p orbital. The 6s population remains the same for both PbTe and PbSe. This is consistent with the relativistic inert pair effect of the Pb 6s shell, which is stabilized considerably by the relativistic mass-velocity contraction resulting

in extra stability of this shell. This is realized by comparing the s populations of Pb and Sn in different species. The lead atom has a 0.07 larger s population than that of the tin atom.

The valence population of Te in PbTe is $s^{1.96}p^{4.33}$. The extra 0.33 negative charge in the p orbital is due to the polarity of the Pb^+Te^- bond. Again, all of the ionization comes from the p orbitals of Te and Se atoms.

The overlap populations decrease in ionizing the chalcogenides. This suggests weakening of the bonding consistent with smaller D_es of the ionic species compared to the neutral species. The overlap populations in general decrease as the species become heavier. This trend is also consistent with the smaller D_es of the heavier chalcogenides.

The photoelectron spectra shown in Figures 1-4 indicate little vibrational excitation when removing an electron from the 3σ orbital. The bond length of the $^2\Sigma^+_{1/2}$ state does not differ very much from that of the $^1\Sigma^+$ ground state. These results imply that the 3σ orbital is more localized on one atom. Since the bonding is quite ionic in these molecules, this suggests M^+Ch^- character and thus the 3σ orbital should be more localized on the chalcogenide atom. This is in agreement with our theoretical calculations although orbital relaxation effects are found to be significant. Therefore, the chemical bonds in the heavy group IV-VI diatomics can be characterized by being partially ionic and partially covalent through the overlaps of the p orbitals on the two atoms.

3.6 Conclusions

We have measured the photoelectron spectra of $SnSe^+$, $SnTe^+$, $PbSe^+$ and $PbTe^+$ with our new high temperature molecular beam source. Vibrational structure was resolved for all the spectra except for $PbTe^+$. Ionization potentials and spectroscopic constants were obtained for all the related ionic states. Franck-Condon factor calculations were shown to be very useful in the data analyses. In the $PbTe^+$ spectrum, autoionization transitions were observed.

The relativistic effect was shown to be very important for the heavier molecules. We performed relativistic quantum chemistry calculations to assist the interpretation of the observed photoelectron spectra. The theoretical ionization potentials and spectroscopic constants were in good agreement with the experimental values. In particular, we calculated the relativistic CI potential energy curves for all the involved states, and found that the Ω=1/2 states ($^2\Pi_{1/2}$ and $^2\Sigma^+_{1/2}$) all underwent avoided curve crossings. The interaction is so strong in $PbTe^+$ that shoulders were developed on the potential energy curves in the avoided crossing region. Experimental evidence for the avoided curve crossings was observed. We further calculated gross and overlap Mulliken populations for all the neutral ground states and the ionic Π states. It was found that appreciable charge transfer occurs from the group IV atoms to the group VI atoms in the neutral ground states. The chemical bond is partially ionic and partially covalent through overlap of the p orbitals on the two atoms.

References

* The theoretical calculations were done in collaboration with K. Balasubramanian; This chapter (LBL-27699) has been published in *J. Chem. Phys.* **92**, 899 (1990) in co-authorship with B. Niu, Y.T. Lee, D.A. Shirley, and K. Balasubramanian.

1. See for example, C. Kittle, *Introduction to Solid State Physics*, Sixth Ed. (John Wiley & Sons, New York, 1986).
2. T.P. Martin, *J. Chem. Phys.* **77**, 3815 (1982).
3. L. Brus, *J. Phys. Chem.* **90**, 2555 (1986).
4. See for example, P. Pyykko, *Chem. Rev.* **88**, 563 (1988); K. Balasubramanian, *J. Phys. Chem.* **93**, 6585 (1989).
5. See for example, J.W. Rabalais, *Principles of Ultraviolet Photoelectron Spectroscopy* (John Wiley & Sons, New York, 1977).
6. M. Wu and T.P. Fehlner, *J. Am. Chem. Soc.* **98**, 7578 (1976).
7. M.G. White, R.A. Rosenberg, S.-T. Lee and D.A. Shirley, *J. Electron Spectrosc. Relat. Phenom.* **17**, 323 (1979).
8. E. A. Colbourn, J.M. Dyke, A. Fackerell, A. Morris and I.R. Trickle, *J. Chem. Soc. Faraday* II **73**, 2278 (1977).
9. E.A. Colbourn, J.M. Dyke, E.P.F. Lee, A. Morris and I.R. Trickle, *Mol. Phys.* **35**, 873 (1978).
10. J.M. Dyke, A.Morris, A.M.A. Ridha and J.G. Snijders, *Chem. Phys.* **67**, 245 (1982).
11. C.Y. Yang and S. Rabii, *J. Chem. Phys.* **69**, 2497 (1978).
12. Y.S. Lee, W.C. Ermler and K.S. Pitzer, *J. Chem. Phys.* **73**, 360 (1980).
13. K. Balasubramanian, *J. Phys. Chem.* **88**, 5759 (1984).
14. K. Balasubramanian and K.S. Pitzer, *Chem. Phys. Lett.* **100**, 273 (1893).
15. K. Balasubramanian, *Chem. Phys. Lett.* **139**, 262 (1987).

16. K. Balasubramanian and K.S. Pitzer, *J. Phys. Chem.* **88**, 1146 (1984).

17. K. Balasubramanian, *J. Chem. Phys.* **85**, 1443 (1986).

18. K. Balasubramanian, *Chem. Rev.* (in press).

19. J.E. Pollard, D.J. Trevor, Y.T. Lee and D.A. Shirley, *Rev. Sci. Instrum.* **52**, 1837 (1981).

20. L.S. Wang, J.E. Reutt-Robey, B. Niu, Y.T. Lee, and D.A. Shirley, *J. Electron Spectrosc. Relat. Phenom.*, (in press).

21. R. Colin and J. Drowart, *Trans. Faraday Soc.* **60**, 673 (1964).

22. R.F. Porter, *J. Chem. Phys.* **34**, 583 (1961).

23. D.A. Northrop, *J. Phys. Chem.* **75**, 118 (1971).

24. L.-S. Wang, B. Niu, Y.T. Lee and D.A. Shirley, *Chem. Phys. Lett.* **158**, 297 (1989).

25. K. Balasubramanian, *J. Phys. Chem.* **91**, 5166 (1987).

26. K. Balasubramanian and Ch. Ravimohan, *J. Mol. Spectrosc.* **126**, 220 (1987).

27. K. Balasubramanian, *J. Chem. Phys.* **89**, 5731 (1988).

28. K. Balasubramanian, *Chem. Phys. Lett.* **127**, 585 (1986).

29. The major authors of the ALCHEMY II are B. Liu, B. Lengsfield and M. Yoshiminie.

30. See for example, J.H.D. Eland, *Photoelectron Spectroscopy*, Second Ed. (Butterworth, London, 1984), P78.

31. A.E. Stevens, C.S. Feigerle and W.C. Lineberger, *J. Chem. Phys.* **78**, 5420 (1983).

32. K.P. Huber and G. Herzberg, *Spectroscopic Constants of Diatomics*, (Van Nostrand Reinhold, New York, 1979).

33. C.E. Moore, *Tables of Atomic Energy Levels*, (U.S. National Bureau of Standards, Washington D.C., 1971).

34. B. Wannberg, D. Nordfors, K.L. Tan, L. Karlsson and L. Mattsson, *J. Electron Spectrosc. Relat. Phenom.* **47**, 147 (1988).

35. K. Balasubramanian and K.S. Pitzer, *J. Chem. Phys.* **78**, 321 (1983).

Table 1. The experimental conditions.

	SnSe	SnTe	PbSe	PbTe
T (K)[a]	990	1090	1010	1000
P (Torr)[b]	200 (He)	600 (Ne)	500 (Ne)	600 (He)
ϕ (mm)[c]	0.15	0.10	0.13	0.14
Power (mAxV)[d]	230x1050	500x750	300x1400	250x1250
Tvib (K)[e]	300±50	470±50	500±50	350±50

a. Temperatures measured with type K (Chromel-Alumel) thermocouples at the rear of the graphite crucibles. They were only relative measures, and are about 100-200 degrees lower than the effective sample temperatures.

b. Carrier gas pressures.

c. Nozzle diameters.

d. Heating powers. About 60-80 Watts power was needed to drive the tungsten filaments. This power was in addition to the heating powers.

e. Vibrational temperatures, obtained through Franck-Condon analyses. See the text.

Table 2. Spectroscopic constants of SnSe[a] and $SnSe^+$.

		r_e (Å)		ω_e (cm^{-1})		IP_{ad} (eV)		IP_{vt} (eV)		D_e (eV)	
		Theo.	Expt.	Theo.	Expt.	Theo.	Expt.	Theo.	Expt.	Theo.	Expt.
SnSe	$^1\Sigma^+$	2.38	2.3256	324	331.2					4.23	4.20
$SnSe^+$	$^2\Pi_{3/2}$	2.55	2.48(1)	257	300(10)	9.20	8.947(10)	9.30	9.092(10)	2.26	2.60
	$^2\Pi_{1/2}$	2.56	2.48(1)	259	300(10)	9.44	9.189(10)	9.53	9.323(10)	2.02	2.35
	$^2\Sigma^+_{1/2}$	2.38	2.34(1)	(274)	310(15)	9.85	9.540(7)				

a. The experimental spectroscopic constants for the neutral $^1\Sigma^+$ ground state are from Ref. 32.

Table 3. Spectroscopic constants of SnTe[a] and $SnTe^+$.

		r_e (Å)		ω_e (cm^{-1})		IP_{ad} (eV)		IP_{vt} (eV)		D_e (eV)	
		Theo.	Expt.	Theo.	Expt.	Theo.	Expt.	Theo.	Expt.	Theo.	Expt.
SnTe	$^1\Sigma^+$	2.59	2.5228	243	259.5					3.30	3.69
$SnTe^+$	$^2\Pi_{3/2}$	2.75	2.668(5)	203	210(6)	7.98	8.435(7)	8.14	8.545(7)	2.10	2.59
	$^2\Pi_{1/2}$	2.76	2.643(5)	205	200(6)	8.33	8.814(7)	8.40	8.864(7)	1.75	2.22
	$^2\Sigma^+_{1/2}$	2.58	2.566(5)	234	255(5)	8.76	9.247(7)				

a. The experimental spectroscopic constants for the neutral $^1\Sigma^+$ ground state are from Ref. 32.

Table 4. Spectroscopic constants of PbSe[a] and $PbSe^+$.

		r_e (Å)		ω_e (cm^{-1})		IP_{ad} (eV)		IP_{vt} (eV)		D_e (eV)	
		Theo.	Expt.	Theo.	Expt.	Theo.	Expt.	Theo.	Expt.	Theo.	Expt.
PbSe	$^1\Sigma^+$	2.45	2.4022	268	277.6					3.5	3.1
$PbSe^+$	$^2\Pi_{3/2}$	2.66	2.577(5)	207	210(6)	8.72	8.671(7)	8.82	8.800(7)	1.38	1.82
	$^2\Pi_{1/2}$	2.67	2.547(5)	205	210(6)	9.04	9.001(7)	9.14	9.104(7)	1.07	1.49
	$^2\Sigma^+_{1/2}$	2.53	2.445(5)	222	242(5)	9.64	9.543(7)				

a. The experimental spectroscopic constants for the neutral $^1\Sigma^+$ ground state are from Ref. 32.

Table 5. Spectroscopic constants of PbTe[a] and $PbTe^+$.

		r_e (Å)		ω_e (cm^{-1})		IP_{ad} (eV)		IP_{vt} (eV)		D_e (eV)	
		Theo.	Expt.	Theo.	Expt.	Theo.	Expt.	Theo.	Expt.	Theo.	Expt.
PbTe	$^1\Sigma^+$	2.67	2.5950	207	212.2					2.76	2.55
$PbTe^+$	$^2\Pi_{3/2}$	2.85		160	(160)	8.50	7.90(4)	8.70	8.22(1)	1.41	2.06
	$^2\Pi_{1/2}$	2.86		160	(160)	9.06	8.48(3)	9.23	8.82(1)	0.85	1.48
	$^2\Sigma^+_{1/2}$	2.76	2.627(5)	180	185(8)	9.43	9.131(7)				

a. The experimental spectroscopic constants for the neutral $^1\Sigma^+$ ground state are from Ref. 32.

Table 6. Gross and overlap Mulliken populations of SnSe, SnTe, PbSe and PbTe, and their ions after removing a π electron.[a]

		M	Ch	M(s)	M(p)	M(d)	Ch(s)	Ch(p)	Ch(d)	Overlap
SnSe	$^1\Sigma^+$	3.40	6.60	1.74	1.56	0.10	1.99	4.46	0.15	0.758
$SnSe^+$	$^2\Pi$	2.84	6.16	1.87	0.97	0.00	2.01	4.02	0.13	0.334
SnTe	$^1\Sigma^+$	3.51	6.49	1.77	1.65	0.09	2.01	4.35	0.14	0.567
$SnTe^+$	$^2\Pi$	2.94	6.06	1.71	1.07	0.16	2.02	3.90	0.13	0.210
PbSe	$^1\Sigma^+$	3.47	6.53	1.83	1.56	0.08	1.98	4.43	0.14	0.742
$PbSe^+$	$^2\Pi$	2.82	6.18	1.84	0.91	0.06	2.00	4.06	0.13	0.355
PbTe	$^1\Sigma^+$	3.57	6.43	1.84	1.63	0.10	1.96	4.33	0.14	0.541
$PbTe^+$	$^2\Pi$	2.94	6.07	1.85	1.02	0.06	1.98	3.93	0.12	0.236

a. M stands for the group IV atom. Ch stands for the group VI atom.

Figure Captions

Figure 1 The HeI photoelectron spectrum of $SnSe^+$. HB means hot band transitions.

Figure 2 The HeI photoelectron spectrum of $SnTe^+$. HB means hot band transitions.

Figure 3 The HeI photoelectron spectrum of $PbSe^+$. HB means hot band transitions.

Figure 4 The HeI photoelectron spectrum of $PbTe^+$. HB means hot band transitions. The shoulders marked as "AI" are assigned to autoionization transitions.

Figure 5 A Franck-Condon factor calculation for the $^2\Sigma^+_{1/2}$ band of $PbSe^+$. The dotted curve is the experimental spectrum. The lines are the individual Franck-Condon factors. The solid curve is the spectrum calculated by convoluting each line with a Gaussian (0.018 eV width).

Figure 6 A Franck-Condon factor calculation for the $^2\Pi_{3/2}$ band of $PbSe^+$. The dotted curve is the experimental spectrum. The lines are the individual Franck-Condon factors. The solid curve is the spectrum calculated by convoluting each line with a Gaussian (0.020 eV width).

Figure 7 RCI potential energy curves for SnSe and $SnSe^+$.

Figure 8 RCI potential energy curves for SnTe and $SnTe^+$.

Figure 9 RCI potential energy curves for PbSe and $PbSe^+$.

Figure 10 RCI potential energy curves for PbTe and $PbTe^+$. The curves labelled as $^2\Sigma^+$ and $^2\Pi$ are simple HF calculations without taking into account the relativistic effect.

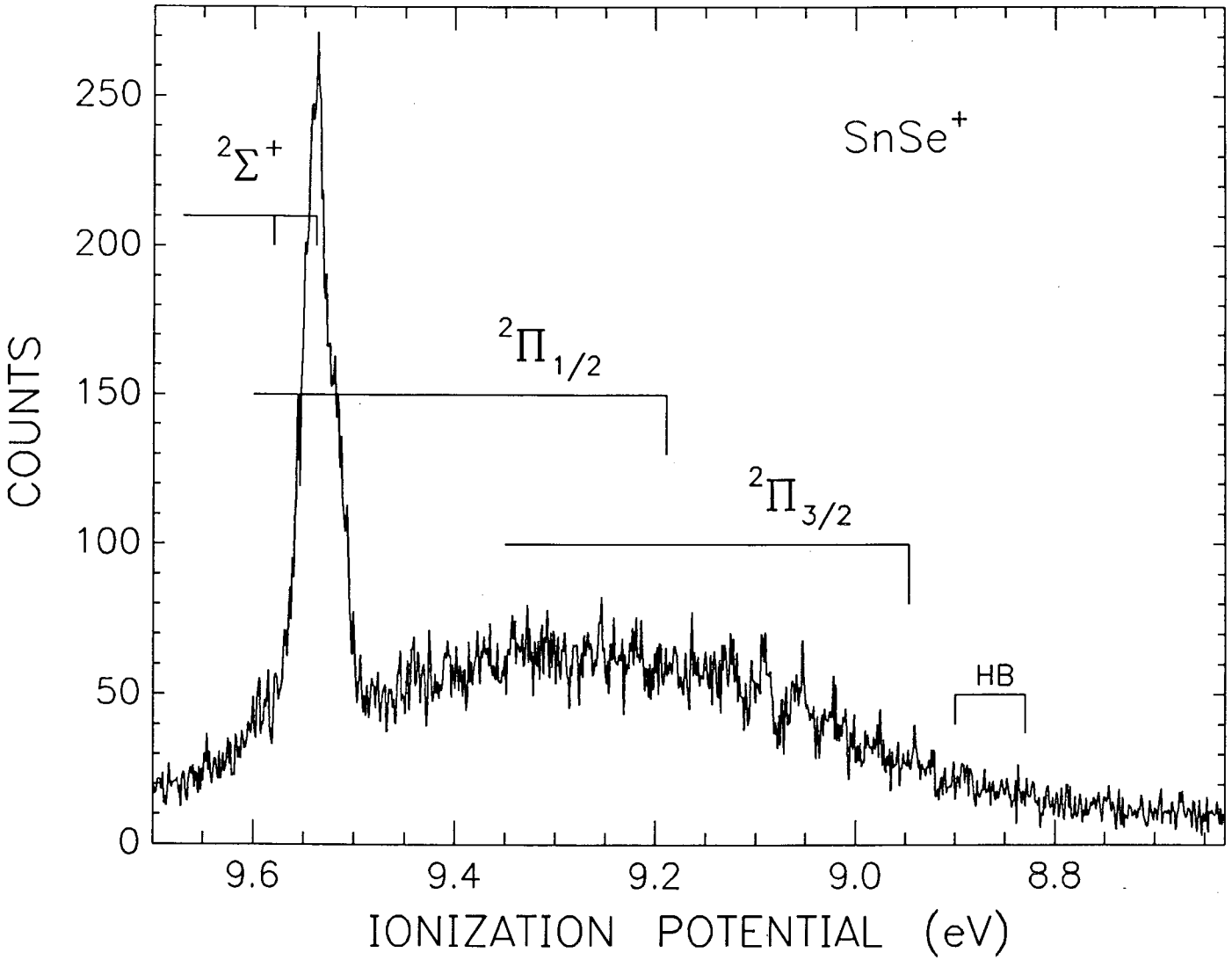

XBL 899-3208

Figure 1

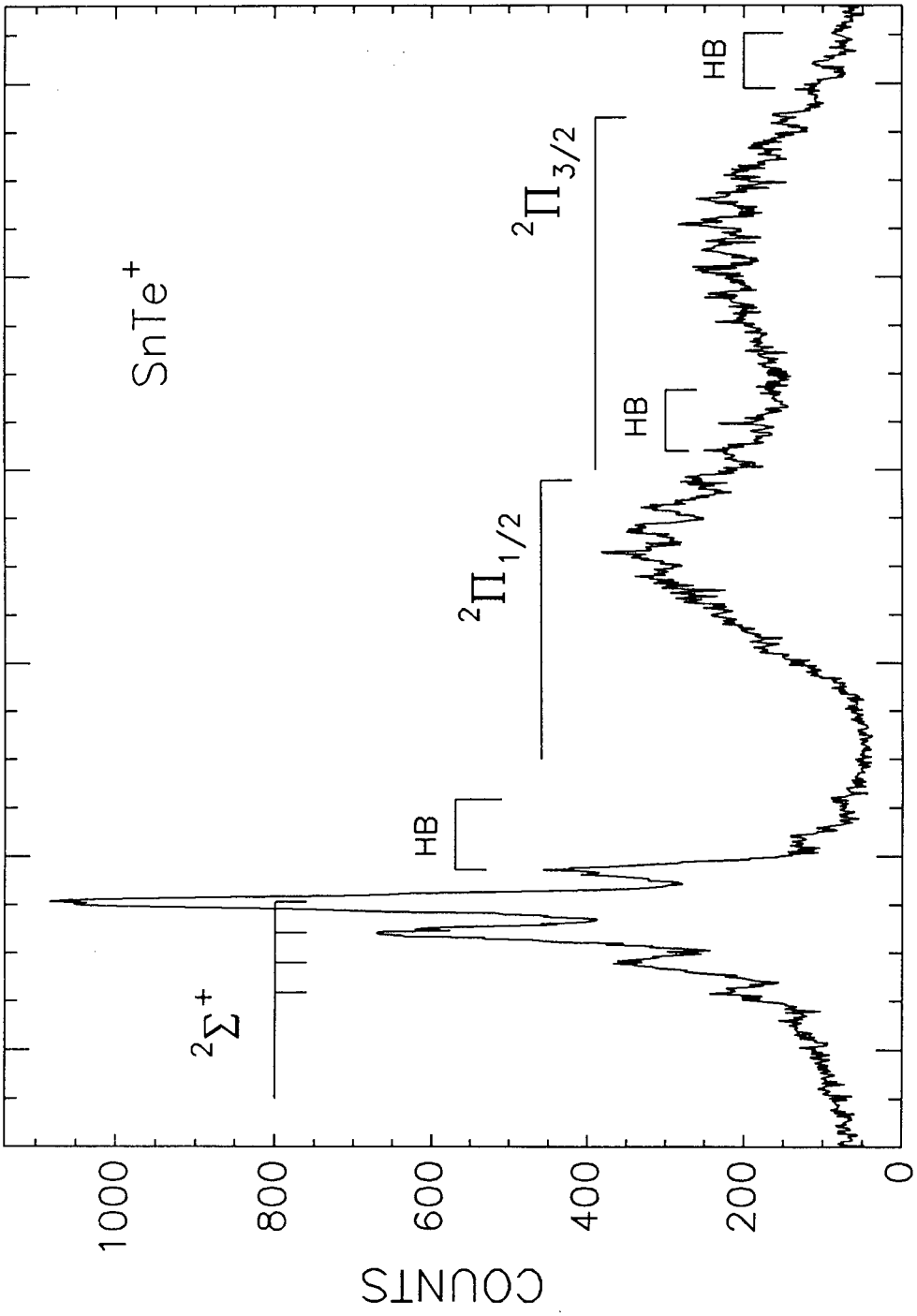

XBL 899-3209

Figure 2

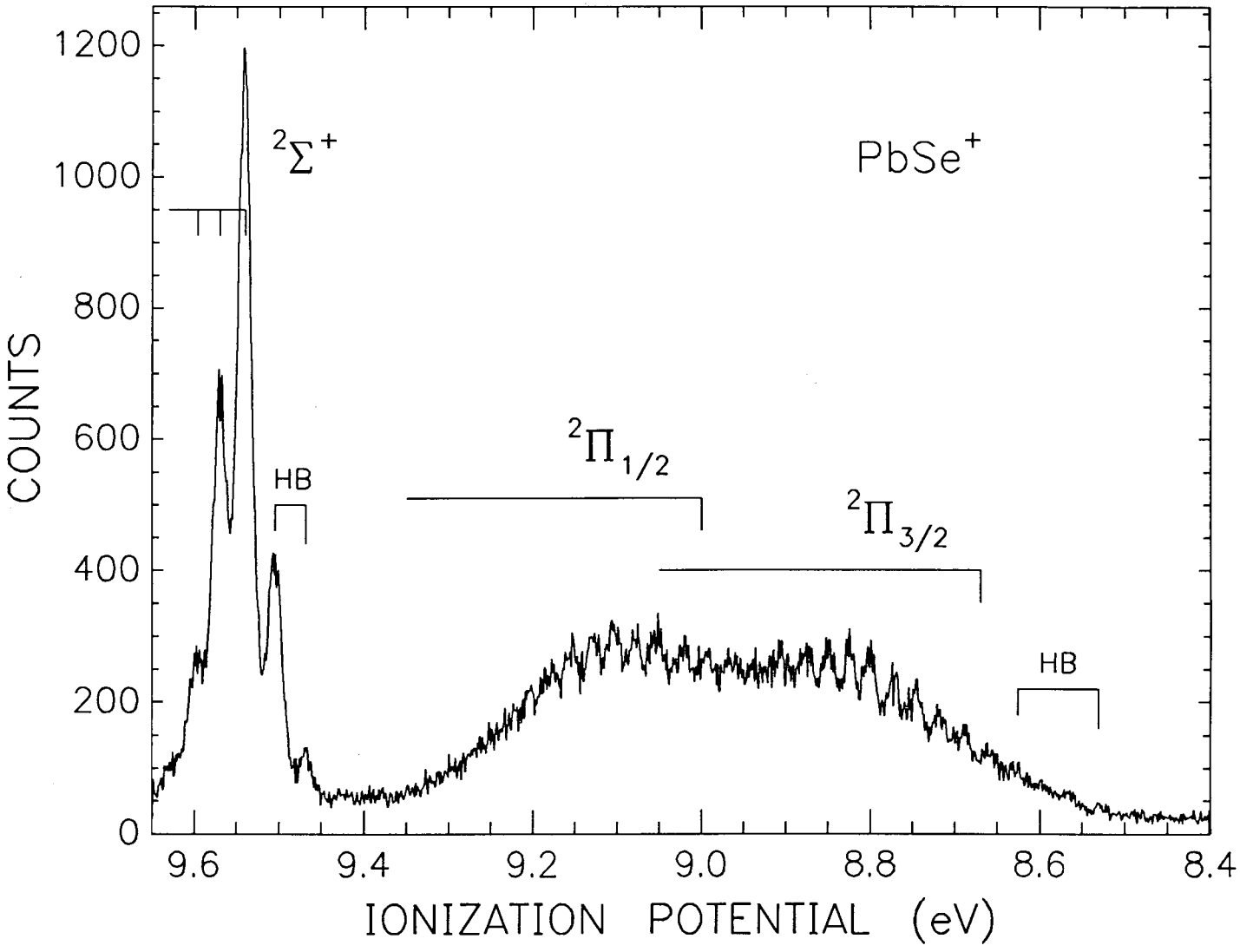

XBL 899-3210

Figure 3

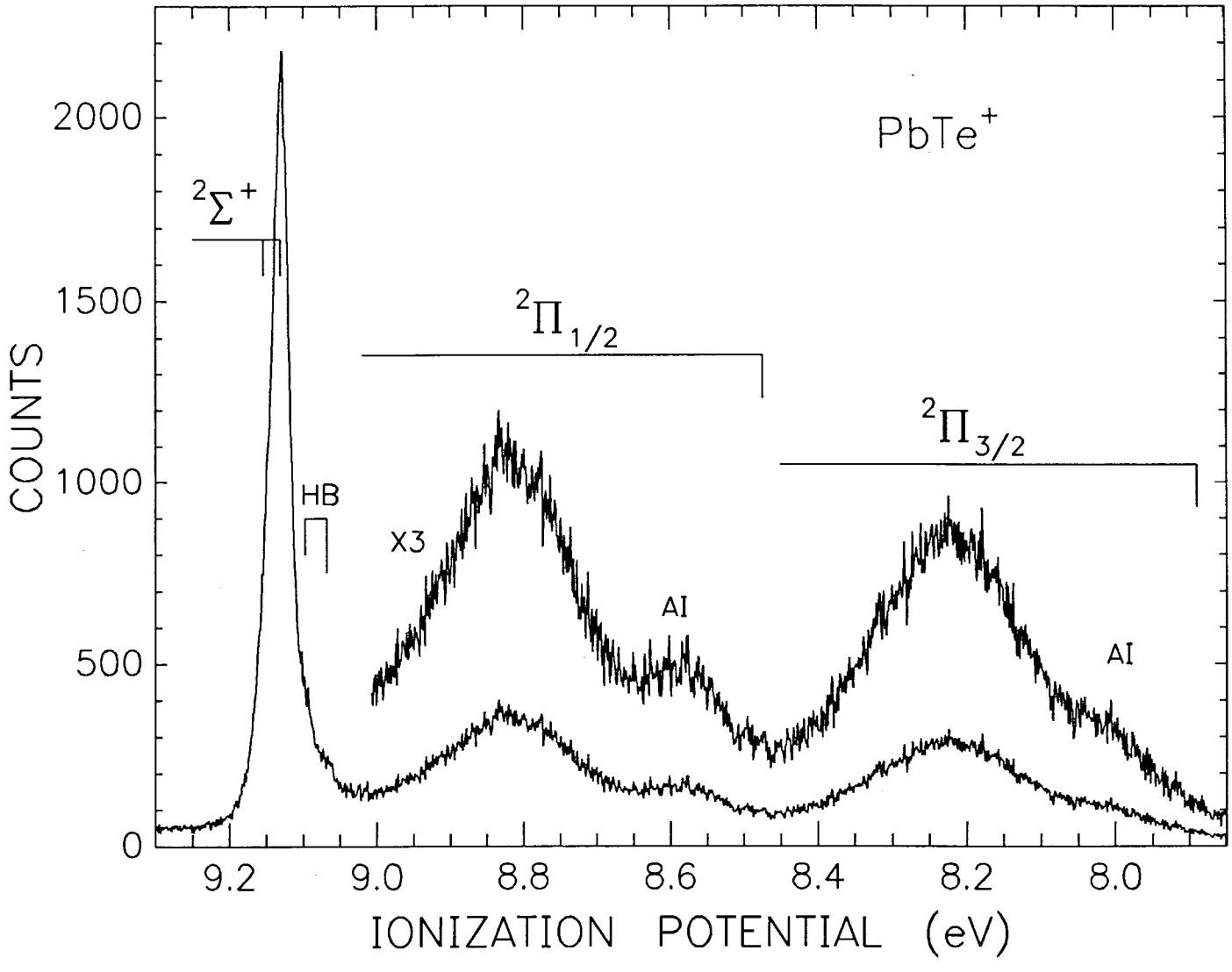

XBL 899-3211

Figure 4

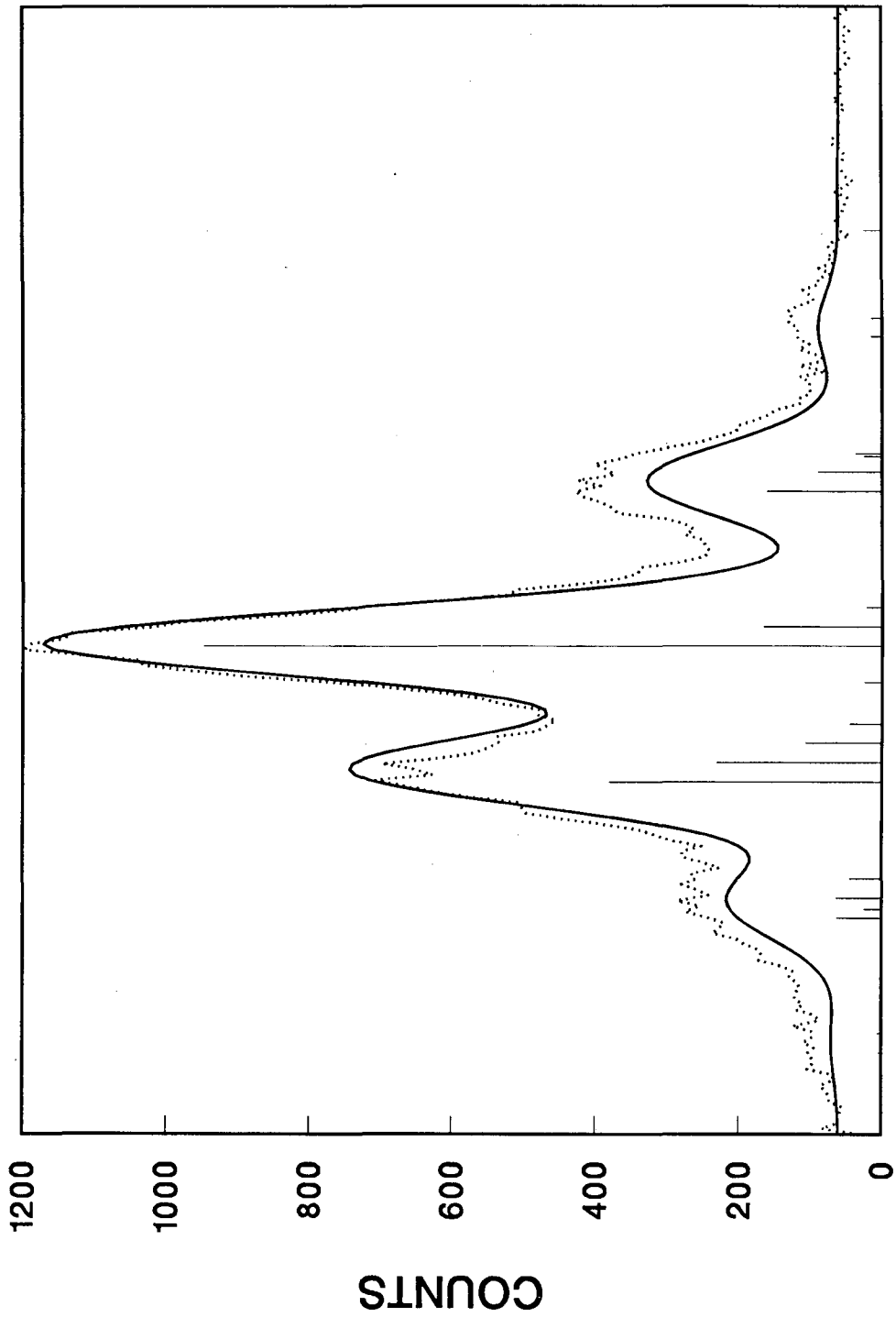

XBL 899-3212

Figure 5

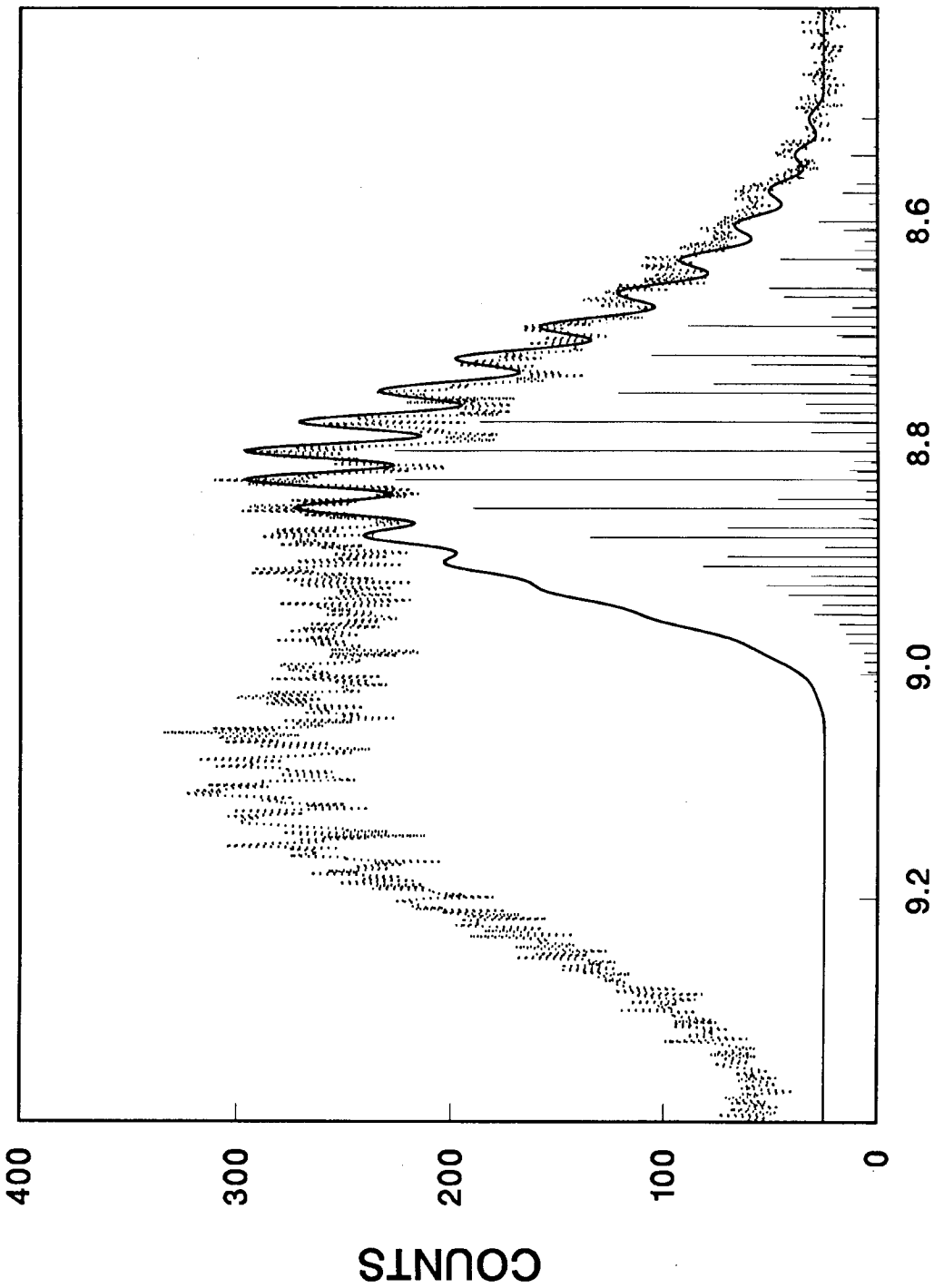

XBL 899-3213

Figure 6

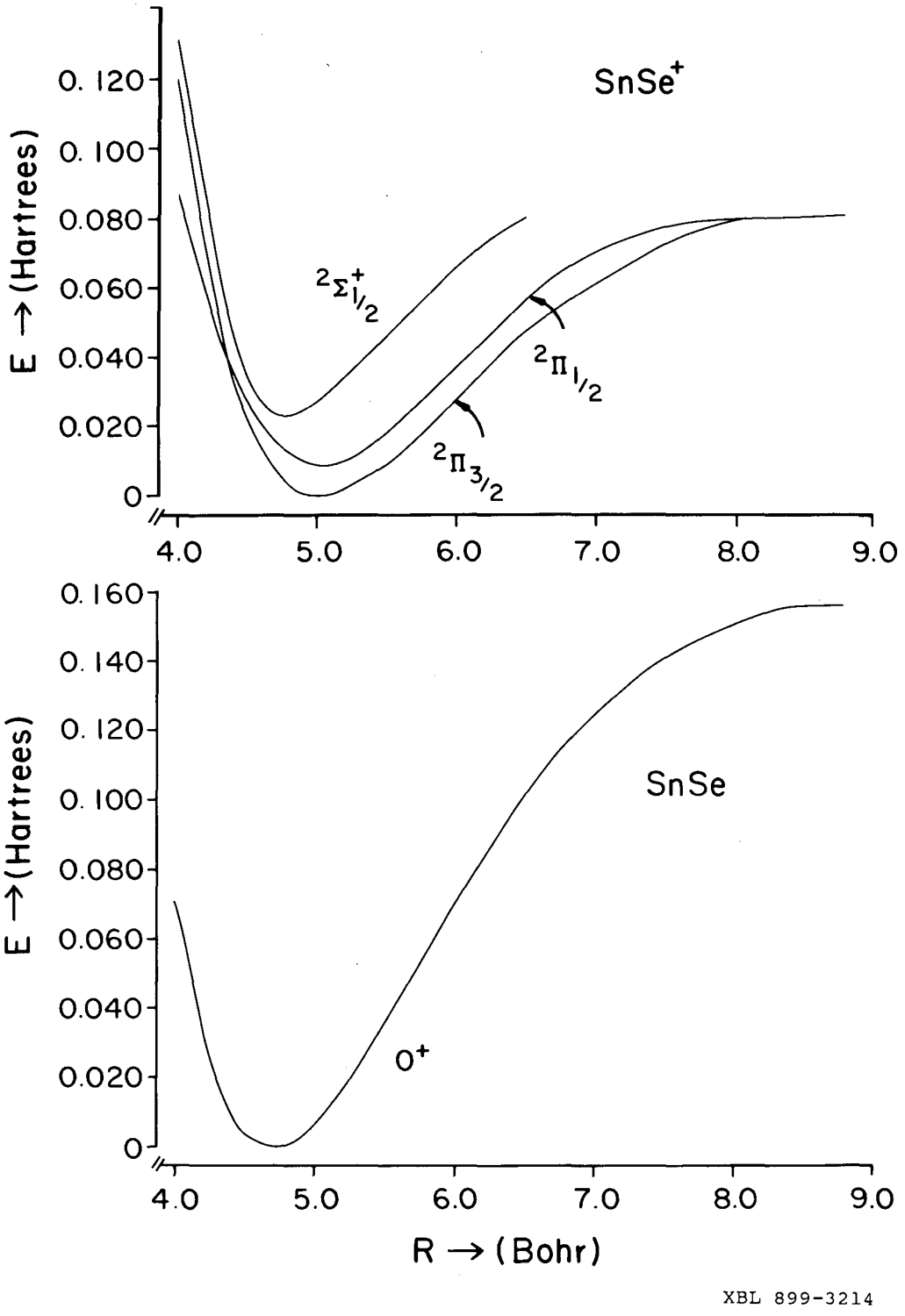
SnSe+
0. 120
0. 100
0.080
0.060
0.040
0.020
0
E → (Hartrees)
$^2\Sigma^+_{1/2}$
$^2\Pi_{1/2}$
$^2\Pi_{3/2}$
4.0
5.0
6.0
7.0
8.0
9.0
0. 160
0. 140
0. 120
0. 100
0.080
0.060
0.040
0.020
0
E → (Hartrees)
SnSe
0+
4.0
5.0
6.0
7.0
8.0
9.0
R → (Bohr)
XBL 899-3214

Figure 7

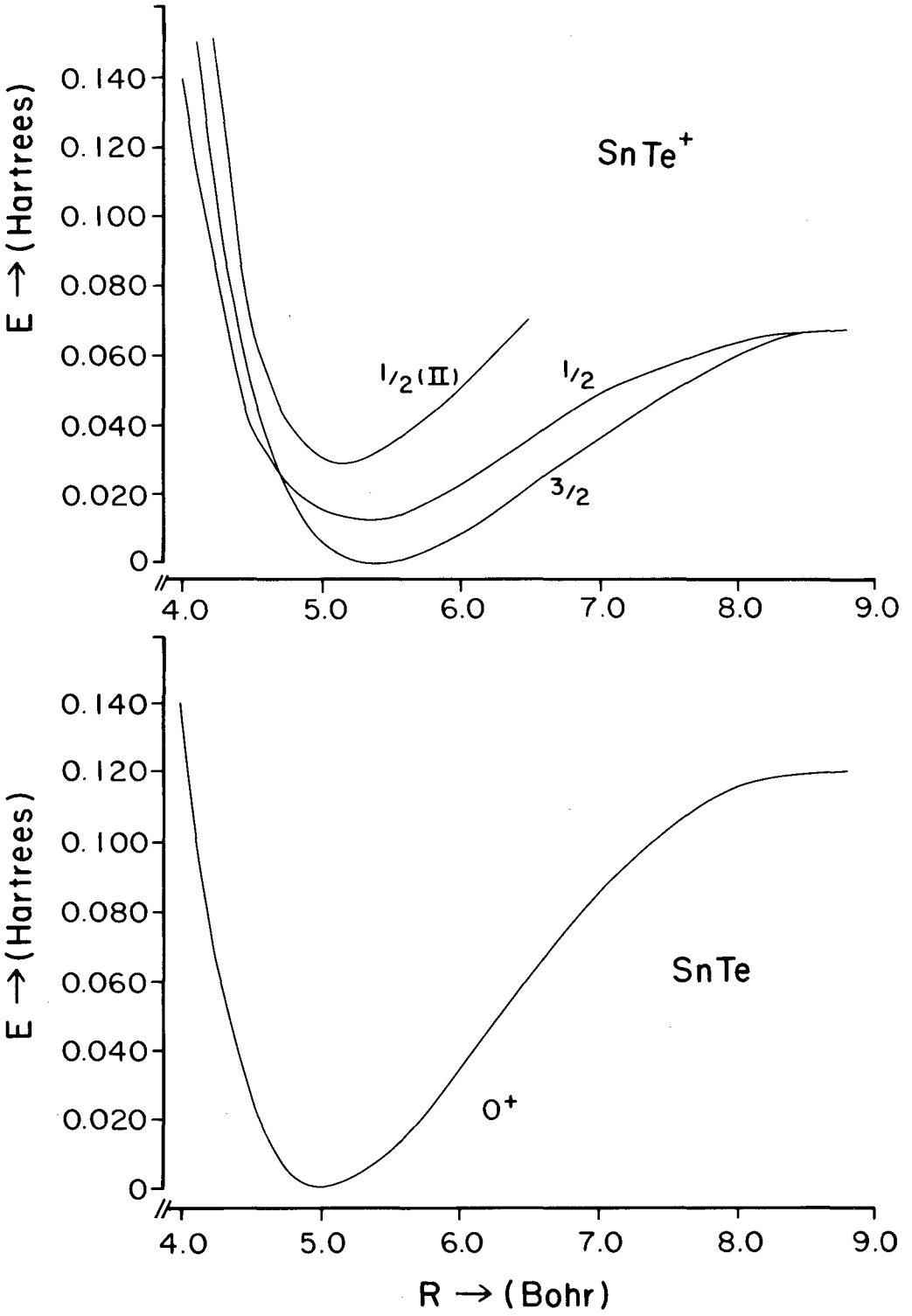
E → (Hartrees)
0.140
0.120
0.100
0.080
0.060
0.040
0.020
0
SnTe+
1/2(II)
1/2
3/2
4.0
5.0
6.0
7.0
8.0
9.0
E → (Hartrees)
SnTe
0+
R → (Bohr)
XBL 899-3215

Figure 8

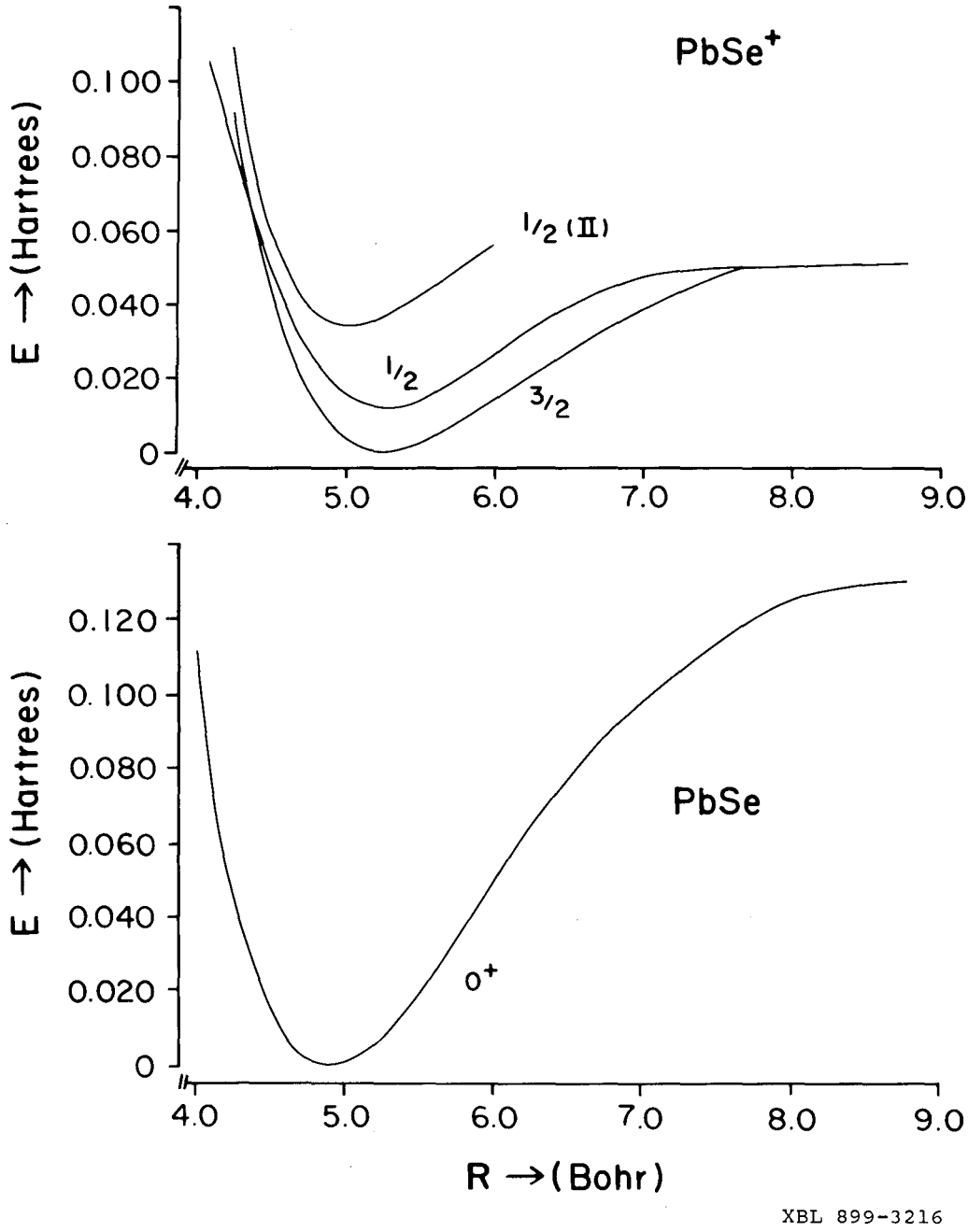
PbSe+
0.100
0.080
0.060
0.040
0.020
0
E → (Hartrees)
1/2 (II)
1/2
3/2
4.0
5.0
6.0
7.0
8.0
9.0
0.120
0.100
0.080
0.060
0.040
0.020
0
E → (Hartrees)
PbSe
0+
4.0
5.0
6.0
7.0
8.0
9.0
R → (Bohr)
XBL 899-3216

Figure 9

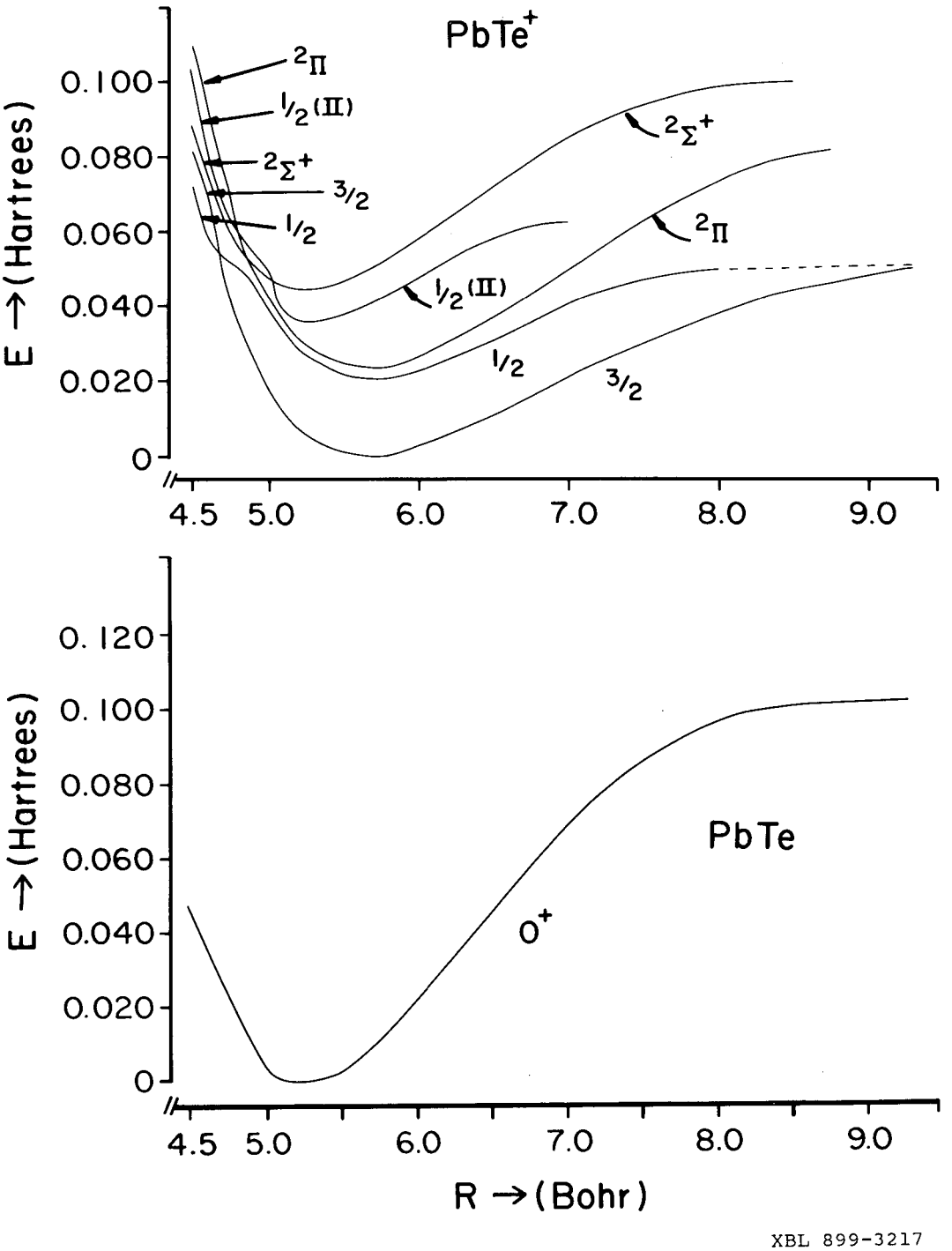
PbTe+
2Π
1/2(II)
2Σ+
3/2
1/2
2Σ+
2Π
1/2(II)
1/2
3/2
E →(Hartrees)
0.100
0.080
0.060
0.040
0.020
0
4.5
5.0
6.0
7.0
8.0
9.0
0.120
0.100
0.080
0.060
0.040
0.020
0
PbTe
0+
R →(Bohr)
XBL 899-3217

Figure 10

Chapter 4

Vibrational Spectra of Se_2^+ and Te_2^+ in Their Ground States*

Abstract

Vibrationally-resolved photoelectron spectra of Se_2^+ and Te_2^+ in their ground states were measured using a newly-constructed high temperature supersonic molecular beam source. Ionization potentials and fundamental spectroscopic constants for the molecular ions were obtained.

4.1 Introduction

Photoelectron spectroscopy (PES) not only yields electronic binding energies, but a well-resolved molecular PE spectrum can also be analyzed to derive the spectroscopic constants of the molecular ion. Especially for diatomic molecules, such parameters as the vibrational frequency and the equilibrium bond length can be obtained. It is therefore important to resolve the vibrational fine structure in PES.

The HeI (584Å) PE spectra of the Group VI diatomics have all been reported: O_2[1,2], S_2[3,4], Se_2[5,6],Te_2[4-6], but vibrationally-resolved spectra were obtained for only O_2[1,2] and S_2[3]. To resolve vibrational structure in Se_2 and Te_2 requires much higher resolution, because their vibrational frequencies are much smaller, and it also may be necessary to use supersonic molecular beams to cool the molecules internally.

The vibrationally-resolved PE spectra of Se_2 and Te_2 are especially interesting, because the relativistic effects are expected to play an increasingly important role going down the Periodic Table[7]. As a matter of fact, relativistic effects have already been invoked to interpret the anomalous $^2\Pi_{g1/2}$ / $^2\Pi_{g3/2}$ intensity ratio in the PE spectra of S_2, Se_2,and Te_2 [8]. Therefore, spectroscopic information derived from vibrationally-resolved PE spectra can be used directly to compare with relativistic quantum chemistry calculations.

In this Chapter, we report vibrationally-resolved PE spectra of Se_2^+ and Te_2^+ in their ground states, using our recently built high-temperature supersonic molecular beam source. A Franck-Condon analysis was used to obtain the equilibrium bond lengths of the respective molecular ions.

4.2 Experimental

The vapors of elemental Se and Te are equilibrium mixtures of 2-6 atom clusters.[9] The best ways to produce the diatomics are either to use a double oven set-up or to start

with alloys of the elements.[5] Te_2 can also be generated from the pure element by carefully controlling the temperature.[4] The spectra reported in this Chapter were obtained during our study of SnSe and SnTe. Se_2 and Te_2 were formed as "outgas" molecules during the preheating periods of the respective samples at about 720 K for Se_2 and 1070 K for Te_2. The outgas processes were slow enough for us to take the spectra reported in this Chapter.

The details of the high temperature molecular beam source has been given in Chapter 2. Basically, it uses electron bombardment heating to avoid the stray fields associated with the simpler resistive heating method. The main components consist of a 0.51 mm Tungsten filament, a Molybdenum electrostatic deflector, a Tungsten vacuum jacket and a graphite crucible. Various types of sample boats can be used with the graphite crucible. However, the samples were loaded directly into the crucible in the current experiments. The nozzle sizes used were 0.152 mm for Se_2 and 0.127 mm for Te_2. A He carrier gas pressure of 150 Torr was used for Se_2 and 200 Torr Ne was used for Te_2. The SnSe and SnTe compounds were commercial samples from CERAC.

The molecular beam PE spectrometer was described in detail elsewhere[10] and in Chapter 2. Briefly, it consists of the high temperature molecular beam source, a rare gas discharge lamp, a quadrupole mass spectrometer, and an electrostatic hemispherical electron analyzer with a multichannel detector. Ar PE peaks were usually used as the kinetic energy calibration. Normally, the energy resolution was about 13 meV at 1 eV pass energy. It was degraded slightly under the current high temperature conditions.

4.3 Results and Discussion

The PE spectra of Se_2^+ and Te_2^+ in their ground states are shown in Figure 1 and Figure 2, respectively, where the dotted spectra are experimental and the line spectra are theoretical, calculated from the Franck-Condon factors (see below). The Se_2^+ spectrum consists of two partially-overlapping bands, as a result of the spin-orbit splitting. The

Franck-Condon factors of only the $^2\Pi_{g1/2}$ state are plotted. In the Te_2^+ spectrum, the $^2\Pi_{g3/2}$ band, with an ionization energy of about 0.47 eV higher,[4,6] was not observed, both because it overlapped with the $SnTe^+$ spectrum and because its intensity was some ten times smaller than that of the $^2\Pi_{g1/2}$ band.[4,6,8] The ionization potentials (IPs) for both molecules are listed in Table 1. As can be seen from the Table, the first peak in each spectrum is a hot band transition. Vibrational temperatures of 350K and 300K fit very well for Se_2 and Te_2, respectively. This demonstrates the advantage of using supersonic molecular beams. We could not make a good estimate of the rotational temperatures, which are expected to be much lower than the respective vibrational temperatures. Part of the linewidths in our spectra, which are higher than the instrumental resolution, is due to the rotational broadening.

The Franck-Condon factor analysis is similar to that used in Ref. 11. Basically, we applied a Morse oscillator, described by expansion as a power series of $(r - r_e)$. The $(r - r_e)^3$ and $(r - r_e)^4$ terms were taken as perturbation corrections to the harmonic oscillator Hamiltonian. In Figures 1 and 2 are plotted the best Franck-Condon fits, which yielded the equilibrium bond lengths of the respective ionic states as listed in Table 2. The vibrational frequencies and the bond dissociation energies are also tabulated in Table 2. In the case of Se_2^+, an accurate value of $2126 \pm 10\ cm^{-1}$ for the spin-orbit splitting was also derived.

Based on the spectroscopic constants given in Table 2, the related Morse potentials can be calculated. They are shown in Figures 3 and 4. Since ionization removes an electron from the anti-bonding Π_g orbital in both $Se_2^+$and Te_2^+, the chemical bonds become stronger in the ionic states. This leads to shortening of the equilibrium bond lengths, and increases of both the vibrational frequencies and the bond dissociation energies in the ionic states. In Se_2^+, we can conclude that the $^2\Pi_{g1/2}$ state is slightly more strongly bound than the $^2\Pi_{g3/2}$ state. It is also interesting to note that, fractionally, the bonds in Se_2^+ and Te_2^+ seem to be more strengthened than that in S_2^+.[3]

In conclusion, we have obtained the high resolution PE spectra of Se_2^+ and Te_2^+ in their ground states. Fundamental spectroscopic constants were derived for the molecular ions, and the advantages of using supersonic molecular beams in high temperature PES were demonstrated.

References

* This Chapter (LBL-26993) has been published in *Chem. Phys. Lett.* **158**, 297 (1989) in co-authorship with B. Biu, Y.T. Lee, and D.A. Shirley.

1. O. Edgvist, E. Lindholm, L.E. Selin and L. Åsbrink, *Phsica Scripta* **1**, 25 (1970).
2. J.W. Rabalais, *Principles of Ultraviolet Photoelectron Spectroscopy* (John Wiley & Sons, New York, 1977).
3. J.M. Dyke, L. Golob, N. Jonanthan and A. Morris, *J. Chem. Soc. Faraday* II **71**, 1026 (1975).
4. J. Berkowithz, *J. Chem. Phys.* **62**, 4074 (1975).
5. D.G. Streets and J. Berkowitz, *J. Electron Spectrosc. Relat. Phenom.* **9**, 269 (1976).
6. A.W. Potts and I. Novak, *J. Electron Spectrosc. Relat. Phenom.* **28**, 267 (1983).
7. See for example, P. Pyykkö, *Chem. Rev.* **88**, 563 (1988).
8. S.-T. Lee, S. Süzer and D.A. Shirley, *Chem. Phys. Lett.* **41**, 25 (1976).
9. A.N. Nesmeyanov, *Vapor Pressure of the Chemical Elements* (Elsevier, Amsterdam, 1963).
10. J.E. Pollard, D.J. Trevor, Y.T. Lee and D.A. Shirley, *Rev. Sci. Instrum.* **52**, 1837 (1981)
11. A.E. Stevens, C.S. Feigerle and W.C. Lineberger, *J. Chem. Phys.* **78**, 5420 (1983).
12. K.P. Huber and G. Herzberg, *Molecular Spectra and Molecular Structure*: IV. *Constants of diatomic molecules* (Van Nostrand Reinhold, New York, 1979).
13. C.E. Moore, *Atomic Energy Levels* (Circular of National Bureau of Standards 467, 1952), Vol. II, P150 and Vol. III, P96.

Table 1. The ionization potentials of Se_2 and Te_2.

		IP (eV)[a]	v	Intervals
Se_2^+	$^2\Pi_{g1/2}$	8.7230	hot band	
		8.7711	0	0.0481
		8.8281	1	0.0570
		8.8845	2	0.0564
		8.9409	3	0.0564
		8.9915	4	0.0506
	$^2\Pi_{g3/2}$	9.0387	0	
		9.0942	1	0.0555
		9.1494	2	0.0552
		9.2043	3	0.0549
Te_2^+	$^2\Pi_{g1/2}$	8.1574	hot band	
		8.1872	0	0.0298
		8.2234	1	0.0362
		8.2581	2	0.0347
		8.2928	3	0.0347

a. The uncertainty for the absolute IPs is ± 0.006 eV. The extended accuracy quoted in the table only has significance when one takes the intervals whose uncertainties are ± 0.0010 eV.

Table 2. The derived spectroscopic constants for Se_2^+ and Te_2^+, together with the respective neutral ground states.[12]

		ω_e (cm^{-1})	r_e (Å)	D_0 (eV)[a]	A (cm^{-1})
Se_2	$^3\Sigma_g^-$ (0_g^+)	385.303	2.1660	3.411	
Se_2^+	$^2\Pi_{g1/2}$	450 ± 10	2.072 ± .005	4.37	
	$^2\Pi_{g3/2}$	443 ± 10	2.080 ± .005	4.38	2126 ± 10
Te_2	$^3\Sigma_g^-$ (0_g^+)	247.070	2.5574	2.677	
Te_2^+	$^2\Pi_{g1/2}$	282 ± 10	2.489 ± .005	3.50	

a. The accuracy of the D_0 values for the ionic states is limited by the accuracy of the atomic IPs, see Ref. 13.

Figure captions

Figure 1 The PE spectrum of Se_2^+, $^2\Pi_{g1/2}$ and $^2\Pi_{g3/2}$ states. HB is a hot band transition. (... experimental spectrum, — calculated FCFs).

Figure 2 The PE spectrum of Te_2^+, $^2\Pi_{g1/2}$ state. HB is a hot band transition. (... experimental spectrum, — calculated FCFs).

Figure 3 The Morse potentials for the transitions Se_2^+ $^2\Pi_{g1/2,3/2} \leftarrow Se_2$ $^2\Sigma_g^-$ (O_g^+).

Figure 4 The Morse potentials for the transition Te_2^+ $^2\Pi_{g1/2} \leftarrow Te_2$ $^2\Sigma_g^-$ (O_g^+).

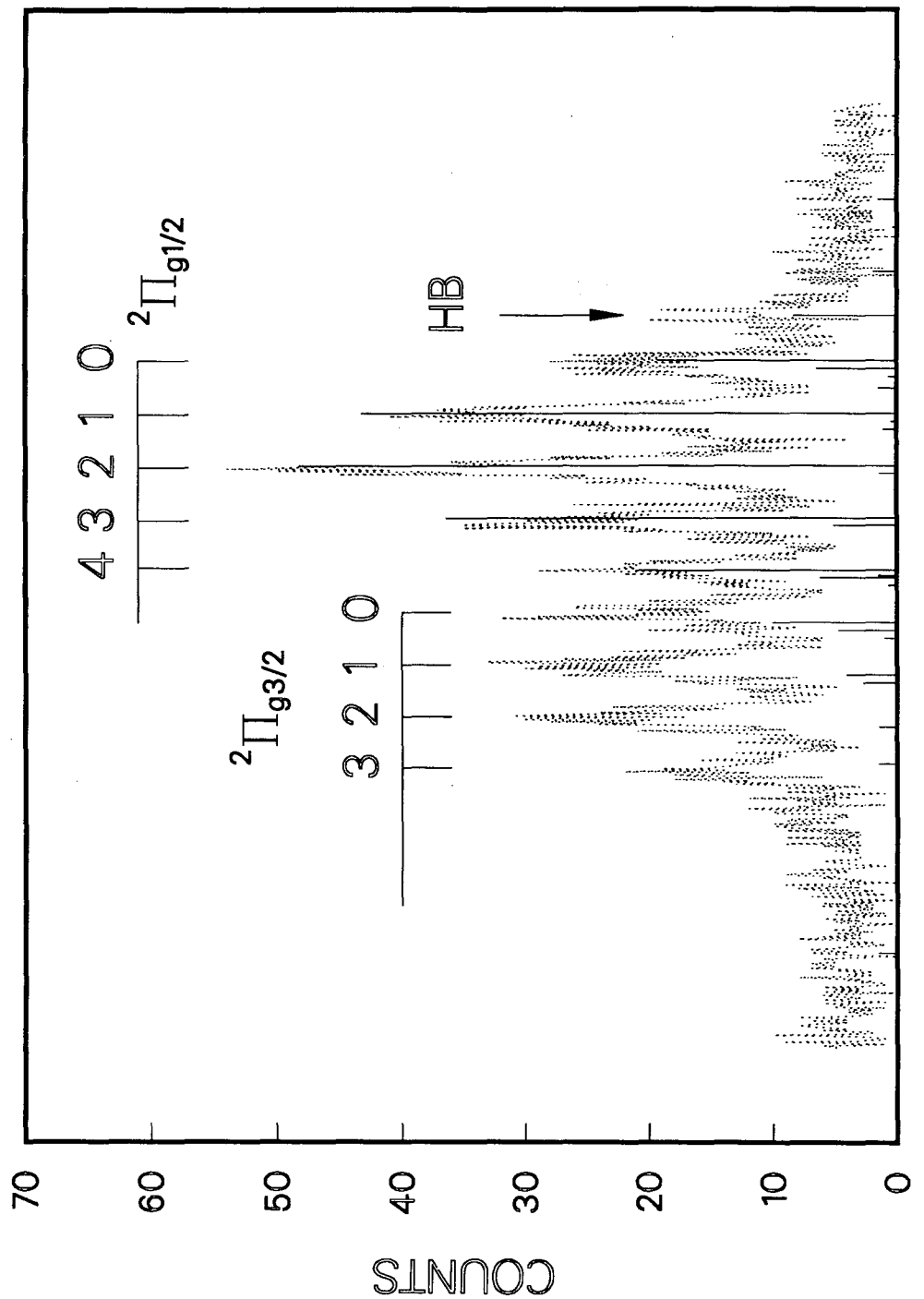

XBL 893-1004

Figure 1

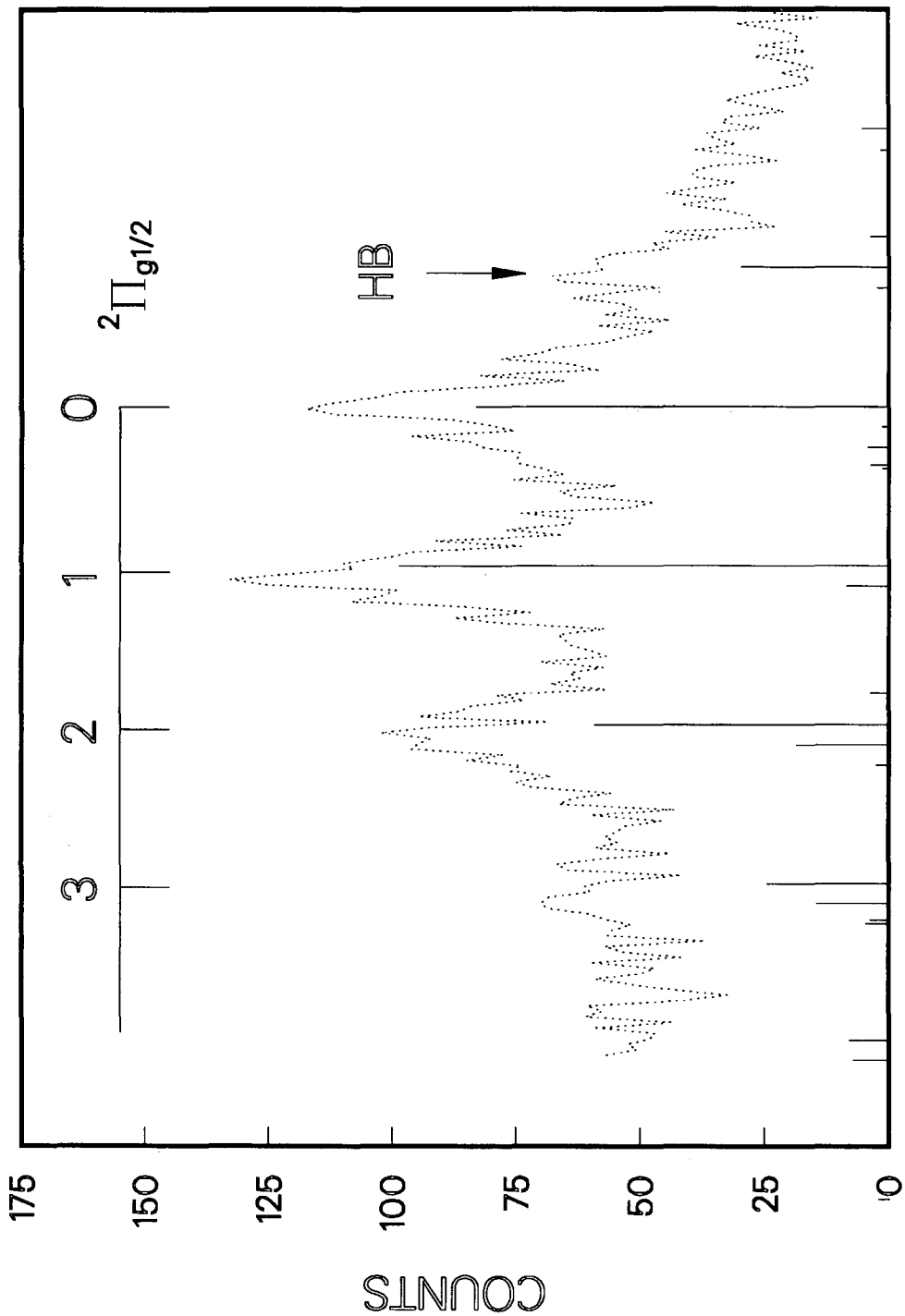

XBL 893-1005

Figure 2

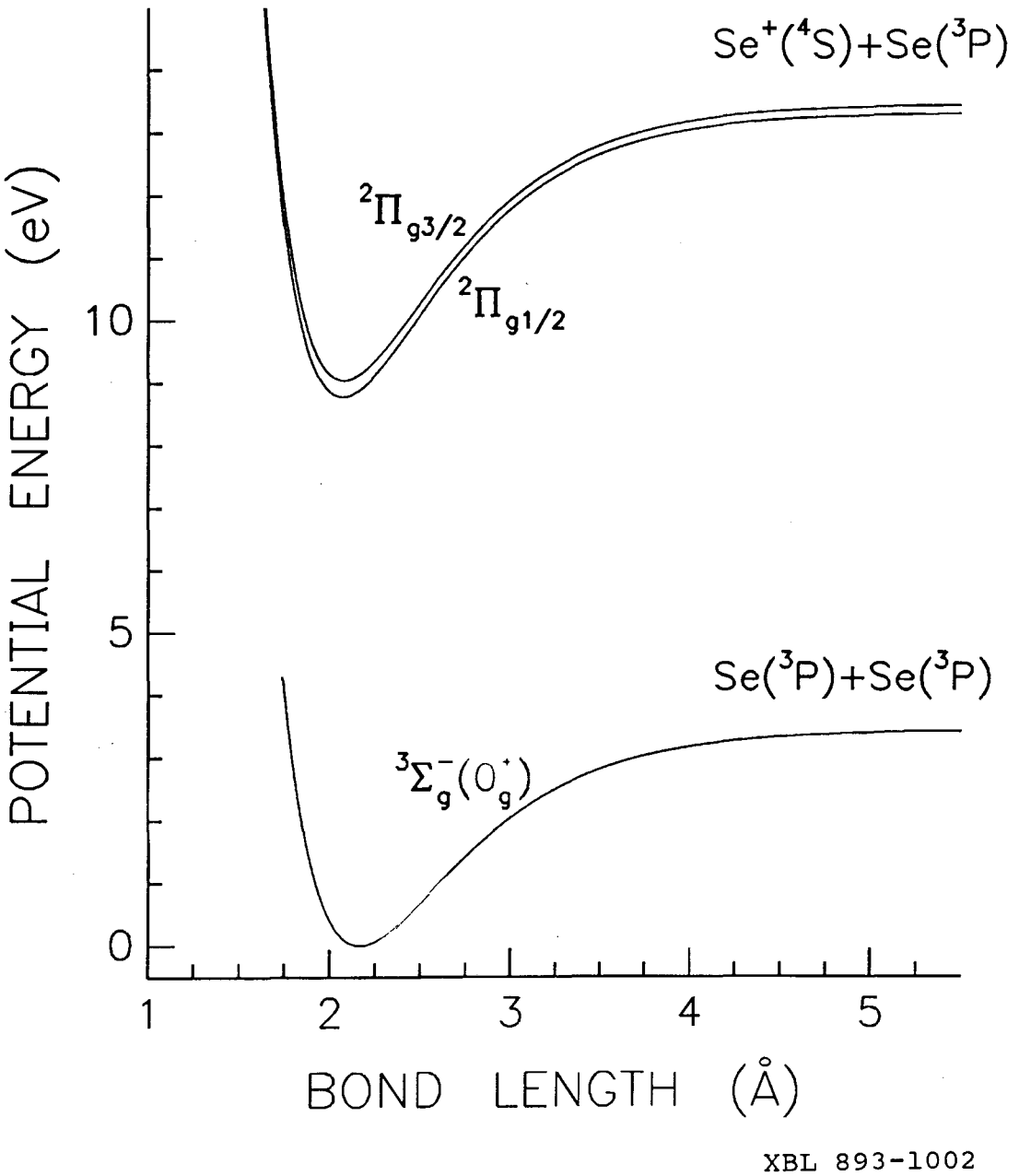
Se+(4S)+Se(3P)
2Πg3/2
2Πg1/2
Se(3P)+Se(3P)
3Σg−(0g+)
POTENTIAL ENERGY (eV)
10
5
0
1
2
3
4
5
BOND LENGTH (Å)
XBL 893-1002

Figure 3

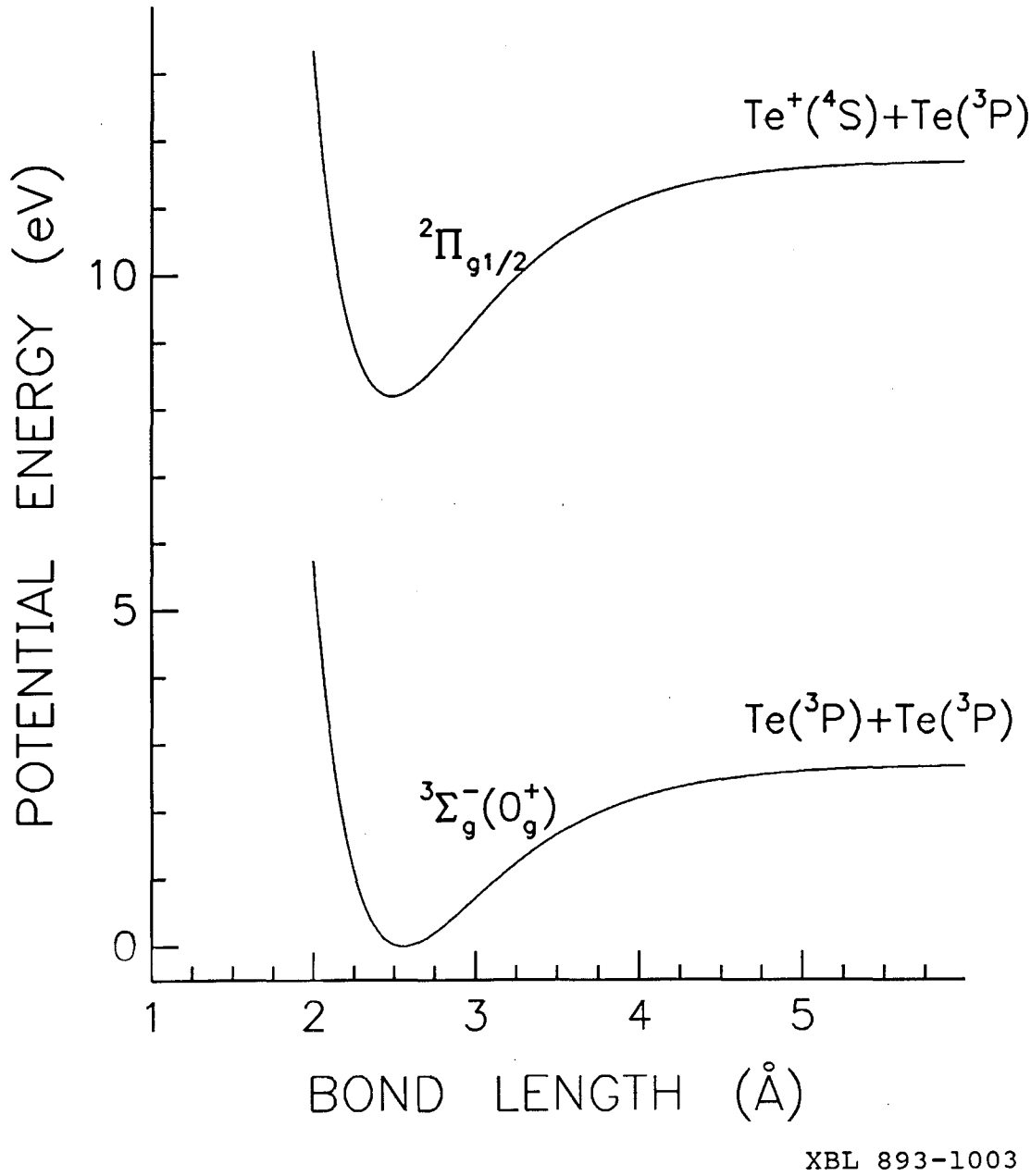
POTENTIAL ENERGY (eV)
10
5
0
1
2
3
4
5
BOND LENGTH (Å)
Te+(4S)+Te(3P)
2Πg1/2
Te(3P)+Te(3P)
3Σg−(0g+)
XBL 893-1003

Figure 4

Chapter 5

Photoelectron Spectroscopy of Clusters of Group V Elements*

Abstract

High resolution HeI (584Å) photoelectron spectra have been measured for clusters of the group V elements: As_2, Sb_2, and Bi_2; P_4, As_4, and Sb_4. For the dimers, vibrational structure was fully resolved in As_2^+. Franck-Condon factor (FCF) calculations were performed for As_2^+ and Bi_2^+, enabling us to derive the spectroscopic constants for the cationic states. The ionization potentials (IPs) of As_2 and Sb_2 were found to be smaller than the corresponding atoms, signaling metallic bonding characters of these elements. For the tetramers, vibrational structure was completely resolved for the $^2A_1$ states of P_4^+ and As_4^+. Similar FCF calculations were carried out, and the bond length changes were obtained for the ions in the $^2A_1$ states. Strong Jahn-Teller distortions took place in the ^2E states of the tetrameric ions in the $\nu_2(e)$ vibrational mode. The E⊗e Jahn-Teller problem was treated in detail, in collaboration with Ghelichkhani and Grant, and the vibronic calculations were carried out to second order (quadratic coupling) for P_4^+, for which vibrational structure was partially resolved. A Jahn-Teller stabilization energy of 0.65 eV was derived for P_4^+, which was characterized in its ground vibronic state as being highly distorted (into D_{2d} symmetry), and highly fluxional as well. Linear-only calculations were

performed for As_4^+ and Sb_4^+, and were shown to be in good agreement with the experiments. The Jahn-Teller stabilization energies for As_4^+ and Sb_4^+ were established to be 0.84 eV and 1.4 eV, respectively. Both Jahn-Teller and spin-orbit effects were found to be operative in the $^2T_2$ states of the tetrameric ions, with the spin-orbit effect being dominant in Sb_4^+ and the Jahn-Teller effect dominant in P_4^+. Vibrational structure was resolved in P_4^+, and the $\nu_3(t_2)$ mode was found to be solely involved in the Jahn-Teller coupling to reduce the symmetry of the molecular ions from T_d to C_{2v}. Strong Ham effect was shown taking place in the $^2T_2$ states, significantly suppressing the Jahn-Teller effect, with respect to the ^2E states. A classical metal droplet model was employed to fit the IPs of the clusters as a function of size, and was found to describe the IP trends reasonably well. The severe deviation of the tetramer IPs from the model were found to be due to the strong Jahn-Teller effect in the ^2E states.

5.1 Introduction

The study of metal clusters has drawn great attention recently because of their importance in many disciplines, including surface sciences, catalysis, inorganic chemistry, materials sciences, etc. The intermediate nature of these species gives rise to many unique chemical and physical properties, such as enhanced chemical reactivity and quantum size effects. A large body of literature including numerous review articles[1] has been devoted to various aspects of this subject. Of particular interest, both for their technological and fundamental importances, are clusters composed of semiconductor elements. Indeed, a number of investigations have focussed on Si clusters[2] and other semiconductor clusters.[3] The group V elements, especially P, As, and Sb, are also important in relation to semiconductor materials. Nevertheless, there have been few studies on their clusters.

One central question in cluster research is the evolution of electronic properties as a function of cluster size. For small clusters, molecular electronic spectroscopic techniques should be well suited for this study. In particular, photoelectron spectroscopy (PES) should be a powerful technique, because it probes directly the electronic energy levels of matter.[4] However, one difficulty in applying PES to cluster species is the need for size-selectivity. Consequently, much effort has been focused on photodetachment of negatively-charged clusters.[5] Only recently have studies employing PES been carried out on size-selected neutral clusters.[6]

We are interested in high resolution PES of small neutral clusters. A high temperature molecular beam source[7,8] has been built to facilitate studies on small neutral clusters and high temperature species. Besides being important semiconductor doping materials, the group V elements are well suited for our study because they provide an easy solution for the size-selectivity. Vapor phases of these elements[9] are mainly composed of tetramer species for P and As; atoms, dimers, and tetramers for Sb; and dimers and atomic species for Bi. Diatomic P and As can be produced by pyrolyzing the tetramers, or by

evaporating an appropriate alloy of these elements. In this Chapter, we present our studies on high resolution PES of As_2, Sb_2, and Bi_2; and P_4, As_4, and Sb_4.

Even though there have been a variety of methods to prepare clusters, they are still difficult to produce, especially in abundance and in a size-selective fashion. Consequently, the largest cluster which has been spectroscopically well characterized heretofore is trimers, in particular, Cu_3,[10] Na_3,[11] and Li_3.[13] It was found that the Jahn-Teller effect[13] played an important role in determining the ground state properties of these species. Essentially, the trimers under D_{3h} symmetry have a ^2E ground state, which can couple with the doubly degenerate $\nu_2(e)$ vibrational mode. In strong coupling cases, the D_{3h} symmetry of the trimer can be broken down to a C_{2v} symmetry. Obviously, the Jahn-Teller effect may well extend to larger cluster systems of appropriate symmetries. The tetramers of P, As, and Sb have T_d symmetry with a $^1A_1$ ground state. In the T_d symmetry, the ground states of the tetrameric cations have ^2E symmetry, and their first excited states have $^2T_2$ symmetry. Both these states, being orbitally degenerate, are susceptible to Jahn-Teller distortion. Thus, these species can be viewed as prototypes for studying the Jahn-Teller effect in metal clusters with T_d symmetry.

Lower resolution HeI (584 Å) PE spectra of P_4,[14] As_2 and As_4,[15] Sb_2[16] and Sb_4,[16,17] and Bi_2[18] have been reported. Except for the $^2A_1$ state of P_4^+, no vibrational resolution was achieved. Hence, little is known about the spectroscopy of the cationic states of these seemingly simple cluster species. In particular, it is essential to resolve vibrational structure in order to investigate the Jahn-Teller effect in the tetrameric species. Theoretically, there have been a few calculations for some of the neutrals of these clusters, P_4,[19] As_2,[20] As_4,[19b,20a] and Sb_4.[17] But none has been done for the ionic states.

We have obtained high resolution PE spectra for all these cluster species. Vibrational structure was completely resolved for the As_2^+ spectrum and the $^2A_1$ states of P_4^+ and As_4^+. Vibrational structure in the Jahn-Teller active ^2E and $^2T_2$ states was only partially resolved due to smaller vibrational frequencies. The spectra of Sb_2 and Sb_4

overlapped with each other, which prevented us from resolving any vibrational structure for the Sb_2 spectrum. The Bi_2 molecule has a very small vibrational frequency, and no vibrational structure could be resolved. Franck-Condon factor (FCF) calculations were carried out to analyze the $^2A_1$ states of P_4^+ and As_4^+, and all the ionic states of As_2^+ and Bi_2^+, allowing us to obtain important spectroscopic constants. The E⊗e Jahn-Teller problem was treated in detail for the ^2E states of the tetrameric cations in collaboration with Ghelichkhani and Grant, which represents the first vibronic studies for T_d clusters. A strong Ham effect was observed for the $^2T_2$ states of the tetrameric cations, which presents an excellent example for studying the interaction between the Jahn-Teller effect and the spin-orbit effect.

This chapter is organized as follows. In Section 5.2, we briefly present the experimental procedure, and in Section 5.3 the results for the dimer species. The theory of the E⊗e Jahn-Teller problem and the results of the tetrameric species are given in Section 5.4. Discussions of the results are presented in Section 5.5 and a brief summary appears in Section 5.6.

5.2 Experimental

The high temperature molecular beam source used in the current experiments has been described in detail in Chapter 2 and previous publications.[7,8] The experimental conditions relevant to the current experiments are given collectively in Table 1. Phosphorus has three allotropic forms, white, red, and black. The white form is too volatile even at room temperature and difficult to handle.[9] The more stable red form was used. Both phosphorus and arsenic evaporated as pure tetramers at the temperatures shown in Table 1. Antimony is less volatile, and a higher temperature was required for the experiment. At the experimental temperature given in Table 1, the vapor of antimony contained three species: atoms, dimers, and tetramers. As a result, the PE spectrum was a

mixture of the three. The bismuth vapor was composed of both atoms and dimers. But the atomic contributions to the PE spectrum can be easily subtracted, and a pure dimer spectrum can be still obtained. Asenic dimer was produced by evaporating Cu_3As alloy, as it was shown that this could yield the pure As_2 species.[15b] All samples (99% purity) were purchased from CERAC and used directly.

The details of the PE spectrometer have also been described in Chapter 2 and published previously.[21] Argon and xenon were used as calibration gases. The energy resolution was 12 meV, as measured with the $Ar^+ {}^2P_{3/2}$ PE peak. To avoid drift of the energy scale under the high temperature conditions, we kept each PE scan under one hour. Multiple scans were taken and added together to increase counting statistics. The effective energy resolution on the final spectrum was about 15 meV.

5.3 The Dimers: As_2, Sb_2, and Bi_2

The group V elements have ns^2np^3 atomic valence electron configurations, where the core electrons have been neglected. From molecular orbital (MO) theory, the homonuclear diatomic molecules of these elements have the following valence electronic configurations: $(\sigma_g ns)^2 (\sigma_u ns)^2 (\sigma_g np)^2 (\pi_u np)^4$, where (nl) denotes the dominant components of the MOs.

The PE spectra are shown in Figures 1-3 for As_2^+, Sb_2^+, and Bi_2^+, respectively. Only the ionizations of the two MOs derived from the np atomic orbitals were observed in our experiments. The atomic ionization cross sections of the ns orbitals are two to three orders of magnitude smaller than that of the np orbitals at the HeI photon energy (21.218 eV).[22] Thus, it is not surprising that the ionizations of the $(\sigma_g ns)$ and $(\sigma_u ns)$ orbitals were not observed. Vibrational structure was well resolved for As_2^+, with the two spin-orbit split $^2\Pi_u$ bands partially overlapped. The $^2\Sigma_g^+$ band is very sharp, with little vibrational structure.

As mentioned in Section 5.2, the antimony spectrum is a mixture of Sb^+, Sb_2^+, and Sb_4^+. Figure 2 shows the $Sb_2^+ + Sb_4^+$ $[(2t_2)^{-1}]$ portion of the spectrum with the three atomic lines subtracted. This could be done because the atomic line shape was known from our calibrations with the rare gases, which were best fitted with Voigt functions. Thus, a Voigt function was fitted to each Sb^+ peak , and then subtracted from the spectrum. The subtracted Sb^+ peaks are also plotted in Figure 2 at their actual peak positions and with their actual line shapes. What is left is still a mixture of the Sb_2^+ and Sb_4^+ spectra, with the Sb_2^+ spectrum sitting on two broad Sb_4^+ bands. The $^2\Sigma_g^+$ band of Sb_2^+ is sharp and easily recognized. Unfortunately, the $^2\Pi_{u1/2}$ and $^2\Pi_{u3/2}$ bands are overlapped heavily with the Sb_4^+ $(2t_2)^{-1}$ bands and cannot be separated and assigned.

The bismuth vapor contained both Bi and Bi_2. At our experimental temperature, there was about 35% Bi_2 in the vapor.[9] The spectrum shown in Figure 3 is the pure Bi_2^+ spectrum after the atomic lines were subtracted. The positions of the three atomic peaks are indicated in Figure 3. We did not plot them in the figure, because they had much higher intensity than the pure Bi_2^+ spectrum. The subtraction procedure was the same as with the Sb^+ lines in Figure 2. The energy range between about 8 to 8.6 eV in Figure 3 was not scanned to save running time, because it was known that there were no peaks in this energy range.[18] The ground state vibrational frequency[23] of Bi_2 is 172.71 cm^{-1}, and it is anticipated to be even smaller in the ion. The vibrational population of Bi_2 in the molecular beam was expected to be high because of its small vibrational frequency and the ineffectiveness of the vibrational relaxation in a molecular beam. Both of these factors contributed to the lack of vibrational resolution in the Bi_2^+ spectrum. In fact, a hot-band transition was observed on the low energy side of the $^2\Sigma_g^+$ band, which was useful for the evaluation of the vibrational temperature.

To analyze the spectra , we carried out FCF simulations for the As_2^+ and Bi_2^+ spectra. The calculations were done in the same way as those in Chapters 3 and 4. Basically, a Morse oscillator was employed and was expanded as a power series in $(r-r_e)$,

where r_e is the equilibrium bond length. The $(r - r_e)^3$ and $(r - r_e)^4$ terms were taken as perturbation corrections to the harmonic oscillator Hamiltonian. A few kinds of valuable information can be obtained from such calculations, e.g., vibrational temperature of the molecules in a beam, vibrational frequency and equilibrium bond length of a particular ionic state, refined values of adiabatic IPs in cases where there are band overlappings or strong hot band transitions. We estimated that the vibrational temperatures for As_2 and Bi_2 under our experimental conditions were 400±50 K and 350±50 K, respectively. These are considerably lower than the oven temperatures, as seen from Table 1, proving the advantage of using molecular beams. The overlapping of the Sb_2^+ and Sb_4^+ spectra prevented us from doing the FCF calculations for Sb_2^+. Since there was no vibrational structure resolved for the two $^2\Pi_u$ bands of Bi_2^+, the results from the calculations can only be regarded as estimates. The derived vibrational frequencies, equilibrium bond lengths, and IPs for all the states of As_2^+ and Bi_2^+ are tabulated in Table 2. Only IPs for Sb_2^+ are given in Table 2.

It is interesting to note from Figures 2 and 3 that the IPs of the diatomic molecules do not change too much from that of the atoms, with each spin-orbit state of the molecular ion corresponding to a particular spin-orbit state of the atomic ion. The dissociation behavior of these heavy diatomic molecular ions have not been studied. From the measured IPs, the dissociation energy (D_e) of the ground ionic state can be calculated from the following:

$$D_e (M_2^+) = D_e (M_2) + IP (M) - IP (M_2) \qquad (1)$$

where $D_e (M_2)$ is the dissociation energy of the neutral ground state, IP (M) is the IP of the atom, IP (M_2) is the adiabatic IP of the molecule measured in this experiment, as given in Table 2. The calculated D_es from Eq. (1) are given in Table 2 for each ion.

The spectroscopic constants of the neutral molecules are also shown in Table 2 for comparisons. According to the simple valence MO picture, the π_u orbital is a bonding

orbital. The removal of an electron from this orbital should weaken the bonding. For the two $^2\Pi_u$ states of As_2^+, this is manifested as lengthening of the bond lengths and decrease of the vibrational frequencies. However, it is surprising that the D_es of these two states appear to be larger than that of the neutral molecule. These are apparently in conflict with each other and cannot be explained simply. It is also unusual for the two spin-orbit states, $^2\Pi_{u1/2}$ and $^2\Pi_{u3/2}$, to have different vibrational frequencies. A similar case has been observed for Br_2^+, where two very different vibrational frequencies were observed for the two spin-orbit states of the $A^2\Pi_u$ band, which was explained by a strong electron correlation effect.[24] It remains a challenge to understand this result for As_2^+ and to calculate the D_es for As_2^+, theoretically.

The $^2\Pi_u$ states of Sb_2^+ also seem to have larger D_es than the neutral ground state. For Bi_2^+, the $^2\Pi_{u3/2}$ state has a smaller D_e value than the neutral ground state. This is caused by the extremely small IP of the Bi atom to the $^3P_0$ state of Bi^+, due to strong spin-orbit effect. As seen from Figure 3, the $^3P_0$ - $^3P_1$ separation in Bi^+ amounts to about 1.65 eV, the largest in the group.

Therefore, we have observed that the dimers of As and Sb have larger D_es in their ground ionic states, in which bonding electrons appeared to be taken away, than the corresponding neutrals. We shall return to this point later in Section 5.5.

5.4 The Tetramers: P_4, As_4, and Sb_4

5.4.1 The Jahn-Teller Theorem and the Ham Effect

5.4.1.1 The Jahn-Teller Theorem

Before discussing the PE spectra of the tetramer species, we shall first recall the Jahn-Teller theorem,[13] which is essential to understand the PE spectra of the tetramers. The Jahn-Teller theorem states that a nonlinear nuclear framework in a degenerate electronic

state (except for the two-fold Kramers degeneracy[25]) is unstable against first order distortion of the nuclear framework. This instability is caused by a linear perturbation on the electronic state, which lowers the symmetry of the nuclear framework and lifts the electronic degeneracy. For a nonlinear molecule, this means that in a degenerate electronic state the potential minimum is no longer at the symmetric position. It is rather located at some distance from the symmetric position along a distortion coordinate. The distortion is eventually limited by the quasielastic forces which resist it. Thus, a nonlinear molecule in a degenerate electronic state has a permanent distortion which lowers its symmetry and produces an observable anisotropy. This is called the static Jahn-Teller effect. The Jahn-Teller effect naturally means the breakdown of the Born-Oppenheimer approximation; that is, one cannot separate the vibrational and electronic degrees of freedom. The vibrational mode which couples to the electronic motions is also degenerate. Therefore, a Jahn-Teller molecule can have more than one distorted position with equal energy and, depending on the barrier, the molecule can fluctuate among these positions. The dynamic Jahn-Teller effect refers to the dynamical coupling between the electronic and vibrational motions, yielding vibronic energy levels.

Both the static and the dynamic Jahn-Teller effects[26] have been extensively studied, especially in solid state physics, in the investigations of transition metal ions in solid matrices, impurity atoms or vacancies in crystal lattices,[27] etc. In the study of Jahn-Teller molecules, one of the interesting aspects is to investigate the geometry of the Jahn-Teller distorted molecule and its potential energy surfaces. Liehr[28] has shown that a Jahn-Teller molecule will lower its symmetry only as far as to the nearest point group which will reduce its electronic degeneracy. He also derived analytically the potential energy surfaces for a great many Jahn-Teller distorted nuclear conformations. Recently, there has been new excitement about the Jahn-Teller effect in metal clusters, in particular, the trimer systems.[10-12]

5.4.1.2 The Ham Effect: Jahn-Teller Effect vs. Spin-Orbit Effect

In PES, one often starts from a closed shell molecule with an initial state of spin 0 and ends up with a final state of spin 1/2. If the ionization is from a degenerate orbital, then the final state with non-zero orbital angular momentum is subject to the spin-orbit effect as well as to the Jahn-Teller effect. These two effects affect each other and, in a sense, compete to lift the orbital degeneracy. In general, when the two effects are of comparable magnitude, the spin-orbit effect reduces the Jahn-Teller effect. This reduction of the Jahn-Teller effect by the spin-orbit effect is often called the Ham effect.[29] There are two other limits. If the spin-orbit coupling is sufficiently strong, it can stabilize a molecule against Jahn-Teller distortions.[26b,30] On the other hand, when the Jahn-Teller effect is dominant and produces a static effect, the spin-orbit interaction can be quenched. The $^2T_2$ state in the PES of the current tetramer species represents such cases, where both the spin-orbit and the Jahn-Teller effects are possible and can affect each other. Depending on the magnitude of each effect, different spectral splittings result. We shall see that this has significant consequences in the resulting PE spectra.

5.4.2 Results

The PE spectra of P_4, As_4, and Sb_4 are shown in Figures 4-6, respectively. The three clusters are isoelectronic and all have the same tetrahedral geometry. Thus, their PE spectra are very similar, with the P_4^+ and As_4^+ spectra showing vibrational resolution. Under T_d symmetry, the valence electronic configuration of these clusters can be written as:

$$(1a_1)^2\,(1t_2)^6\,(2a_1)^2\,(2t_2)^6\,(1e)^4$$

where the $1a_1$ and $1t_2$ MOs are mainly of the valence atomic s orbital character, and the $2a_1$, $2t_2$, and 1e MOs of the valence p character. For the same reason as in the dimers, the $1a_1$ and $1t_2$ MOs have very small ionization cross sections. Thus, only the ionizations of the outermost three MOs were observed, as shown in Figures 4-6. The Sb_4^+ spectrum has a

contribution from the Sb_2 species, as indicated in Figure 6. The $^2\Pi_u$ bands of Sb_2^+ overlap exactly with the $(2t_2)^{-1}$ bands of Sb_4^+, though the contribution from the $^2\Pi_u$ bands of Sb_2^+ is expected to be small. Figure 2 is actually a portion of Figure 6. Both the small vibrational frequencies and the poor statistics in the Sb_4^+ spectrum are responsible for the lack of vibrational structure, in particular, in the $(2a_1)^{-1}$ band.

With T_d symmetry, these three clusters have $^1A_1$ ground states. Removal of an electron from the 1e or $2t_2$ MOs creates ^2E and $^2T_2$ final states in the ions, respectively. The ^2E state is orbitally doubly degenerate and the $^2T_2$ state triply degenerate. According to the Jahn-Teller theorem, these two states are Jahn-Teller active and the tetrahedral geometries of the molecular ions are unstable in these two states against asymmetric vibrations. The $^2A_1$ excited state of the molecular ions from $(2a_1)^{-1}$ is not orbitally degenerate and should maintain the T_d symmetry.

The six normal modes of vibration for a tetrahedral M_4 molecule are shown in Figure 7. The ν_2 (e) mode is doubly degenerate and the ν_3 (t_2) mode triply degenerate. The vibrational frequencies for P_4, As_4, and Sb_4 are given in Table 3. The ν_1 (a) mode is totally symmetric and cannot distort the T_d symmetry. However, the ν_2 and ν_3 modes are both Jahn-Teller active. From group theory,[25] only the ν_2 mode can be Jahn-Teller active in the ^2E state while both the ν_2 and ν_3 modes can be coupled in the $^2T_2$ state.

It can be seen from Figures 4-6 that two PE bands were observed for ionization of the 1e orbital in each case as a result of the Jahn-Teller coupling with the ν_2 vibrations. Three bands were resolved for ionization of the $2t_2$ orbital while a single band was seen for that of $2a_1$. In P_4^+ and As_4^+, beautiful vibrational structure was resolved for the $^2A_1$ bands. The IPs and the observed vibrational spacings are listed in Table 4 for each molecule. Because of the strong Jahn-Teller effect, adiabatic IPs to the ground ^2E states could not be obtained, and only upper limits were estimated from the experimental PE spectra, which are given in the square parentheses. As discussed below, vibronic

calculations yield better values for the adiabatic IPs, which are shown in Table 4. In the following, we discuss each band separately.

5.4.3 The $(1e)^{-1}$ Bands: Theoretical Treatment of the E⊗e Jahn-Teller Effect

5.4.3.1 Theoretical Background of the E⊗e Jahn-Teller Problem

The $(1e)^{-1}$ bands together with the $(2t_2)^{-1}$ bands are shown separately in Figures 8-10 for P_4^+, As_4^+, and Sb_4^+, respectively. The prominent two-peaked spectral intensity distributions evident to a remarkable similar degree in the $(1e)^{-1}$ bands of all three tetramers signal strong Jahn-Teller distortions differentiating the molecular ion ground states from the highly symmetric tetrahedral configurations of the corresponding neutrals. As noted above, the ^2E ($G_{3/2}$) terms associated with these 1e-orbital vacancies are, in each case, subject to Jahn-Teller vibronic coupling in the $\nu_2(e)$ normal coordinate. This coupling displaces stable molecular configurations from high symmetry, and, as a consequence, distributes spectral intensity over progressions of vibronically excited bands. A qualitative understanding of this effect can be achieved by examining the adiabatic potential energy surfaces of the Jahn-Teller active system in classical terms.

Let $\psi_\pm$ denote the complex electronic wave functions of the doubly degenerate electronic term, and $H_e(Q_0)$ the electronic Hamiltonian at the undistorted nuclear configuration. Surfaces of the single-mode E⊗e Jahn-Teller problem are obtained most simply by diagonalizing the electronic Hamiltonian in a diabatic basis that spans the symmetry-induced two-fold electronic degeneracy:[28,31]

$$\begin{bmatrix} \langle\psi_+|H_e(Q_0)|\psi_+\rangle - E(Q) & \langle\psi_+|H_e(Q_0)|\psi_-\rangle \\ \langle\psi_-|H_e(Q_0)|\psi_+\rangle & \langle\psi_-|H_e(Q_0)|\psi_-\rangle - E(Q) \end{bmatrix} \begin{bmatrix} a(Q) \\ b(Q) \end{bmatrix} = 0 \ , \qquad (2)$$

in which, as indicated explicitly below, single-term harmonic expansions conventionally approximate diagonal matrix elements, while linear terms lead expansions of off-diagonal elements.[26d] Eq.(2) is the quantum mechanical starting point to discuss the Jahn-Teller coupling between a doubly degenerate electronic state and a doubly degenerate vibrational mode. The resulting surfaces, E(Q), show, in lowest order, linear divergence from the symmetric point, characteristic of a conical intersection, which, when combined with a harmonic restoring force, produces the familiar cylindrically symmetric sombrero double-valued potential, described by the equation:

$$E_{\pm}(Q) = \frac{1}{2}\rho^2 \pm k\rho \quad , \tag{3}$$

where k is the linear coupling coefficient expressed in units for which λ, the harmonic force constant, equals one. Figure 11 illustrates this simplest Jahn-Teller potential surface.

The level structure and vibrational dynamics associated with such potentials are generally more complex, characterized by spectral irregularity and the facile exchange of angular momentum between vibrational and electronic subsystems.[26f,32] However, for low-lying levels carried far from the conical intersection by strong linear coupling, a simple adiabatic separation can provide an intuitively appealing picture, that accounts for evident patterns of transitions by mapping observed structure on the model of a radial oscillator combined with a free internal rotor moving on the lower sheet. The quantum states of this limit are approximately described by the simple expression:[26c]

$$W(n,j) = nh\omega + Aj^2 \tag{4}$$

in which ω is the characteristic frequency, n is the quantum number of the radial oscillator, and A is an internal rotation constant:

$$A = \frac{h^2}{2M\rho_0} \tag{5}$$

where M is the reduced mass of the mode and ρ_0 is the radial minimum on the lower surface. j is the vibrational angular momentum quantum number, constrained to be half-odd integral by boundary conditions imposed by topological phase.[33]

The simple picture of a system of transitions from the ground state of the neutral to vibrational levels of the cylindrically distorted adiabatic lower surface accounts well for the long progressions of the bands that characterize the first broad peaks of the spectra of P_4^+, As_4^+, and Sb_4^+. Similarly extending an adiabatic separation to the upper surface, we can calculate a harmonic set of widely spaced eigenstates of the steeper upper potential. In reality, these are, of course, imbedded in the dense manifold of states of the lower sheet, to which they are coupled by nonadiabatic terms. However, as discussed below, in exact nonadiabatic calculations based on the lower-order Hamiltonian, they survive as quasi-resonances,[10c] which have been recognized in theory as useful semiclassical markers of coupling strength.[34] Thus, we can associate the second broad maximum in the PE spectra with a concentration of Franck-Condon intensity about the origin of the upper sheet, and predict additional maxima at intervals of higher energy.

Though the properties of such cone resonances, and the coupling conditions under which they can be expected to appear, are well characterized theoretically,[10c,34,35] no experimental examples exist that show oscillatory behavior beyond the broad bifurcation also evident in the present PE spectra. This may be a question of resolution; conventional PES resolves well electronic separations, but tends to smear structure on the scale of vibrational progressions, particularly for heavier, lower-frequency systems. The present data offer a higher resolution view of what are evidently strongly coupled systems. It is thus worthwhile to compare these spectra with theory at the highest feasible level of exact calculation in an effort to refine our semiclassical understanding of higher-lying quantum states in realistic strongly-coupled systems.

5.4.3.2 Exact Nonadiabatic Calculations

Retaining the form of the Hamiltonian (2), which assumes a well-isolated degenerate electronic term, and further assuming the adequacy of a harmonic basis to describe motion in Q, we can write the Schrodinger equation to second order in vibrational amplitude, ρ, and phase, ϕ:

$$\left[T_N \mathbf{1} + \begin{bmatrix} \frac{\rho^2}{2} & k\rho e^{-i\phi} + \frac{g\rho^2 e^{2i\phi}}{2} \\ k\rho e^{i\phi} + \frac{g\rho^2 e^{-2i\phi}}{2} & \frac{\rho^2}{2} \end{bmatrix} \right] \begin{bmatrix} \chi_+ \\ \chi_- \end{bmatrix} = W \begin{bmatrix} \chi_+ \\ \chi_- \end{bmatrix} , \qquad (6)$$

in which nuclear kinetic energy T_N is diagonal, and coefficients k and g characterize linear and quadratic distortion terms, in units of the harmonic restoring force. We expand χ_+ and χ_- in a basis of isotropic harmonic oscillator wave functions:

$$\chi_+ = \sum a_{v,l} |v,l\rangle \qquad (7)$$

$$\chi_- = \sum b_{v,l} |v,l\rangle \qquad (8)$$

$$v = 0, 1, 2, \ldots \qquad (9)$$

$$l = -v, -v+2, \ldots, v-2, v \qquad (10)$$

where the oscillator frequency is chosen so that $|v,l\rangle$ are eigenfunctions of the diagonal vibrational Hamiltonian. The explicit form of the expanded matrix is simplified by recognizing that the polar normal coordinates, $\rho e^{-i\phi}$ and $\rho e^{i\phi}$, function as raising and lowering operators with respect to the l vibrational angular momentum quantum number, viz:

$$\langle v, l \,|\rho e^{-i\phi}|v+1, l+1\rangle = \sqrt{\frac{(v+l+1)}{2}} \quad , \tag{11}$$

$$\langle v-1, l \,|\rho e^{i\phi}|v, l\,\rangle = \sqrt{\frac{(v-l-1)}{2}} \tag{12}$$

and, with

$$\langle v, l \,|\rho^2 e^{-2i\phi}|v', l'\rangle = \sum_{v'',l''} \langle v,l \,|\rho e^{-i\phi}|v'',l''\rangle\langle v'',l'' \,|\rho e^{-i\phi}|v',l'\rangle \tag{13}$$

we construct non-zero matrix elements of the quadratic terms:

$$\langle v, l \,|\rho^2 e^{-2i\phi}|v, l+2\rangle = \sqrt{(v+l+1)(v-l-1)} \tag{14}$$

$$\langle v, l \,|\rho^2 e^{-2i\phi}|v+2, l+2\rangle = \frac{\sqrt{(v+l+1)(v+l+3)}}{2} \tag{15}$$

$$\langle v, l \,|\rho^2 e^{-2i\phi}|v-2, l+2\rangle = \frac{\sqrt{(v-l-1)(v-l-3)}}{2} \tag{16}$$

The resulting sparse matrix is diagonalized to obtain level energies and spectral overlaps.

5.4.3.3 Distortion and Hindered Fluxionality in the Ground State of P_4^+

The vibronic spectrum of the conical intersection is particularly simple for the case in which it is assumed that g = 0. The problem then block-factors according to the quantum number j, corresponding to the half-odd integral vibrational angular momentum, and only blocks with $j = \pm\frac{1}{2}$ carry transition intensity. Under such conditions, fully converged calculations can be extended over a large range of energy using conventionally available diagonalization subroutines. Figure 12 shows a correlation diagram giving the relative energies of the first few excited states of the linearly coupled Hamiltonian as a

function of the stabilization energy, $D = \frac{1}{2}k^2$, from D = 0 to the adiabatically separable limit. Figure 13 compares theoretical positions and intensities with experimental results for P_4^+, for a model that assumes single-mode linear coupling with k = 5.75 in units of the zeroth-order frequency, which is taken to be 315 cm^{-1}, the experimentally observed vibrational spacing. It can be seen that the theory and experiment agree very well, particularly in the qualitative shape of the first broad maximum and the leading edge of the second band. The fit of the theoretical envelope to the experimental one yields an improved estimate of the adiabatic ionization threshold, 8.95 eV, which is difficult to obtain from the experimental PE spectrum. With reference to Figure 11, the Jahn-Teller stabilization energy of P_4^+ in this simple linear model is 0.65 eV, which places the conical intersection at an ionization potential of 9.60 eV, and fully 15 levels of radial oscillation between the zero point and the beginning of the upper sheet. Theoretical intensities show a slight modulation in the upper range of the spectral envelope associated with the cone-resonances phenomenon noted above. Experimental limitations imposed by resolution together with the proximity of the $(2t_2)^{-1}$ transition prevent the confirmation of such structure in the data, though the bandshape observed certainly does not rule out this intensity pattern.

The question of the subtle pattern of intensities and the degree to which they match the predictions of the simple linear model is one of qualitative importance. If a system such as P_4^+ is accurately described by a Hamiltonian coupled strictly to first order in the distortion coordinates, it then follows that the potential in these coordinates is cylindrically symmetric, presenting no barrier to vibronic pseudorotation. Under such circumstances, we must characterize the system not only as strongly distorted, but highly fluxional as well. If, on the other hand, theory requires higher-order coupling terms to account for spectral positions and intensities, we must then recognize potential barriers that quench free rotation in the phase of the distortion for the lowest radial levels.

Diagonalizing the electronic part of the problem as in (2) for the explicit matrix elements expressed in the linear-plus-quadratic Hamiltonian (6) yields a more complex adiabatic potential:

$$E_{\pm}(\rho,\phi) = \tfrac{1}{2}\rho^2 \pm k\rho\left[1+ \frac{g\rho}{k}\cos(3\phi) + \frac{g^2\rho^2}{4k^2}\right]^{1/2} \qquad (17)$$

For small g/k, this expression simplifies to read:

$$E_{\pm}(\rho,\phi) = \tfrac{1}{2}\left[\rho^2 \pm g\rho^2\cos(3\phi)\right] \pm k\rho \qquad (18)$$

using (18) to identify maxima and minima in the floor of the lower sheet, we can solve for the pseudorotation barrier as a function of k and g:

$$E(\rho_0,\phi_{max/min}) = -\frac{k^2}{2(1\pm g)} \qquad (19)$$

The matrix elements that produce these modulations couple vibrational basis states in a scheme that block-factors as j' = j mod 3. As a result, with reference to the correlation diagram in Figure 12, accidentally degenerate eigenstates of the linear-only Hamiltonian with j = ± 3/2, 9/2, 15/2,... split, and other levels, which are closely lying in the linear approximation and belong to the same j' block, similarly diverge and share intensity. Figure 14 illustrates the effect of including quadratic coupling on the simulated spectrum of P_4^+, retaining the linear parameter of Figure 13. As can be seen, by distributing the oscillator strength of the radial fundamentals over all the added states of the j = ± 1/2 mod 3 block, higher-order coupling greatly increases the density of allowed transitions. Interestingly, however, broader intensity patterns are less affected, and when simulated spectra are convoluted with a 15 meV instrumental function, the overall bandshape remains roughly constant over the full range of quadratic coupling for which we can obtain converged intensities.

However, one important trend can be recognized. For g = 0, the family of transitions to the j = 1/2 radial fundamentals form a highly regular progression of bands. The addition of quadratic barriers of a magnitude comparable to the zero-point energy initially disrupts this structure, spreading intensity over an irregular distribution of states, and thus smoothing the leading edge of the first band for values of g that fall in the range from 0.005 to 0.02. For g greater than 0.02 quadratic pseudorotation barriers significantly exceed the radial vibrational frequency. These larger modulations of the pseudorotation moat trap lower-lying vibrational states in three-fold wells. The associated vibrational structure tends toward that of statically distorted isomers, with an increased periodicity, broken by tunneling splitting and above-barrier reflection. As a result, we recognize that lower and higher extremes of quadratic coupling are spectroscopically characterized by periodic intensity modulations. The P_4^+ spectrum displays sufficient resolution to show periodic structure on the trailing edge of the first band. But, the leading edge of this band is comparatively smooth. Such behavior is encompassed by only a relatively narrow range of quadratic coupling coefficients, including g from about 0.01 to 0.02.

Thus, we have a quantitative picture of the Jahn-Teller coupling in the ^2E state of P_4^+ that is reasonably secure to second order. The largest term coupling the electronic degeneracy is linear in the e vibrational coordinate, producing a strong distortion, stabilized by 0.65 eV relative to the symmetric configuration. The resulting vibronic pseudorotation trough is modulated by a moderate higher-order coupling, which erects a three-fold barrier with a height comparable to the zero-point energy. A potential energy surface illustrating the relative magnitude of these effects is presented in Figure 15. The principal observable consequence of the dominant linear distortion is the transfer of Franck-Condon intensity to transitions that produce vibronically excited ions, which form a spectrum with a distinctive double maximum. By quenching vibronic angular momentum, quadratic coupling widens this intensity distribution to include transitions forbidden under conditions of linear

coupling alone, which, at the level appropriate to explain the P_4^+ spectrum, smooths the leading edge of the first band.

5.4.3.4 Strong Vibronic Couplings in As_4^+ and Sb_4^+: the Case for Cone Resonances in Realistic Systems

The qualitative features of the $(1e)^{-1}$ bands of As_4^+ and Sb_4^+ are similar to that of P_4^+ and can be interpreted similarly. However, it is more difficult to be as precise in our vibronic assessments of As_4^+ and Sb_4^+. Neither spectrum exhibits discernable structure that can be associated with individual vibrational bands. Nevertheless, the neutral ground state frequencies are known,[36] and a simple linear approach can be used just as with P_4^+ to characterize the gross properties of vibronic distortions responsible for the observed PE spectra. Figures 16 and 17 show our spectral simulations for linear coupling parameters of k = 9.5 and 12.5, respectively. The spectral envelopes obtained from these linear-only simulations correspond with experimental ones quite well, even though it appears very likely that a complete description will require some degree of higher-order coupling: leading linear terms are larger for As_4^+ and Sb_4^+ than for P_4^+, and spectral intensity is sufficiently redistributed to obscure discrete band structure. Most interesting is the absence in the experimental spectra of continuing intensity oscillations beyond the first. These oscillations are the exact manifestations in linearly coupled calculations of the semiclassical cone resonances discussed above. The linear coupling terms for the cases at hand are too large, and the energies that need to be considered too high, to extend calculations to the dimensions required for the addition of quadratic terms, so we cannot test the persistence of these features at higher orders of theory. We suspect that they will be moderate, and that their absence in the present spectra can be explained by a realistic order of coupling, with attendant mixing and disruption of cone resonances.

By analogy with P_4^+, linearly-coupled spectral simulations suffice to broadly characterize vibronic distortion in these systems. Taken together, the resulting coupling

parameters establish obvious trends in the potential energy surfaces and vibronic state distributions for the $(1e)^{-1}$ band of the group V tetramer cations. As noted above, correspondence between experiment and theory places the adiabatic IP of P_4 at 8.95 eV, with about 15 radial vibronic energy levels between the distorted zero point of the cation and its symmetric conical intersection 0.65 eV higher. In As_4^+ and Sb_4^+, distortions are successively deeper. The adiabatic IP of As_4, established by linear simulation to be 7.83 eV, lies 0.84 eV below the energy of the cationic conical intersection. For Sb_4^+, we estimate an adiabatic threshold of 6.61 eV, stabilized 1.4 eV by the Jahn-Teller distortion. Adding to the impact of these moderately deepening distortions is the effect of diminishing vibrational frequency. Because the associated frequencies are so much smaller, the potential surfaces of the heavier systems contain many more adiabatically separable vibronic states; respective pseudorotation troughs support about 45 overtones of the radial oscillation for As_4^+, and nearly 80 for Sb_4^+.

5.4.4 The $(2t_2)^{-1}$ Bands: Jahn-Teller Effect vs. Ham Effect

As can be seen from Figures 8-10, the $(2t_2)^{-1}$ bands are more complicated, and each is composed of three components, which are indicated with Voigt functions in the Figures. The Voigt functions merely serve to show the positions of the three components and to enhance the visibility. Two factors can be attributed to the spectral complexity, Jahn-Teller effect and spin-orbit effect. Unlike the ^2E state, in the $^2T_2$ term, both the $\nu_2(e)$ and $\nu_3(t_2)$ modes are active in the Jahn-Teller coupling. Moreover, as mentioned in 5.4.3, the ^2E and $^2T_2$ terms are close to each other in energy, and can have interactions which would further complicate the spectrum.

Nice vibrational structure was resolved for the first component in the P_4^+ spectrum, with a vibrational spacing of about 400 cm^{-1}, as shown in Table 4. Compared with the P_4 neutral vibrational frequencies, this spacing is larger than the ν_2 frequency, but smaller than

the ν_3 frequency. The $2t_2$ MO should be a bonding orbital. Thus, it is reasonable to assign the observed vibrational structure in the P_4^+ spectrum to the ν_3 mode. This means that the $\nu_3(t_2)$ mode is the Jahn-Teller active mode in the vibronic interaction while the $\nu_2(e)$ mode may have little involvement. Just the T⊗t Jahn-Teller problem alone is a fairly complicated one. In the present context, we shall restrict ourself only to interpret the qualitative features of the spectra and study the possible Jahn-Teller splittings and the spin-orbit effect, by assuming explicitly a single-mode and single-state problem.

In a T_d point group, the orbital angular momentum of an E term is largely quenched but not for a T term.[27] Therefore, we must consider the spin-orbit effect as well as the Jahn-Teller effect in the $(2t_2)^{-1}$ bands, especially for the Sb_4^+ case, where spin-orbit interaction is anticipated to be very important. From Table 4 and Figures 8-10, we see that the splitting between the first and second components in the $(2t_2)^{-1}$ band increases considerably from P_4^+ to Sb_4^+. For Sb_4^+, this splitting is almost the same as the spin-orbit splitting in Sb^+,while that in P_4^+ is much larger than the spin-orbit splitting in P^+. From Figure 10, it is seen that this splitting is the same as that of the Sb_2^+ $^2\Pi u$ spin-orbit splitting, since they overlap almost exactly. Thus, we can account for the splitting between the first and second components in Sb_4^+ as being due to the spin-orbit effect. The splitting between the second and third components decreases a little bit from P_4^+ to Sb_4^+. Hence, the splittings in P_4^+ should be principally due to the Jahn-Teller effect. Here is an excellent example demonstrating the transition from strong Jahn-Teller effect for P_4^+ to strong spin-orbit effect in Sb_4^+. However, the spin-orbit effect in P_4^+ is not negligible. It manifests itself as a result of the Ham effect. It is clear that the Jahn-Teller splitting in the $(2t_2)^{-1}$ bands of P_4^+ is significantly smaller than that in the $(1e)^{-1}$ band, strongly suggesting the importance of the Ham effect. That is, the spin-orbit effect suppresses the Jahn-Teller effect in the $^2T_2$ states.

It is of interest to consider the symmetry of the Jahn-Teller distorted nuclear configurations. As seen from Figure 7, the $\nu_2(e)$ vibrations tend to distort a tetrahedral M_4

molecule to a D_{2d} symmetry. Thus, the ground states of P_4^+, As_4^+, and Sb_4^+ discussed in Section 5.4.3 should possess a reduced symmetry of D_{2d}, instead of T_d. On the other hand, the $\nu_3(t_2)$ vibrations would distort the T_d M_4 molecule to a C_{2v} symmetry. Hence, a $^2T_2$ term under strong Jahn-Teller coupling with the $\nu_3(t_2)$ mode should split as follows:[25]

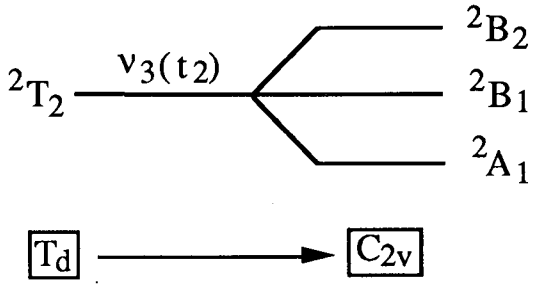

(20)

This should be the case for P_4^+, where the Jahn-Teller effect dominates the spin-orbit effect. A schematic representation of the Jahn-Teller splittings based on this scheme is shown in Figure 18(a). This diagram represents a section of the potential energy hyper-surfaces along the t_2 distortion coordinate, ρ. The potential energy hyper-surfaces have cylindrical symmetry in a harmonic approximation.[27b] The neutral ground state is shown with the vibrational wave function, which has been shown to have its maximum not at $\rho=0$, but rather at some distance along the distortion coordinate. Franck-Condon transitions from the ground state to the three Jahn-Teller split levels give the observed three components in the $(2t_2)^{-1}$ bands. The vibronic level structures are expected to be very complicated at energies above the $^2A_1$ level, which accounts for the lack of vibrational resolution at higher energies beyond the first component.

For Sb_4^+, however, a different splitting pattern should be expected, because the spin-orbit effect is dominant. The spin state of a single unpaired electron transforms as $E_{1/2}$ in the T_d point group, and the direct product of $E_{1/2}$ with $^2T_2$ gives the following results:[25]

$$^2T_2 \times E_{1/2} = {}^2E_{5/2} + {}^2G_{3/2} \qquad (21)$$

where the component $^2E_{5/2}$ has no spatial degeneracy (only the two-fold Kramers degeneracy), and the component $^2G_{3/2}$ has two-fold spatial degeneracy and is susceptible to further Jahn-Teller splitting. Thus, the following should be a more appropriate splitting scheme for the $(2t_2)^{-1}$ band of Sb_4^+:

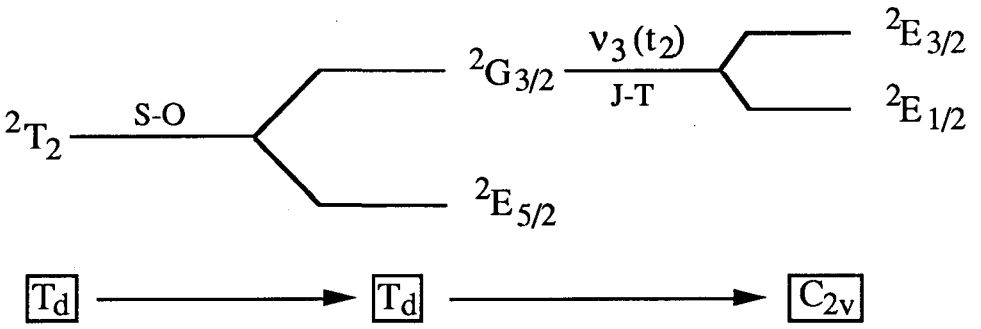

(21)

where S-O stands for the spin-orbit interaction, and J-T the Jahn-Teller coupling. A schematic representation based on this splitting scheme is shown in Figure 18(b). The $^2E_{5/2}$ component should maintain the T_d symmetry and still have the $\nu_3(t_2)$ vibrational excitation. This is a stabilization caused by the strong spin-orbit effect against the Jahn-Teller distortion.[27]

Between P_4^+ and Sb_4^+ is As_4^+, which has comparable strengths of spin-orbit and Jahn-Teller effects. The splitting of the $(2t_2)^{-1}$ bands of As_4^+ is perhaps better described by (21) with a smaller spin-orbit splitting. With (20) and (21), we may have a qualitative understanding of the $(2t_2)^{-1}$ bands of the group V tetramer cations. In either case, the $^2T_2$ state would be split into three levels. With reference to Figure 18, Franck-Condon transitions from the neutral ground state to the three final split levels would yield PE spectra like those experimentally observed.

5.4.5 The $(1a_1)^{-1}$ bands: Franck-Condon Analyses

The $^2A_1$ state of P_4^+, As_4^+, and Sb_4^+ is not spatially degenerate, and is not subject to Jahn-Teller or spin-orbit splitting. A single band was observed in each case. Beautiful vibrational structure was resolved in P_4^+ and As_4^+, for which the IPs are given in Tables 5 and 6, respectively. From the vibrational spacings, there is no doubt that the ν_1 mode was excited in each case, just as one would expected. As can be seen, some hot band transitions due to thermal populations of the neutral molecules were resolved, as shown in Figures 4 and 5, and Tables 5 and 6.

The ν_1 vibrational mode depicts the stretching motions of the four atoms in phase and maintains the symmetry of the molecule, as shown in Figure 7. Therefore, one should be able to evaluate the bond length change from the observed vibrational spectrum with a simple one-dimensional harmonic oscillator. This involves a transformation from the bond stretches to the normal coordinate. This can be conveniently written as:[37]

$$Q_1 = 2\sqrt{m}\, r, \qquad (22)$$

where Q_1 is the normal coordinate, m is the atomic mass, and r is the bond stretch from the center of the tetrahedral molecule. With Eq. (22), we can calculate the FCFs for the M_4^+ species at hand just like what we did for the dimers. Figures 19 and 20 illustrate the comparison of the theoretical calculations with the experimental spectra. The agreement for P_4^+ is excellent while it is only qualitative for As_4^+. The vibrational temperatures obtained from these calculations are 450±50 K and 350±50 K for P_4^+ and As_4^+, respectively.

The bond length for a tetrahedral M_4 molecule is measured by $r_{m\text{-}m}$, which has the following relationship with the bond stretch, r, described in the ν_1 vibrational mode as in Eq. (22):

$$r_{m\text{-}m} = 2\left(\sin\frac{109°28'}{2}\right)r \qquad (23)$$

The derived r_{m-m} values from the FCF calculations for P_4^+ and As_4^+ are given in Table 7, together with the ground state values. The sensitivity in the simulations was ±0.003 Å. Since only the changes of bond length were obtained in the calculations, that the accuracy of r_{m-m} for the ions is ultimately limited by the known ground-state bond lengths.

From the hot-band transitions, moreover, we can evaluate the vibrational frequency of the ground state. The derived vibrational frequencies for both the neutrals and the cations are also given in Table 7. With reference to Table 3, it is noteworthy that the ν_1 frequency of 360 cm^{-1} obtained from our fitting for As_4 is significantly larger than the known Raman measurement[36(a)] while that of P_4 obtained in our fitting agree well with the previous optical measurement.[38] It was difficult to study these species, and, in light of this work, it may be of interest to remeasure their fundamental vibrational frequencies.

5.5 Discussion

In Figure 21 are plotted the IPs of the atoms, dimers, and tetramers of the group V elements known today. The atomic IPs are from Moore's table,[38] the IPs of N_2 and P_2 from Ref. 40, and the rest from the current work. It should be kept in mind that it was difficult to obtain the adiabatic IPs for the tetramers from the experimental spectra due to poor Franck-Condon factors. Only upper limits could be estimated from the experimental PE spectra. The values employed in Figure 21 were established from the vibronic simulations, as given in Table 4.

It is interesting first to see the trend of the IPs from the atoms to diatomics. We see from Figure 21 that, for N and P, the IP increases upon dimerization, characteristic of valence bonding formation. However, for As and Sb, the IP decreases for the dimers, which is responsible for the puzzling results that the D_es of the molecular ions are larger than that of the neutrals, for As_2 and Sb_2, as mentioned in Section 5.3. For Bi, the

diatomic molecule has a higher IP than the atom, which was explained earlier as largely due to the extremely large spin-orbit splitting.

It is known that, descending the periodic table from N to Bi, the elements become more metallic. As a matter of fact, As, Sb, and Bi are all semimetals.[41] They are semimetals only because of their rhombohedral crystal lattices. Were they to have simple cubic crystal lattices, they would be very good metals indeed. Could it mean metallic bonding character that the As and Sb dimers have smaller IPs than the respective atoms? It may be instructive to consider some cases of real metals, the alkali elements. Hydrogen is non-metallic (at least in standard conditions), and forms the well-know covalently-bonded hydrogen molecule, which has a higher IP than the hydrogen atom. Going down the periodic table are the well-known best free-electron metals, the alkali elements. Leutwyler *et al.*[42] have measured the IPs of Na_2 and K_2 accurately. Interestingly, both these dimers have smaller IPs than the corresponding atoms. Consequently, the molecular ions of these species have larger D_es than the neutral dimers. Although these results have gone unquestioned, they must be related to the metallic properties of these elements. At least, the simple valence MO picture is seemingly incomplete for describing these systems, because one expects to have a valence bonding MO derived from the outer s atomic orbitals for the dimers, just as in the hydrogen molecule. Removal of an electron from this MO should weaken the bond in the cation, hence diminish the D_e. This is remarkably similar to the situation for the group V elements, and should provide some important clues for an explanation of the results on the As and Sb dimers. In analogy to the alkali systems, the lower IPs in As and Sb dimers may be related to the metallic bonding property of these elements.

Generally for metal clusters, the IP decreases as a function of increasing size, approaching the bulk work function eventually. A classical spherical drop model[43] has been proposed to describe this change of IP as a function of cluster size. The following simple result was obtained for a small metal droplet:

$$IP(R) = W_\infty + \frac{3}{8}\frac{q^2}{R} \qquad (24)$$

where W_∞ is the bulk work function, q is the electron charge, and R is the radius of a cluster. This formula has has shown to describe a number of metal cluster systems to a remarkable degree,[44] including the alkali clusters. In fact, Walstedt and Bell[45] have applied Eq. (24) to Bi clusters for their electron impact ionization data, and obtained good qualitative agreement with their experimental IPs. Recently, Mahov *et al.*[46] have shown that the correct classical result for the size dependence of the IPs of spherical clusters should be the following, instead of (24):

$$IP(R) = W_\infty + \frac{1}{2}\frac{q^2}{R} \qquad (25)$$

It was concluded that Eq. (25) should account better for big clusters, while Eq. (24) fit well for small clusters due to quantum corrections to Eq. (25).

Determination of R for a particular cluster is obviously a difficult task, which requires knowledge of the atomic volume in that particular cluster. To first approximation, one could use:

$$R = n^{1/3} r_0 \qquad (26)$$

where n is the number of atoms in a cluster, and r_0 can be chosen as half of the average bulk atomic separation or half of the diatomic bond length.[44] The later is used here, and the bond lengths are the ones shown in Table 2. We found that Eq. (25) described As_n well while Eq. (24) fit better for Sb_n and Bi_n. It was not clear why Eq. (25) should fit better for As_n. Obviously, a larger data set would be desirable. The dashed curves in Figure 21 illustrate the calculated IPs of As_n, Sb_n, and Bi_n for n up to 10, with each curve converging to its bulk work function,[47] when n approaches infinity. It is seen that the IPs of As_4, and, in particular, Sb_4 deviate severely from the model. It should be emphasized that the Jahn-Teller effect profoundly altered the IPs of the tetramers. It completely

changed the geometric structure of the cluster cations, hence, their electronic structure. The Jahn-Teller distortion of the T_d symmetry in the ^2E state to D_{2d} certainly made the cluster ions less spherical. Were there no Jahn-Teller distortions in the cations, the IPs of the tetramers would have much better agreement with the model. Therefore, the agreement with the experimental IPs should still be regarded to be gratifying, considering the approximate nature of the model and the crudeness of determining the cluster radius. The model should correctly follow the experimental trends of the IP dependence for larger cluster sizes, as shown with Bi_n.[45]

5.6 Summary

The high resolution PE spectra of the dimers and tetramers of the group V elements were obtained. For the dimers, FCF calculations were carried out to analyze the PE spectra, and spectroscopic constants were derived for the molecular ions. The vibrational frequencies of the spin-orbit split $^2\Pi_{u1/2}$ and $^2\Pi_{u3/2}$ states were found to differ significantly for As_2^+. The IPs of As_2 and Sb_2 were found to be surprisingly smaller than that of the corresponding atoms, and the D_es of As_2^+ and Sb_2^+ are consequently larger than that of the respective neutrals, which were interpreted as due to the metallic bonding property of the elements in analogy with the alkali metals.

For the tetramers, vibrational structure in the $\nu_1(a_1)$ mode was fully resolved for P_4^+ and As_4^+ in the $^2A_1$ states, which enabled us to do FCF calculations for the $^2A_1$ states and obtain the bond length changes in the $^2A_1$ states of the two cationic species. Incidentally, from our FCF fitting, the ν_1 vibrational frequency of As_4 reported before was found to be too small.

The ^2E states of all three tetramers, P_4^+, As_4^+, and Sb_4^+, were found to undergo strong Jahn-Teller distortions, coupled with the $\nu_2(e)$ vibrational mode. Detailed vibronic calculations of the E⊗e Jahn-Teller problem was carried out for P_4^+ in collaboration with

Ghelichkhani and Grant. Calculations with a linear coupling constant of k=5.75 were in good agreement with the experimental results. The quadratic coupling constant was found to be rather small, resulting in quadratic barriers to pseudorotation comparable to the zero-energy. Thus, P_4^+ was completely characterized in its ground vibronic state as being not only highly distorted, but also highly fluxional. The cone-resonance phenomenon was indicated in the calculations, and limited experimental evidence for it was obtained. Linear-only calculations on As_4^+ and Sb_4^+ were also in good agreement with the experiments, though higher order couplings were required for full descriptions of these systems. The linear coupling calculations also yielded improved values of the adiabatic IPs and Jahn-Teller stabilization energies.

Both Jahn-Teller and spin-orbit effects were shown to play important roles in the $^2T_2$ states of the tetramers. The spin-orbit effect became the dominant effect in the case of Sb_4^+, while the Jahn-Teller effect was dominant in P_4^+. From the resolved vibrational structure in P_4^+, the $\nu_3(t_2)$ vibrational mode was found to be the one which was involved in the Jahn-Teller coupling, reducing the symmetry of the molecular ions from T_d to C_{2v}. Strong Ham effects were shown in the $^2T_2$ states, significantly suppressing the Jahn-Teller effect in comparison with the ^2E states, where there was no spin-orbit interaction.

A classical metal droplet model was used to fit the trends of the IPs of the clusters as a function of size. The model was shown to work reasonably well, although a larger data set with larger cluster sizes would be desirable. The severe deviation of the tetramer IPs from the model was found to be caused by the strong Jahn-Teller effect.

References

* The theoretical calculations on the E⊗e Jahn-Teller problem of the tetramers were done in collaboration with A. Ghelichkhani and E.R. Grant.

1. See for example, (a) T.P. Martin, *Phys. Rep.* **95**, 167 (1983); (b) J.C. Phillips, *Chem. Rev.* **86**, 619 (1986); (c) M.D. Morse, *Chem. Rev.* **86**, 1049 (1986); (d) W. P. Halperin, *Rev. Modern Phys.* **58**, 533 (1986); (e) D.R. Salahub, *Adv. Chem. Phys.* **69**, 447 (1987); (f) M.M. Kappes, *Chem. Rev.* **88**, 369 (1988).
2. See for example, (a) K. Raghavachari, *J. Chem. Phys.* **83**, 3520 (1985); (b) L.A. Bloomfield, R.R. Freeman, and W.L. Brown, *Phys. Rev. Lett.* **54**, 2246 (1985); (c) J.C. Phillips, *J. Chem. Phys.* **83**, 3330 (1985); (d) D. Tomanek and M.A. Schluter, *Phys. Rev.* **B36**, 1208 (1987); (e) K. Balasubramanian, *Chem. Phys. Lett.* **135**, 283 (1987); (f) J.L. Elkind, J.M. Alford, F.D. Weiss, R.T. Laaksonen, and R.E. Smalley, *J. Chem. Phys.* **87**, 2397 (1987); (g) M.L. Mandich, W.D. Reents, Jr., and M.F. Jarrold, *J. Chem. Phys.* **88**, 1703 (1988); (h) J. C. Phillips, *J. Chem. Phys.* **88**, 2090 (1988).
3. See for example, (a) T.P. Martin and H. Schaber, *J. Chem. Phys.* **83**, 855 (1985); (b) S.C. O'Brien, Y. Lin, Q. Zhang, J.R. Heath, F.K. Tittel, R.F. Curl, and R.E. Smalley, *J. Chem. Phys.* **84**, 4074 (1986); (c) K. Balasubramanian, *J. Chem. Phys.* **86**, 3410 (1987); (d) J.C. Phillips, *J. Chem. Phys.* **87**, 1712 (1987); (e) W. Schulze, B. Winter, and I. Goldenfeld, J. *Chem. Phys.* **87**, 2402 (1987); (f) L.B. Knight, Jr. and J.T. Petty, *J. Chem. Phys.* **88**, 481 (1988).
4. See for example, J.W. Rabalais, *Principles of Ultraviolet Photoelectron Spectroscopy* (Wiley, New York, 1977).
5. (a) O. Cheshnovsky, S.H. Yang, C.C. Pettiette, M.J. Craycraft, and R.E. Smalley, *Rev. Sci. Instrum.* **58**, 2131 (1987); (b) K. M. Ervin, J. Ho, and W.C. Lineberger, *J. Chem. Phys.* **89**, 4514 (1988).

6. K. Rademann, *Ber. Bunsenges. Phys. Chem.* **93**, 653 (1989).

7. (a) L.S. Wang, B. Niu, Y.T. Lee, and D.A. Shirley, *Chem. Phys. Lett.* **158**, 297 (1989); (b) L.S. Wang, B. Niu, Y.T. Lee, D.A. Shirley, and K. Balasubramanian, *J. Chem. Phys.* **92**, 899 (1990).

8. L.S. Wang, J.E. Reutt-Robey, B. Niu, Y.T. Lee, and D.A. Shirley, J. *Electron Spectrosc. Relat. Phenom.*, 1990 (in press). LBL-27583.

9. A.N. Nesmeyanov, R. Gary (ed.), *Vapor Pressure of the Chemical Elements* (Elsevier, Amsterdam, 1957).

10. (a) D.P. DiLella, K.V. Taylor, and M. Moskovits, *J. Phys. Chem.* **87**, 524 (1983); (b) M.D. Morse, J.B. Hopkins, P.R.R. Langridge-Smith, and R.E. Smalley, *J. Chem. Phys.* **79**, 5316 (1983); (c) T.C. Thompson, D.G. Truhlar, and C.A. Mead, *J. Chem. Phys.* **82**, 2392 (1985); (d) W.H. Crumley, J.S. Hayden, and J.L. Gole, *J. Chem. Phys.* **84**, 5250 (1986).

11. (a) A. Herrmann, M. Hofmann, S. Leutwyler, E. Schumacher, and L. Woste, *Chem. Phys. Lett.* **62**, 216 (1979); (b) J.L. Gole, G.J. Green, S.A. Pace, and D.R. Preuss, *J. Chem. Phys.* **76**, 2247 (1982); (c) S.C. Ritchtsmeler, M.L. Hendewerk, D.A. Dixon, and J.L. Gole, *J. Phys. Chem.*, **86**, 3932 (1982); (d) M. Broyer, G. Delacretaz, P. Labastie, J.P.Wolf, and L. Woste, *Phys. Rev. Lett.* **57**, 1851 (1986); (e) M. Broyer, G. Delacretaz, G.Q. Ni, R.L. Whetten, J.P. Wolf, and L. Woste, *Phys. Rev. Lett.*, **62**, 2100 (1989).

12. (a) W.H. Gerber, abd E. Schumacher, *J. Chem. Phys.* **69**, 1692 (1978); (b) J.L. Gole, R.H. Childs, D.A. Dixon, and R.A. Eades, *J. Chem. Phys.* **72**, 6368 (1980); (c) R.A. Eades, M.L. Hendewerk, R. Frey, D.A. Dixon, and J.L. Gole, *J. Chem. Phys.* **76**, 3075 (1982); (d) J.L. Martins, R. Car, and J. Buttet, *J. Chem. Phys.* **78**, 5646 (1983); (e) T.C. Thompson, G. Izmirlian, Jr., S.J. Lemon, D.G. Truhlar, and C. A. Mead, *J. Chem. Phys.* **82**, 5597 (1985); (f) J.D. Wolf, G. Delacretaz, and L. Woste, *Phys. Rev. Lett.* **63**, 1946 (1989).

13. H.A. Jahn and E. Teller, *Proc. Roy. Soc.* **A161**, 220 (1937).

14. (a) S. Evans, P.J. Joachim, A.F. Orchard, and D.W. Turner, *Int. J. Mass Spectrom. Ion Phys.* **9**, 41 (1972); (b) C.R. Brundle, N.A. Kuebler, M.B. Robin, and H. Basch, *Inorg. Chem.* **11**, 20 (1972); (c) H. Bock and H. Muller, *Inorg. Chem.* **23**, 4365 (1984).

15. (a) S. Elbel, H.T. Dieck, H. Walther, and J. Krizek, *Inorg. Chim. Acta* **53**, L101 (1981); (b) J.M. Dyke, S. Elbel, A. Morris, and J.C.H. Stevens, *J.Chem. Soc. Faraday Trans.* II **82**, 637 (1986).

16. J.M. Dyke, A. Morris, and J.C.H. Stevens, *Chem. Phys.* **102**, 29 (1986).

17. S. Elbel, J. Kudnig, M. Grodzicki, and H.J. Lempka, *Chem. Phys. Lett.* **109**, 312 (1984).

18. S. Suzer, S.T. Lee, and D.A. Shirley, *J. Chem. Phys.* **65**, 412 (1976).

19. (a) M.F. Guest, I.H. Hillier, and V.R. Saunders, *J. Chem. Soc. Faraday Trans* II **68**, 2070 (1972); (b) G. Trinquier, J.P. Malrieu, and J.P. Daudey, *Chem. Phys. Lett.* **80**, 552 (1981); (c) U. Wedig, H. Stoll, and H. Preuss, *Chem. Phys.* **61**, 117 (1981); (d) K. Raghavachari, R.C. Haddon, and J.S. Binkley, *Chem. Phys. Lett.* **122**, 219 (1985).

20. (a) J. Andzelm, N. Russo, and D.R. Salahub, *Chem. Phys. Lett.* **142**, 169 (1987); (b) K. Balasubramanian, *J. Mol. Spectrosc.* **121**, 465 (1987).

21.J.E. Pollard, D.J. Trevor, Y.T. Lee, and D.A. Shirley, *Rev. Sci. Instrum.* **52**, 1837 (1981).

22. J.J. Yeh and I. Lindau, *Atmoic Data and Nuclear Data Tables* **32**, 1 (1985).

23. K. Manzel, U. Engelhardt, H. Abe, W. Schulze, and F.W. Froben, *Chem. Phys. Lett.* **77**, 514 (1981).

24. K. Balasubramanian, *Chem. Phys.* **119**, 41 (1988).

25. G. Herzberg, *Molecular Spectra and Molecular Structure III. Electronic Spectra and Electronic Structure of Polyatomic Molecules* (Van Nostrand Reinhold, New York, 1966).

26. (a) I.B. Bersuker, *The Jahn-Teller Effect and Vibronic Interactions in Modern Chemistry* (Plenum Pree, New York, 1984); (b) U. Opik and M.H.L. Pryce, *Proc. Roy. Soc.* **A238**, 425 (1957); (c) H.C. Longuet-Higgins, U. Opik, M.H.L. Pryce, and R.A. Sack, *Proc. Roy. Soc.* **A244**, 1 (1958); (d) H.C. Longuet-Higgins, *Adv. Spectrosc.* **2**, 429 (1961); (e)B.R. Judd, *Adv. Chem. Phys.* **57**, 247 (1984); (f) H. Koppel, W. Domcke, and L.S. Cederbaum, *Adv. Chem. Phys.* **57**, 59 (1984).

27. (a) M. Wagner, *Z. Phys.* **230**, 460 (1970); (b) M.D. Sturge, *Solid State Phys.* **20**, 91 (1967).

28. A.D. Liehr, *J. Phys. Chem.* **67**, 389, 471 (1963).

29. F.S. Ham, *Phys. Rev.* **A138**, 1727 (1965).

30. J.H. Van Vleck, *Physica* **26**, 544 (1960).

31. A.D. Liehr, *Ann. Rev. Phys. Chem.* **13**, 41 (1962).

32. (a) R.L. Whetten, G.S. Ezra, and E.R. Grant, *Ann. Rev. Phys. Chem.* **36**, 277 (1985); (b) J.W. Zwanziger, E.R. Grant, and G.S. Ezra, *J. Chem. Phys.* **85**, 2089 (1986); (c) J.W. Zwanziger and E.R. Grant, J. *Chem. Phys.* **90**, 2357 (1989); (d) H. Koppel, L.S. Cederbaum, W. Domcke, S.S. Shaik, *Angew. Chem. Int. Ed.* **22**, 210 (1983).

33. J.W. Zwanziger and E.R. Grant, *J. Chem. Phys.* **87**, 2954 (1987).

34. H. Koppel, E.Haller, L.S. Cederbaum, and W. Domcke, *Mol. Phys.* **41**, 669 (1980).

35. R.L. Whetten, K.S. Maber, and E.R. Grant, *J. Chem. Phys.* **84**, 1270 (1986).

36. (a) S.B. Brumbach and G.M. Rosenblatt, *J. Chem. Phys.* **56**, 3110 (1972); (b) V.E. Bondybey, G.P. Schwartz, and J.E. Griffiths, *J. Mol. Spectrosc.* **89**, 328 (1981).

37. G. Herzberg, *Molecular Spectra and Molecular Structure II. Infrared and Raman Spectra of Polyatomic Molecules* (Van Nostrand Reinhold, New York, 1945).

38. H.S. Gutowsky and L.J. Hoffman, J. *Am. Chem. Soc.* **72**, 5751 (1950).

39. C.E. Moore, *Tables of Atomic Energy Levels* (U.S. National Bureau of Standards, Washington D.C., 1971).

40. K.P. Huber and G. Herzberg, *Molecular Spectra and Molecular Structure IV. Constants of Diatomic Molecules* (Van Nostrand Reinhold, New York, 1979).

41. N.W. Ashcroft and N.D. Mermin, *Solid State Physics* (Saunders College, Philadelphia, 1976).

42. S. Leutwyler, M. Hofmann, H.P. Harri, and E. Schumacher, *Chem. Phys. Lett.* **77**, 257 (1981).

43. D.M. Wood, *Phys. Rev. Lett.* **46**, 749 (1981).

44. (a) M.M. Kappes, M. Schar, P. Radi, and E. Schumacher, *J. Chem. Phys.* **84**, 1863 (1986); (b) D.G. Leopold, J. Ho, and W.C. Lineberger, *J. Chem. Phys.* **86**, 1715 (1987).

45. R.E. Walstedt and R.F. Bell, *Phys. Rev.* **A33**, 2830 (1986).

46. G. Makov, A. Nitzan, and L.E. Brus, *J. Chem. Phys.* **88**, 5076 (1988).

47. R.C. Weast, M.J. Astle, and W.H. Beyer, Eds., *CRC Handbook of Chemistry and Physics, 67th edition* (CRC Press, Boca Raton, 1986).

48. D.R. Pooler, in *The Dynamical Jahn-Teller Effect in Localized Systems*, Y.E. Perlin and Wagner, eds, (Elsevier, New York, 1984).

Table 1. Experimental conditions.

	T (K)[a]	P (Torr)[b]	ϕ (mm)[c]	Starting materials[d]
P_4	620	500 (He)	0.16	Pure red phosphorus
As_2	1400	350 (Ne)	0.13	Cu_3As
As_4	650	200 (He)	0.16	Pure arsenic
Sb_2	1150	600 (Ne)	0.13	Pure antimony
Sb_4	1150	600 (Ne)	0.13	Pure antimony
Bi_2	1100	500 (Ne)	0.13	Pure bismuth

a. Oven temperature (±50 K).

b. Carrier gas pressure.

c. Nozzle diameter.

d. Samples were all purchased from CERAC.

Table 2. The spectroscopic constants[a] for As_2^+, Sb_2^+, and Bi_2^+.

	ω_e (cm^{-1})	r_e (eV)	D_e (eV)	IPa (eV)[b]	IPv (eV)[c]
As_2					
$^1\Sigma_g^+$	429.55	2.1026	3.96		
As_2^+					
$^2\Pi_{u3/2}$	400(6)	2.23(1)	4.17	9.580(6)	9.779(6)
$^2\Pi_{u1/2}$	380(6)	2.24(1)		9.810(6)	9.994(6)
$^2\Sigma_g^+$	390(6)	2.118(3)		10.230(5)	
Sb_2					
$^1\Sigma_g^+$	269.98	2.3415	3.09		
Sb_2^+					
$^2\Pi_{u3/2}$			(3.23)	(8.5)	(8.7)
$^2\Pi_{u1/2}$				(8.9)	(9.1)
$^2\Sigma_g^+$				9.275(5)	
Bi_2					
$^1\Sigma_g^+$	172.71	2.6596	2.04		
Bi_2^+					
$^2\Pi_{u3/2}$	(140)	(2.86)	1.89	7.440(7)	7.623(7)
$^2\Pi_{u1/2}$	(140)	(2.84)		8.865(7)	8.991(7)
$^2\Sigma_g^+$	150(5)	2.701(3)		9.991(5)	

a. Values for the neutrals are from Ref. 40.

b. Adiabatic ionization potential.

c. Vertical ionization potential.

Table 3. Ground state vibrational frequencies (cm^{-1}) of P_4, As_4, and Sb_4.

	P_4[a]	As_4[b]	Sb_4[c]
$\nu_1(a_1)$	606	344	241
$\nu_2(e)$	363	210	140
$\nu_3(t_2)$	464.5	255	179

a. From Ref. 38.

b. From Ref. 36(a).

c. From Ref. 36(b).

Table 4. Ionization potentials (IP) and the observed vibrational spacings (VS) in the PE spectra of P_4, As_4, and Sb_4.

		IPa (eV)[a]	IPv (eV)[b]	VS (cm^{-1})
P_4	$(1e)^{-1}$	8.95 [9.1]	9.46(1)	315(10)
			9.92(1)	275(10)
	$(2t_2)^{-1}$		10.36(1)	400(10)
			10.53(1)	(370)
			10.72(2)	
	$(2a_1)^{-1}$	11.776(3)	11.847(3)	576(3)
As_4	$(1e)^{-1}$	7.83 [8.4]	8.75(1)	
			9.16(1)	
	$(2t_2)^{-1}$		9.76(2)	(240)
			9.97(1)	(290)
			10.11(3)	
	$(2a_1)^{-1}$	11.017(3)	11.058(3)	350(5)
Sb_4	$(1e)^{-1}$	6.61 [7.5]	7.85(1)	
			8.27(1)	
	$(2t_2)^{-1}$		8.69(1)	
			9.09(1)	
			9.22(3)	
	$(2a_1)^{-1}$	9.8	9.89(1)	

a. Adiabatic IP, evaluated from vibronic calculations (see Section 5.4.3). The values in the square parentheses are estimated upper limits from the observed PE spectrum thresholds.

b. Vertical IP.

Table 5. Ionization potentials (IP) and assignments of the $P_4^+ {}^2A_1$ state.

IP (eV)	Interval (meV)	v (ν_1)[a]
11.700(3)		Hot band (1→0)
11.777(3)	77	0
11.847(3)	70	1
11.916(3)	69	2
11.985(3)	69	3
12.053(4)	68	4
12.121(4)	68	5

a. Vibrational quanta of the ν_1 mode.

Table 6. Ionization potentials and assignments of the As_4^+ $^2A_1$ state.

IP (eV)	Interval (meV)	v (ν_1)[a]
10.929(3)		Hot band (2→0)
10.973(3)	44	Hot band (1→0)
11.017(3)	44	0
11.058(3)	41	1
11.098(3)	40	2
11.138(3)	40	3
11.175(4)	37	4
11.210(5)	35	5

a. Vibrational quanta of the ν_1 mode.

Table 7. Spectroscopic constants of the $^2A_1$ states of P_4^+ and As_4^+.

		ω_e (ν_1) (cm^{-1}) [a]	r_{m-m} (Å) [b]
P_4	$^1A_1$	610(10) [c]	2.21 [d]
P_4^+	$^2A_1$	577(5) [c]	2.264 [e]
As_4	$^1A_1$	360(6) [c]	2.435 [d]
As_4^+	$^2A_1$	350(6) [c]	2.495 [f]

a. Vibrational frequency of the ν_1 mode.

b. Equilibrium bond distance between two atoms.

c. From this work.

d. From Ref. 19(b).

e. Franck-Condon factor calculations yielded the change of r_{m-m}, which was 0.054 ± 0.003 Å.

f. Franck-Condon factor calculations yielded the change of r_{m-m}, which was 0.060 ± 0.003 Å.

Figure Captions

Figure 1 The HeI photoelectron spectrum of As_2^+.

Figure 2 The HeI photoelectron spectrum of Sb_2^+. The $^3P_2$, $^3P_1$, and $^3P_0$ peaks shown are the subtracted atomic lines. The $^2\Pi_{u1/2}$ and $^2\Pi_{u3/2}$ bands have large contributions from Sb_4^+ $(2t_2)^{-1}$ bands.

Figure 3 The HeI photoelectron spectrum of Bi_2^+. The arrows indicate positions of the three subtracted atomic lines ($^3P_2$, $^3P_1$, and $^3P_0$).

Figure 4 The HeI photoelectron spectrum of P_4^+.

Figure 5 The HeI photoelectron spectrum of As_4^+.

Figure 6 The HeI photoelectron spectrum of Sb_4^+. The arrow indicates the $^2\Sigma_g^+$ band of Sb_2^+. The atomic lines were subtracted as in Figure 2. The $(2t_2)^{-1}$ bands have some contributions from the $^2\Pi_{u1/2}$ and $^2\Pi_{u3/2}$ bands of Sb_2^+.

Figure 7 The normal modes of vibration for tetrahedral M_4 molecules. The x, y, and z axes are along the three two-fold axes.

Figure 8 The $(1e)^{-1}$ and $(2t_2)^{-1}$ bands of the P_4^+ spectrum. Three Voigt functions are drawn to show the three components in the $(2t_2)^{-1}$.

Figure 9 The $(1e)^{-1}$ and $(2t_2)^{-1}$ bands of the As_4^+ spectrum. Three Voigt functions are drawn to show the three components in the $(2t_2)^{-1}$.

Figure 10 The $(1e)^{-1}$ and $(2t_2)^{-1}$ bands of the Sb_4^+ spectrum. Three Voigt functions are drawn to show the three components in the $(2t_2)^{-1}$.

Figure 11 Diagram showing the adiabatic potential energy surfaces of the linear E⊗e Jahn-Teller Hamiltonian. $E(\rho,\phi)$ is plotted according to Eq. (3), for $k = 5.75$, a value deduced from spectral simulations to be that most appropriate for P_4^+. The floor of the potential lies at an energy of 16.5, in units of the zeroth-order harmonic frequency, below the conical intersection.

Figure 12 Correlation diagram showing the relative energies of the exact vibronic levels of the linear E⊗e Hamiltonian as a function of the distortion parameter, $D = 1/2k^2$. $|j| = 1/2$ harmonics of the radial oscillator are shown as solid lines. Other curves trace the $|j| > 1/2$ states of excited pseudorotation. In the linear limit, only transitions to states of the $|j| = 1/2$ block are allowed. Higher-order coupling mixes levels as j mod 3, altering the correlation diagram by avoided crossings and the spectrum by intensity sharing.

Figure 13 Linear Jahn-Teller fit to the vibronic profile of the $(1e)^{-1}$ band of the PE spectrum of P_4^+. The linear coupling parameter, k, in units for which the harmonic force constant is 1, is 5.75. The progression of transitions to $j = 1/2$ radial harmonics originates at an adiabatic ionization energy of 8.95 eV. Positions and intensities were obtained at the converged eigenvalues and eigenvectors of Eq. (6) for $g = 0$, diagonalized exactly in a basis of 800 two-dimensional harmonic oscillator wavefunctions.

Figure 14 Spectral simulations of P_4^+ spectrum constructed by convoluting theoretical positions and intensities (sticks), calculated for $k = 5.75$ and g from 0 to 0.1, with a 15 meV FWHM Gaussian instrumental function. Theoretical positions and intensities for $g > 0$ were obtained by diagonalizing Eq. (6) iteratively in a basis of 1302 isotropic two-dimensional harmonic oscillator wavefunctions using the Lanczos method.[48] (a) $g = 0$; (b) $g = 0.005$; (c) $g = 0.008$; (d) $g = 0.01$; (e) $g = 0.02$; (f) $g = 0.05$; (g) $g = 0.1$.

Figure 15 Diagram illustrating the adiabatic potential energy surfaces of the linear plus quadratic E⊗e Jahn-Teller Hamiltonian. $E(\rho,\phi)$ is plotted according to Eq. (18), for $k = 5.75$ and $g = 0.02$. The floor of the potential is modulated by three barriers that extend to a height of 0.66 in units of the zeroth-order harmonic frequency.

Figure 16 Linear Jahn-Teller fit to the $(1e)^{-1}$ band of the As_4^+ PE spectrum. The linear coupling parameter, k, in units for which the harmonic force constant is 1, is 9.7. The progression of transitions to j = 1/2 radial harmonics originates at an adiabatic ionization energy of 7.83 eV. Positions and intensities were obtained as in Figure 13.

Figure 17 Linear Jahn-Teller fit to the $(1e)^{-1}$ band of the Sb_4^+ PE spectrum. The linear coupling parameter, k, in units for which the harmonic force constant is 1, is 12.5. The progression of transitions to j = 1/2 radial harmonics originates at an adiabatic ionization energy of 6.61 eV. Positions and intensities were obtained as in Figure 13.

Figure 18 Configuration-coordinate diagram showing the transitions from the ground state to a Jahn-Teller split $^2T_2$ state of a tetrahedral M_4 molecule coupled with the $\nu_3(t_2)$ vibrations: (a) zero spin-orbit splitting; (b) strong spin-orbit splitting.

Figure 19 Comparison of calculated Franck-Condon factors with the experiment of P_4^+ $^2A_1$ state. (— calculation, ... experiment).

Figure 20 Comparison of calculated Franck-Condon factors with the experiment of As_4^+ $^2A_1$ state. (— calculation, ... experiment).

Figure 21 Ionization potentials as a function of cluster size for the group V elements. (— experiments, - - - calculated according to Eq. (24) and (25), see the text).

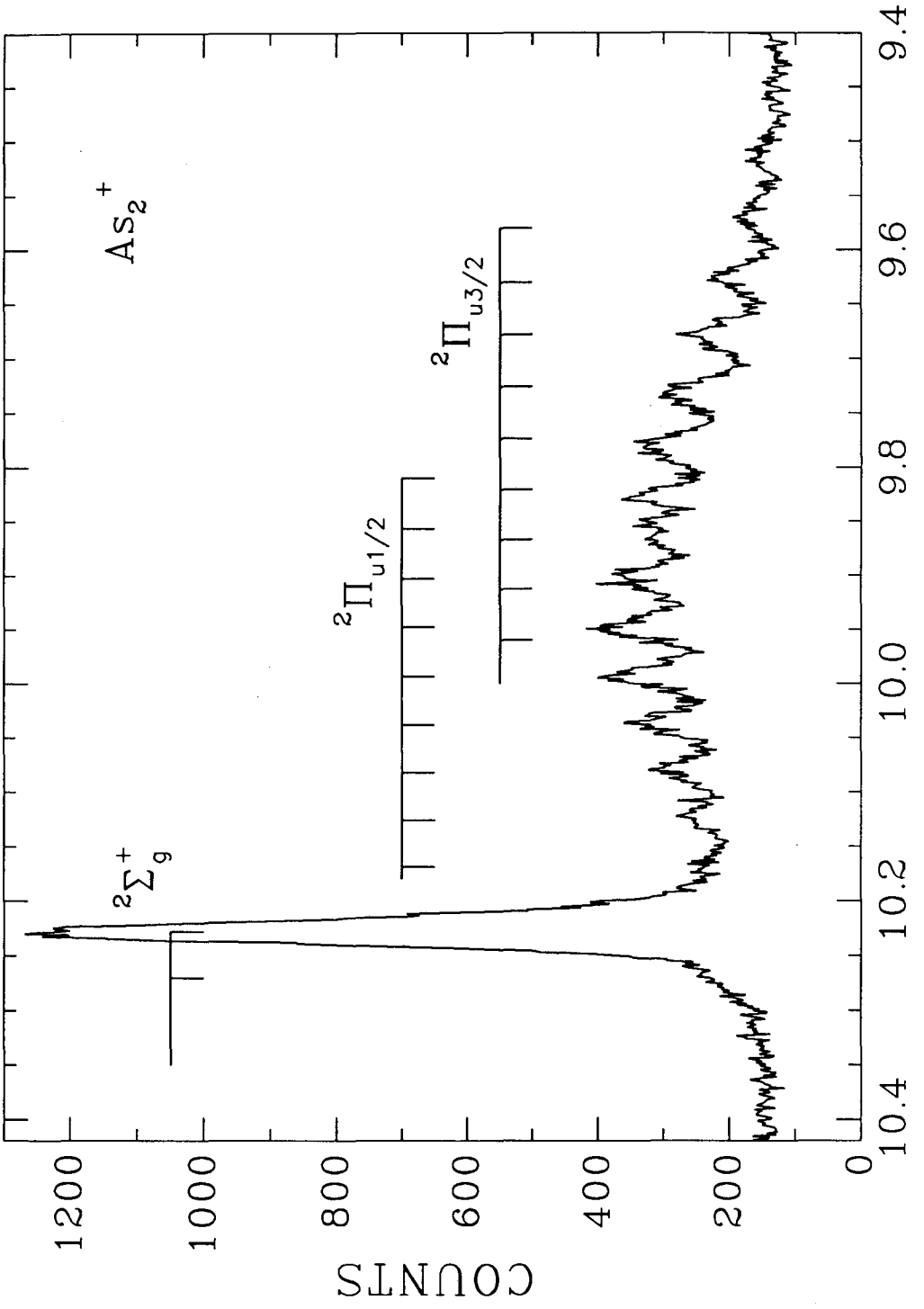

XBL 902-401

Figure 1

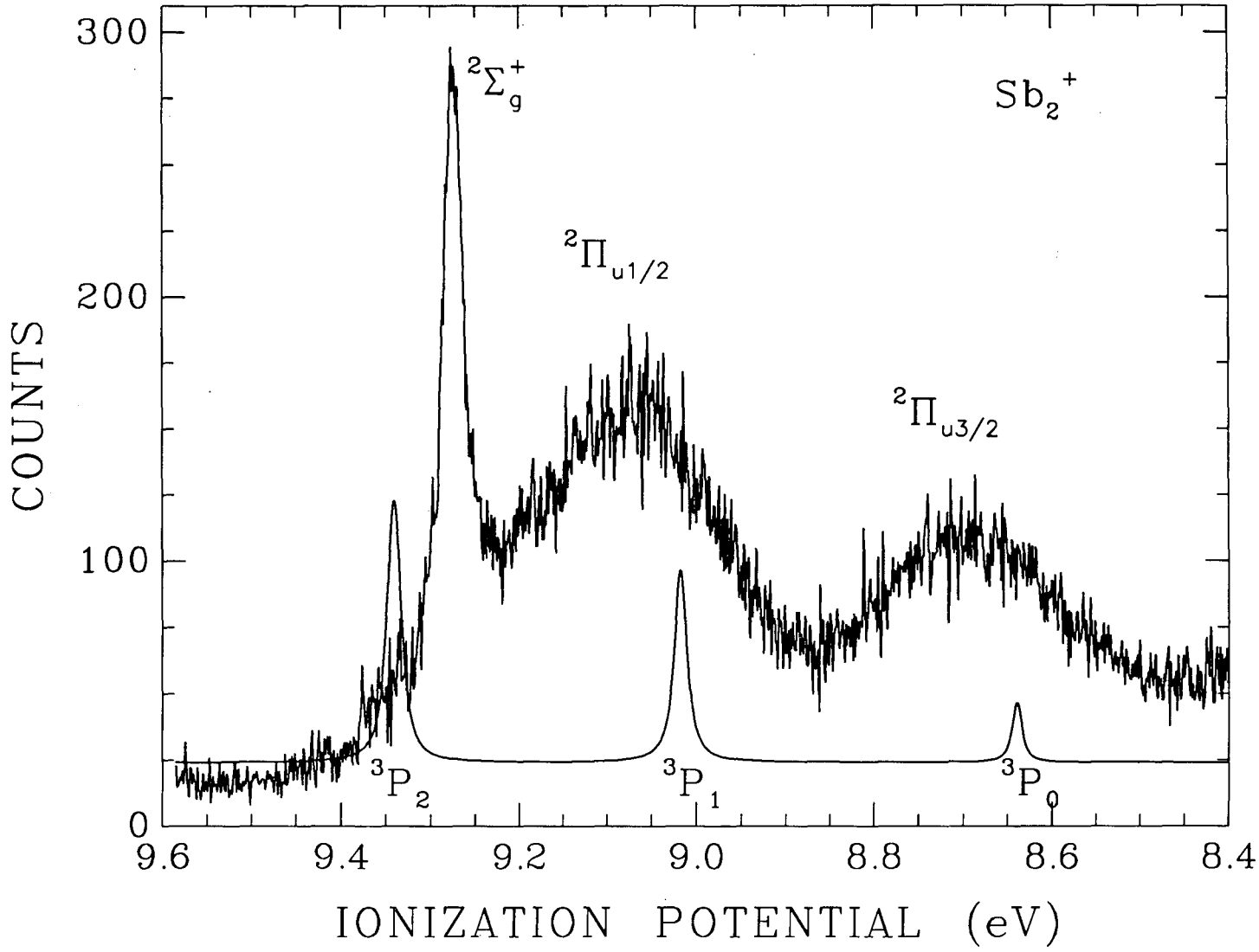

XBL 902-402

Figure 2

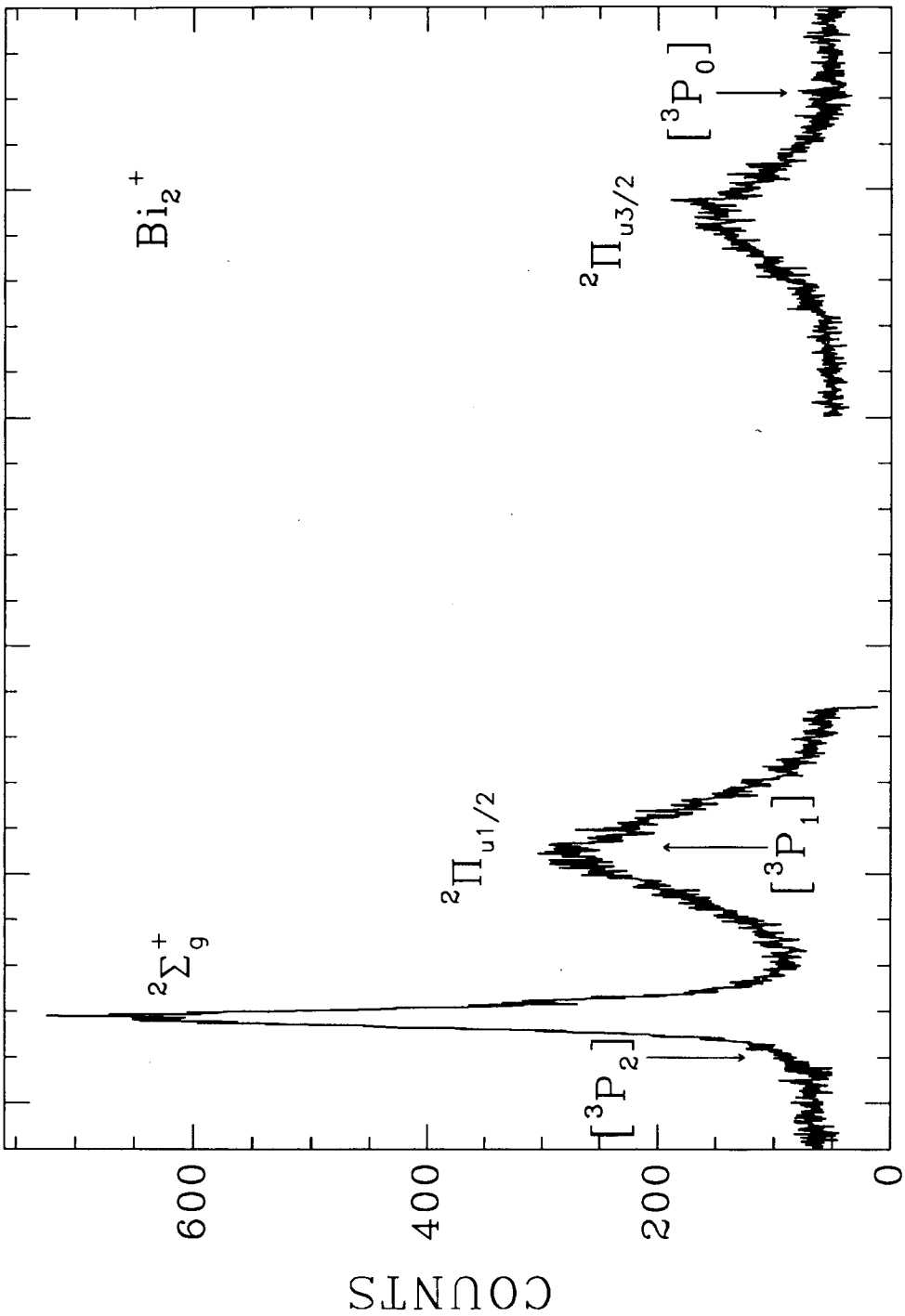

XBL 902-403

Figure 3

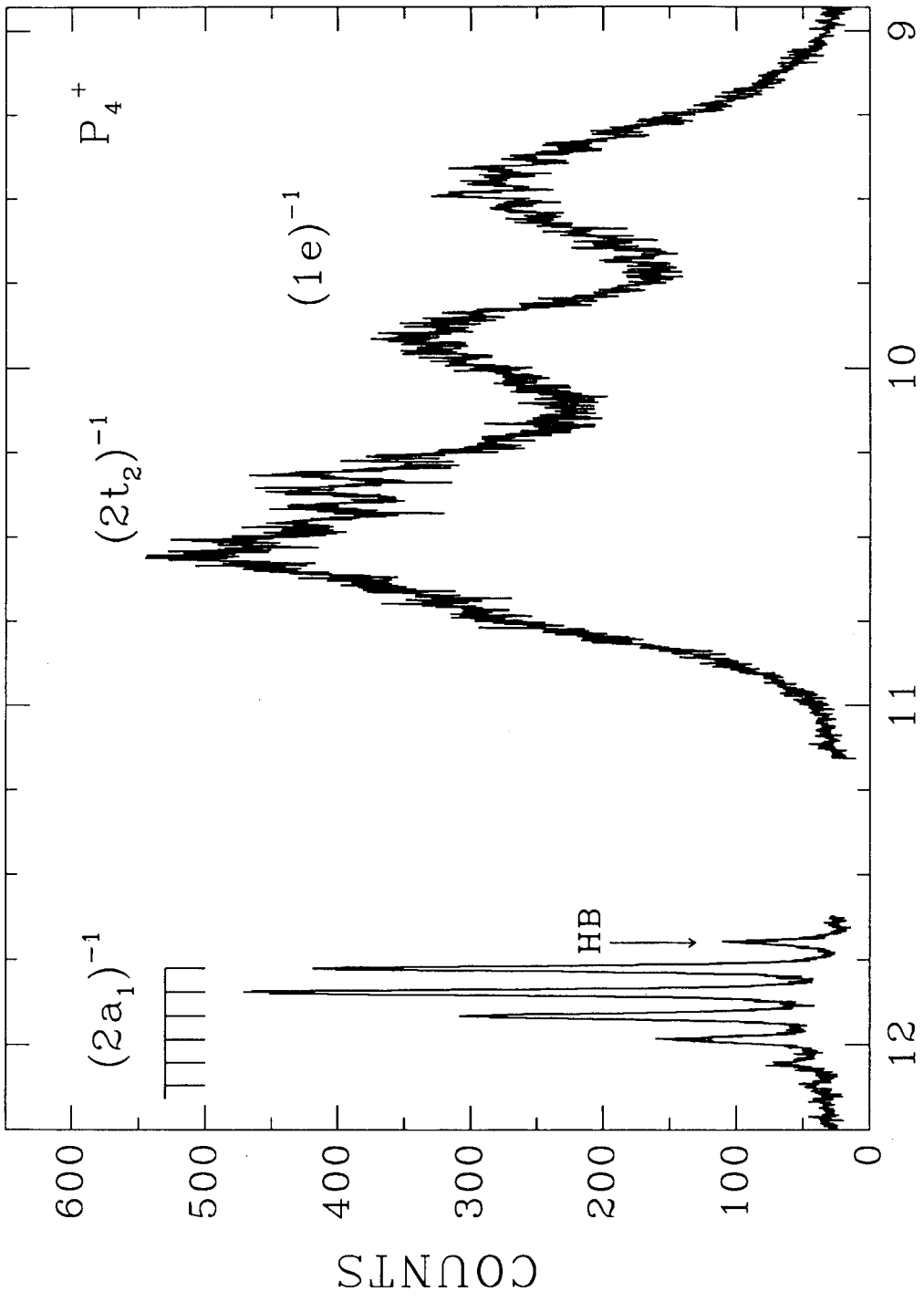

XBL 902-404

Figure 4

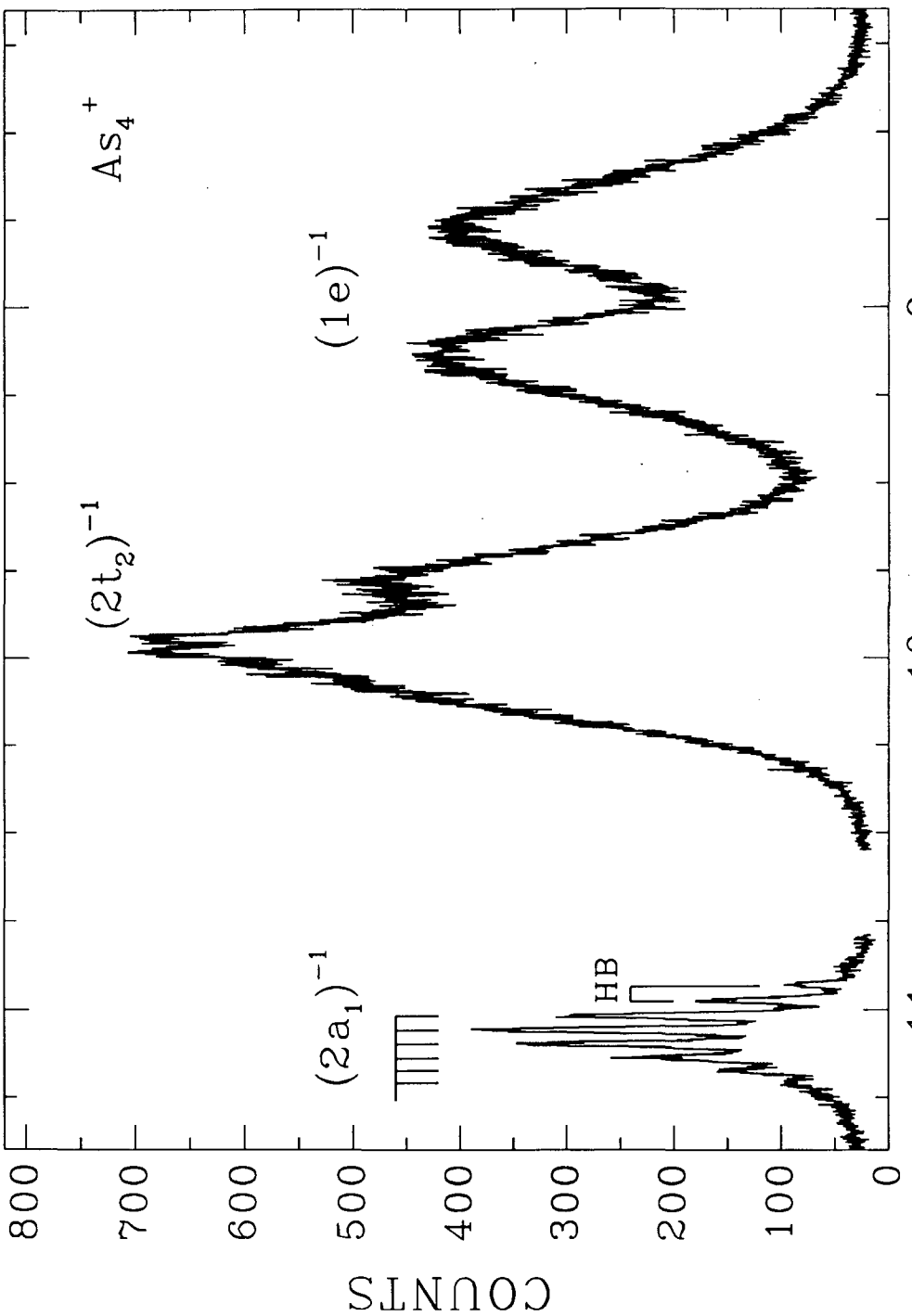

Figure 5

XBL 902-405

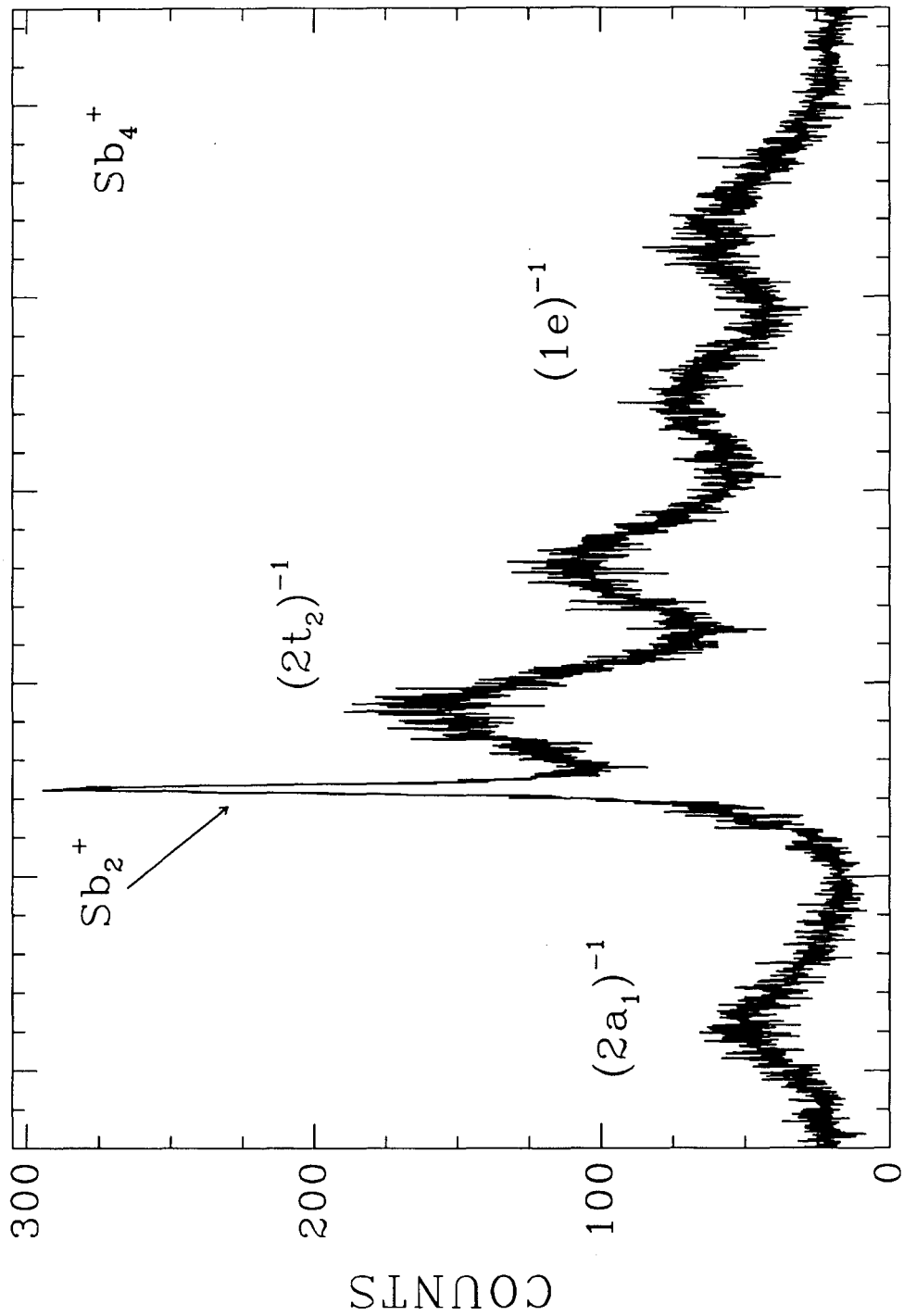

XBL 902-406

Figure 6

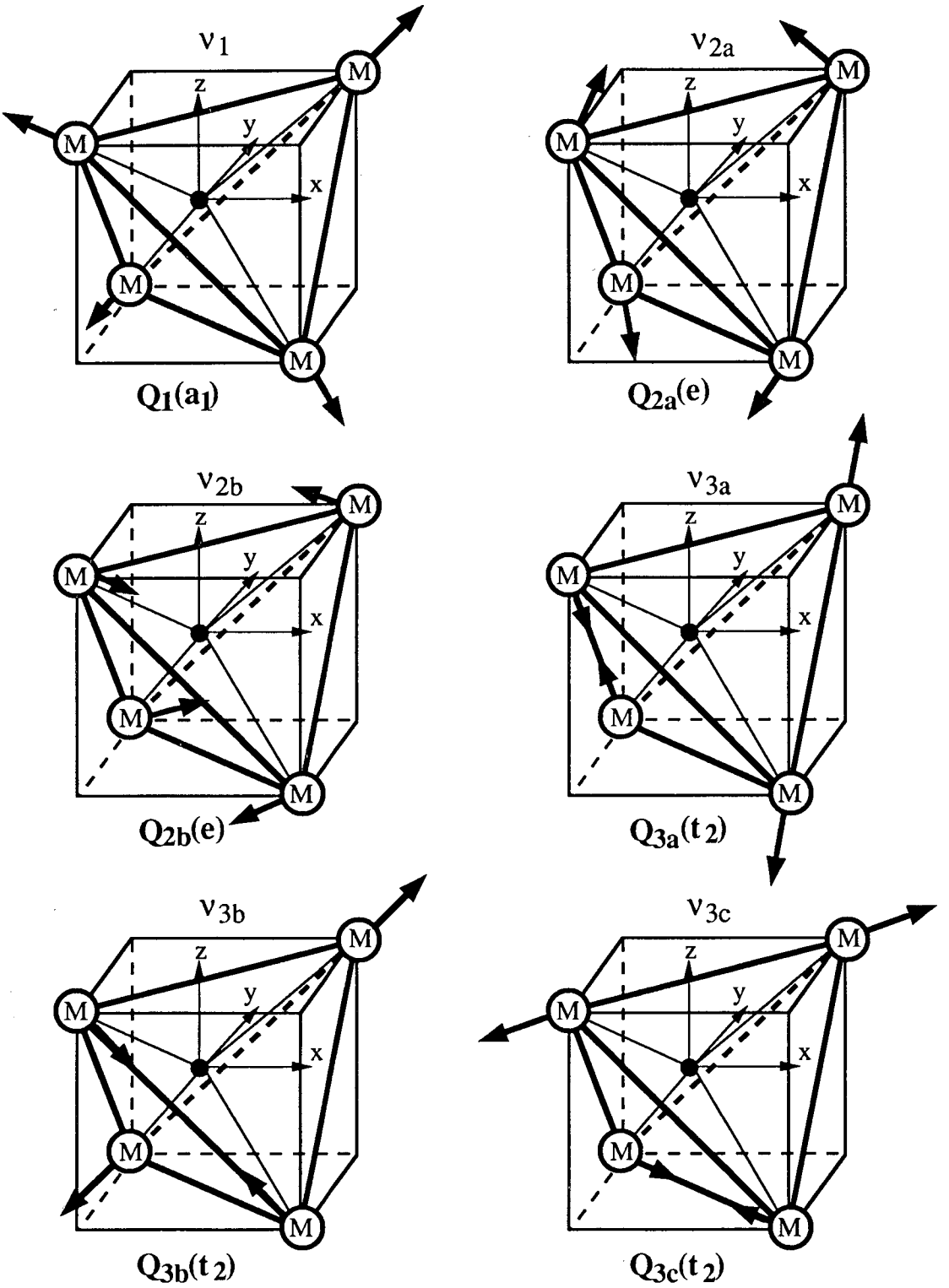
ν1
z
y
x
M
M
M
M
Q1(a1)
ν2a
Q2a(e)
ν2b
Q2b(e)
ν3a
Q3a(t2)
ν3b
Q3b(t2)
ν3c
Q3c(t2)

Figure 7

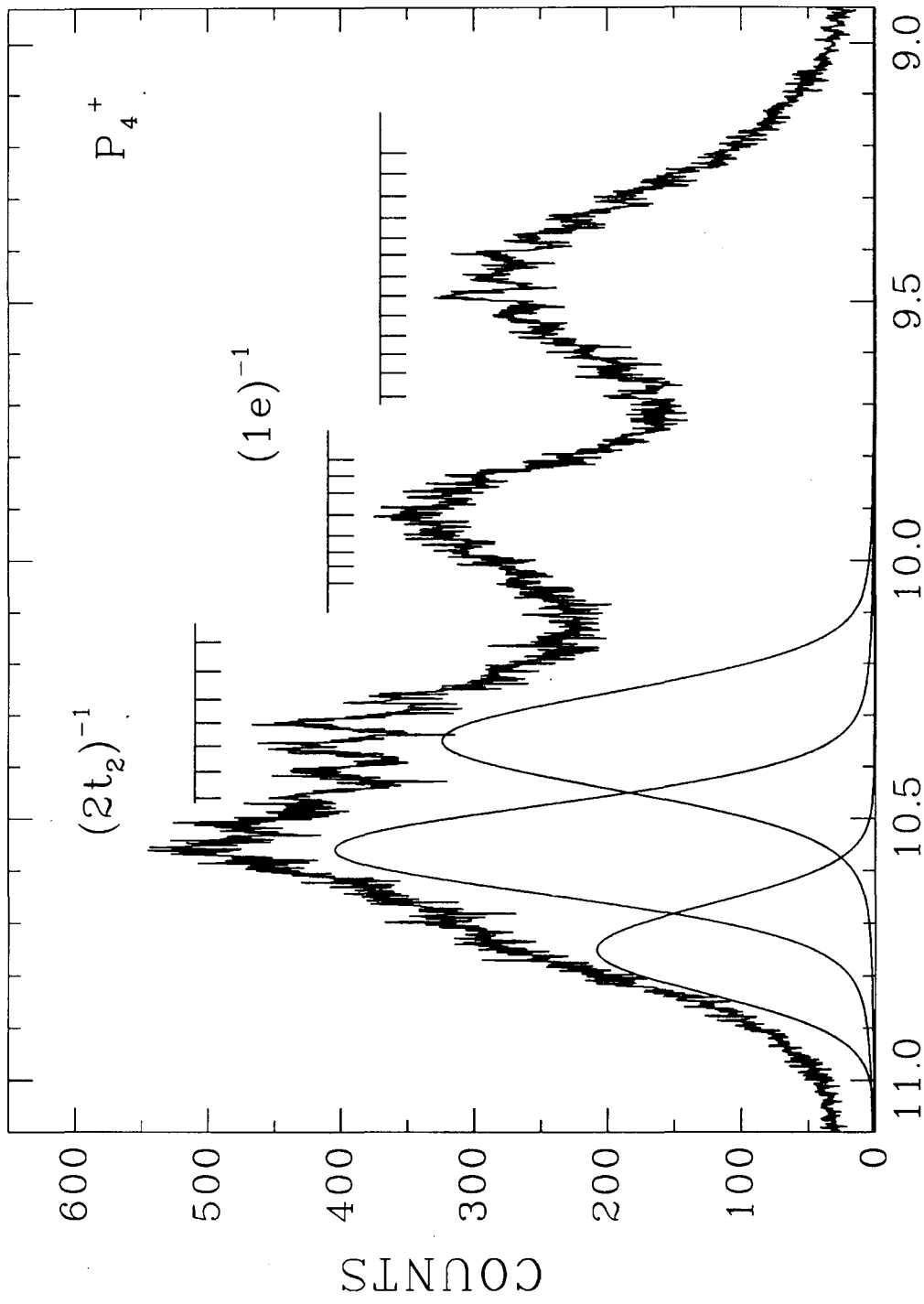

XBL 902-407

Figure 8

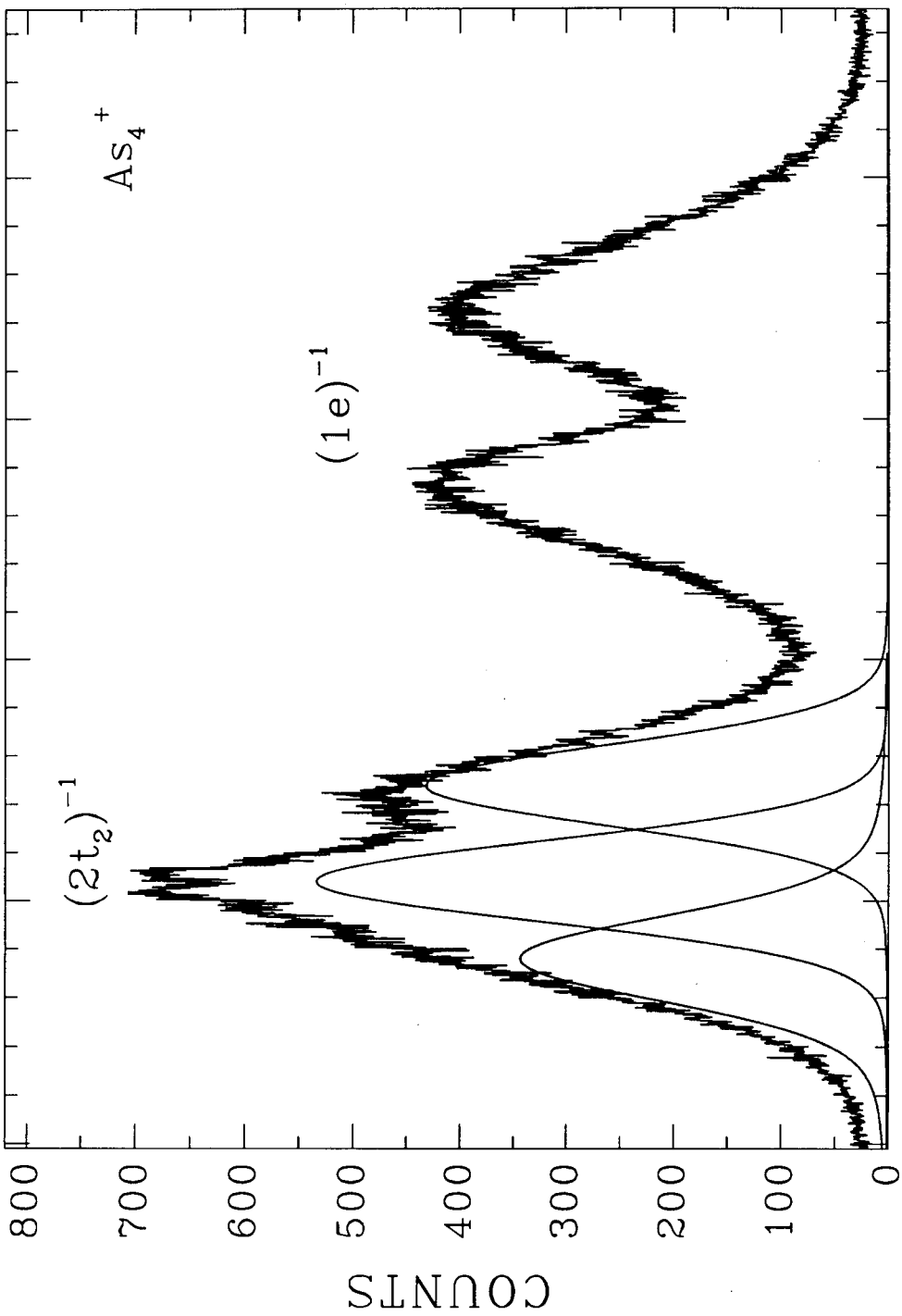

XBL 902-408

Figure 9

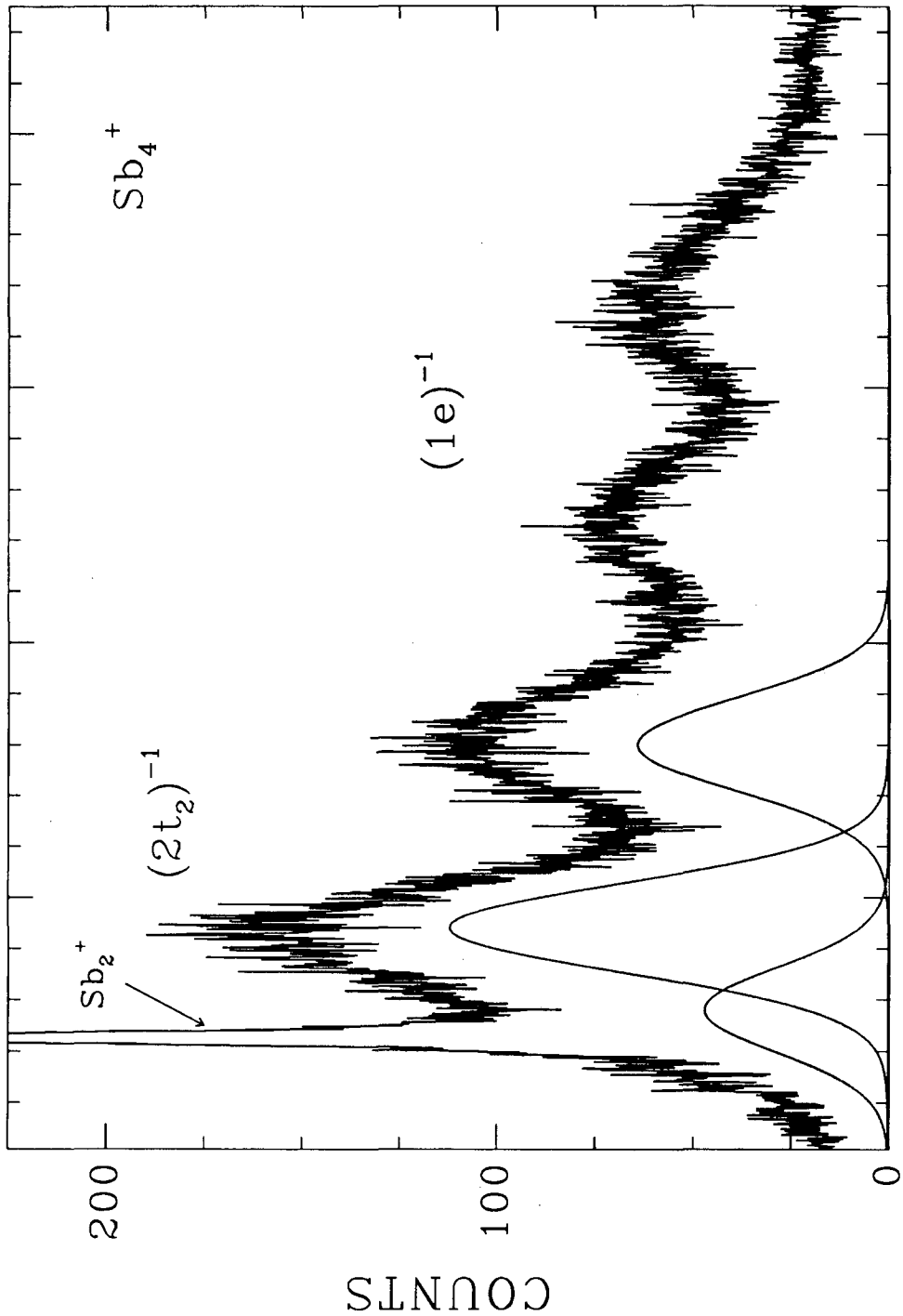

XBL 902-409

Figure 10

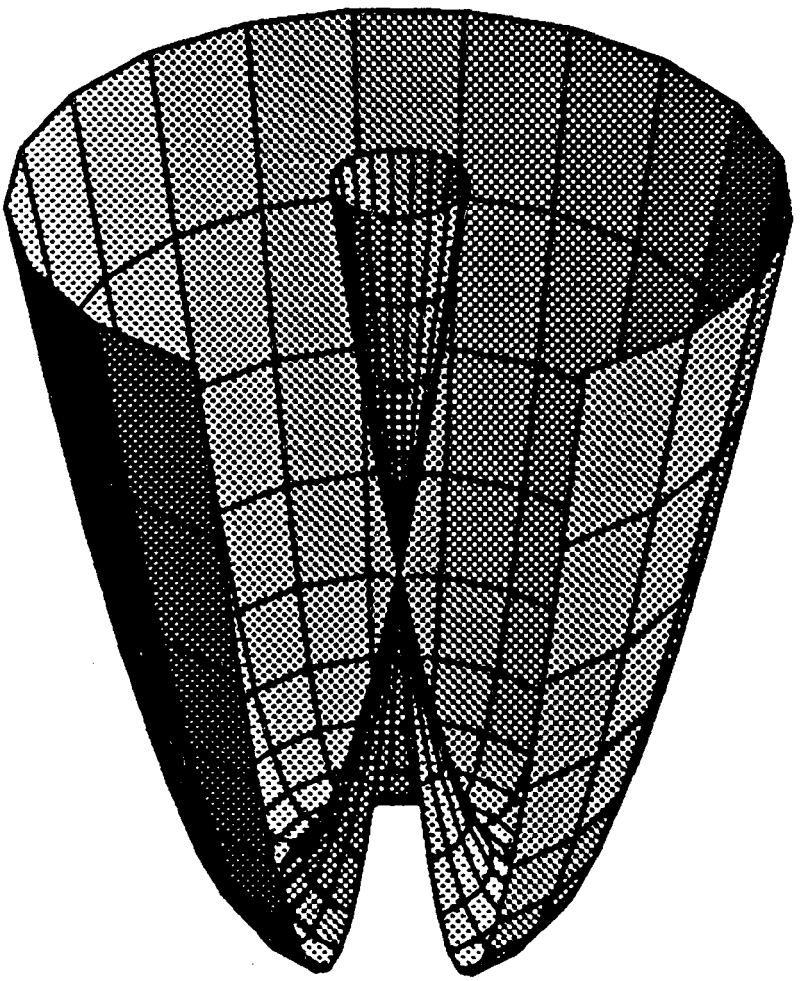

XBL 902-410

Figure 11

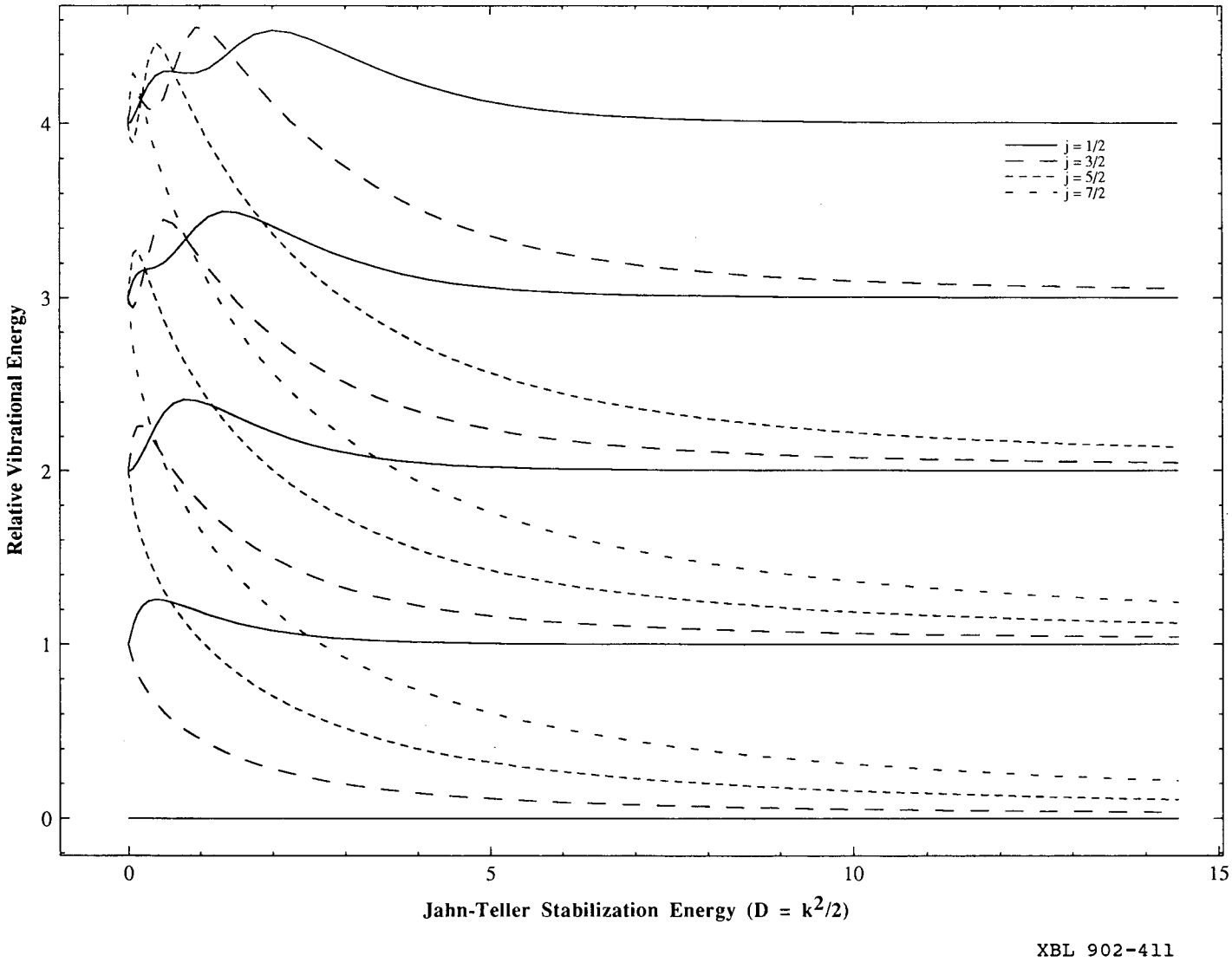
Relative Vibrational Energy
Jahn-Teller Stabilization Energy (D = k²/2)
j = 1/2
j = 3/2
j = 5/2
j = 7/2
0
1
2
3
4
0
5
10
15
XBL 902-411

Figure 12

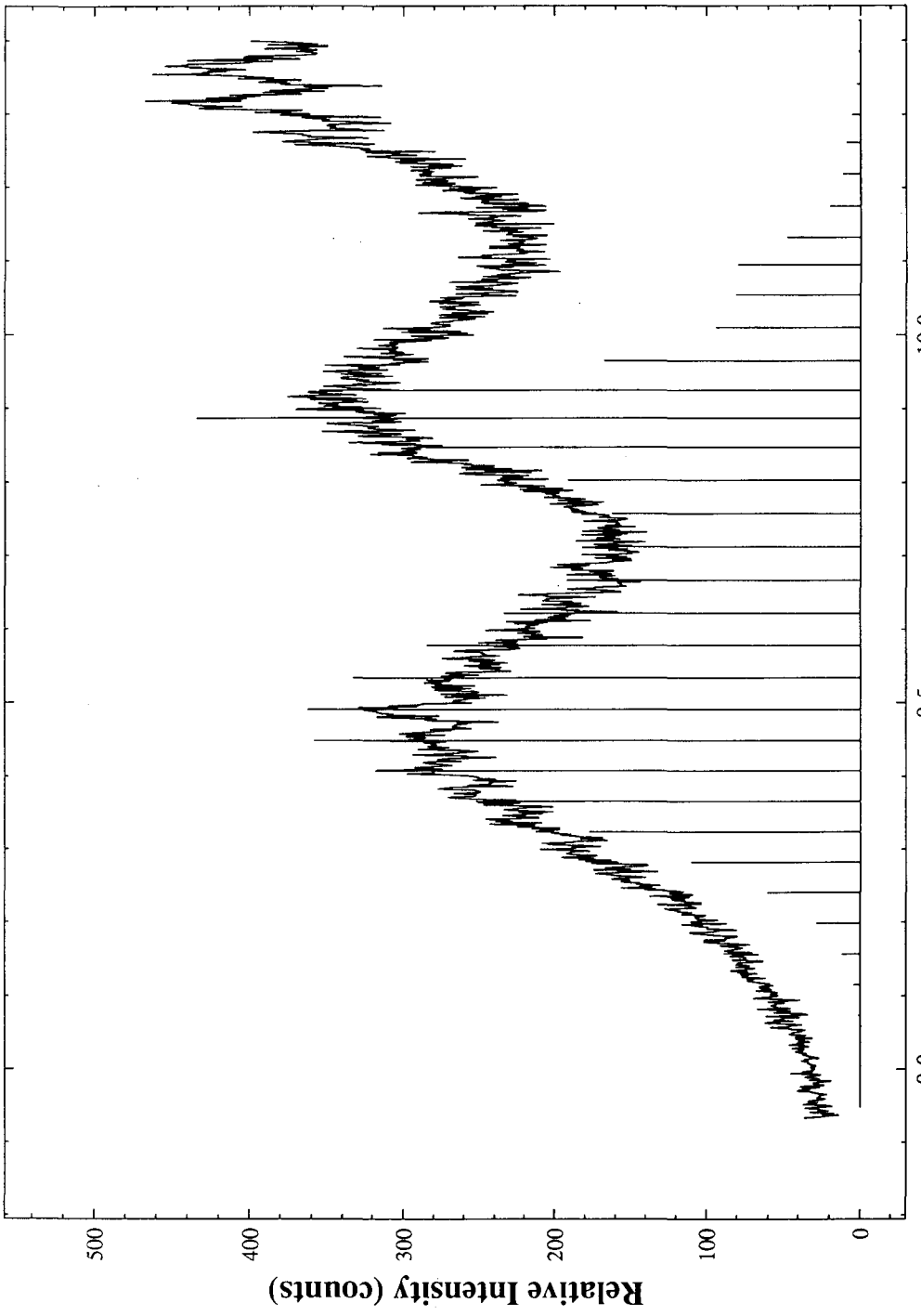
Relative Intensity (counts)
0
100
200
300
400
500
9.0
9.5
10.0
Ionization Potential (eV)
XBL 902-412

Figure 13

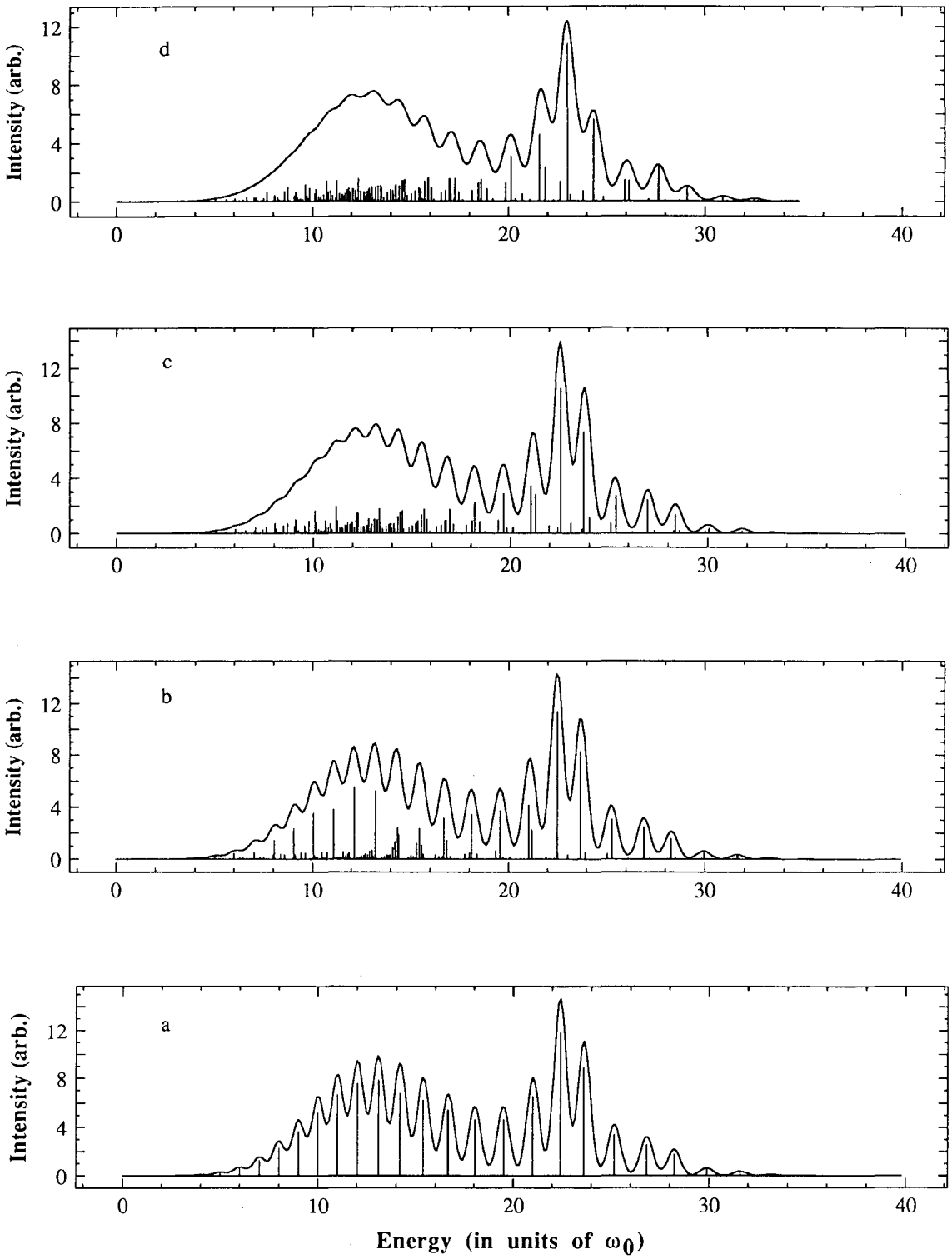
d
c
b
a
Intensity (arb.)
0
4
8
12
0
10
20
30
40
Energy (in units of ω_0)
XBL 902-413

Figure 14

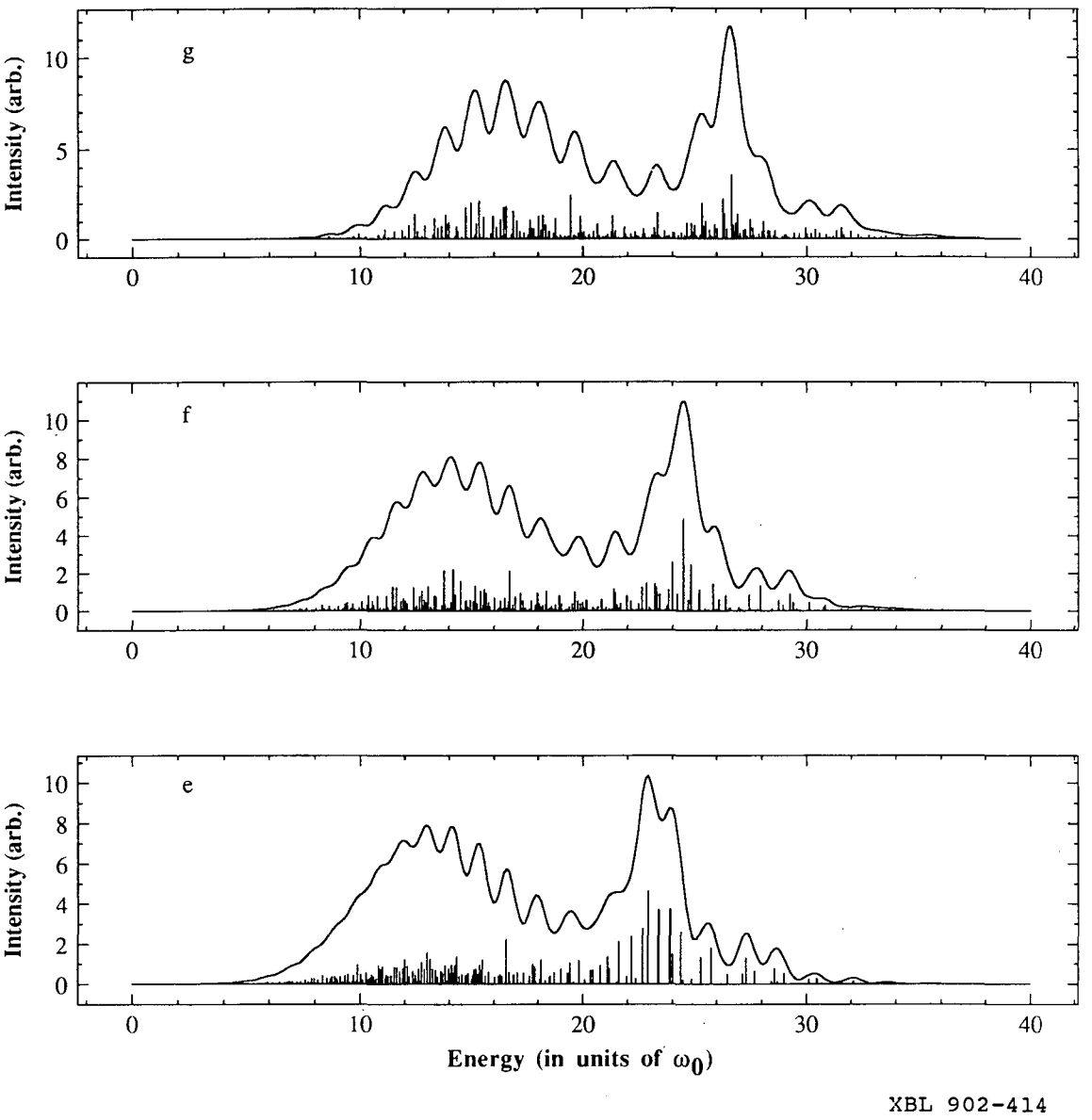

Figure 14 (Cont'd)

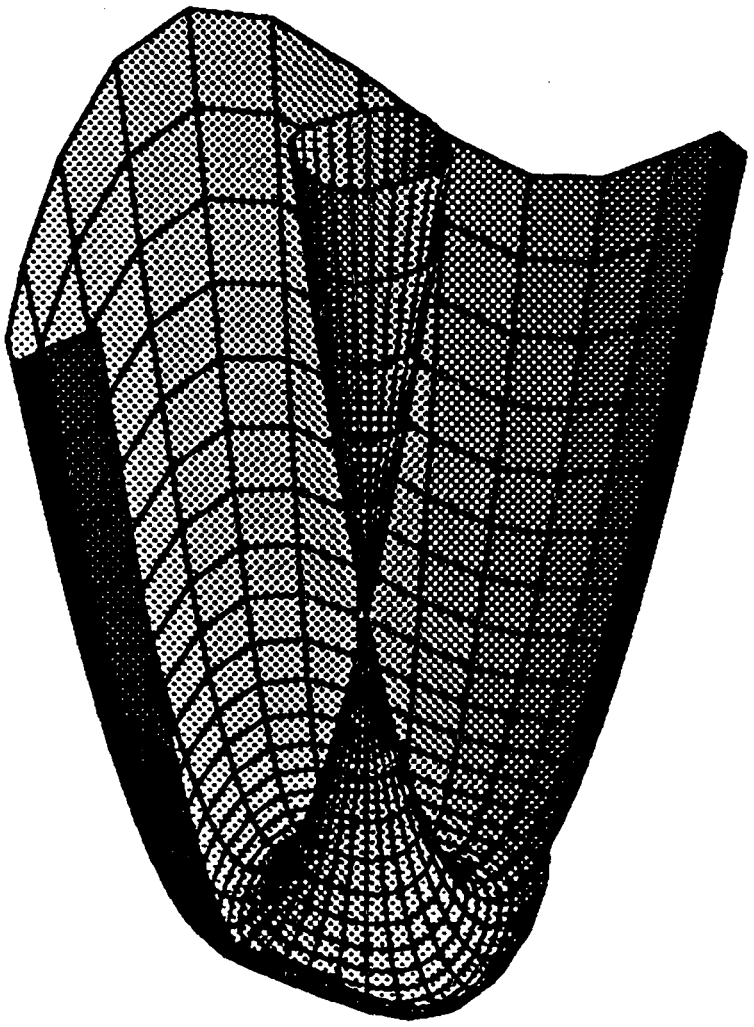

XBL 902-415

Figure 15

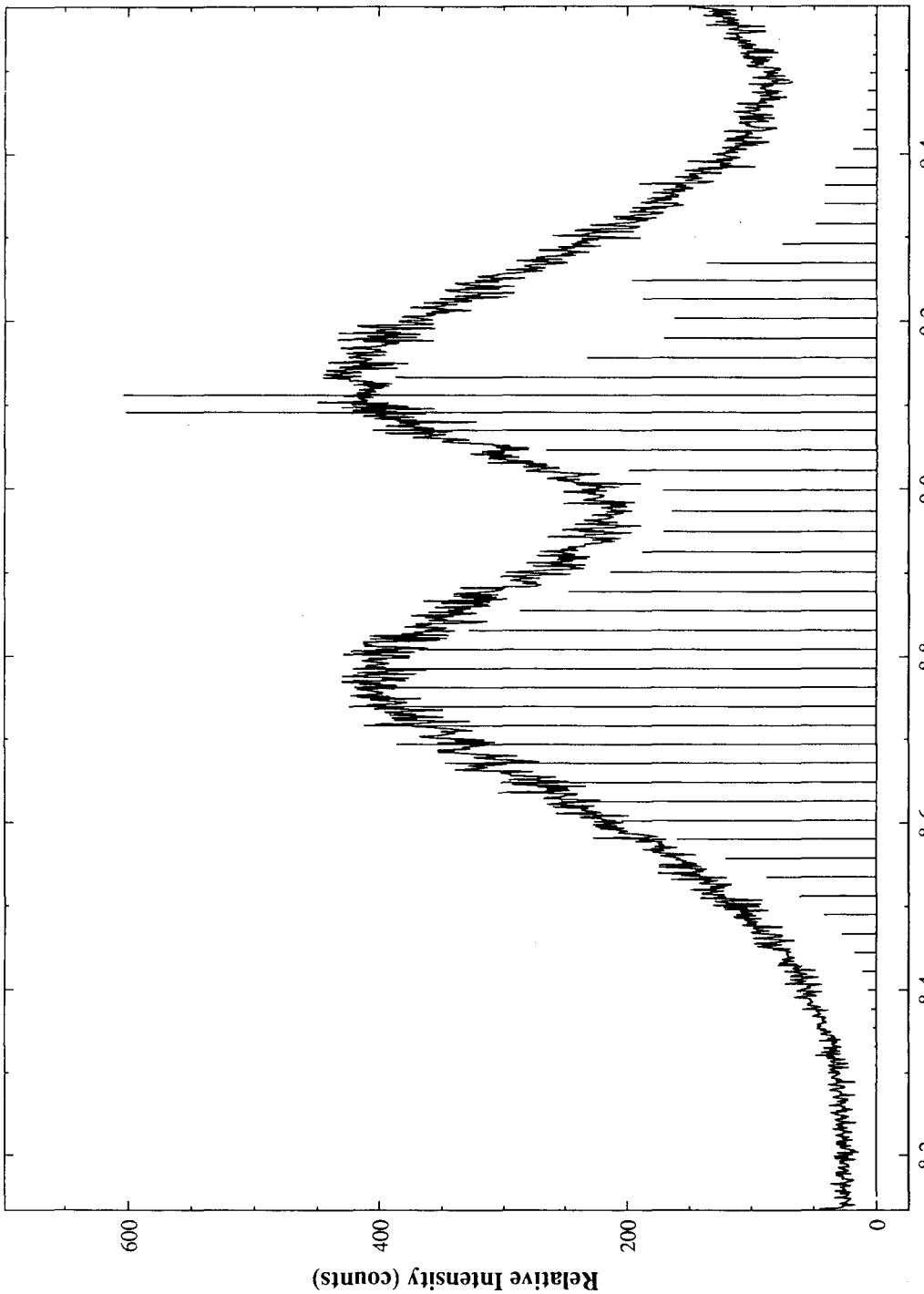
Relative Intensity (counts)
0
200
400
600
8.2
8.4
8.6
8.8
9.0
9.2
9.4
Ionization Potential (eV)
XBL 902-416

Figure 16

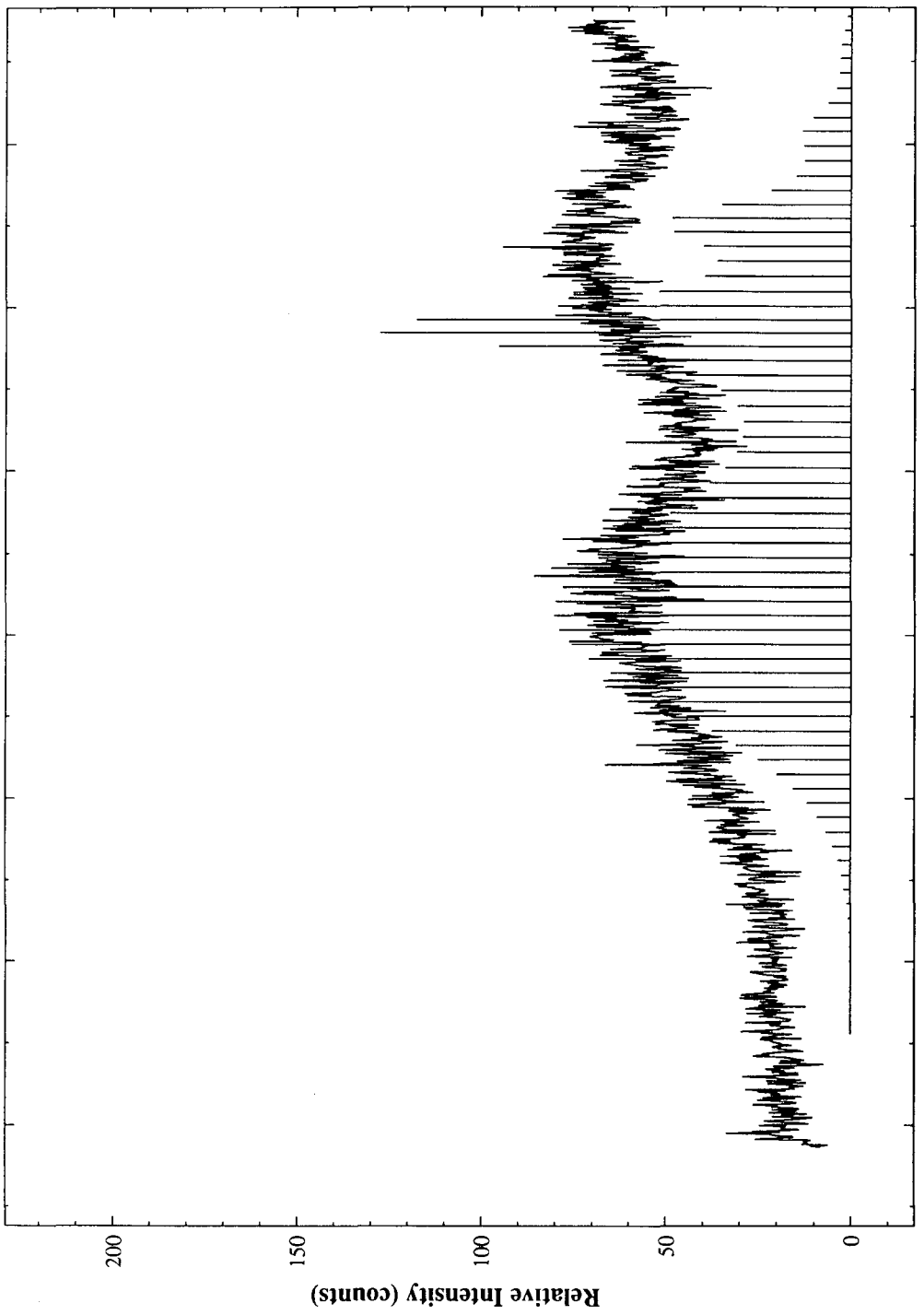
Relative Intensity (counts)
0
50
100
150
200
7.2
7.4
7.6
7.8
8.0
8.2
8.4
Ionization Potential Energy (eV)
XBL 902-417

Figure 17

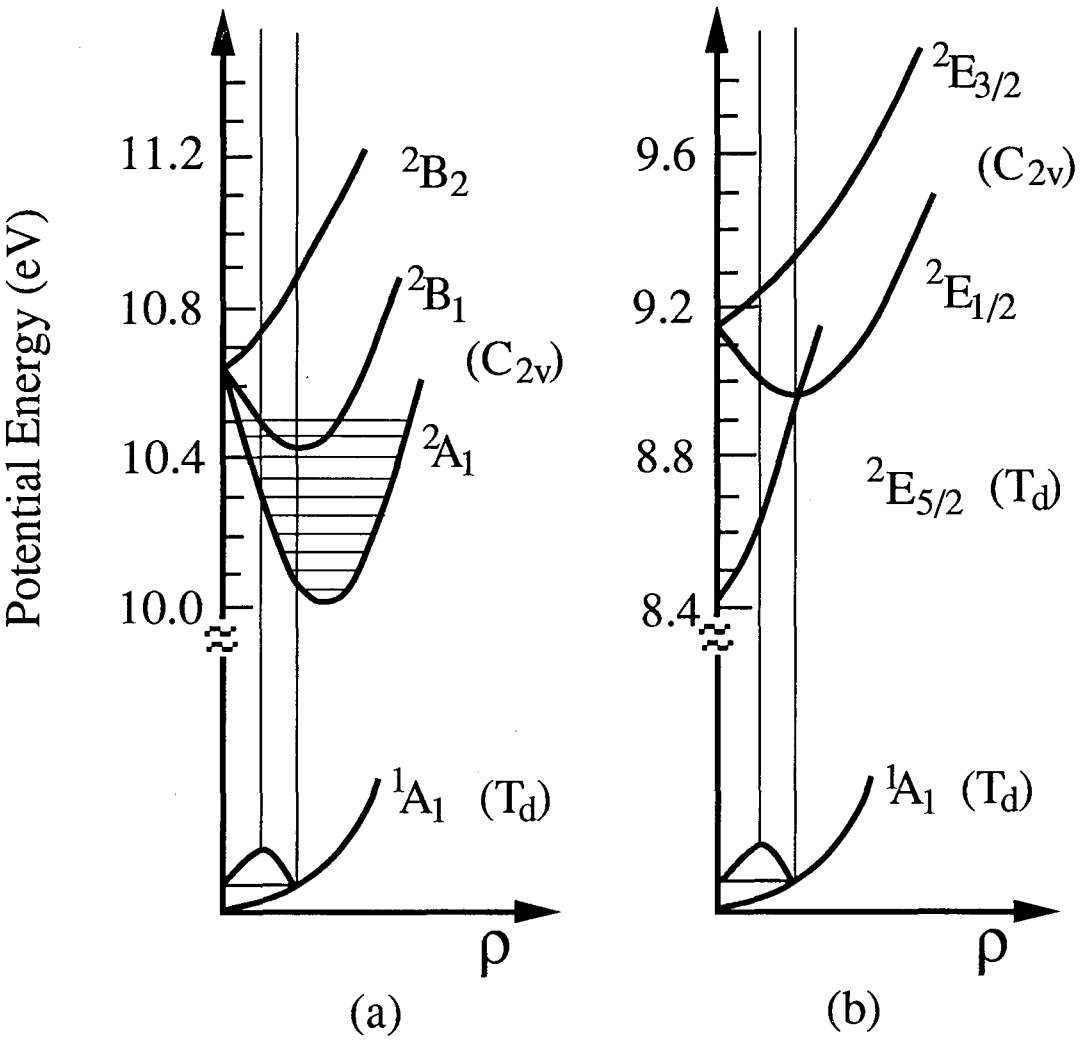
Potential Energy (eV)
11.2
10.8
10.4
10.0
$^2B_2$
$^2B_1$
(C_{2v})
$^2A_1$
$^1A_1$ (T_d)
ρ
(a)
9.6
9.2
8.8
8.4
$^2E_{3/2}$
(C_{2v})
$^2E_{1/2}$
$^2E_{5/2}$ (T_d)
$^1A_1$ (T_d)
ρ
(b)

Figure 18

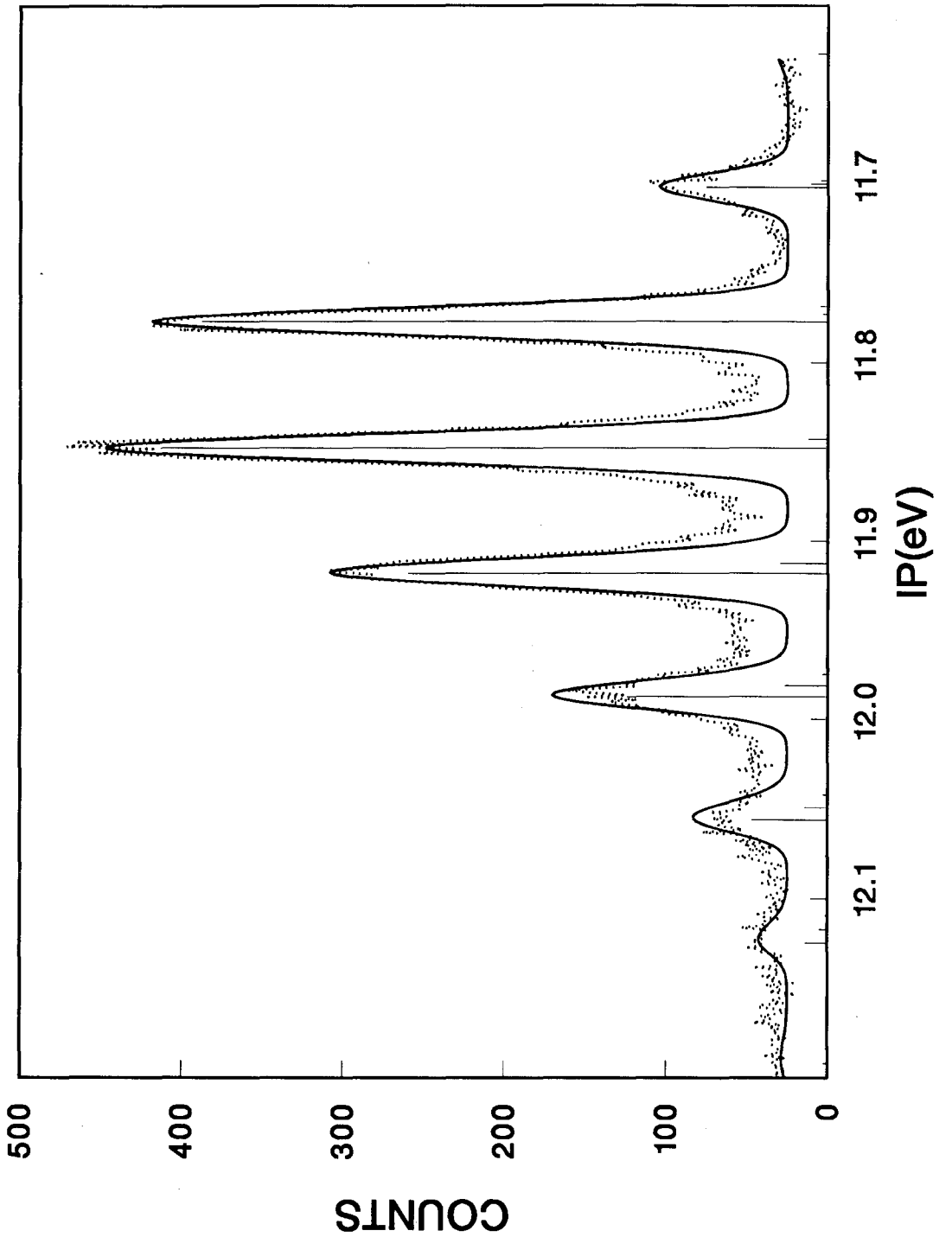

XBL 902-418

Figure 19

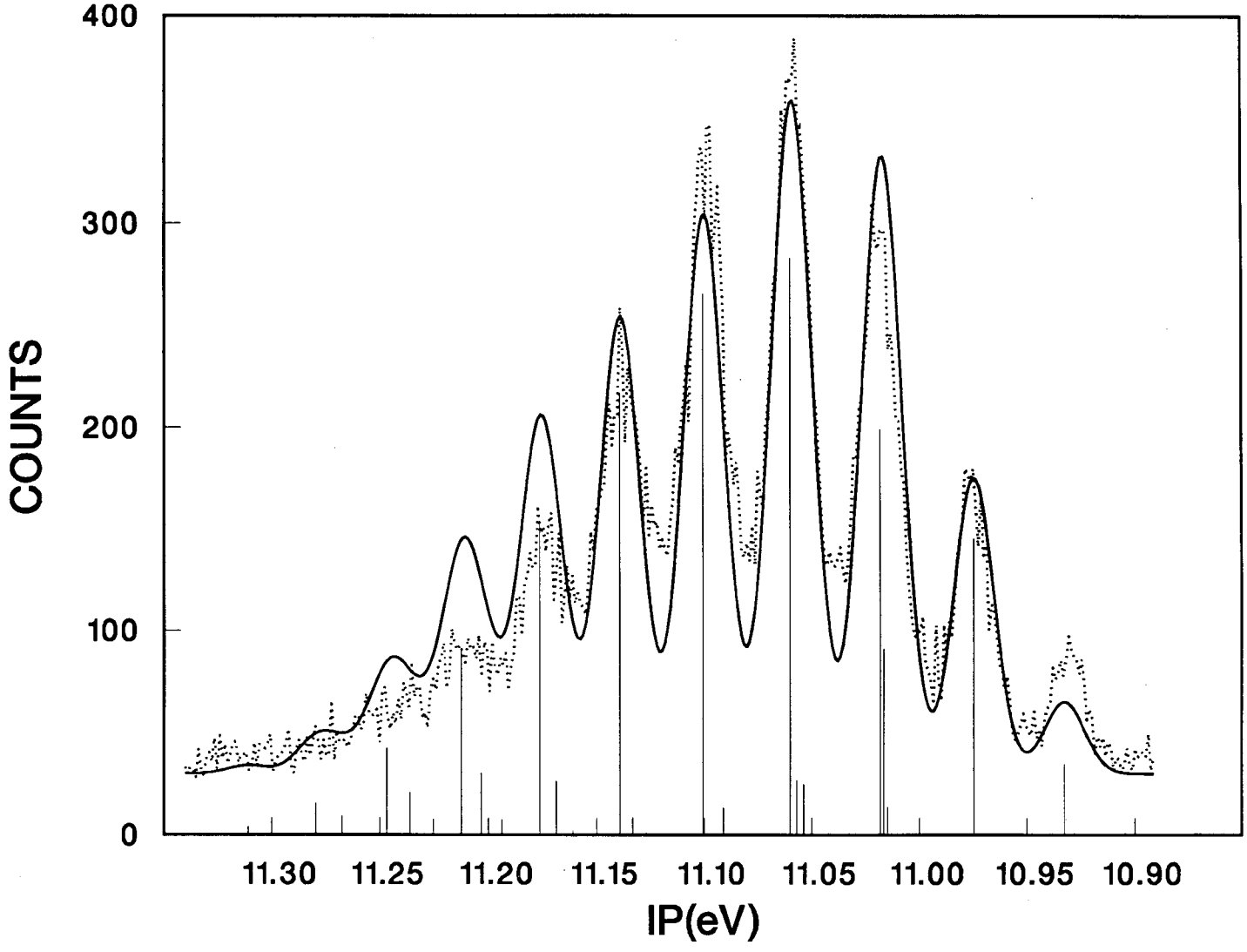

Figure 20

XBL 902-419

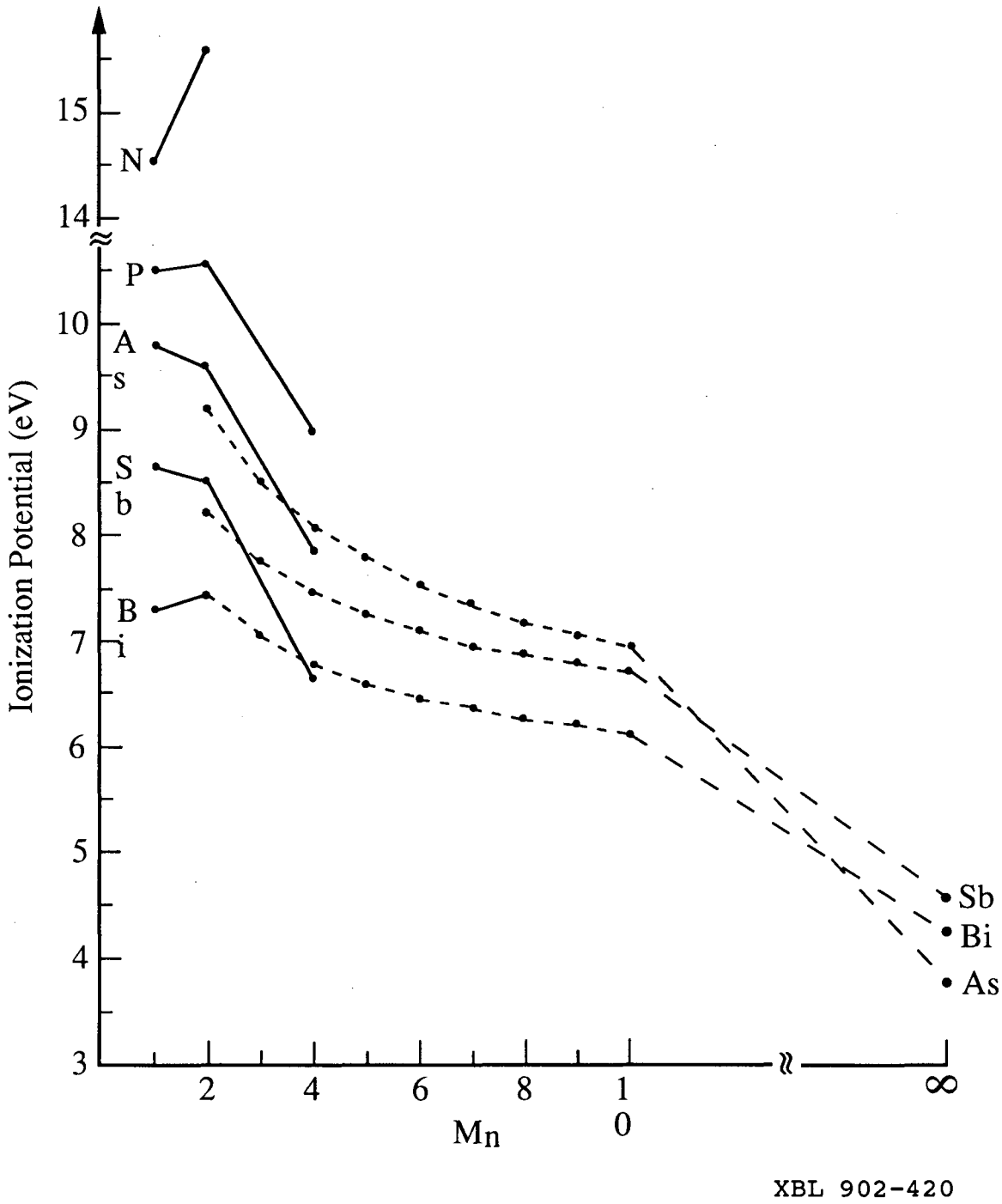
Ionization Potential (eV)
15
14
10
9
8
7
6
5
4
3
N
P
A
s
S
b
B
i
Sb
Bi
As
2
4
6
8
1
0
∞
Mn
XBL 902-420

Figure 21

Chapter 6

Electronic Structure and Chemical Bonding of the First Row Transition Metal Dichlorides, $MnCl_2$, $NiCl_2$, and $ZnCl_2$: A High Resolution Photoelectron Spectroscopic Study

Abstract

High resolution HeI (584Å) photoelectron spectra of $ZnCl_2$, $MnCl_2$, and $NiCl_2$ were measured using a high temperature supersonic molecular beam source. In $ZnCl_2$, vibrational structures were resolved, and spectroscopic constants were derived for the observed molecular ion states. The $C^2\Sigma_g^+$ state of $ZnCl_2^+$ was found to have a double-well potential along the Q_3 coordinate with an asymmetric $ZnCl_2^+$ geometry of $[Cl\cdots Zn-Cl]^+$ in its ground vibrational state. For the open-shell molecules, $MnCl_2$ and $NiCl_2$, no vibrational structure could be resolved because of their very low bending frequencies. Transitions from the ligand orbital and metal d orbital ionizations were clearly resolved, with those of the d orbitals having considerably narrower band widths. Even though many final states are expected for ionization of the open-shell d orbitals, only a few states were

observed. This was explained in $MnCl_2$ by the one-electron spin selection rule: $S_f = S_i \pm 1/2$. Besides the spin selection rule, a propensity toward high spin was proposed to account for the spectrum of $NiCl_2$. From the metal d orbital and ligand orbital splittings, the degree of covalent bonding was inferred to be in the order of: $MnCl_2 > NiCl_2 > ZnCl_2$.

6.1 Introduction

The first row transition metals are the lightest elements in the Periodic Table for which the free atoms have d orbitals that must be taken into account in chemical bonding. These d orbitals often impart interesting chemical and physical properties to the transition metal compounds.[1] Even though the first row transition metal dihalides are among the simplest transition metal compounds which can be studied as free molecules, they are still difficult to study and are incompletely characterized spectroscopically. Still, much remains to be understood about these compounds. There have been earlier infrared[2,3] and ultraviolet[4-6] absorption studies both in the gas phase and in rare gas matrices, and electron diffraction studies[7] to determine the geometric structure. The dichlorides are now known to be linear and symmetric[7,8] with a very small bending frequency.[3,9]

Theoretically, these molecules are difficult subjects, too, because of their open-shell character and the large number of electrons involved. Electron correlation, spin-orbit, and spin-spin effects should be taken into account, and large basis sets are required. Consequently, there have been few ab initio quantum chemical calculations on these molecules.[10-12]

There is also considerable discussion about the degree to which the d orbitals participate in chemical bonding, particularly in the transition metal dimers which have drawn great interest recently within the chemical physics community in the context of studying transition metal clusters. It is generally believed that when two transition metal atoms form a diatomic molecule the bonding involves mainly the 4s orbitals, while the 3d orbitals are largely localized on the two atoms. The unpaired d electrons on the two atoms can couple to form many low-lying excited states. Indeed, just for the Fe_2 molecule alone, Shim and Gingerich[13] have predicted that 112 states would lie within about 0.6 eV above the ground state. However, in a Fe_2^- negative ion photodetachment experiment recently by Leopold and Lineberger,[14] only two pronounced bands were observed within about 0.6 eV

above the Fe_2 ground state. Based on this observation, the authors tentatively concluded that the 3d orbitals were more strongly bound in Fe_2 than previously thought and hence did not produce a large number of low-lying excited states through the weak d-d coupling.

The bonding situation in the transition metal dichlorides is different from that in the transition metal dimers. Nevertheless, these molecules also have open-shell 3d orbitals, and the unpaired 3d electrons can in principle couple to give many final states upon photoionization. The small number of final states evident in the Fe_2^- negative ion photodetachment experiment enhances the interest of a high resolution photoelectron spectroscopic study of the transition metal dichlorides. An initial question is: can we observe all the predicted final states in the photoelectron spectra of the transition metal dichlorides?

There have been three previous photoelectron spectroscopic investigations of the first row transition metal dichlorides.[15-17] Unfortunately, due in part to the limited resolution in these studies, the spectral assignments have not been consistent.

We have recently built a high temperature molecular beam source,[18-20] which is especially suitable to study these molecules with high resolution. We are also interested in resolving vibrational structures in the photoelectron spectra of these molecules. These would provide important information about the chemical bonding and a better spectroscopic characterization of the molecular ions. It is also our hope that these experimental studies can spur more theoretical interest[21] on these relatively simple transition metal complexes.

Zinc, with a closed 3d shell, is not considered to be a transition metal. However, $ZnCl_2$ is a much simpler molecule in terms of electronic structure, and has been better understood than the transition metal dihalides. There have been numerous photoelectron spectroscopic investigations of $ZnCl_2$ at low resolution,[22-27] none of which has resolved any vibrational structure. Besides the interest in studying $ZnCl_2$ at higher resolution, we include it in this study as a comparison with the more complicated transition metal molecules, $MnCl_2$ and $NiCl_2$.

6.2 Experimental

The experiments were performed with a newly-constructed high temperature molecular beam source, recently described elsewhere,[18-20] and in Chapter 2. Only a brief description, and features related to the current experiments will be given here. The source used electron-bombardment heating and a graphite crucible, and it had the capability to entrain carrier gases to produce seeded supersonic beams of high temperature species with internal cooling. The experimental conditions for each experiment are summarized in Table 1.

Thermodynamically, $ZnCl_2$, $MnCl_2$, and $NiCl_2$ are known to evaporate mainly as monomers.[28-31] All samples were purchased commercially from Johnson Matthey Inc., $NiCl_2$ in its hydrated form, and $ZnCl_2$ and $MnCl_2$ in their anhydrous forms. These materials are extremely hygroscopic, and were all dried before use. Moreover, each sample underwent prolonged heating at a temperature below its melting point in vacuum to be dehydrated further. Even with these efforts, small amounts of water and hydrogen chloride, due to the reaction of water with the metal dichlorides, were still observable at the beginning of each experiment. In the case of $ZnCl_2$, minute amounts of these impurities persisted during the full course of the experiment, due to the lower temperature needed for the evaporation. In the cases of $MnCl_2$ and $NiCl_2$, these impurities disappeared shortly after the operating temperatures were reached.

It was not necessary to have absolutely accurate temperature measurements in these experiments. In general, about 1 - 5 Torr vapor was needed to be able to collect a spectrum. Both a quadrupole mass spectrometer and the photoelectron spectrometer were used to monitor the evaporation process. Once a reasonable photoelectron count level was reached, the temperature was stabilized and the whole experiment was done at this

temperature. The beam source pressure was kept below $5x10^{-4}$ Torr during an experiment. The carrier gas pressure was adjusted to maintain this vacuum in the beam source.

Special care had to be exercised for running $ZnCl_2$ and $MnCl_2$ because they were evaporated above their melting points. It was found that the carrier gas could spill the liquid samples in the graphite crucible and make liquid jets. Special quartz sample cells had to be used to confine the liquid samples inside the crucible in these cases, as shown in Figure 1. The two openings (6.35mm diameter holes) in the cell always faced up. $NiCl_2$ had a high enough sublimation pressure below its melting point, and was loaded into the graphite crucible directly without using a sample cell.

The details of the photoelectron spectrometer have also been published previously,[32] and descibed in Chapter 2. Briefly, it consists of a helium discharge lamp as the photon source (584Å), a quadrupole mass spectrometer and a hemispherical electron energy analyzer with a multichannel detector. The energy resolution of the analyzer was about 12 meV, as measured with the $Ar^+ {}^2P_{3/2}$ photoelectron peak which was used for calibration. Under high temperature conditions, drift of the energy scale was severe, and shorter scans were taken and the spectra were later added to enhance the counting statistics. As a result, the effective resolution in the final spectra was about 15 meV.

6.3 Results and Discussion

6.3.1 General Remarks

Before discussing the spectra, let us first examine the molecular orbitals and the chemical bonding in the first row transition metal dichlorides. It is generally believed that the participation of the 3d orbitals in chemical bonding decreases from the left to the right side of the Periodic Table. For Zn, a closed shell element, the 3d orbitals should be core-like, with little bonding capability. Ligand field theory[33,34] has been used to describe the

chemical bonding in these molecules. In this theory, we allow the two Cl^- ligands to approach the central metal ion M^{2+} colinearly and split the fivefold degenerate d orbitals into σ_g, π_g, and δ_g orbitals. The ligands can back-transfer charge to the 3d orbitals, facilitating covalent bonding character between the ligands and the central metal atom. Obviously, there cannot be any back transfer in $ZnCl_2$, and the bonding should be primarily electrostatic. The valence molecular orbitals can be written as follows:

$$\underbrace{\delta_g \pi_g \sigma_g}_{(3d)} \underbrace{\sigma_g \sigma_u \pi_u \pi_g}_{(Cl\ 3p)}$$

where only the Cl 3p and the metal-atom 3d orbitals are shown. The first three orbitals (δ_g, π_g, and σ_g) are mainly from the metal atom 3d orbitals and the later four (σ_g, σ_u, π_u, and π_g) are mainly from the Cl 3p orbitals. A schematic pictorial representation of these orbitals is shown in Figure 2. For the closed-shell $ZnCl_2$ molecule, the above orbital sequence is correct, with the 3d orbitals being almost core-like. However, the situations are more complicated for $MnCl_2$ and $NiCl_2$, where the 3d orbitals are only partially filled. It is now fairly well established that the ground states of these molecules assume the states of maximum multiplicity[4,5,10] just as in the free atoms and ions. Therefore, we have the following valence electronic configurations for the ground states of $ZnCl_2$, $MnCl_2$, and $NiCl_2$:

$$\cdots 1\delta_g^4\, 2\pi_g^4\, 8\sigma_g^2\, 9\sigma_g^2\, 7\sigma_u^2\, 4\pi_u^4\, 2\pi_g^4 \qquad {}^1\Sigma_g^+ \qquad ZnCl_2$$

$$\cdots 8\sigma_g^2\, 7\sigma_u^2\, 4\pi_u^4\, 2\pi_g^4\, 1\delta_g^2\, 3\pi_g^2\, 9\sigma_g^1 \qquad {}^6\Sigma_g^+ \qquad MnCl_2$$

$$\cdots 8\sigma_g^2\, 7\sigma_u^2\, 4\pi_u^4\, 2\pi_g^4\, 1\delta_g^4\, 3\pi_g^3\, 9\sigma_g^1 \qquad {}^3\Pi_g \qquad NiCl_2$$

To avoid confusion in later discussions, we numbered each molecular orbital by counting the inner orbitals. It is to be noted that the $1\delta_g$, $2\pi_g$, and $8\sigma_g$ orbitals correspond to the 3d orbitals in $ZnCl_2$, while the $1\delta_g$, $3\pi_g$, and $9\sigma_g$ orbitals correspond to the 3d orbitals in $MnCl_2$ and $NiCl_2$. The rest of the orbitals corresponds to the Cl 3p orbitals. The orbitals

omitted in the above all have ionization potentials too high to show up in the HeI (584Å) photoelectron spectrum.

The closed-shell configuration of $ZnCl_2$ implies a simple photoelectron spectrum from a one-electron point of view. Ionization of each orbital produces one photoelectron band, neglecting spin-orbit splittings. However, the situations are much more complicated in $MnCl_2$ and $NiCl_2$ because of the open d-shell. Table 2 lists all the possible final states upon d-electron ionization in $MnCl_2$ and $NiCl_2$, assuming Russell-Saunders coupling.[35] There are indeed many possible final states for each one-electron ionization, except for the $9\sigma_g$ orbital in $NiCl_2$. It should be interesting to see how or whether all these final states will show up in the photoelectron spectra. For each ligand-orbital ionization there would be also a large number of possible final states because of the presence of the unpaired d electrons. We assume that the coupling between the ligand orbital electrons and the 3d electrons is weak, and we shall not consider it here. In other words, we should still expect only one band for each ligand orbital ionization. In the following, we shall first discuss the $ZnCl_2$ spectrum and then proceed to $MnCl_2$ and $NiCl_2$.

6.3.2 $ZnCl_2$

The photoelectron spectrum of $ZnCl_2$ has been extensively studied and the spectral assignments are well established.[22-27] The ground state vibrational frequencies[36] of $ZnCl_2$ are $\omega_e(\nu_1) = 358\ cm^{-1}$, $\omega_e(\nu_2) = 295\ cm^{-1}$, and $\omega_e(\nu_3) = 516\ cm^{-1}$. These are well within our experimental resolution. We should be able to resolve vibrational structure in the spectrum if the vibrational frequencies do not change very much in the molecular ion.

Figures 3-5 illustrate the photoelectron spectrum of $ZnCl_2$ obtained in the current study. Figure 3 shows the three bands from the $7\sigma_u$, $4\pi_u$, and $2\pi_g$ orbitals. Figures 4 and 5 show the spectrum of the $9\sigma_g$ and the d orbitals, respectively. Spin-orbit splitting is partly resolved in the $X^2\Pi_g$ band, while the two spin-orbit components in the $A^2\Pi_u$ band

are completely overlapped. This is because the $4\pi_u$ orbital is a bonding orbital and has a broader Franck-Condon envelope. Two Gaussians were fitted to the broad band and are plotted in Figure 3 to show the two spin-orbit components. The spin-orbit splittings here are comparable to that in Cl_2^+.[37] The overlapping of the two spin-orbit components in these two bands apparently tends to smear out the vibrational structures, which are only partially resolved. For the $X^2\Pi_g$ band, the ν_2 mode was observed to be excited with frequencies of about 240 cm^{-1} and 260 cm^{-1} for the $^2\Pi_{g3/2}$ and $^2\Pi_{g1/2}$ components, respectively. For the $A^2\Pi_{u3/2}$ band, two frequencies of 360 cm^{-1} and 280 cm^{-1} are discernible. These should be due to the ν_1 and ν_2 modes, respectively. For the $A^2\Pi_{u1/2}$ component, only a frequency of 280 cm^{-1}, corresponding to the ν_2 mode, can be recognized at the high ionization energy side. It is likely that the ν_1 mode was also excited with its features getting buried in the other spin-orbit component. These vibrational structures are indicated in Figure 3.

A broad and featureless band was observed for the $B^2\Sigma_u^+$ state, as can be seen from Figure 3. It is surprising that no vibrational structure was resolved in this band, since there is no complication from the spin-orbit effect. This could, in principle, arise from either of two factors. The first one is lifetime broadening. This would mean that the $B^2\Sigma_u^+$ state is unbound, which is not likely. More probably, the vibrational frequencies become smaller in the $B^2\Sigma_u^+$ state and all three vibrational modes got strongly excited. This would produce a very congested and featureless band such as the one observed. If this is the case, even higher resolution might resolve vibrational structures in this band.

A beautifully-resolved spectrum was observed for the $C^2\Sigma_g^+$ band, which is displayed in Figure 4, separately. It appears at first sight that the resolved vibrational structure is due to a single vibrational progression. However, it cannot be assigned to a single vibrational mode, as can be seen from Table 3, where the ionization energy of each peak and the spacings between the peaks are listed. Based on the known ground-state vibrational frequencies, we assigned the spectrum as shown in Figure 4 and Table 3. This

yields the following set of vibrational frequencies, $\omega_e(\nu_1) = 360\ cm^{-1}$, $\omega_e(\nu_2) = 280\ cm^{-1}$, and $\omega_e(\nu_3) = 510\ cm^{-1}$, which are remarkably similar to those of the neutral ground state.

It is seen from Figure 4 that the vertical transition is to the 002 level, two quanta of the ν_3 mode. The ν_3 mode is the asymmetric stretching mode, and only even quantum levels are accessible from the totally symmetric ground state. In linear and symmetric triatomic molecules, such a mode is not usually excited in photoelectron spectroscopy because of unfavorable Franck-Condon factors, unless there is a dramatic geometric change in the ionic state and the molecular ion becomes asymmetric. The vertical transition to the $\nu_3 = 2$ level in the $C^2\Sigma_g^+$ state strongly suggests that the $ZnCl_2^+$ molecular ion in the C state is no longer symmetric, with two unequal Zn–Cl bonds. This means that there is a barrier to change from structure $[Cl\cdots Zn{-}Cl]^+$ to $[Cl{-}Zn\cdots Cl]^+$, and a double-well potential along the Q_3 coordinate. We cannot determine the barrier height, but it must be sufficient to support more than two quanta of the ν_3 vibration. This is a somewhat surprising result, which can be understood if we examine the main constituents of the $9\sigma_g$ orbital from which an electron has been removed. As can be seen from Figure 2, the $9\sigma_g$ orbital is derived mainly from the Cl $3p_z$ orbitals, with contributions from the Zn 4s and $3d_{z2}$ orbitals. The above result implies that the charge is rather localized on the two Cl atoms in the $9\sigma_g$ orbital. Removing an electron from this orbital destroys the symmetric charge distribution and results in an unsymmetrical $[Cl\cdots Zn{-}Cl]^+$ structure in the C state, in which the remaining $9\sigma_g$ (Cl $3p_z$) electron is more localized on a single chlorine.

The spectrum of the 3d region of $ZnCl_2$ is shown in Figure 5. Bancroft *et al.*[27] and others[24] have studied this part of the spectrum extensively, to probe the bonding characters of the 3d orbitals in Zn. They were the first to resolve the two spin-orbit components of the $^2\Pi_g$ and $^2\Delta_g$ states. The current spectrum is in good agreement with the previous studies, but with a better resolution. One difference is that there do not appear to be any sizable vibrational excitations, in contrast to the assignment by Bancroft *et al.* The extra feature at about 19.55 eV and the less visible feature at about 19.28 eV cannot be assigned

to any vibrational levels, because their spacings relative to the immediate peaks at the lower energy side are not close to any vibrational frequencies. Considering the non-bonding character of the d orbitals, the vibrational frequencies in the molecular ion should not be very different from those in the neutral ground state. Bancroft *et al.* attributed these features to vibrational excitations without giving any specific assignments.[27] It should be pointed out that they only observed these features in their HeII (304Å) spectrum, but not in the HeI spectrum. Therefore, they may arise, e.g., from multi-electron processes, as it has been pointed out that electron correlation effects are important in this molecule.[38] Thus, the spectrum in the 3d region is very sharp, with little or no apparent vibrational excitation. This is in accord with the expectation that the 3d orbitals of Zn are core-like, with little bonding capability.

The ionization potentials and the derived spectroscopic constants from the current study of $ZnCl_2^+$ are summarized in Table 4.

6.3.3 $MnCl_2$

The photoelectron spectrum of $MnCl_2$ is shown in Figure 6. The very low value of the bending frequency of $MnCl_2$ makes it impossible for us to resolve any vibrational structure. There are no gas phase measurements of the bending frequency available, but Thompson and Carlson[3] measured it as 83 cm^{-1} in a argon matrix: such a small value is beyond our current experimental resolution. Both hot band transitions, from thermal population of the ν_2 mode in the ground state, and excitation of this mode in the final state accompanying the photoionization process would smear out any vibrational structure. Vibrational cooling in a supersonic expansion is relatively inefficient, and there should be a substantial thermal population of the low-frequency bending mode in our experiment.

For the spectral assignment, Lee *et al.*[17] used intensity differences between HeI (584Å) and HeII (304Å) spectra to identify features from the d orbitals. It was assumed

that the d orbitals have an enhanced ionization cross section at the HeII photon energy. In Figure 6, we have fitted each observed band with a Gaussian, also plotted. There are three relatively sharp bands at ionization energies of 11.03 eV, 12.40 eV, and 13.96 eV. Two of these bands (11.03 eV and 13.96 eV) were assigned as being from the d orbitals by Lee *et al.* They observed no definite intensity enhancement of the 12.40 eV peak in their HeII spectrum, and did not assign this band to the d orbitals. However, from the sharpness of the band at 12.40 eV, we tentatively assign it as arising from the d orbitals. This illustrates one of the advantages of having high resolution. In the three previous investigations[15-17] at lower resolution, this assignment could not be made from the spectral width.

After identifying the bands arising from the d orbitals, we should easily be able to assign the rest of the bands from the ligands by analogy with the $ZnCl_2$ spectrum discussed in the above section. However, there is an extra band at 14.51 eV, which Lee et al. could not assign. They speculated that it was a satellite band. Lee *et al.*[17] did an *ab initio* molecular orbital calculation on $MnCl_2$ along with their experimental study. Although the overall accuracy of the calculation was not high enough to assign the spectrum, they found a remarkably large spin-spin splitting for the ionization of the $8\sigma_g$ orbital (~1 eV), but only very small spin-spin splittings for the ionizations of the other ligand orbitals. Based on this, we assign this extra band at 14.51 eV to be the low-spin state from ionization of the $8\sigma_g$ orbital. The high-spin band should be the one at 13.60 eV. The three bands at ionization energies of 11.68 eV, 11.96 eV, and 12.18 eV are assigned to be from the $2\pi_g$, $4\pi_u$, and $7\sigma_u$ orbitals, respectively. It is natural to assign the three bands from the d orbitals at 11.03 eV, 12.40 eV, and 13.96 eV to be from the $9\sigma_g$, $3\pi_g$, and $1\delta_g$ orbitals, respectively. The overall assignments, the ionization energies, and the band widths from the Gaussian fitting are all tabulated in Table 5. The assignments by Lee *et al.* are also given in Table 5 for comparison.

With reference to Table 2, how do we explain the fact that there are only three bands observed for the ionizations of the d orbitals, much fewer than shown there? We notice that, for a one-electron transition, the spin selection rule says:

$$S_i = S_f \pm 1/2$$

where S_i is the initial spin in the neutral molecule, and S_f the final state spin in the cation. The free photoelectron can carry either up or down spin. In $MnCl_2$, the five d electrons are all parallel to each other, giving the $^6\Sigma_g^+$ ground state. From the spin selection rule, only quintet states are allowed in a strictly one-electron transition. From Table 2, there are only three allowed final quintet states, arising from each of the three d orbitals, in excellent agreement with our experimental observation. However, it is well known that electron correlation effects are strong in this open-shell system, resulting in multi-electron processes, which would give rise to the other terms listed in Table 2. This notwithstanding, multi-electron transitions usually have much smaller cross sections, and may have eluded the experimental observation. For the ionizations of the ligand orbitals, both septet and quintet states are allowed. As mentioned above, only for the $8\sigma_g$ orbital both low-spin and high-spin states were explicitly observed, and the spin-spin splittings for the other three ligand orbitals may be too small to be resolved experimentally.

We can gain additional insight into the $MnCl_2$ spectrum by considering the ionic limit, $Cl^-Mn^{2+}Cl^-$, for the ground state, in which Mn^{2+} has the free-ion character ($3d^5$; ^6S) of a high-spin half-filled shell, and the chlorine ions have filled $3p^6$ shells. In this model, removal of a 3d electron can only lead to a quintet final state. Crystal field theory leads unambiguously to the orbital order $9\sigma_g^{-1}$; $3\pi_g^{-1}$; $1\delta_g^{-1}$ for the $3d^{-1}$ final states through repulsive interaction with the chlorine ions. In the case of chlorine 3p ionization, it is helpful to consider a small degree of covalency. Only the $8\sigma_g$ combination of $3p_z$ orbitals can form a bond of reasonable strength (Figure 2), and this orbital will clearly have the highest binding energy because the $3p_z$ orbitals both form a bonding combination and overlap with the attractive potential of the Mn^{2+} ion. The order, $7\sigma_u$; $4\pi_u$; $2\pi_g$, is also

expected on similar arguments, as are the similar binding energies of these orbitals and their separation from the $8\sigma_g$ orbital. Thus, the large multiplet splitting occurred only in the $8\sigma_g$ orbital, because only the $8\sigma_g$ orbital has any appreciable density across the Mn^{2+} ion, facilitating large exchange integrals. In fact, the two peak ($^7\Sigma_g^+$ - $^5\Sigma_g^+$) multiplet pattern is strongly similar to the two peak ^7S - ^5S pattern, well-known[39] in the 3s photoelectron spectrum of ionic Mn^{2+}, in which a 3s electron couples to the ($3d^5$; ^6S) shell through exchange, parallel to form ^7S and anti-parallel to form ^5S. The smaller splitting in $MnCl_2$ is expected because the $8\sigma_g$ orbital cannot overlap with the Mn 3d shell as much as a Mn 3s electron. Even the width and lower (than statistical, 5 : 7) relative intensity of the $^5\Sigma_g^+$ peak is analogous, probably arising from electron correlation.[40]

6.3.4 $NiCl_2$

The spectrum of $NiCl_2$ is shown in Figure 7, with the Gaussian fit plotted underneath each observed band. The ground state of $NiCl_2$ also has a very low bending vibrational frequency (85 cm^{-1}),[3] so no vibrational structure could be resolved. It is remarkable that four relatively narrow bands were resolved at low ionization energy. In all the previous investigations,[15-17] only one band was resolved in the same energy range. Evidently these four bands should be from the d orbitals, on the basis of their small band widths. It is noticed that there is some nitrogen impurity from the background at high ionization energy. There are no other sharp bands in the entire spectrum, so the first four bands are apparently the only features from the d orbitals. The rest of the spectrum can be assigned by analogy with those of $ZnCl_2$ and $MnCl_2$, as shown in Table 6.

An expanded portion of the d region is plotted in Figure 8. Only four components are evident, by either visual inspection or curve-fitting. Additional peaks could be present, either coincident in energy or with low intensity. In associating these peaks to the eleven possible final states listed in Table 2, there are many possibilities. In none of the previous

work[15-17] has any of these components been resolved. We make the very tentative assignment shown in Figure 9. This assignment is neither firm nor unique. Its basis is as follows: we assume that photoionization, which removes a d electron from the triplet ground state of $NiCl_2$, will access any of the doublet or quartet final states of $NiCl_2^+$, given in Table 2, for which $S_f = S_i \pm 1/2$. We assume further that some intensity is observed in ionization from each of the d-orbitals, $9\sigma_g$, $3\pi_g$, and $1\delta_g$. Finally, we invoke a "weak form" of a high-spin propensity rule. That is, the highest-spin final states will appear to be enhanced relative to low-spin states. There are two firm reasons for this. First, the (2S+1) spin multiplicity favors high-spin states. Second, electron correlation effects tend to distribute the intensity of photoelectron transitions to low-spin states over several peaks, reducing the intensity in the "main" peak. A clear example of this is in the photoionization of Mn^{2+} in a solid.[40]

In applying these assumptions, we note from Table 2 that the ionization of the $9\sigma_g$ orbital results in only one state ($^2\Pi_g$), the ionization of the $3\pi_g$ orbital leads to only one state with maximum multiplicity ($^4\Sigma_g^-$), and the ionization of the $1\delta_g$ orbital produces two states with maximum multiplicity ($^4\Phi_g$ and $^4\Pi_g$). According to the Hund's rules, the $^4\Pi_g$ state should have higher energy than the $^4\Phi_g$ state. So, the four bands from the d orbitals can be very tentatively assigned as shown in Figure 9 and given in Table 6. Also given in Table 6 are all the ionization energies and the assignments and the band widths from the Gaussian fittings, together with the assignments by Lee *et al.*[17] for comparison.

6.3.5 Discussion

The photoelectron spectroscopy of the open-shell transition metal molecules is apparently very complicated. Evidently, not all the final states arising from an open-shell electron configuration would be observed experimentally. In the one-electron transition, first of all, the spin selection rule is obeyed. Even within the spin selection rule, we still

found that there was a propensity toward high-spin final states in $NiCl_2^+$. The states with low spin and the states arising from electron correlations may have much smaller cross sections, and require much higher signal level to be observed. The fact that these were low signal experiments implied that there were many final states sharing the oscillator strength, and only the ones with large enough cross sections were experimentally observed. These may well apply to the transition metal cluster systems, where a large number of final states are expected from their open-shell nature, and caution must be taken to interpret the observed spectra. Quantum chemical calculations of the final state energy levels and partial cross sections would be very helpful.

Another question concerns spin-orbit splitting in the spectra of $MnCl_2$ and $NiCl_2$. For the ligand bands, the spin-orbit components must be contained in one band, based on the bandwidths and by comparison with the spectrum of $ZnCl_2$. For the bands of the d orbitals, it is also possible that the two spin-orbit components are contained in each band because the spin-orbit splitting parameters are comparable to the bandwidths. A different explanation could be offered for $NiCl_2$ if its ground state configuration was assumed to be closed-shell ($\cdots 1\delta_g^4\, 3\pi_g^4\, 9\sigma_g^0$). This configuration would yield the correct number of final states including the spin-orbit splittings, as shown in the following:

$$\cdots 1\delta_g^4\, 3\pi_g^4\, (^1\Sigma_g^+) \rightarrow \cdots 1\delta_g^4\, 3\pi_g^3, \quad {}^2\Pi_g \rightarrow {}^2\Pi_{g3/2}, {}^2\Pi_{g1/2}$$

$$\rightarrow \cdots 1\delta_g^3\, 3\pi_g^4, \quad {}^2\Delta_g \rightarrow {}^2\Delta_{g5/2}, {}^2\Delta_{g3/2}$$

The observed four d bands could be assigned to the above four spin-orbit components, and this even yields reasonable spin-orbit splitting parameters, 0.16 eV for the $^2\Pi_g$ state, and 0.20 eV for the $^2\Delta_g$ state. Indeed, two previous investigations[15,16] have assumed this ground state configuration for $NiCl_2$, although only one d band was resolved in these studies. Unfortunately, this ground state configuration of $NiCl_2$ is in apparent conflict with previous optical absorption studies[4-6] which concluded that the ground state configuration

of $NiCl_2$ should be $\cdots 1\delta_g^4\ 3\pi_g^3\ 9\sigma_g^1\ (^3\Pi_g)$. Therefore, the closed-shell configuration cannot be taken for the spectral assignments of $NiCl_2$.

In Table 7 are given all the orbital ionization energies of $ZnCl_2$, $NiCl_2$, and $MnCl_2$. In cases where there are spin-orbit or spin-spin splittings, an average was taken as the orbital ionization energy. A correlation diagram of these orbital ionization energies is shown in Figure 9. It is seen that the ligand orbital ionization energies of $NiCl_2$ are similar to that of $ZnCl_2$, while that of the $MnCl_2$ ligand orbital ionization energies show a slightly different pattern. It is known that the metal-ligand bonding in $ZnCl_2$ is primarily electrostatic. This suggests that the metal-ligand interaction is stronger in $MnCl_2$ than in $NiCl_2$, that is, there is more covalent character in the bonding of $MnCl_2$ than in that of $NiCl_2$. The ligand field splittings of the d orbitals support this view. While the splittings in $MnCl_2$ are very large, they are quite small in $NiCl_2$, being very close to that in $ZnCl_2$.

It is also instructive to examine the d orbital bandwidths. In the spectrum of $ZnCl_2$ shown in Figure 5, the bands are very narrow, on the order of the instrumental resolution, with little vibrational excitation. However, the d band widths are considerably broadened in $MnCl_2$ and $NiCl_2$. The broadening cannot be fully explained by spin-orbit and thermal effects. There must be some vibrational excitations, most likely of the low frequency bending mode, suggesting significant covalent bonding between the central metal atom and the ligands in $MnCl_2$ and $NiCl_2$ in comparison with $ZnCl_2$. This supports the general conviction that the participation in chemical bonding of the 3d orbitals in the first row transition metal elements weakens from left to right in the Periodic Table.

6.4 Summary

We have measured the high resolution HeI (584Å) photoelectron spectra of $ZnCl_2$, $MnCl_2$, and $NiCl_2$. Vibrational structures were resolved in $ZnCl_2$ and the $C^2\Sigma_g^+$ state of $ZnCl_2^+$ was found to be asymmetric, as inferred from the resolved vibrational structure.

Spin-orbit splitting was partly resolved in the $X^2\Pi_g$ state while the two spin-orbit components were heavily overlapped in the $A^2\Pi_u$ state. Vibrational structure was partially resolved in these two states. Five peaks were clearly resolved for the d orbitals including the spin-orbit effect, with little or no vibrational excitation.

No vibrational structure was resolved in the cases of $MnCl_2$ and $NiCl_2$ because of their very low bending vibrational frequencies. However, the high resolution was very helpful to identify the bands arising from the d orbitals, and their bandwidths yielded information about the bonding character. The much broader bandwidths indicated significant covalent bonding involvement of the 3d electrons. However, much fewer final states were observed than expected from their open-shell configurations. In $MnCl_2^+$, only three bands could be attributed to the d orbitals, which were assigned to the three highest-spin final states, for which there was no spin-flip (spin selection rule). Only four peaks could be clearly resolved in $NiCl_2^+$, which may be associated to the d orbitals. For assignment of these four states, a propensity toward high-spin states was proposed in addition to the spin selection rule. The spectra of the ligand orbitals in $MnCl_2^+$ and $NiCl_2^+$ are similar to that of $ZnCl_2^+$, except that the separation between the σ_g orbital and the other ligand orbitals increases in the order $MnCl_2 > NiCl_2 > ZnCl_2$, supporting the view that the covalent bonding character increases in the same order.

References

1. See for example, F.A. Cotton and G. Wilkinson, *Advanced Inorganic Chemistry*, Second Ed. (John Wiley & Sons, New York, 1966).
2. G.E. Leroi, T.C. James, J.T. Hougen, and W. Klempere, *J. Chem. Phys.* **36**, 1879 (1962).
3. K. Thompson and K.D. Carlson, *J. Chem. Phys.* **49**, 4379 (1968).
4. J.T. Hougen, G.E. Leroi, and T.C. James, *J. Chem. Phys.* **34**, 1670 (1961).
5. C.W. DeKock and D.M. Gruen, *J. Chem. Phys.* **44**, 4387 (1966).
6. A.B.P. Lever and B.R. Hollebone, *Inorg. Chem.* **11**, 2183 (1972).
7. I. Hargittai and J. Tremmel, *Coord. Chem. Rev.* **18**, 257 (1976).
8. A. Buchler, J.L. Stauffer, and W. Klemperer, *J. Chem. Phys.* **40**, 3471 (1964).
9. L. Brewer, G.R. Somayajulu, and E. Brachett, *Chem. Rev.* **63**, 111 (1963).
10. C.D. Garner, I.H. Hillier, and C. Wood, *Inorg. Chem.* **17**, 168 (1978).
11. M. Costas and A. Garritz, *Int. J. Quant. Chem., Quant. Chem. Symp.* **13**, 141 (1979).
12. W. von Niessen and L.S. Cederbaum, *Mol. Phys.* **43**, 897 (1981).
13. I. Shim and K.A. Gingerich, *J. Chem. Phys.* **77**, 2490 (1982).
14. G.G. Leopold and W.C. Lineberger, *J. Chem. Phys.* **85**, 51 (1986).
15. J. Berkowitz, D.G. Streets, and A. Garritz, *J. Chem. Phys.* **70**, 1305 (1979).
16. R.M. MacNaughton, J.E. Bloor, R.E. Sherrod, and G.K. Schweitzer, *J. Electron Spectrosc. Relat. Phenom.* **22**, 1 (1981).
17. E.P.F. Lee, A.W. Potts, M. Doran, I.H. Hillier, J.J. Delaney, R.W. Hawksworth, and M.F. Guest, *J. Chem. Soc. Faraday* II **76**, 506 (1980).
18. L.-S. Wang, B. Niu, Y.T. Lee, and D.A. Shirley, *Chem. Phys. Lett.* **158**, 297 (1989).
19. L.-S. Wang, B, Niu, Y.T. Lee, D.A. Shirley, and K. Balasubramanian, *J. Chem.*

Phys. **92**, 899 (1990).

20. L.-S. Wang, J.E. Reutt-Robey, B. Niu, Y.T. Lee, and D.A. Shirley, *J. Electron Spectrosc. Relat. Phenom.*, in press, LBL-27583.
21. C.W. Bauschlicher, Jr., private communication.
22. G.W. Boggess, J.D. Allen Jr, and G.K. Schweitzer, *J. Electron Spectrosc. Relat. Phenom.* **2**, 467 (1973).
23. J. Berkowitz, *J. Chem. Phys.* **61**, 407 (1974).
24. A.F. Orchard and N.V. Richardson, *J. Electron Spectrosc. Relat. Phenom.* **6**, 61 (1975).
25. E.P.F. Lee and A.W. Potts, *J. Electron Spectrosc. Relat. Phenom.* **22**, 247 (1981).
26. D.J. Bristow, G.M. Bancroft, and J.S. Tse, *Chem. Phys.* **75**, 263 (1983).
27. G.M. Bancroft, D.J. Bristow, and J.S. Tse, *Chem. Phys.* **75**, 277 (1983).
28. J.H. Canterford and R. Colton, *Halides of the First Row Transition Metals* (Interscience, New York, 1968).
29. D.W. Rice and N.W. Gregory, *J. Phys. Chem.* **72**, 3361 (1968).
30. F.J. Keneshea and D. Cubicciotti, *J. Chem. Phys.* **40**, 191 (1964).
31. R.C. Schoomaker, A.H. Friedman, and R.F. Porter, *J. Chem. Phys.* **31**, 1586 (1959).
32. J.E. Pollard, D.J. Trevor, Y.T. Lee, and D.A. Shirley, *Rev. Sci. Instrum.* **52**, 1837 (1981).
33. J.H. Van Vleck and A. Sherman, *Rev. Modern Phys.* **7**, 167 (1935).
34. A.D. Liehr, *J. Chem. Educ.* **39**, 135 (1962).
35. G. Herzberg, *Molecular Spectra and Molecular Structure I. Spectra of Diatomic Molecules*, Second Ed. (Van Nostrand Reinhold, New York, 1950), P333.
36. A. Loewenschuss, A. Ron, and O. Schnepp, *J. Chem. Phys.* **49**, 272 (1968).
37. H. van Lonkhuyzen and C.A. de Lange, *Chem. Phys.* **89**, 313 (1984).

38. L.S. Cederbaum, W. Domcke, J. Schirmer, and W. von Niessen, *Adv. Chem. Phys.* **65**, 115 (1986).

39. C.S. Fadley, D.A. Shirley, A.J. Freeman, P.S. Bagus, and J.V. Mallow, *Phys. Rev. Lett.* **23**, 1397 (1969).

40. S.P. Kowalczyk, L. Ley, R.A. Pollak, F.R. McFeely, and D.A. Shirley, *Phys. Rev.* **B7**, 4009 (1973).

Table 1. Experimental Conditions.

	$ZnCl_2$	$MnCl_2$	$NiCl_2$
T (K)[a]	800	1000	960
P (Torr)[b]	110 (He)	120 (He)	500 (He)
ϕ (mm)[c]	0.18	0.23	0.16
Power (mAxV)[d]	30x600	200x600	60x1200
Starting Materials	Pure $ZnCl_2$	Pure $MnCl_2$	Pure $NiCl_2$

a. Accuracy of temperature measurements was ± 50K.

b. Carrier gas pressure.

c. Nozzle diameters.

d. Heating power, emission current (mA) times applied high voltage (V). About 60 watts power was needed to drive the tungsten filament, which is in addition to the heating power.

Table 2. Terms of Electron Configurations after Removing a d Electron in $MnCl_2$ and $NiCl_2$.

$MnCl_2$: $\cdots 8\sigma_g^2\, 7\sigma_u^2\, 4\pi_u^4\, 2\pi_g^4\, 1\delta_g^2\, 3\pi_g^2\, 9\sigma_g^1$ $^6\Sigma_g^-$		
Orbitals Ionized	Electron Configuration	Molecular Electronic Terms
$9\sigma_g^{-1}$	$\cdots 1\delta_g^2\, 3\pi_g^2$	$^5\Sigma_g^-$, $^3\Sigma_g^-(2)$, $^3\Delta_g$, $^3\Gamma_g$, $^1\Sigma_g^+(2)$, $^1\Delta_g(2)$, $^1\Gamma_g$, ^1I_g
$3\pi_g^{-1}$	$\cdots 1\delta_g^2\, 3\pi_g^1\, 9\sigma_g^1$	$^5\Pi_g$, $^3\Pi_g(2)$, $^3\Phi_g$, ^3H_g, $^1\Pi_g(2)$, $^1\Phi_g$, ^1H_g
$1\delta_g^{-1}$	$\cdots 1\delta_g^1\, 3\pi_g^2\, 9\sigma_g^1$	$^5\Delta_g$, $^3\Sigma_g^+$, $^3\Sigma_g^-$, $^3\Delta_g(2)$, $^3\Gamma_g$, $^1\Sigma_g^+$, $^1\Sigma_g^-$, $^1\Delta_g(2)$, $^1\Gamma_g$
$NiCl_2$: $\cdots 8\sigma_g^2\, 7\sigma_u^2\, 4\pi_u^4\, 2\pi_g^4\, 1\delta_g^4\, 3\pi_g^3\, 9\sigma_g^1$ $^3\Pi_g$		
Orbitals Ionized	Electron Configuration	Molecular Electronic Terms
$9\sigma_g^{-1}$	$\cdots 1\delta_g^4\, 3\pi_g^3$	$^2\Pi_g$
$3\pi_g^{-1}$	$\cdots 1\delta_g^4\, 3\pi_g^2\, 9\sigma_g^1$	$^4\Sigma_g^-$, $^2\Sigma_g^+$, $^2\Sigma_g^-$, $^2\Delta_g$
$1\delta_g^{-1}$	$\cdots 1\delta_g^3\, 3\pi_g^3\, 9\sigma_g^1$	$^4\Pi_g$, $^4\Phi_g$, $^2\Pi_g(2)$, $^2\Phi_g(2)$

Table 3. Ionization Energies (eV) and Assignments of the $C^2\Sigma_g^+$ state of $ZnCl_2^+$.

Ionization Energy	Assignment			Spacing (meV)		
	ν_1	ν_2	ν_3	ν_1	ν_2	$2\nu_3$
13.975 (6)	0	0	0			
14.020 (5)	1	0	0	45		
14.065 (5)	2	0	0	45		
14.101 (4)	0	0	2			126
14.136 (6)	0	1	2		35	
14.170 (7)	0	2	2		34	

Table 4. Spectroscopic Constants of $ZnCl_2^+$.

	IPa (eV)[a]	IPv (eV)[b]	A (eV)[c]	$\omega_e(\nu_1)$ (cm^{-1})	$\omega_e(\nu_2)$ (cm^{-1})	$\omega_e(\nu_3)$ (cm^{-1})
X $^2\Pi_{g3/2}$		11.802 (5)			240 (20)	
$^2\Pi_{g1/2}$		11.880 (5)	0.078		260 (20)	
A $^2\Pi_{u3/2}$		12.341 (10)		(360)	(280)	
$^2\Pi_{u3/2}$		12.451 (10)	0.110		(280)	
B $^2\Sigma_u^+$		13.103 (15)				
C $^2\Sigma_g^+$	13.975 (6)	14.065 (5)		360 (8)	280 (10)	510 (8)
3d bands						
D $^2\Sigma_g^+$	19.037 (5)	19.037 (5)				
E $^2\Pi_{g3/2}$	19.163 (5)	19.163 (5)				
$^2\Pi_{g1/2}$	19.434 (5)	19.434 (5)	0.271			
F $^2\Delta_{g5/2}$	19.213 (6)	19.213 (6)				
$^2\Delta_{g3/2}$	19.499 (6)	19.499 (6)	0.286			

a. Adiabatic ionization potentials.

b. Vertical ionization potentials.

c. Spin-orbit splitting parameters.

Table 5. Ionization Energies (eV) and Assignments for $MnCl_2$. ,

IP[a]	Assignment	Electronic Term	FWHM (eV)[b]	Lee *et al.*[c]
11.03	$9\sigma_g^{-1}$ (3d)	$^5\Sigma_g^+$	0.184	$9\sigma_g$, $3\pi_g$
11.68	$2\pi_g^{-1}$	$^7\Pi_g$	0.367	$4\pi_u$, $2\pi_g$, $7\sigma_u$
11.96	$4\pi_u^{-1}$	$^7\Pi_u$	0.332	(did not
12.18	$7\sigma_u^{-1}$	$^7\Sigma_u^+$	0.314	specify)
12.40	$3\pi_g^{-1}$ (3d)	$^5\Pi_g$	0.160	
13.60	$8\sigma_g^{-1}$	$^7\Sigma_g^+$	0.360	$1\delta_g$, $8\sigma_g$
13.96	$1\delta_g^{-1}$ (3d)	$^5\Delta_g$	0.115	(did not resolve)
14.51	$8\sigma_g^{-1}$	$^5\Sigma_g^+$	0.396	Satellite?

a. Vertical ionization energies, uncertainty = ± 0.01 eV.

b. Full Width at Half Maximum of the fitted Gaussian.

c. Reference 17.

Table 6. Ionization Energies (eV) and Assignments for $NiCl_2$.

IP[a]	Assignment	Electronic Term	FWHM (eV)[b]	Lee *et al.*[c]
11.24	$9\sigma_g^{-1}$ (3d)	$^2\Pi_g$	0.166	$9\sigma_g$, $3\pi_g$, $1\delta_g$ (Only resoled one band)
11.40	$3\pi_g^{-1}$ (3d)	$^4\Sigma_g^-$	0.135	
11.56	$1\delta_g^{-1}$ (3d)	$^4\Phi_g$	0.183	
11.76	$1\delta_g^{-1}$ (3d)	$^4\Pi_g$	0.150	
12.08	$2\pi_g^{-1}$	$^4\Delta_g$	0.322	$4\pi_u$, $2\pi_g$, $7\sigma_u$ (did not specify)
12.60	$4\pi_u^{-1}$	$^4\Delta_u$	0.352	
13.00	$7\sigma_u^{-1}$	$^4\Pi_u$	0.302	
13.70	$8\sigma_g^{-1}$	$^4\Pi_g$	0.450	$8\sigma_g$
15.25	$8\sigma_g^{-1}$	$^2\Pi_g$	.400	$3\pi_g$, Satellite?

a. Vertical ionization energies, uncertainty = ± 0.01 eV.

b. Full Width at Half Maximum of the fitted Gaussian.

c. Reference 17.

Table 7. Vertical Ionization Potentials (eV) of the Ligand Orbitals and the d Orbitals of $ZnCl_2$, $MnCl_2$, and $NiCl_2$.[a]

	Ionization Potentials of the Ligand Orbitals			
	π_g	π_u	σ_u	σ_g
$ZnCl_2$	11.84	12.40	13.10	14.10
$NiCl_2$	12.07	12.60	13.01	14.47
$MnCl_2$	11.68	11.90	12.18	14.06
	Ionization Potentials of the d orbitals			
	σ_g	π_g	δ_g	
$ZnCl_2$	19.04	19.30	19.35	
$NiCl_2$	11.24	11.40	11.70	
$MnCl_2$	11.03	12.41	13.96	

a. In cases where there are spin-orbit or spin-spin splittings, an average value was taken as the ionization potential of the orbital.

Figure Captions

Figure 1 The graphite crucible configuration with a sample cell.

Figure 2 A schematic pictorial representation of the valence molecular orbitals of a linear MCl_2 molecules (M = first row transition metals, Cu, and Zn). Only one component is drawn for the π_g and π_u orbitals of the ligands, and for the π_g and δ_g orbitals of the central metal atom.

Figure 3 The HeI photoelectron spectrum from the $2\pi_g$, $4\pi_u$, and $7\sigma_u$ orbitals of $ZnCl_2$. Gaussians were fitted to the $A^2\Pi_u$ band and are plotted in the spectrum to show the spin-orbit components.

Figure 4 The HeI photoelectron spectrum from the $9\sigma_g$ orbital of $ZnCl_2$, with the vibrational assignments.

Figure 5 The HeI photoelectron spectrum from the Zn 3d orbitals ($8\sigma_g$, $2\pi_g$, and $1\delta_u$) of $ZnCl_2$, with the assignments.

Figure 6 The HeI photoelectron spectrum of $MnCl_2$. Individual Gaussians were fitted to the observed bands and are plotted in the spectrum.

Figure 7 The HeI photoelectron spectrum of $NiCl_2$. Individual Gaussians were fitted to the observed bands and are plotted in the spectrum.

Figure 8 An expanded portion of the HeI photoelectron spectrum of the d bands region of $NiCl_2$, with the assignments and the individual Gaussians.

Figure 9 Correlation diagram showing the valence orbital ionization potentials of $MnCl_2$, $NiCl_2$, and $ZnCl_2$. The d orbitals are not labelled.

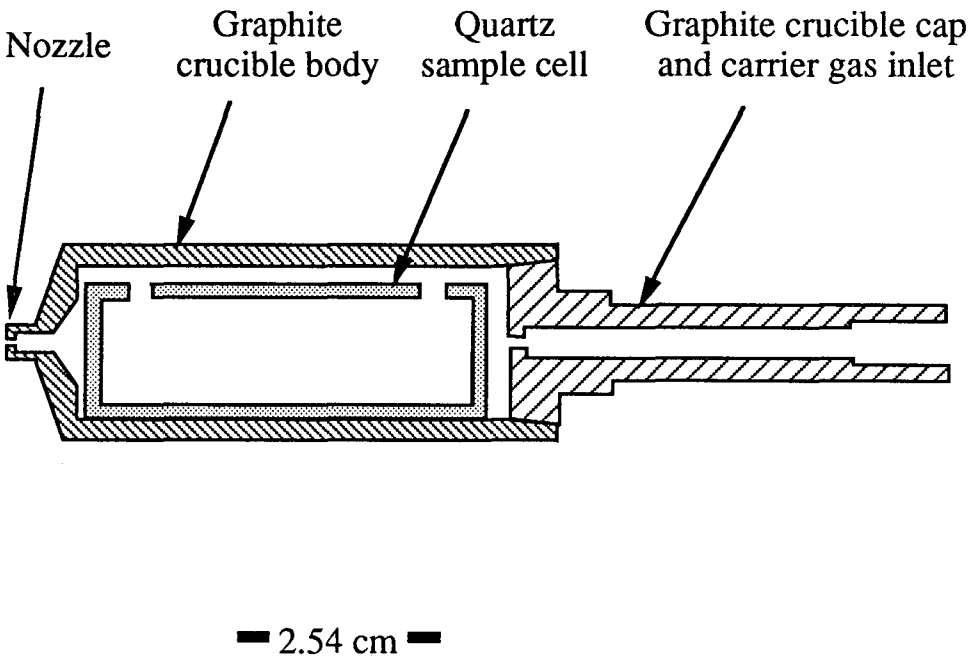
Nozzle
Graphite crucible body
Quartz sample cell
Graphite crucible cap and carrier gas inlet
2.54 cm

Figure 1

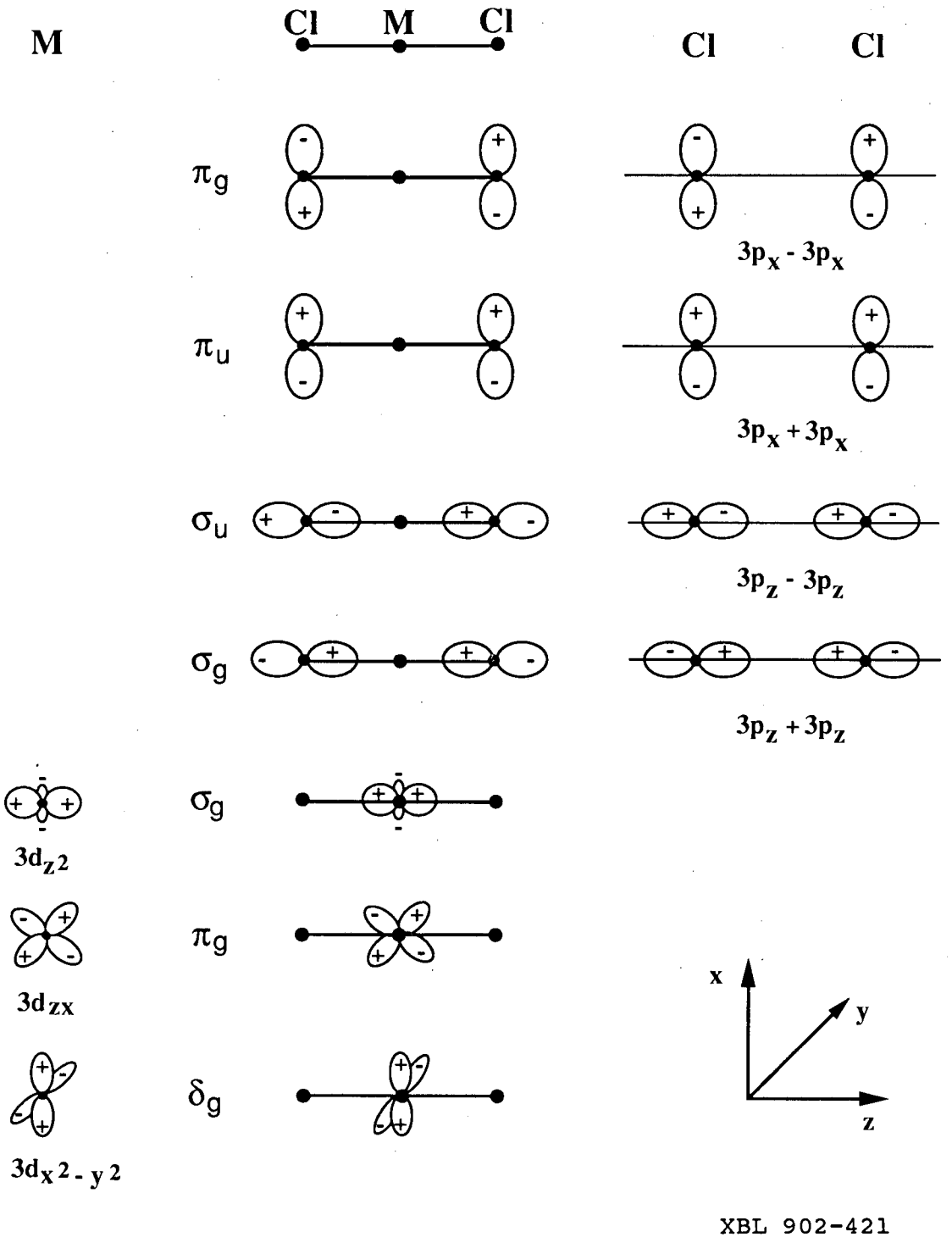
M
Cl M Cl
Cl Cl
π_g
$3p_x - 3p_x$
π_u
$3p_x + 3p_x$
σ_u
$3p_z - 3p_z$
σ_g
$3p_z + 3p_z$
σ_g
$3d_{z2}$
π_g
$3d_{zx}$
δ_g
$3d_{x2-y2}$
x
y
z
XBL 902-421

Figure 2

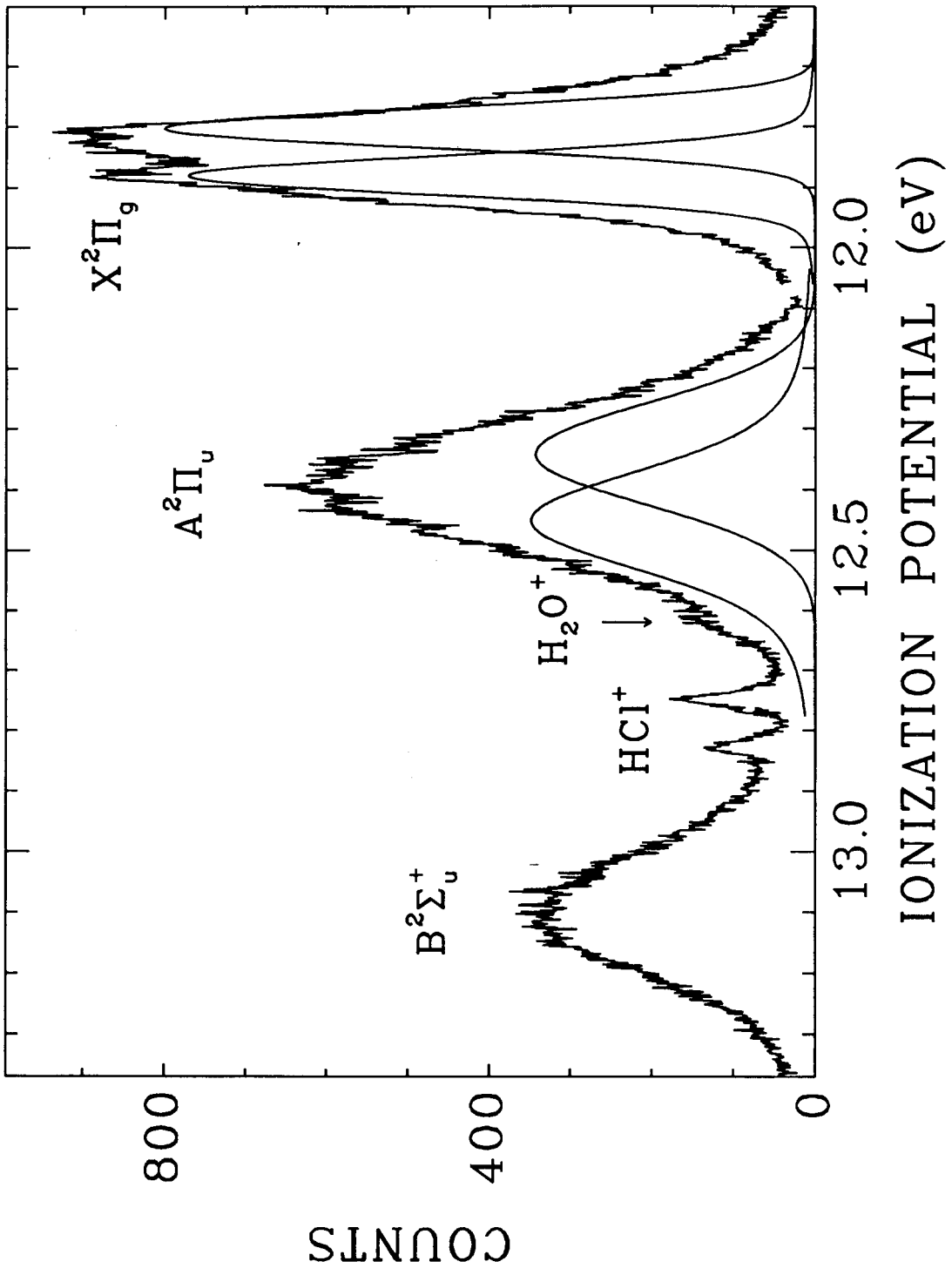

XBL 902-422

Figure 3

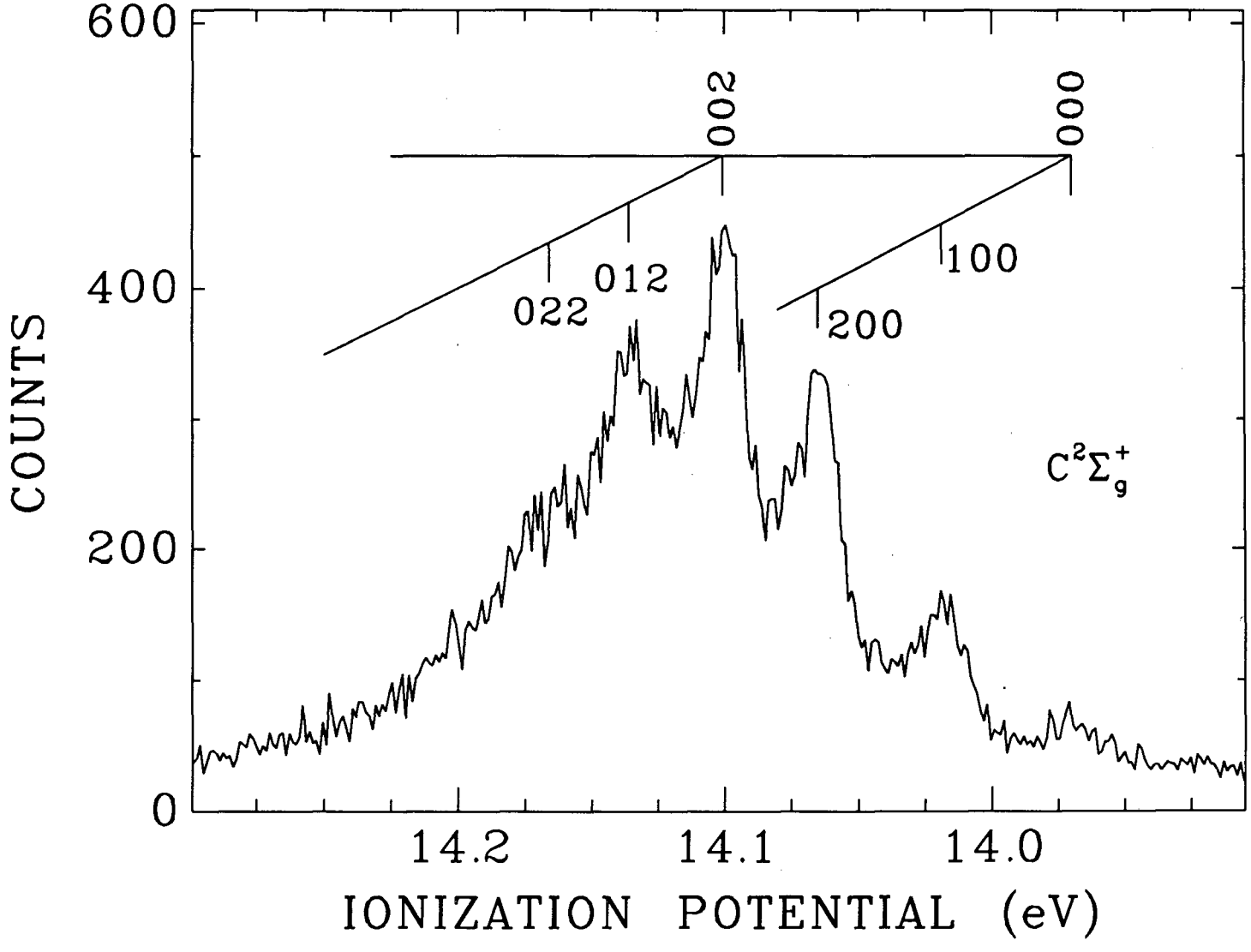

Figure 4

XBL 902-423

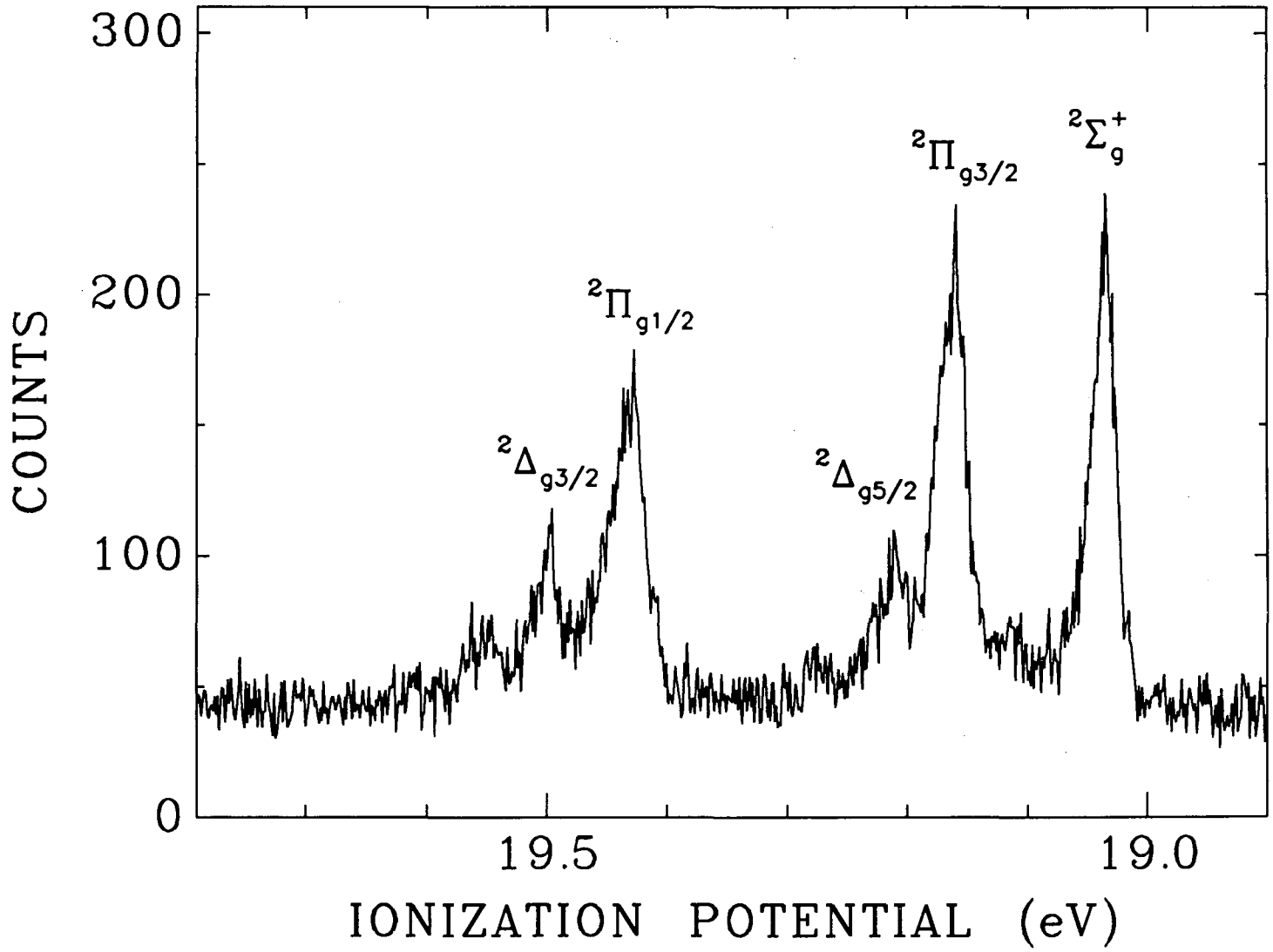

Figure 5

XBL 902-424

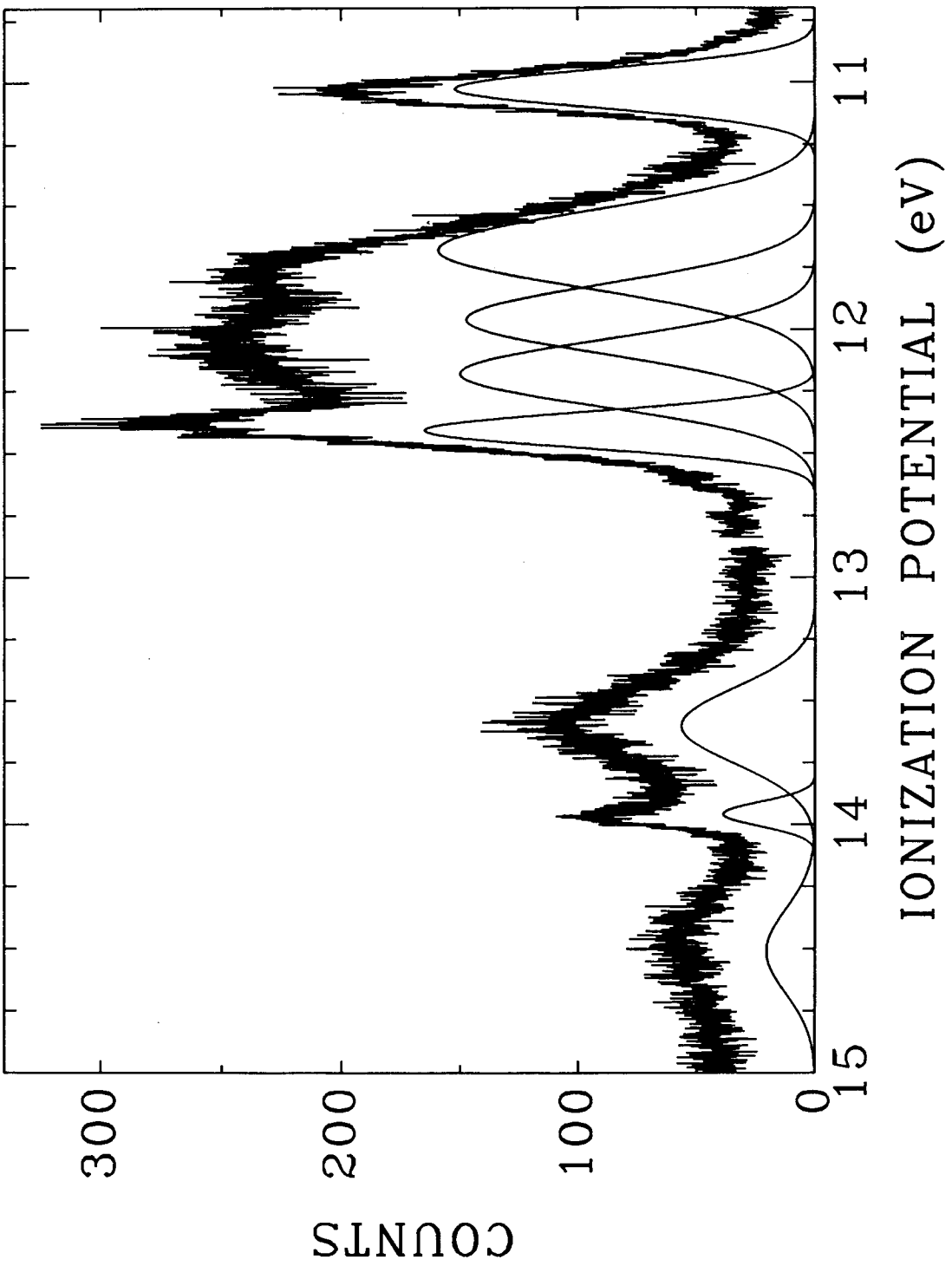

XBL 902-425

Figure 6

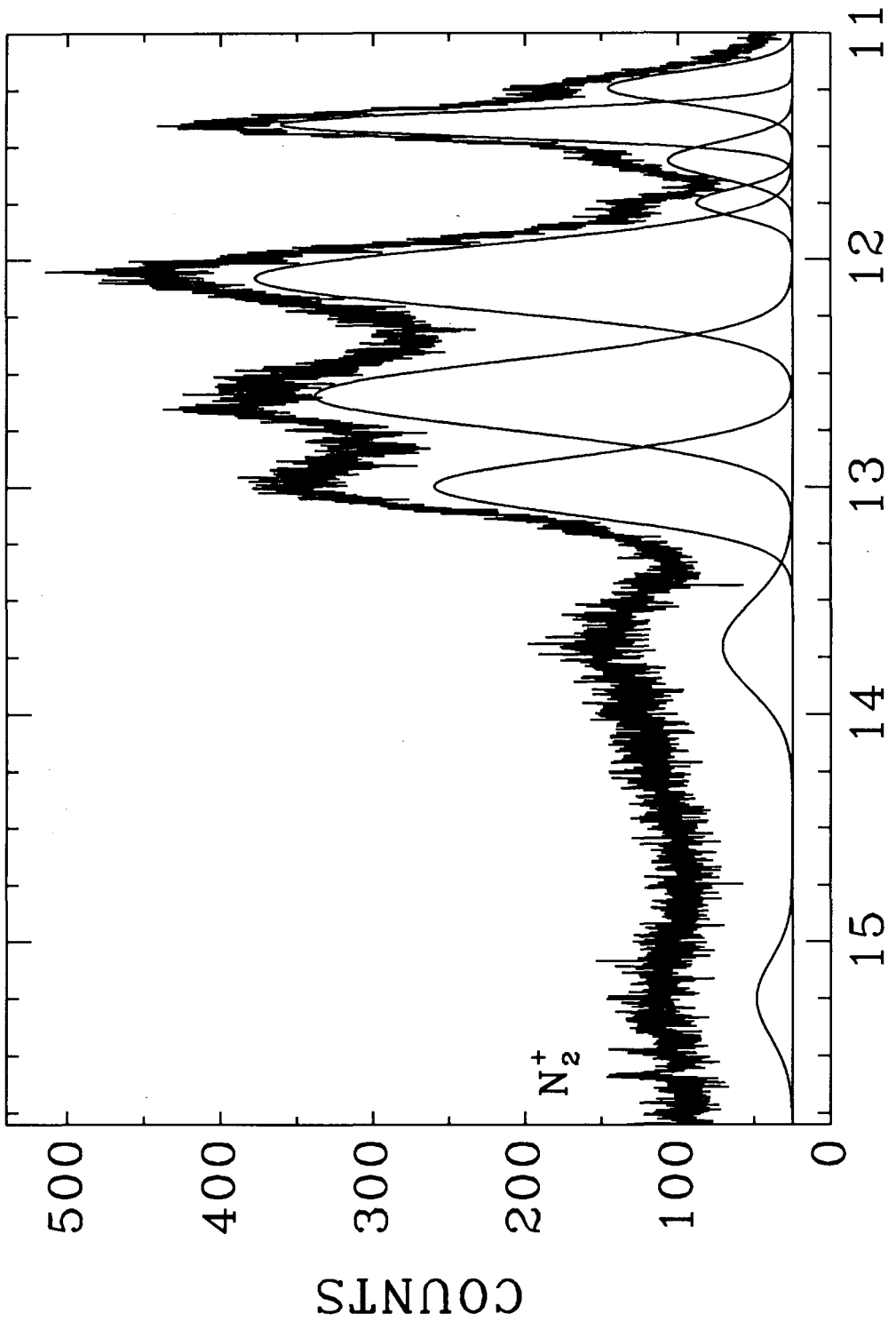

XBL 902-426

Figure 7

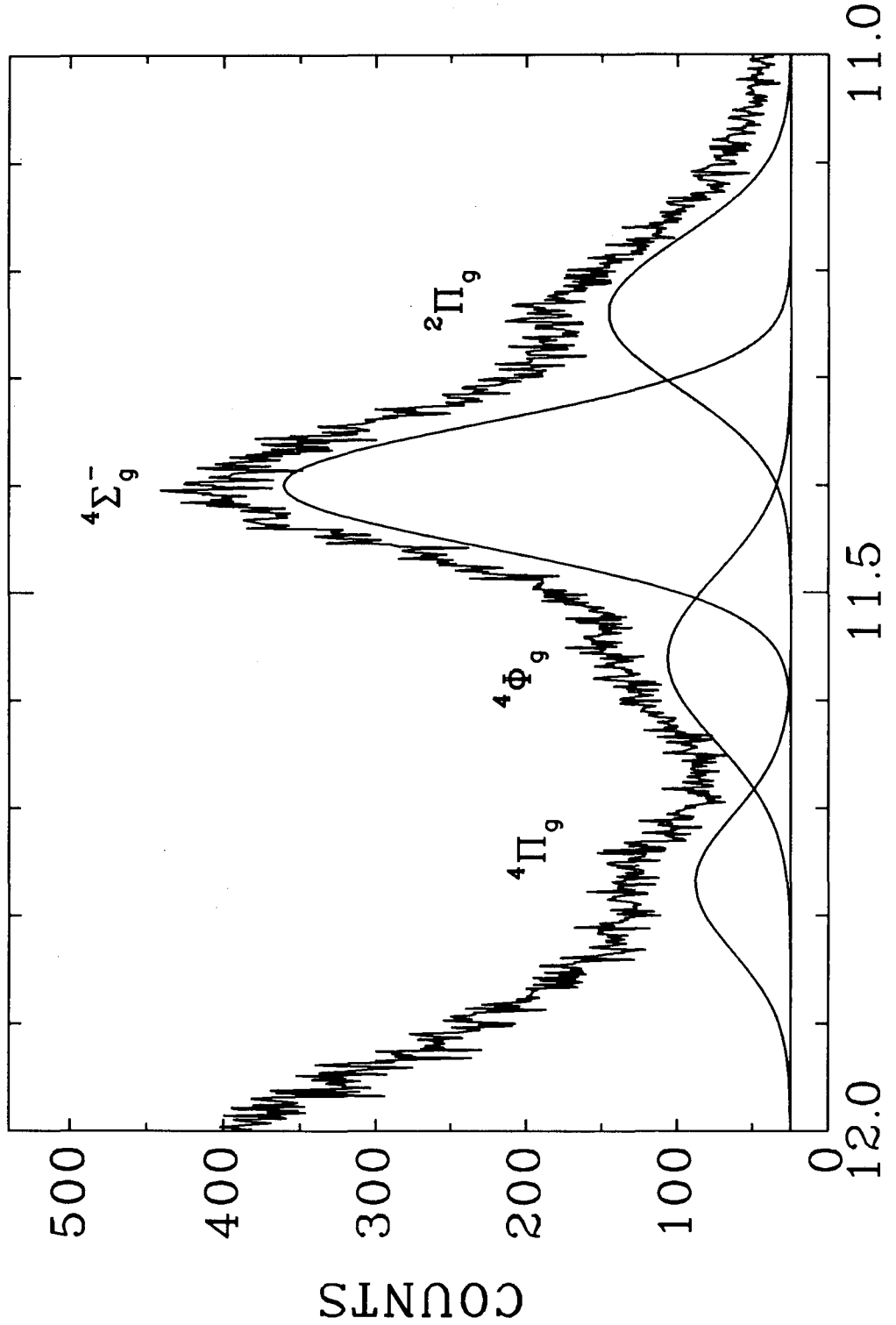

XBL 902-427

Figure 8

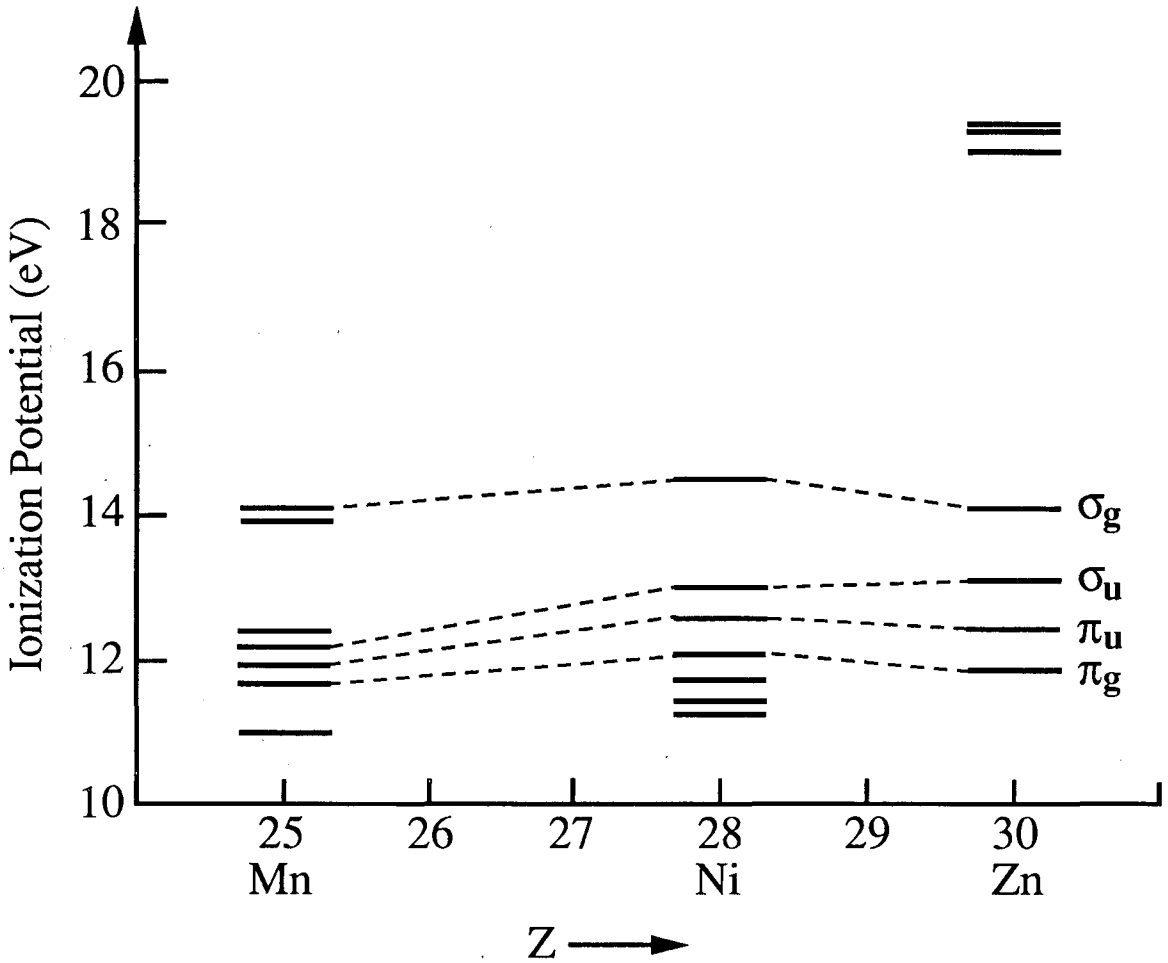
Ionization Potential (eV)
20
18
16
14
12
10
25
Mn
26
27
28
Ni
29
30
Zn
Z
σ_g
σ_u
π_u
π_g

Figure 9

Appendix

Publications from Graduate Work

1. "Photoelectron Spectroscopy and Infrared Femtosecond Intramolecular Dynamics of $C_2H_2^+$ and $C_2D_2^+$",
   J.E. Reutt, L.S. Wang, J.E. Pollard, D.J. Trevor, Y.T. Lee, and D.A. Shirley
   J. Chem. Phys. **84**, 3022 (1986)

2. "Molecular Beam Photoelectron Spectroscopy of $Ni(CO)_4$",
   J.E. Reutt, L.S. Wang, Y.T. Lee, and D.A. Shirley
   Chem. Phys. Lett. **126**, 399 (1986)

3. "Molecular Beam Photoelectron Spectroscopy and Femtosecond Intramolecular Dynamics of H_2O^+ and D_2O^+",
   J.E. Reutt, L.S. Wang, Y.T. Lee, and D.A. Shirley
   J. Chem. Phys. **85**, 6928 (1986)

4. "Molecular Beam Photoelectron Spectroscopy: The $C_2D_4^+$ ($X\ ^2B_3$) Ground State",
   L.S. Wang, J.E. Pollard, Y.T. Lee, and D.A. Shirley
   J. Chem. Phys. **86**, 3216 (1987)

5. "Molecular Beam Photoelectron Spectroscopy of SO_2: Geometry, Spectroscopy, and Dynamics of SO_2^+",
   L.S. Wang, Y.T. Lee, and D.A. Shirley
   J. Chem. Phys. **87**, 2489 (1987)

6. "High Resolution UV Photoelectron Spectroscopy of CO_2^+, COS^+, and CS_2^+ Using Supersonic Molecular Beams",
   L.S. Wang, J.E. Reutt, Y.T. Lee, and D.A. Shirley

7. "Vibrational Spectra of Se_2^+ and Te_2^+ in Their Ground States",
   L.S. Wang, B. Niu, Y.T. Lee, and D.A. Shirley
   Chem. Phys. Lett. **158**, 297 (1989)

8. "Photoelectron Spectroscopy and Electronic Structure of Heavy Group IV-VI diatomics",
   L.S. Wang, B. Niu, Y.T. Lee, D.A. Shirley, and K. Balasubramanian
   J. Chem. Phys. **92**, 899 (1990)

9. "High Temperature and High Resolution UV Photoelectron Spectroscopy Using Supersonic Molecular Beams",
   L.S. Wang, J.E. Reutt-Robey, B. Niu, Y.T. Lee, and D.A. Shirley
   J. Electron Spectrosc. Relat. Phenom. (in press); LBL-27583

10. "High Resolution Photoelectron Spectroscopy of Clusters of Group V Elements",
    L.S. Wang, B. Niu, Y.T. Lee, and D.A. Shirley
    Physica Scripta (in press); LBL-27584

11. "Electronic Structure and Chemical Bonding of the First Row Transition Metal Dichlorides: $MnCl_2$, $NiCl_2$, and $ZnCl_2$ — A High Resolution Photoelectron Spectroscopic Study",
    L.S. Wang, B. Niu, Y.T. Lee, and D.A. Shirley
    Submitted to *J. Chem. Phys.*; LBL-27925

12. "Photoelectron Spectroscopy and Electronic Structure of Clusters of Group V Elements. I. Dimers",
    L.S. Wang, Y.T. Lee, D.A. Shirley, P. Feng, and K. Balasubramanian
    (In preparation)

13. "Photoelectron Spectroscopy and Electronic Structure of Clusters of Group V Elements. II. Tetramers: The ^2E state and the Theory of the E⊗e Jahn-Teller Problem in Tetrahedral Clusters",
    E.R. Grant, A. Ghelichkhani, L.S. Wang, B.Niu, Y.T. Lee, and D.A. Shirley
    (In preparation)

14. "Photoelectron Spectroscopy and Electronic Structure of Clusters of Group V Elements. III. Tetramers: The $^2T_2$ and $^2A_1$ states",
    L.S. Wang, B.Niu, Y.T. Lee, D.A. Shirley, A. Ghelichkhani, and E.R. Grant
    (In preparation)

15. "Fourier Transform Photoelectron Spectroscopy of H_2S and D_2S"
    L.S. Wang, Y.T. Lee, and D.A. Shirley
    (In preparation)

Acknowledgment

Many people have helped me during my graduate study at Berkeley and contributed to this thesis. I wish to take this opportunity to acknowledge those who affected me the most.

I have had the privilege to work with two distinguished scientists, Professor David A. Shirley and Professor Yuan T. Lee, to whom I am greatly indebted for their support and encouragement. They each have taught me much both scientifically and otherwise. Their insights and approaches to science have eminently influenced every one who has come into contact with them and shall benefit me immeasurably. Their generosities and supports for younger scientists are very well appreciated. In particular, I am much obliged to Dave, who has read the manuscript of every single Chapter of this thesis both critically and thoroughly.

Foremost, I would like to thank Janice Reutt. She patiently taught me high resolution photoelectron spectroscopy and the working of the machine. She should also be credited with the initial design and construction of the high temperature molecular beam source, on which this thesis is based. Baohua Niu joined me in the last stage of the high temperature project. I am grateful for his collaboration on a number of high temperature experiments and for working long hours with me. I also benefited from many stimulating conversations with Jim Pollard and Dennis Trevor, who were responsible for building the molecular beam photoelectron spectrometer.

I was fortunate to have the opportunities to collaborate with Professor K. Balasubramanian, Professor E.R. Grant, and Mr. A. Ghelichkhani on the theoretical part of this thesis. Prof. Balasubramanian did the calculations in Chapter 3; Prof. Grant and Mr. Ghelichkhani did the vibronic calculations in Chapter 5. I have learnt a great deal from

many enjoyable discussions with them. I am also appreciative to Dr. Dan Neumark for providing me a copy of the code for calculating the Franck-Condon factors for diatomic molecules.

I wish to thank the entire Shirley group and Lee group. It has been intellectually stimulating to interact with many individuals from these groups. The Lee group has been always friendly and willing to help when I just needed to borrow some parts or even a mechanical pump. In particular, my thanks go to Phil Heimann with whom I have had many invaluable discussions. Alexis Schach von Wittenan and Lou Terminello deserve special mentions for their efforts in maintaining the Shirley group computing facilities. Dr. K. Tong Leung was always very encouraging. I have also had many live conversations with Jane Medhurst and Zheng-qing Huang.

Many others at LBL have provided support services, without which nothing could have been accomplished. Wini Heppler and Barbara Moriguchi previously, and James Walker most recently, have managed to keep the Shirley group running. Ann Weightman has also been helpful. Joe Katz was always willing to answer my questions and solve my electronic problems. Herb Riebe and Ed Voronin machined many parts vital to the experiments.

Many friends have made my stay much more enjoyable and pleasant. Special thanks go to: Phil Heimann and Louisa Bonet, Dz-Hung Gwo, and Yunbo Shi. Shi-Jiang Lu and Han-Song Cheng have kept in touch with me from long distances; I appreciate their friendships.

My wife, Li-Qiong, has been a good company and colleague. She has assisted me so much that a lot has been taken for granted. This thesis is as much mine as hers. Her love, support, and encouragement have meant much to me and have been constant sources of inspiration. I also wish to thank my parents for their love and support throughout all these years. I thank my parents-in-law for their encouragement and understanding.

Importantly, I am thankful to my high school teachers in China, Xiu-Cheng Guo, Ting-Cai Hu, Zhen-Long Zhang, and Yu-Lan Wang, for fostering my interests in sciences and encouraging me to pursue a higher education. Teacher Guo directed my interest into Chemistry; Teacher Hu aroused my interest in Mathematics.

Finally, I would like to acknowledge the Chinese Academy of Sciences in conjunction with the Institute of Chemistry for initializing a fellowship program from which I benefited.

This work was supported by the Director, Office of Energy Research, Office of Basic Energy Sciences, Chemical Sciences Division of the U.S. Department of Energy under the Contract No. DE-AC03-76SF00098

LAWRENCE BERKELEY LABORATORY
TECHNICAL INFORMATION DEPARTMENT
1 CYCLOTRON ROAD
BERKELEY, CALIFORNIA 94720